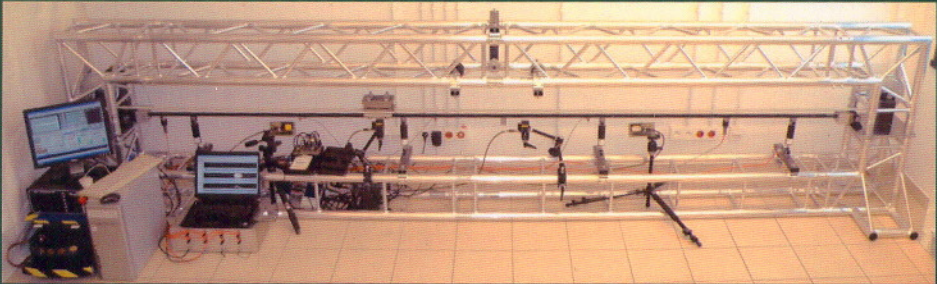


**BIBLIOTEKA MECHANIKI STOSOWANEJ**

**VIBRATION CONTROL  
WITH SMART MATERIALS**

**Czesław Bajer  
Bartłomiej Dyniewicz  
Dominik Pisarski  
Jacek M. Bajkowski**



Instytut Podstawowych Problemów Techniki  
Polskiej Akademii Nauk

**VIBRATION CONTROL  
WITH SMART MATERIALS**

P O L S K A      A K A D E M I A      N A U K  
INSTYTUT PODSTAWOWYCH PROBLEMÓW TECHNIKI

---

**BIBLIOTEKA  
MECHANIKI  
STOSOWANEJ**

**APPLIED  
MECHANICS  
SERIES**

**Seria A. Monografie  
Series A. Monographs**

KOMITET REDAKCYJNY / EDITORIAL COMMITTEE

Zenon Mróz – Przewodniczący/Chairman

Tomasz Kowalewski, Zbigniew Kowalewski

Henryk Petryk, Ryszard Pęcherski

Jerzy Rojek, Kazimierz Sobczyk

Bogusław Lempkowski – Sekretarz/Secretary

Edited by Institute of Fundamental Technological Research  
Polish Academy of Sciences

Wydawnictwo Instytutu Podstawowych Problemów Techniki PAN

WARSZAWA

P O L S K A      A K A D E M I A      N A U K  
INSTYTUT PODSTAWOWYCH PROBLEMÓW TECHNIKI

---

**Czesław I. Bajer**  
**Bartłomiej Dyniewicz**  
**Dominik Pisarski**  
**Jacek M. Bajkowski**

# **Vibration control with smart materials**

WARSZAWA 2015

© Copyright by Instytut Podstawowych Problemów Techniki PAN  
Warszawa 2015

ISBN 978-83-89687-92-0

---

Wydanie I  
Druk ukończono w lutym 2015 r.  
Nakład 200 egz.  
Skład w systemie L<sup>A</sup>T<sub>E</sub>X  
Druk i oprawa: Drukarnia EXPOL P. Rybiński, J. Dąbek Sp. J.  
Włocławek, ul. Brzeska 4

---

# Contents

<b>1. Introduction</b>	<b>11</b>
1.1. Research Fields . . . . .	14
1.2. Solution Methods . . . . .	17
1.3. Vibration Control . . . . .	21
1.4. Vibrating Structures . . . . .	22
1.4.1. Structures under Moving Loads . . . . .	23
1.4.2. Shafts . . . . .	24
1.4.3. Control of Sandwich Structures . . . . .	24
<b>Bibliography</b>	<b>27</b>
<b>2. Smart Materials in Vibrations Damping</b>	<b>29</b>
2.1. Magnetorheological Fluids . . . . .	31
2.1.1. Magnetorheological Devices and Applications . . . . .	35
2.1.2. Linear Stroke Damper . . . . .	39
2.1.3. Rotary Damper . . . . .	45
2.1.4. Designing Linear Stroke Magnetorheological Dampers . . . . .	49
2.1.5. Designing Rotary Magnetorheological Devices . . . . .	59
2.2. Magnetorheological Elastomers . . . . .	60
2.2.1. Beam with Magnetorheological Elastomer . . . . .	64
2.3. Granular Materials . . . . .	68
2.3.1. Granular Structure Subjected to Underpressure . . . . .	69
2.3.2. Beam with Smart Granular Structure . . . . .	73
<b>Bibliography</b>	<b>81</b>
<b>3. Controlled Structures</b>	<b>87</b>
3.1. The Beam Span under the Inertial Moving Load . . . . .	90
3.1.1. Mathematical Model . . . . .	96
3.1.2. Semi-analytical Solution . . . . .	100
3.1.3. Numerical Description of the Problem . . . . .	104

3.2.	The Shaft under the Harmonic Excitation . . . . .	111
3.2.1.	Mathematical Model . . . . .	113
3.2.2.	Analytical Solution . . . . .	114
3.2.3.	Semi-analytical Solution and Numerical Model . . . . .	117
3.3.	Vibrations of the Sandwich Beam Induced by the Initial Con- ditions . . . . .	119
3.3.1.	Mathematical Model . . . . .	120
3.3.2.	Analytical Solution . . . . .	124
3.4.	The Structure Based on the Granular Material . . . . .	127
3.4.1.	Mathematical Model . . . . .	128
3.4.2.	Analytical Solution . . . . .	130
<b>Bibliography</b>		<b>133</b>
<b>4.</b>	<b>Optimal Control for Vibrating Mechanical Systems</b>	<b>139</b>
4.1.	State of the Art . . . . .	140
4.2.	Finite Horizon Optimal Control Problem . . . . .	144
4.2.1.	First Order Necessary Optimality Condition . . . . .	145
4.2.2.	Solution Methods . . . . .	148
4.3.	Optimal Control Problem for Switched Systems . . . . .	150
4.4.	Distributed Optimal Control via Nash Games . . . . .	152
4.5.	Receding Horizon Control Scheme . . . . .	156
4.6.	Optimal Control Problem for Semi-Active Systems . . . . .	157
4.6.1.	Necessary Optimality Condition . . . . .	159
4.6.2.	Prediction of Switches in Optimal Controls . . . . .	160
4.6.3.	Numerical Example: Optimal Semi-Active Controlled Oscillator (Gradient Based Method) . . . . .	162
4.6.4.	The Method of Parameterized Switching Times . . . . .	166
4.6.5.	Numerical Example: Optimal Semi-Active Controlled Oscillator (Method of Switching Times) . . . . .	170
<b>Bibliography</b>		<b>177</b>
<b>5.</b>	<b>Engineering Problems</b>	<b>181</b>
5.1.	Semi-active Control of Beam Subjected to a Moving Load . . . . .	182
5.1.1.	Passive Cases . . . . .	185
5.1.2.	Optimal Case (Gradient Based Method) . . . . .	185
5.1.3.	Optimal Case (Switching Times Method) . . . . .	187
5.2.	Beam Under the Moving Mass . . . . .	192
5.2.1.	Experimental results . . . . .	198

---

5.2.2. Conclusions . . . . .	202
5.3. Rotating Shaft . . . . .	205
5.3.1. Optimal Control Problem for the Vibrations . . . . .	205
5.3.2. Experiment . . . . .	209
5.4. Sandwich Beam with Magnetic Elastomer . . . . .	216
5.4.1. Experimental Verification . . . . .	220
5.4.2. Conclusions . . . . .	223
5.5. Granular Material . . . . .	224
5.5.1. Identification of the Parameters . . . . .	224
5.5.2. Adaptive Control Strategy . . . . .	227
5.5.3. Experimental Study . . . . .	230
5.5.4. Conclusions . . . . .	233
<b>Bibliography</b>	<b>235</b>
<b>6. Conclusions and Perspectives</b>	<b>237</b>
6.1. Perspectives . . . . .	238
6.2. Recommendations . . . . .	240



# Preface

Elimination of vibration is the important task in the period of rapid technological development. Although theoretical basis was created many years ago, practical solutions are not sufficiently implemented. The vibration theory and the control theory are the base of our further considerations.

The work was carried out at the Institute of Fundamental Technological Research (IPPT), Polish Academy of Sciences, and at the Faculty of Automotive and Construction Machinery Engineering (SIMR), Warsaw University of Technology. The research team consists mostly of the members of the Laboratory of the Control and Dynamics of Structures. They represent a wide scope of interest: mathematical analysis, mechanics, computational dynamics, control theory, and experimental studies. Our research group is involved in research in vibrations of mechanical systems. In a special interest we place transport dynamics, vibration induced by moving loads, both massless and inertial, coupled loads, dynamics of sandwich beams and rotating shafts. Deep analytical investigations followed by numerical and experimental verifications resulted in some discovered phenomena. However, engineering applications are a serious challenge. Theoretically simple and clear analytical dependencies that prove efficiency of the solution, turn out to be incorrect and ineffective in practice. Incorrect assumptions, material parameters and constitutive laws are the common reason of the defeat, or at least a decrease of the efficiency. Therefore experimental tests are on pair with the analysis.

Semi-active control of vibrations enhances damping properties of structural elements. This technique can be performed in several ways. The friction or the damping are good examples of possible parametric control in the differential equation. Magnetorheological dampers have become popular in recent years. Unfortunately, the fluid contained in them exhibits disadvantages. We will try to use alternatively elastomers and granular materials, both controlled externally. And again theoretical derivations should be related to experiments.

The book is addressed to PhD students, researchers, as well as engineers. It covers the fields of control of structures in civil engineering and machinery engineering. We hope that in the book the reader will find the theoretical background of structural vibrations, optimal semi-active control strategies and examples of numerical simulations of real engineering structures. Non-classical materials will deliver data that could be used in further research.

The work was supported by the National Centre for Research and Development, Lider/26/40/L-2/10/NCBiR/2011.

# Chapter 1

## Introduction

Vibration as a mechanical phenomenon occurs practically in all areas of our life. The oscillatory motion about the equilibrium state is characterised by several parameters. Our simple systematics divides the oscillatory motion into two groups: oscillations with low or high frequency, in which the motion of material points is considered, and waves, where a disturbance travels through a material domain, accompanied by a transfer of energy. In both cases we usually apply different methods of elimination of vibration.

The exploitation of existing engineering structures in terms of increased operational requirements associated with an increase of the load and the frequency of its occurrence, forces us to take into account in the design process the effects associated with the dynamics of the structure. Technical devices are more complex nowadays and are subjected to extreme loads. For example an increase of the speed and weight of trains causes new problems, so far poorly investigated. These adverse phenomena caused wave effects. Wave processes play an increasingly important role in the rail vehicle-track systems, as the travelling speed approaches some characteristic critical velocity values. A sharp increase of vibration amplitude is a harmful external effect. This in turn raises the noise level, increase of wear and reduction of reliability and safety of the structure. One of many practical applications of the research can be found in how to protect buildings from vibrations caused by travelling rail vehicles in the case of wear of rolling surfaces (Fig. 1.1).

Moving sources of vibrations in transportation can not be entirely eliminated. They are joined with the nature of rolling phenomenon, periodicity of a track and waved wear of rolling surfaces of wheels and rails. This problem has been studied extensively in many centres in the country and abroad. It

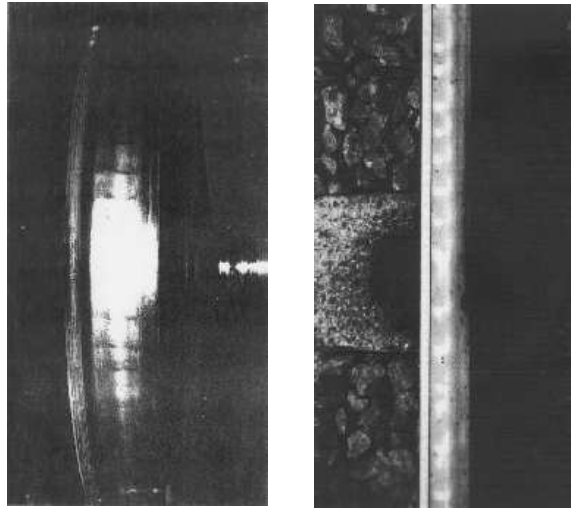


**Figure 1.1.** Corrugated wheel and rail.

was shown that, despite the smooth surface and a rectilinear motion of the wheel axis, we observe oscillations of contact forces [3]. With the increase of rolling speed the number of oscillations related to the circumference of a circle decreases, increasing the amplitude of vibration and amplitude of the contact force. Also, in the direction transverse to the direction of rolling of wheels we deal with excitation of vibrations of the track and the sub-grade. The wheel rolling on the road or on the track is affected by a complex load. Dynamic phenomena cause changes in the relationship of individual components. Some of the forces act in a manner similar to the stationary type, the other in an oscillatory way, or short-term, for example, while driving through irregularities (Fig. 1.2). Research carried out in our team enabled to describe the phenomenon of lateral slip [15]. On the base of experimental data recorded on the foundation of the subway track, on the sleeper of the classical railway and on the laboratory stand the existence of double periodic vibrations induced by lateral slipping was proven. This type of phenomenon increases the amplitude of vibration and noise caused by passing trains. Another important factor is the thermal expansion of the rails. In our climate the temperature of rails during the year varies significantly and the interval may exceed  $70^{\circ}\text{C}$ . In tracks made in non-contact technology, axial internal stresses arise. The increase of compressive stress in rails increases their eigen-frequencies, shifting ranges of frequency response and

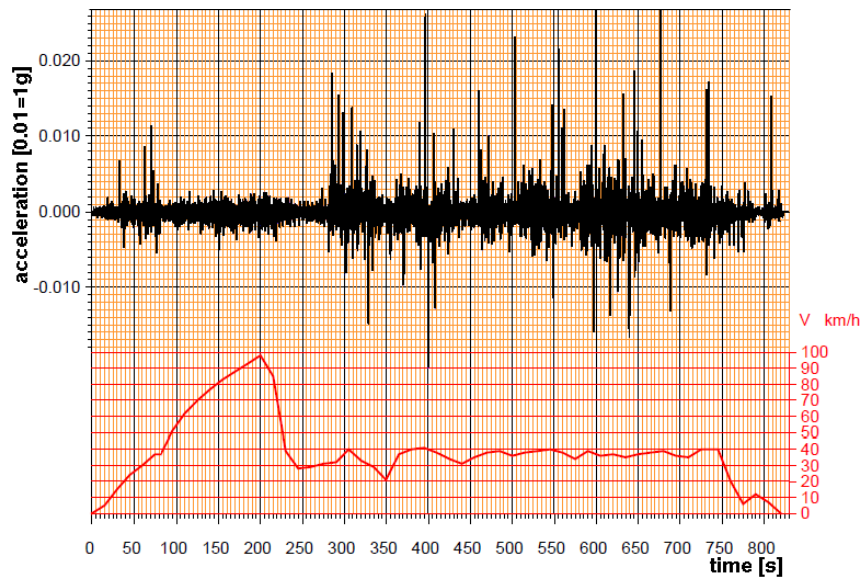


**Figure 1.2.** Vertical accelerations of the axle box of a rail vehicle on the track at different velocities.

decay bands. These bands play a key role in the propagation of travelling waves caused by passing trains, increasing amplitudes of rail vibrations. The increase of vibrations worsens traction properties, reducing its lifetime and produces noise propagating in the ground and air. The increase of the speed and mass of trains in the future will intensify this effect.

Various smart materials can be used in technical applications that require dynamic control. The most popular are the following:

- **Piezoelectric materials** that produce a voltage when stress is applied. This effect is reversible. A voltage applied to the sample will produce mechanical strain. Suitably designed structures made of these materials can bend, expand or contract under the voltage.
- **Thermoresponsive polymer materials** that exhibit a drastic and discontinuous change of their physical properties with temperature.
- **Magnetorheological and electrorheological fluids** that exhibit increased viscosity under magnetic or electric field. MR fluids are made of iron particles in oil that form chains along the magnetic field lines

and therefore they resist to shear perpendicularly to chains. ER fluids contain mineral particles rearranged in the electric field induced by high voltage, but low current.

- **Ferrofluids** which are liquids that become strongly magnetized in the presence of a magnetic field. The size of particles differs ferrofluid from magnetorheological fluid. MR fluids contain micrometre-scale particles while ferrofluids have nanoparticles that are suspended by Brownian motion and generally will not settle under normal gravity conditions.
- **Magnetorheological elastomers** that are rubber-like materials containing ferromagnetic particles, allowing the increase of stiffness under magnetic field.
- **Ionic polymer-metal composites (IPMCs)** are synthetic nanomaterials that exhibit deformations under an applied voltage or electric field. From this point of view they can be considered as artificial muscles. IPMCs are composed of an ionic polymer like Nafion or Flemion. Under an applied voltage, 1–5 V for a 1×4 cm sample, 0.2 mm thick, ion migration and redistribution due to the imposed voltage across a strip of IPMCs result in a bending deformation.
- **Granular materials** controlled by underpressure, that exhibit significant change of stiffness under atmospheric pressure when small underpressure is applied to the envelope containing granules. The increase of inter-granular friction is observed and that is why the material can be used to fill shared structural elements.

In the further chapters we will present the control of mechanical vibrations with magnetorheological fluids, magnetorheological elastomers, and granular materials.

## 1.1. Research Fields

Problems with vibrations occur practically in all areas of life. Some of them, still important, are gradually dominated by others. Evolution of technology and social requirements change the interest of researchers. Let us take a look at issues that are of special interest.

**Structure health monitoring** In this item we place damage detection based on dynamic response of a structure of its elements. People for ages have captured anomalies using the senses of hearing and touch.

Nowadays we try to do the same automatically. We want to localize a damage and determine its size. A detection of instantaneous parameters, for example loads or temperature influences is also important for exploitation. The proper detection of both the structure parameters and external instantaneous factors allows us to avoid progressive wear or destruction. In power engineering sensors can be placed in pylons and energetic cables loaded by ice and forced by wind. Off-shore structures exposed to wind and waves are intensively examined to avoid environmental contamination. The same technology is applied in aviation. Sensors immediately report excessive vibrations of vital elements of a plane. This field of research is being increasingly developed.

**Dynamics of bridges** This item is extensively investigated, especially for damage detection. Old bridges must carry increasing loads and resist to vehicles at higher speed. The cost of reconstruction is high, especially if it doubles due to construction detours. This question is joined with the influence of the intensity of the traffic, instability of a span under dynamic course, wind induced vibrations of the bridge deck, human structure interaction in slender cable structures, or influence of temperature effects. The damage detection based on dynamic responses induced by a traffic load nowadays is the most attractive domain.

**Infrastructure systems and historical structures** Damages caused by vibrations in surrounding infrastructure are particularly acute in vulnerable historic buildings. Historic brick buildings are fragile, very susceptible to deformation. The low susceptibility of the material, which does not succumb to excessive momentary or long-term deformation is the main reason of damages. The negative impact of infrastructure on the surrounding buildings, particularly in historic sites, forces us to take action to reduce the adverse external effects. We assume the concept of modification of the track structure, to enable influencing its dynamic properties. The size of the load, the speed of motion, the effect of dynamic coupling, as well as external temperature which incorporates axial forces in rails, can be considered as variable factors.

**Energy harvesting** Power recuperation from vibrating objects is in focus of researches. There exist some devices that can generate small amount of power to activate electric circuits far from energy sources. There are attempts of transforming vibration of the oceanic wave motion into

electric power. If the process is widespread, we will be able to reduce the emission of carbon dioxide produced by marine transportation. We will also be able to substitute the conventional thermal power plant by ocean wave power generators. Deep water floating wind turbines can also be a good example of new environments for known mechanical devices. Practically all kinds of motion can be used for changing the mechanical energy into electricity. We can also use: oscillations of a vehicle, vibrations of footbridges, pedestrian steps transformed in boots, etc.

The solution to the problem is not evident. From one point of view we want to retrieve energy from vibrating structures and the higher is the vibration, the more energy will be recovered. From another point of view, oscillations consume energy. Only in the case when vibrations are inevitable we can develop this technology. Otherwise, the reinforcement of the structure, for example the bridge, reduces the energy spent for passage. Then less can be restored.

**Railway transport** Railway transportation returns as a vital link in the economy. Increasing requirements focus attention on technical problems. The crucial goals are: safety, reduced wear of rolling surfaces, noise reduction, protection of surrounding buildings against para-seismic vibrations. Research is mainly based on experiments. Computer simulations are complex since various factors must be taken into account in a proper formulation of the problem. They are: material non-linearity with plasticity of materials and strength hardening, friction, contact between rolling wheels and rails, dynamics, wave phenomena (especially arising from periodicity of the track and interaction between moving contact points induced both by a track and a vehicle), complexity of a rail vehicle and the whole train, and difficulty in determining the ballast and the soil parameters.

**Earthquake engineering** Civil engineering constructions are designed to carry gravitational forces. Vertical loads contribute most to load schemes. Horizontal forces are significant in bridge cranes, wind load of masts, high buildings, bridges, etc. Incidental but important kinematic loads are contributed by earthquakes. Their significant components are horizontal. Constructions are sensitive to such a load. Civil engineers admit two ways in designing: rigid structures that can resist to kinematic excitation and flexible structures that permit large rotations in pre-designed joints and large horizontal displacements. Such

a predicted scenario of deformations can not take into account in advance every unknown excitation. We must steer the random process towards provided schemes. Intelligent technologies should do it for us.

**Damping and base isolation systems** This item is common in machinery engineering and civil engineering. The subject is relatively well explored. Computer simulations facilitate the task. Recently passive damping of vibrations has been replaced with semi-active control. Intelligent materials are developed and progressively applied. New materials, for example shape memory materials or those having reverse characteristics are extensively developed.

## 1.2. Solution Methods

In dynamics we use two types of analyses. The first one is the eigenvalue problem. We determine natural frequencies of vibrations and related natural forms. This task is relatively simple and for discrete analysis it requires stiffness and inertial coefficients or matrices. We usually search for the first several eigenvalues of the matrix. They correspond to first natural frequencies and we compare them with frequencies of possible excitation, to avoid resonant coincidence. The giant number of degrees of freedom is not a condition of high accuracy of results. Even a coarse discretisation results in quite precise result. Unfortunately, poor knowledge of the art of computer modelling forces the growth of the power of computing tools.

The second type of analysis is a group of initial boundary value problems. We perform the discretisation in the same way as in the eigenvalue problem. Additionally we must prescribe boundary conditions to avoid free motion of the structure or its parts. Moreover, a pair of initial conditions, i.e. for example initial velocities and initial displacements of all nodes, must be given. Then the process of time integration of the differential motion equation allows us to create step-by-step the animation, and survey for domains with exceeded stresses (Fig. 1.3).

A more general approach to time integration can be carried on with the space-time finite element approach [1, 2, 4, 7]. An essential feature which distinguish the space-time element method from traditional approaches to solving initial-boundary problems is its discretisation of the differential equation. Classically, two-step interpolation is used. The spatial variables are separated from the time. Therefore, in the first stage, the system of partial differential equations is transformed into a system of ordinary differential equations in time of the basic state variables, and further purely numeri-

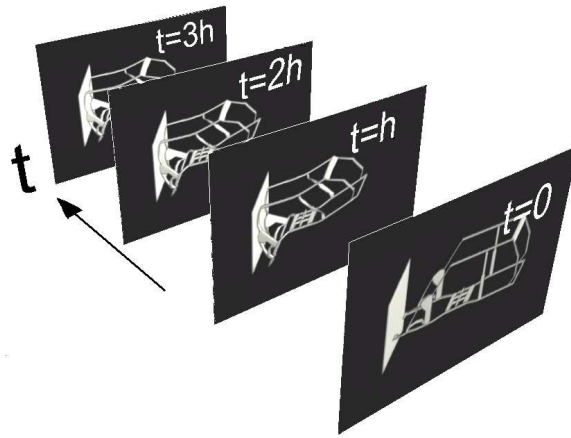


**Figure 1.3.** Dynamic problem as a series of static tasks.

cal procedures are applied for the integration of the differential equations in time. This approach has its advantages, mainly due to the possibility of selecting the most effective tools separately for each stage, including strict methods. In addition, the passage from the static to the dynamic solution is simpler. Most numerical procedures for static analysis are easy to use in this situation. In fact, the solution to the dynamics reduces to the solution of a set of static tasks. The control of the estimation error and the unconditional stability of the solution due to the time step involved in the integration of the differential equation are also significant. All this makes the most popular methods, i.e., the finite element method combined with the method of integration over time, e.g. the Newmark method, a permanent part of the practise of simulation calculations.

One of the drawbacks of the classical approach is the need for partition (discretisation) of the considered spatial area which is constant in time (stationary). In this case, the local adaptation of the mesh to the processes involved (e.g., the development of plastic zones, zones of contact, propagation of cracks, the movement of the load) is very difficult. The existing methods of adaptation, including multigrid methods, or moving meshes, are an attempt to adapt a numerical process to a phenomenon, and to remove this defect.

The second major drawback is usually the use of the same procedure in time integration for all mesh nodes of the structure. Although it is possible to use locally procedures for the time integration of differential equations with

higher accuracy, in order to describe all variables of the physical phenomena within the same time interval, we generally do not improve the numerical model of the problem.

The space-time approximation opens up new opportunities by applying simplicial space-time subdomains (Fig. 1.4).

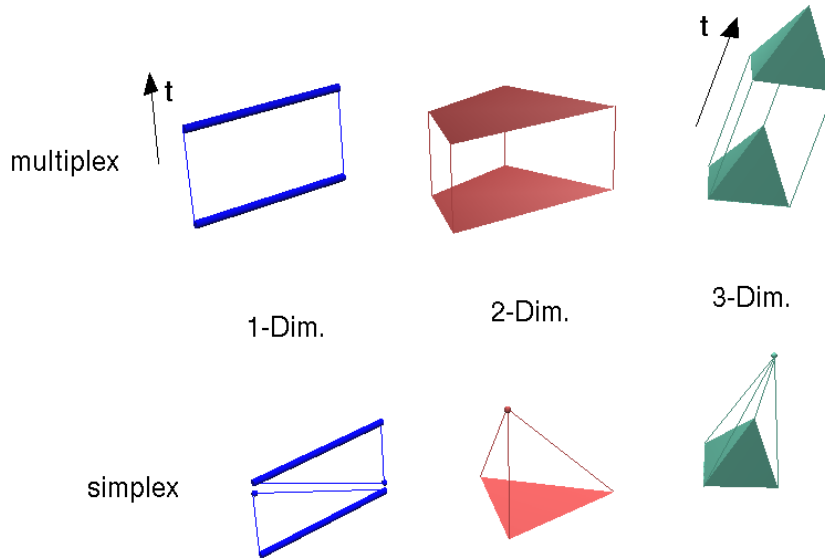


**Figure 1.4.** Examples of multiplex and simplex elements of one-, two-, and three-dimensional objects.

Of course all the complexities of the calculations can not categorically determine the advantages and disadvantages of the different groups of methods. Artificial damping of higher frequency vibrations by one method of calculation is a defect in wave problems, but an advantage in the analysis of structural vibrations. The selection of a computational tool is carried out based on the type of task, the phenomena under examination, the required accuracy of the arithmetical operations which can be performed on the computer, and non-substantive factors (e.g., the availability of numerical procedures, one's own experiences, etc.).

The space-time approximation of solutions to dynamic problems lacks some of these drawbacks of the classical numerical methods. However, the method is not perfect. In essence, it reduces to the fact that func-

tions  $\mathbf{w}$ , characterising a solution, are described in space-time sub-areas through nodal parameters  $\mathbf{q}_e$  (Fig. 1.5)

$$\mathbf{w}(\mathbf{x}, t) = \mathbf{N}(\mathbf{x}, t) \mathbf{q}_e. \quad (1.1)$$

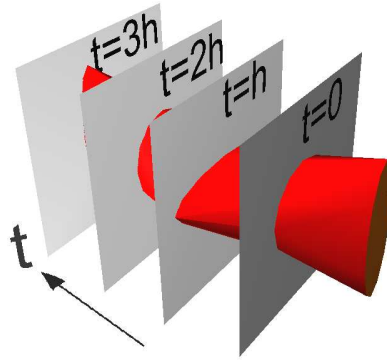


**Figure 1.5.** Continuous representation time of a dynamic problem.

The matrix  $\mathbf{N}(\mathbf{x}, t)$  is a matrix of interpolation functions, depending on the spatial variables and the time. In the classical approach the spatial discretisation uses the interpolation formula  $\mathbf{w}(\mathbf{x}, t) = \mathbf{N}(\mathbf{x}) \mathbf{q}_e(t)$ . The space-time approach assumes a continuous distribution of characteristic functions, such as displacement or velocity, in the whole space-time domain  $\Omega = \{\mathbf{x}, t : \mathbf{x} \in V(t), 0 \leq t < \infty\}$  where the structure is considered. In discrete time  $t_i, i = 0, 1, 2, \dots$ , we can use different bases of nodes (with certain restrictions), and therefore adapt the mesh to current requirements. This has the following possibilities:

- the possibility of redistributing the mesh, depending on the changing distribution of the approximation error,
- moving the zone of a mesh refinement together with a travelling load,
- the ability to adjust the sides of the elements to characteristic lines determined in the space-time domain: the front of the plastic area, the front of the material phase change, in particular — the possibility of modelling a moving edge of a body,

- the use of mesh shapes other than the space-mesh multiplexed meshes: multiplexed networks are the result of an evolution of the spatial grid in the layer of time and the corresponding elements have the same number of nodes in the initial and final time; other meshes, such as simplices, have new, important properties; simplex elements with dimension  $n$  have  $n + 1$  nodes at the initial time and  $i + 1$  nodes at the final time ( $i = 0, 1, \dots, n$ ),
- the possibility of individual formulation of the time integration in an active manner for each spatial element,
- the particular case of space-time approximation can give a classical method of solution, based on fixed grid nodes (evolving only with the material).

This last point can be expanded to a statement that space-time approximation and the resultant space-time element method are a generalisation of the finite element method, classically referred to a real space. By the real space we mean the space of spatial variables  $x, y, z$ , in contrast to space-time, which is described by the spatial variables  $x, y, z$ , and the time  $t$ .

### 1.3. Vibration Control

Self-adaptive structures are currently extensively investigated. Properly designed structures allow significant improvement of dynamic properties of systems, comparing to their passive equivalents. First, the structure gains higher load carrying capacity with the same weight. Second, we obtain lower displacements, and thus we improve the fatigue strength, increasing the safety of the structure. Therefore the synergy of a layered structure and semi-active controlled smart material in many cases will reduce the weight and the cost of the structure. Properly selected control strategy applied to some factors of the structure enables us to use this type of innovative solutions in numerous practical applications.

Lightweight structures have been intensively investigated in recent years. Optimal design with low weight is insufficient in the case of dynamic behaviour of the structure. There are some approaches to decreasing vibration level.

**Passive vibration absorbers** The idea is performed by means of dynamic vibration absorbers as a set of tuned mass dampers. Both transverse

and rotational types of absorbers can be applied. They are efficient in the case of instantaneous increase of amplitudes or in shocks.

**Active control** Control forces are generated by electric or hydraulic actuators imposed to selected points or to tendons [19]. The actuators can generate both transverse control force and bending moment. It enables us to control the predominant lowest vibration modes of the structure whereas the piezo-electric actuators are used to control higher ones. The possibility of unstable behaviour in the case of improper design is the disadvantage of this solution. Applications are energy consuming.

**Semi-active damping** The control is performed by viscous dampers installed in the structure [16]. For example the span of the beam can be supported by viscous dampers. The damping properties are changed according to displacements of selected points or to other, more complex observation of the structure response. Such a control always results in stable responses.

Semi-active structural control has been intensively studied for many years in the team. The literature devoted to control techniques is numerous. The use of semi-active supports for the structure subjected to a moving load was first proposed by Bajer and Bogacz in [8]. By means of numerical simulations the authors demonstrated that in a wide range of travel velocities the switching damping strategies outperform standard passive solution. The idea was then extended by Pisarski and Bajer in [17] and [18], where by introducing rigorous analysis and optimisation techniques the authors concluded that even one switching action in each damper can provide smooth load passages. The total deflection of the load trajectory from the straight line was reduced up to 50%. This research was continued by Dyniewicz et al. [7, 9, 10, 13]. Adaptive damping has also been successfully applied to torsionally vibrating systems [11, 12]. Periodic activation of rotary magneto-rheological dampers effected the reduction of vibration amplitudes to a greater extent than in the case of the passive solution. The developed control concept has been successfully verified experimentally. Elaborated stabilisation algorithms are used in devices such as the coal mills or helicopter rotors.

## 1.4. Vibrating Structures

Various sources induce vibrations. Usually they are classified in two groups: natural sources and effects of human activity. In the first group we can place wind blows, waves in water reservoirs, earthquakes. Human activity is much

more extensive. The industrial and home machinery, vehicles, vibrations induced by drive systems, suspension and motion over wavy road or periodic track, etc.

In all the cases we focus our attention on structural elements that are essential for our life comfort. They are buildings, bridges, tracks, generally infrastructure, machines, vehicles, planes, but also ultrasonic devices, musical instruments etc.

Let us look at some engineering problems that can be treated with semi-active control.

#### 1.4.1. Structures under Moving Loads

In the literature we can find complete analytical solutions of the constant force moving along a structure, which is characterised by zero inertia. An excellent summary of these works is given by Frýba in his monograph [14], discussing in detail the majority of these works. Unfortunately, the influence of inertia is essential, especially in the case of wave problems. If we consider small displacements in our mathematical model, the discontinuity of the trajectory of a moving material point near the end support appears. At points of discontinuity one should expect a sharp increase of the speed of transverse displacements and forces acting on the system. In practice, this corresponds to an impact near the end support. Such effects are observed in reality. Semi-analytical solutions are not very versatile. Assumption of other boundary conditions forces an elaboration of a new method of calculation. Semi-analytical solutions are not suitable in engineering applications. However, they are well suited for the verification of numerical solutions. Problems show up when we perform computer simulations. In the case of wave problem numerical description of the moving inertial loads requires great mathematical care. Otherwise we get a wrong solution. Nowadays there are no commercial computing packages that would enable direct simulation of loads, both gravity and inertial, moving at high velocity. Inclusion of inertia of the moving load requires not only modification of the right-hand side vector in the system of equations, but also selected parts of global matrices of inertia, damping and stiffness of the system, step by step. The first study discussing the influence of inertia of the moving mass is given in [20]. It relates to an inertial load moving at constant speed on the Euler beam. Further works are also related to beams or plates in which the nodal displacements and rotation angles are interpolated by cubic polynomials. Application of displacements interpolation at nodes by the 3rd order polynomial poses no problem with the derivation of the matrix responsible

for the description of the travelling mass particle. Unfortunately, the Euler beam equation is not a purely wave equation. The study of wave phenomena is possible by using a more complex model of the Timoshenko beam in which the vibration equation takes into account the influence of lateral forces and moments of inertia on the line deflection of a beam. Independent interpolation of displacements and rotation angles of the Timoshenko beam causes serious problems. Linear interpolation of nodal physical parameters with shape functions precludes designation of a centrifugal acceleration of a moving mass particle. In our previous works [5, 6], we presented a method for determining matrices responsible for the description of the moving mass of the space-time finite element method using linear interpolation. Original finite elements carrying a moving mass particle were elaborated. In the literature correct solutions for this group of problems were reported in [7].

#### **1.4.2. Shafts**

Rotating elements always generate vibrations. Unbalance is sometimes required. However, usually we eliminate sources of centrifugal forces as much as possible. We also tend to distribute uniformly in time the torque. This is important in the transfer of power in a variety of devices: generators in power plants, high-speed turbines, wind turbines, etc. Wind turbines work under turbulent and unpredictable environmental conditions. Controlled influence on mechanical properties of rotating machines is essential. A good way is to modify the inertia distribution of the shaft by adding supplementary rotating masses. It can be done by means of a magnetorheological clutch. Mistuning allows to avoid resonant frequencies. Another method involves the control of the motor supply. Other techniques reduce clearances in gears and transmission of drive.

#### **1.4.3. Control of Sandwich Structures**

Sandwich structures with a core made of an intelligent material can be used to stabilise motion of various types of structures. One of the branches of applications is the aerospace industry. Aerospace engineering is based on layered structures with viscoelastic core. Modern airliners are built in nearly 50% of the layered structures. The ability to modify the internal layer parameters allows us to influence dynamic properties of the structure. The increase of load carrying capacity and requirement of reduction of the weight of airplanes will lower fuel consumption per transported ton. This allows us to reduce cost of flights or increase the range of airliners. Lower fuel consump-

tion enables to reduce the emission of harmful gases into the atmosphere.

Another possible application of adaptive layered construction is the stabilisation of the offshore oil platforms. Unexpected load increase, e.g. during a severe storm can cause damage to the structure. The platform adapting to a new situation will prevent ecological disasters associated with the oil spill, not to mention the financial loss. The new design of the drilling platform would also enlarge regions of extraction in the area so far uneconomic, due to the hard work conditions.

The automotive industry may also be a potential recipient of the smart layered solutions. Vibrations generated by the vehicle drive system and the suspension could be suppressed by the self-adaptive absorbers. Such solutions enable to improve the travelling comfort. Statistics show that drivers fatigue is one of the leading factors of car accidents. However, it seems that the most important potential recipient of intelligent sandwich structure applications are modern bridges. Only in the United States about 40% bridges are obsolete or are not able to support current requirements. Research proves that half of the cost of maintenance the bridge is traffic redirection to another route, during its construction or reconstruction. In the world there are attempts to construct bridges with composite structures. The use of the lightweight layered prefabricated elements allows us to speed up the construction significantly and thereby save tax cash. Additionally, there is a benefit associated with a lack of corrosion. In this type of structure the layered elements with an intelligent core could be used. Properly developed adaptive control strategies in smart sandwich structures subjected to a moving load would significantly increase load carrying capacity of the bridge.

The core material influences the beam properties. Its controllability gives us new opportunities for modelling. The control of the shear variable is the simplest way to modify the stiffness. Both outer bending elements can be joined in many ways. Frictional junction can be performed by various locks, for example electromagnetic. Friction dissipates energy or shifts frequencies of vibration to higher modes. In such a case the energy of vibrations at higher frequencies dissipates more intensively than at lower frequencies. Frictional elements can not be designed as structural elements. They require a supplementary material. In our opinion a uniform intelligent filling material in sandwich beams is more promising. Elastomers and granular materials will be used in further investigations. Various kinds of each of them require proceeding study of material parameters. Static stiffness, inter-granular friction, dissipation, and resulting homogenisation must be determined dynamically and finally verified in various structures. Otherwise results will not be credible. In the next Chapter we will present properties of exemplary materials

used in our study. Flexibility to shape and ability to fill the space is assumed as their major advantage.

In the book we will present some adaptive techniques efficient in applications to bended or twisted elements. Beams with semi-active control of transverse displacements and rotating shafts will be considered as commonly used structural elements in civil and machinery engineering.

First non-classical materials useful in the control will be described. Magneto-rheological fluids, magnetic elastomers and vacuum-steered granular materials will be presented. Then selected engineering problems will be formulated and analytically solved. Methods of numerical analysis will also be derived. Further contributions to the control theory and semi-active methods will be given. Analytical and numerical examples will prove the efficiency of the approach. Finally experimental verifications of prior analyses will demonstrate practical efficiency of semi-active methods of the vibration control in comparison with passive damping. Comments and remarks will reveal the prospects for further research and applications.

# Bibliography

- [1] C. I. Bajer. Triangular and tetrahedral space–time finite elements in vibration analysis. *International Journal for Numerical Methods in Engineering*, 23:2031–2048, 1986.
- [2] C. I. Bajer. Notes on the stability of non–rectangular space–time finite elements. *International Journal for Numerical Methods in Engineering*, 24:1721–1739, 1987.
- [3] C. I. Bajer. The space-time approach to rail/wheel contact and corrugations problem. *Comp. Ass. Mech. Eng. Sci.*, 5(2):267–283, 1998.
- [4] C. I. Bajer and C. Bohatier. The soft way method and the velocity formulation. *Computers and Structures*, 55(6):1015–1025, 1995.
- [5] C. I. Bajer and B. Dyniewicz. Space-time approach to numerical analysis of a string with a moving mass. *International Journal for Numerical Methods in Engineering*, 76(10):1528–1543, 2008.
- [6] C. I. Bajer and B. Dyniewicz. Numerical modelling of structure vibrations under inertial moving load. *Archive of Applied Mechanics*, 79(6-7):499–508, 2009.
- [7] C. I. Bajer and B. Dyniewicz. *Numerical analysis of vibrations of structures under moving inertial load*. Springer, 2012.
- [8] R. Bogacz and C. I. Bajer. Active control of beams under moving load. *Journal of Theoretical and Applied Mechanics*, 38(3):523–530, 2000.
- [9] B. Dyniewicz. Space-time finite element approach to general description of a moving inertial load. *Finite Elem. Anal. and Des.*, 62:8–17, 2012.
- [10] B. Dyniewicz. Efficient numerical approach to unbounded systems subjected to a moving load. *Computational Mechanics*, 54(2):321–329, 2014.
- [11] B. Dyniewicz, A. Pęgowska, and C. I. Bajer. Adaptive control of a rotating system. *Mechanical Systems and Signal Processing*, 43(1-2):185–192, 2014.
- [12] B. Dyniewicz, R. Konowrocki, and C.I. Bajer. Intelligent adaptive control of the vehicle-span/track system (doi: 10.1016/j.ymsp.2014.12.007). *Mechanical Systems and Signal Processing*, 2015.
- [13] B. Dyniewicz, D. Pisarski, and R. Konowrocki. Semi-active control of track subjected to an inertial moving load. In *XXV Symp. Vibrations in Physical Systems*, pages 147–152, Poznań–Będlewo, 2012.
- [14] L. Frýba. *Vibrations of solids and structures under moving loads*. Thomas Telford House, 1999.
- [15] R. Konowrocki and C. I. Bajer. Friction rolling with lateral slip in rail vehicles. *Journal of Theoretical and Applied Mechanics*, 47(2):275–293, 2009.
- [16] J. Onoda and K. Minesugi. Semiactive vibration suppression by variable-damping members. *AIAA Journal*, 34(2):355–361, 1996.
- [17] D. Pisarski and C. I. Bajer. Semi-active control of 1d continuum vibrations under a travelling load. *Journal of Sound and Vibration*, 329(2):140–149, 2010.

- [18] D. Pisarski and C. I. Bajer. Smart suspension system for linear guideways. *Journal of Intelligent & Robotic Systems*, 62(3-4):451–466, 2011.
- [19] H. Reckmann, K. Popp, and M. Ruskowski. Control of an elastic guideway using linear drivers. In *LIDIA98*, pages 114–117, Tokyo, 1998.
- [20] D. M. Yoshida and W. Weaver. Finite-element analysis of beams and plates with moving loads. *Int. Assoc. Bridge Struc. Engr.*, 31(1):179–195, 1971.

# Chapter 2

## Smart Materials in Vibrations Damping

In the process of machinery and structures designing, whether bridges, buildings, suspension of a car or an airplane wing, actions leading to vibration attenuation prevents the system from the risky states and failures, assure its robustness, enhance the fatigue life and the comfort of use. The development of modern engineering materials motivates to study the possibility of improving the damping properties of structures.

The commonly used term for material that exhibits adjustable, time-dependent response is *the intelligent material*. Structures which use these materials as a basis for their operation are called *intelligent structures*. To be classified as intelligent material, it needs to have some kind of built in or intrinsic sensing mechanism, processing ability, and respond to a stimulus in a predetermined manner, and extent in a reasonably short time. As the stimulus is removed, the material should retain possibility to revert to its original state, thus having some kind of feedback mechanism.

Moreover, the term *smart materials* is often used alternatively to intelligent materials, adaptive structures or even multifunctional materials. The main features of these structures seem quite general, but they describe qualities which are necessary for the material to be classified as smart, and have been repeatedly expanded and clarified in numerous works [1, 60, 70]. The term *intelligent* seems somehow exaggerated, so *smart material* is rather preferred. However, some authors precisely distinguish these two groups, specifying smart materials as those that possess only some of the features

attributed to more complex, intelligent materials. In this work we limit the expression *smart* in relation to materials that change their properties under the influence of external stimuli in a prescribed manner, and exhibit almost real-time, reversible response.

The group of smart materials ranges from photo-, thermo- and electrochromic materials, through photo-, thermo- and electroluminescent substances, piezoelectrics, magnetostrictive materials, magnetorheological and electrorheological fluids and gels, self-healing materials and many others. In each of these groups we can distinguish materials that take on different states of matter. They can be a product of various fields of technology and share specific features that can be classified as smart. In the following sections we will concentrate on the basic properties and operation principals of smart materials that are most commonly used for the semi-active vibration attenuation.

To face undesired dynamical effects, either passive, active or semi-active damping method needs to be put into practice. The obvious drawback of a passive damping system is the lack of possibility to dynamically adjust its parameters. Once the mass, stiffness or damping properties of the system are configured, these parameters cannot be changed easily and passive vibration damping strategies become ineffective, when the dynamics of the system or frequency of disturbance vary in time. Materials mostly used in passive damping are composites [42], polymers, urethanes and synthetic rubbers [18, 19, 85] or viscous fluids [69].

There are numerous techniques that are more efficient in vibration attenuation than a simple, passive material damping. The active damping solutions, which are usually based on the force actuators attached to a vibrating structure require an external power source to operate. The parameters of the system can be controlled in real time to increase its stability or perform the desired trajectories of motion [46, 68]. The most interesting damping method seems to be the semi-active control. Parameters of the mechanical system, such as the stiffness or coefficients of damping can be modified to increase the stability of the system or to obtain the desired dynamical response. This is where the adjustable smart materials like magneto- and electrorheological fluids or controllable elastomers may show their full potential. In our work we also investigate the possibility to use the controlled special granular structures as a lightweight, low cost, interesting alternative for the common damping solutions.

## 2.1. Magnetorheological Fluids

Controllable fluids are one of the branches of smart materials. They are characteristic of the possibility of changing their rheological properties in response to an external control. The most recognized and common of this group are the electrorheological and magnetorheological (MR) fluids. Basically, these materials share similar mechanical behaviour, but the magnetorheological fluids (MRF) turned out to be more popular. They are easier to control, and provide better rheological properties than the electrorheological fluids. The yield stress displayed by the electrorheological fluids are in the range of 3–5 kPa, whereas the yield stress of magnetorheological fluids reaches up to 150 kPa, which requires generation of the magnetic field of intensity 150–250 kA/m. The voltage source requirement for electrorheological fluids is 2–5 kV, while MR devices operates with 24 V DC power supply.

The phenomenon of changing mechanical properties of a specially composed fluid placed in an electrostatic field was first observed by Willis Winslow in the late 30's of XX'th century, and presented in [82]. Soon, after Winslow discovered his liquid with electrorheological properties, another scientist, Jacob Rabinow composed a fluid with mechanical properties depending on the magnetic field. Since the discovery of the magnetorheological effect by Rabinow in 1948 [57, 58], these type of smart materials have developed into a family with MR fluids, foams, greases, gels, and elastomers. Generally, the MR materials are ferromagnetic, micrometer sized, carbonyl iron particles suspended in a carrier medium. The most common in this group are the fluids, with ferrous particles usually suspended in a silicone oil, glycol, liquid hydrocarbon or hydrofluor [5].

Typical MR fluid contains 75–80% weight, spherical, carbonyl iron particles with the density of 7500–8000 kg/m<sup>3</sup>. The diameter of the iron particles ranges from 3.0 μm up to 8.0 μm, as presented in Fig. 2.2a. The carbonyl iron particles are coated by a thin layer of an active, anti-oxidation agent, which also prevents them from clustering and settlement.

The carrier fluid serves as an insulating medium, and is chosen due its temperature stability, compressibility, and corrosiveness. When exposed to the magnetic field, the ferrous particles polarize along the magnetic flux lines in a chain-like structures (Fig. 2.1b and 2.2b). The rheology of the fluid reversibly and instantaneously changes from the free-flowing, Newtonian like behaviour, to a semi-solid state, which is called the active one or ON-state.

The yield stress of the fluid increases as a consequence of the particles rearrangement, which start to form a highly ordered structures. The intensity of the process can be controlled by adjusting the magnetic field which

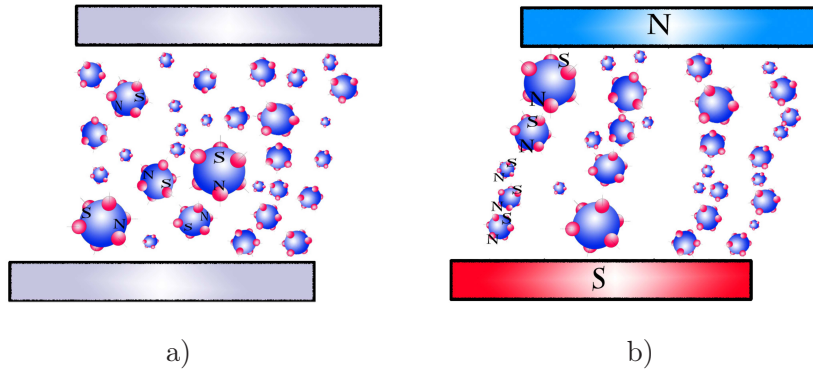


**Figure 2.1.** Behaviour of the ferromagnetic particles in OFF state a) and in the presence of magnetic field b).

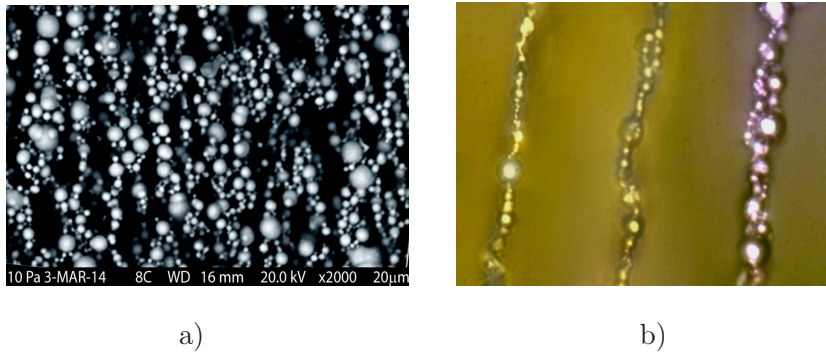


**Figure 2.2.** SEM images of ferromagnetic particles, randomly dispersed for no magnetic field a), and forming chain like structures in active state b).

is usually generated by an electric coil. The transition between the ON- and OFF-state is a fully reversible process and takes only several milliseconds to complete. The possibility of controlling the yield stress of the MR fluids by means of the magnetic field predestines them to be utilized in devices like dashpots, rotary brakes, clutches, bearings, stabilisers, etc. The characteristic of typical MR fluid is presented in Fig. 2.3.

The magnetic saturation of the fluid is an important thing to be noticed. When certain value of the magnetic field is achieved, further increase has no effect on the value of the yield stress. The non-linear characteristic of the smart fluids hinders designing an accurate model of their complex behaviour. This non-linearity represents the relationship between the applied magnetic field and the resulting resistance force.

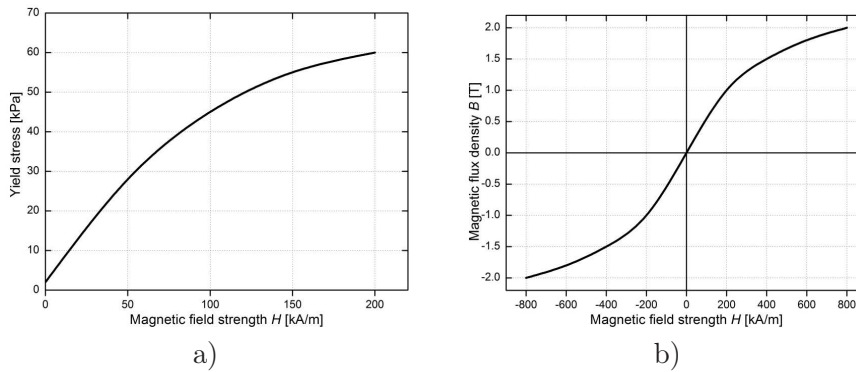


**Figure 2.3.** Properties of a typical magnetorheological fluid MRF-140CG by Lord: yield stress vs. magnetic field strength a) and magnetization curve b).

For the analysis and design purposes, the most common description of the quasi-static behaviour of the magnetorheological fluid is carried out with the Bingham model. It is represented by an ideal plastic solid in parallel with a linear viscous fluid, as presented in Fig. 2.4a. In this model the material does not flow until it is stressed beyond the critical yield stress. When the critical yield stress is reached the behaviour is close to the Newtonian fluid at constant viscosity (Fig. 2.4b). The following expression describes its behaviour

$$\tau = \tau_0(B)\text{sgn}(\dot{\gamma}) + \mu\dot{\gamma}, \quad (2.1)$$

where  $\tau_0$  is the yield stress caused by the applied magnetic field,  $\dot{\gamma}$  is the shear strain rate,  $\mu$  is the plastic flow viscosity, and  $\text{sgn}$  is the signum function.

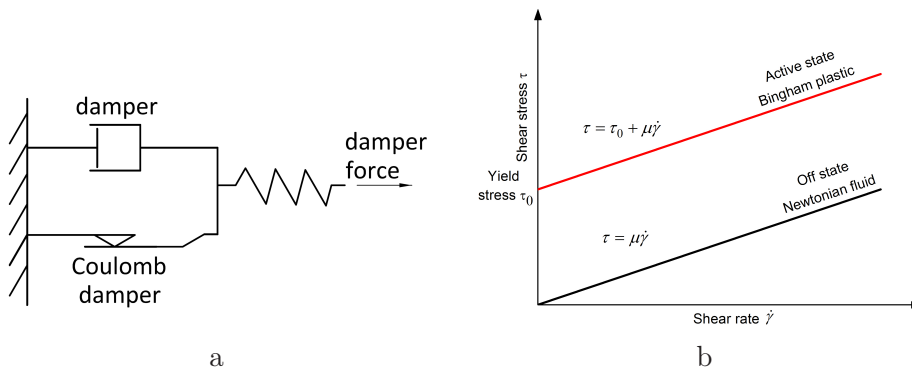


**Figure 2.4.** Lumped parameter Bingham model a), and its characteristic for different states of the magnetorheological fluid b).

Although numerous research results strongly support the Bingham viscoplastic behaviour of the MR fluids, one need to be aware that more advanced approach should be considered to model complex and more realistic behaviour. In addition, MR fluids may exhibit shear thickening or shear thinning behaviour. Figure 2.5 compares the quasi-steady response for Bingham model with the shear thickening or shear thinning behaviour, where the apparent viscosity tends to change with the shear rate.

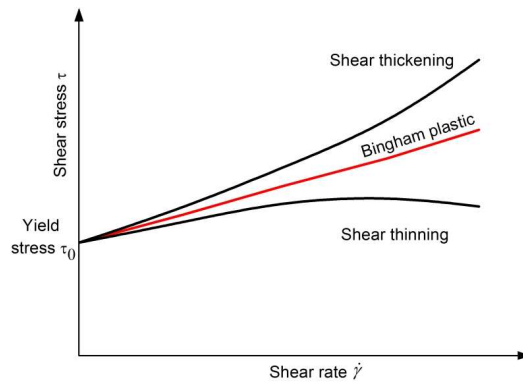


**Figure 2.5.** Shear thickening and shear thinning behaviour of MR fluids.

In order to illustrate the complex response of the fluid, numerous models are being developed. The most popular are the Bouc-Wen hysteresis model [81], Herschel-Bulkley [36], Gamota and Filisko [26], Casson [25], McKinley [21], BingMax [14], fractional models and others.

Despite the fact of growing number of practical applications, producing high-quality MR fluids with desired properties is still hard to achieve. Different types of commercially available fluids share similar limitations like susceptibility to settling and sedimentation, wearing of the ferrous iron particles and clustering. They also tend to change their properties with temperature [5], which may result in decreased efficiency of the devices working in a heavy-duty conditions. Moreover, the high content of magnetic particles comprised in a carrier fluid is an inevitable condition for enhanced magnetorheological performance, leading to constitution of a high-weight system. This stimulates searching for modified types of fluids with the improved properties.

In [29] the authors modified the MRF by mixing and adding amine antioxidant additives Zn-DTP and Mo-DTC to improve the stability and anti-wear properties. According to [39], incorporation of the magnetic fibers to the MRF composition results in a remarkable increase of the yield stress.

In [75] authors discussed encapsulating MR fluid in a polymeric solid to achieve higher yield stress value, which was later studied in [76]. The iron nanopowder and micron-powder were mixed with the hydraulic oil to create the nanoscale MRF, more resistant to settlement [61, 65]. Magnetorheological gels exhibit good stability and low sedimentation, and high shear yield stress value. They can be injected into elastomers, as described in [78]. In [86], the MR material based on supermolecular interactions between the low molecular weight hydrogelators and the surface modified magnetic nanoparticles was introduced as an alternative to typical MR gels.

There are also studies on the rheological properties of MRF with the addition of non-magnetic, polymer spheres filled with gas. The addition of specially composed, polymer particles allows to obtain a compressible, non-Newtonian fluid with properties different from the common MRF. The lightweight compressible additive introduces elastic behaviour and affects the viscosity and yield stress. Moreover, such a fluid retains the possibility of controlling its state by the magnetic field [23, 56]. It also significantly reduces density of the fluid, prevents the particles from settling, and thus can lead to an enhanced practical efficiency of the device. The cognitive study of a damper with non-typical kind of fluid is also described in a dedicated subsection 2.1.2 (page 43).

### 2.1.1. Magnetorheological Devices and Applications

Although the magnetorheological devices differ in operation mode and mechanical construction, whether a linear stroke or rotary damper, clutch or brake, the principles of operation are similar. The magnetorheological fluid devices have a semi-controllable output that depends on the input signal which is usually an electric current or voltage. For example, magnetorheological fluid dampers have a controllable damping force that depends on the current which is the electric coil's input. On the other hand, the rotary damper have a semi-controllable torque output that also depends on the electric current which generates the magnetic field. Basically there are three modes of operation for the MR device: flow/valve mode, direct shear mode, and squeeze-flow mode, which are illustrated in Fig. 2.6.

In the classic linear stroke damper the fluid operates in the **valve regime** (Fig. 2.6a), which is the basic mode for most of the MR devices. In this mode the annular throttled flow is treated as a flow between two parallel fixed plates, which form a narrow gap. The flow resistance is controlled by affecting the magnetic field. The vector of the magnetic field is normal to the direction of the flow. The adjustment is performed by changing the coil's

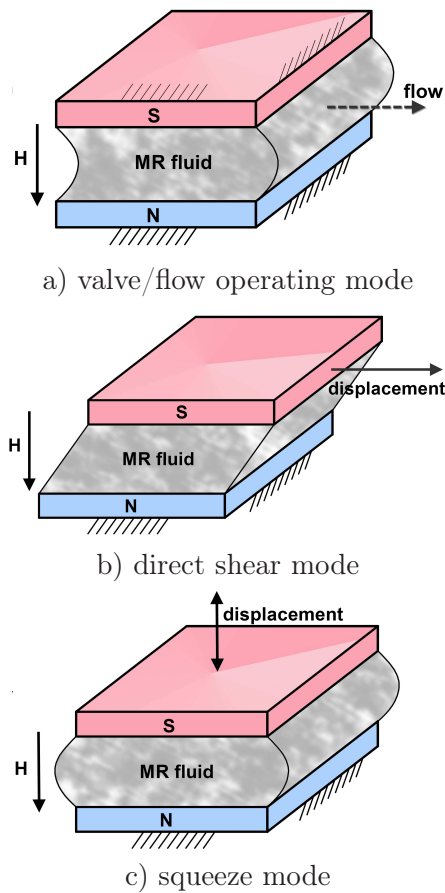


**Figure 2.6.** Different operation modes of the magnetorheological fluid.

electric current. The valve mode is valid when the height of the gap is much smaller than its length and width, therefore the flow is considered as a flow between two parallel plates.

In the **shear mode** (Fig. 2.6b) the fluid is sheared between two parallel plates. One or both of them are either rotating or sliding. This mode is typical for rotating MR devices like torsion dampers, brakes and clutches.

The **squeeze mode** (Fig. 2.6c) is the least frequently used. One or both of the plates are free to move in the direction parallel to the applied magnetic field. This movement depends on the fluid's tension, compression, and shear forces. This mode is most suitable when the system requires small displacements and large forces to control, such as in engine mounts subjected to axial load.

The number of solutions utilising smart materials like the magnetorheological fluids, still does not reach the number of applications supported with typical, hydraulic and pneumatic systems. Insufficiently developed proposed and evaluated solutions based on controllable fluids holds back the application engineers from the deployment of such devices. The high cost and difficult access to quality fluids are the other important factors. The evolutionary devices are mainly prototype units designed at academic or research centres. The recently observed interest in the field of smart fluids by the industry, academic and research institutes, may fortunately facilitate to introduce them to a greater number of engineering applications.

Magnetorheological dampers are successfully used in the automotive industry as parts of an intelligent suspension. They have also been used as the isolators for driver seats, usually applied in heavy-duty trucks to improve the comfort and safety of travelling [37]. The first shock absorber solution that was affordable for casual customers was known as MagneRide. It was manufactured for primary vehicle suspension system by Delphi Co. and used the MR fluid produced by LORD company.

The unexpected, dangerous vibrations still occasionally plague modern structures. The MR dampers are also applied in stabilisation of buildings vulnerable to seismic activity [49] or in semi-active control of bridge structures [7]. The use of the concrete girder bridge over the Volga River (Fig. 2.7a) was inaugurated in October 2009 and closed by the authorities to all motor traffic on May 2010, due to severe, wind-driven twisted mode vibrations. The problem was solved in fall 2011, by installing a complex, tuned mass damping system, based on the magnetorheological dashpots (Fig. 2.7b). The solution was described thoroughly in [77]. That type of the



a)



b)

**Figure 2.7.** Volga Bridge plagued by the unwanted oscillations in 2009 a), and the tuned mass magnetorheological damping system installed in 2011 b) [77].

solution was also found to be effective in mitigating vibration of the London Millennium Footbridge which was closed since the opening day in 2000, due to the unexpected synchronous lateral movements. The MR dampers have been also used in suspension bridges for vibrations abatement of stay cables, like in the Dong Ting Lake Bridge in China or cable stayed bridge near Dubrovnik (Croatia), equipped with several MR dampers to counteract gusts of wind (Fig. 2.8a).

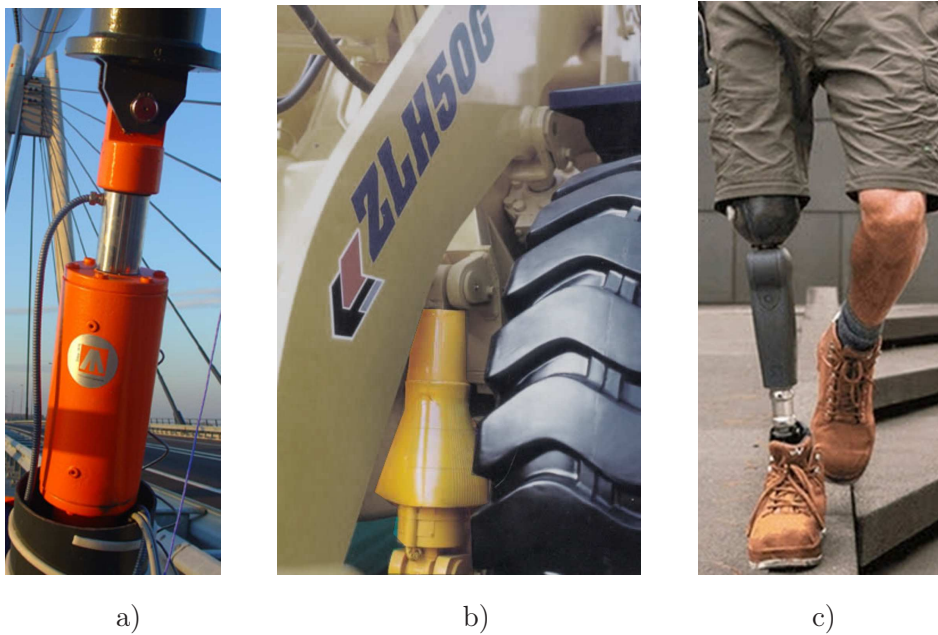


**Figure 2.8.** MR dampers installed on the cable stayed bridge near Dubrovnik a), and the MR damper by Pangu MRF (China) used in ZLH50 excavator b), integrated magnetorheological prosthesis unit RheoKnee c) (Source: Empa, Pangumrf, Ossur).

Specially designed dampers have been used for vibration attenuation in large-scale washing machines drums, and for damping of excavator blades and hydraulically controlled booms (Fig. 2.8b). Currently, an intensive work is carried on to adapt the MR dampers in orthopedics, particularly in the construction of prostheses and orthoses. Figure 2.8c shows RheoKnee using magnetorheological dampers controlled by the microprocessor, applied as lower limb intelligent prosthesis.

The magnetorheological fluids are also used as non-contact, self-repair seals for rotating shafts of engines operating under special conditions, such as in mines, fans and assemblies of chemical and biochemical reactors [34, 72].

They have also been used in special purpose finishing machines, used for manufacturing complex optics with figure accuracy  $<50$  nm and surface roughness  $<1$  nm [27, 29].

### 2.1.2. Linear Stroke Damper

One of the most typical design of a linear stroke magnetorheological damper is presented in Fig. 2.9a. The photography of the real prototype device named T-MR-SIMR is presented in Fig. 2.9b, with the disassembled parts of the device in Fig. 2.9c.

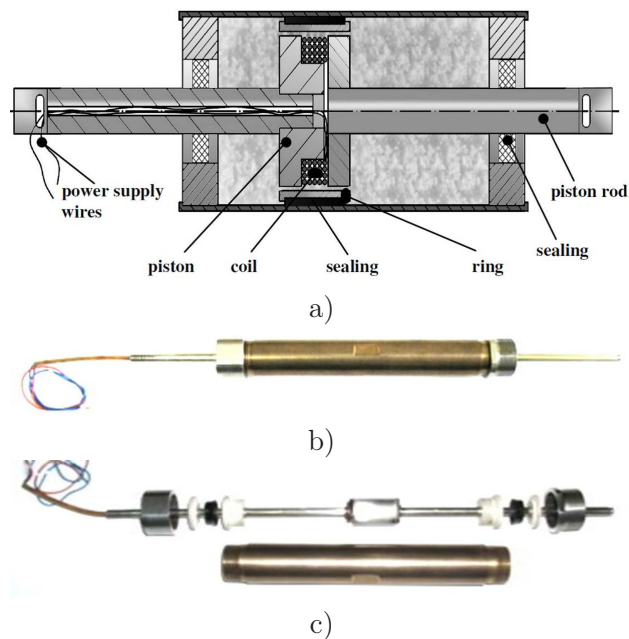
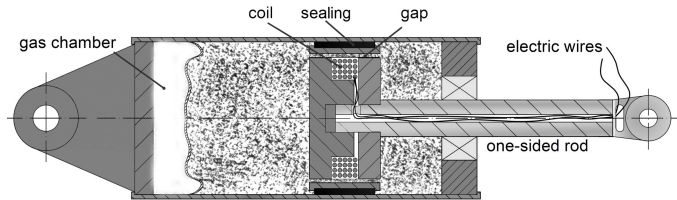


**Figure 2.9.** Design of a typical MR damper a), photography of the prototype unit named T-MR-SIMR b) and the disassembled parts of the device c).

This is a custom made prototype unit filled with MRF-132DG by LORD type of fluid. The chosen fluid is a suspension of a  $10\ \mu\text{m}$  sized, magnetically susceptible particles in a hydrocarbon fluid. According to the datasheet, the density of the fluid is  $3000\ \text{kg/m}^3$  and the viscosity is  $0.09\ \text{Pa}\cdot\text{s}$ . The maximum yield stress value is  $50\ \text{kPa}$ , and it is achieved for the magnetic induction of  $1.5\ \text{T}$ . The fluid features fast response time, and high yield stress in the presence of the magnetic flux, and very low yield stress in absence. It enables a wide range of controllability. The coil is powered through the

electric wires placed inside the double sided rod. In the magnetic field, particles align with the direction of the flux lines in a chain-like combination, thereby restricting the fluid's movement within the gap, in proportion to the strength of the magnetic field.

An alternative design of the magnetorheological absorber involves one-sided rod and a gas accumulator placed inside one of the chambers, that serves to balance the volume change during the rod's motion. One of the most popular commercially available dampers of this type is LORD RD-1005-3. The gas-filled membrane as a spring introducing additional elastic force, that counteracts the movement of the pressed piston. The design of such a device is presented in Fig. 2.10.

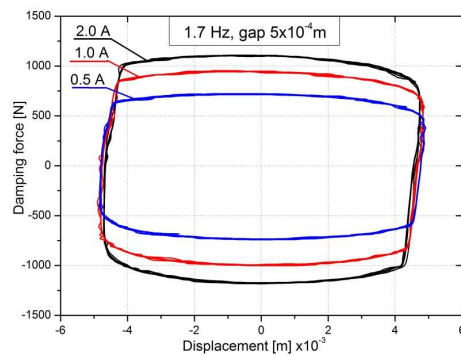
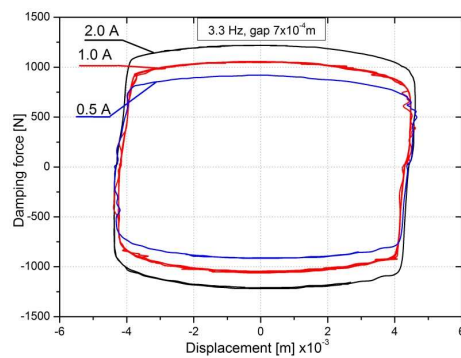
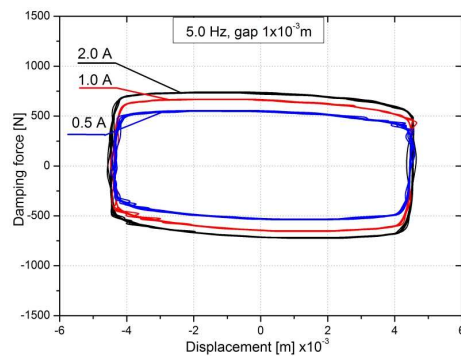


**Figure 2.10.** Linear stroke MR damper with one-sided rod and gas accumulator.

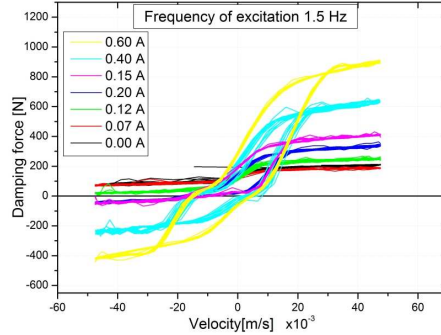
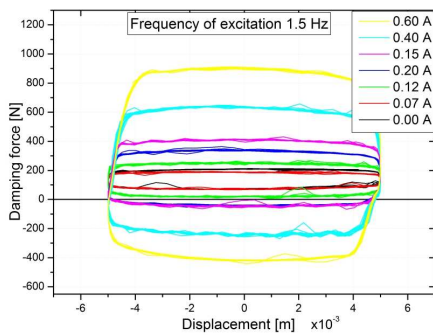
Let us take a closer look at the unique performance of linear stroke MR dampers. Sample results of the  $F(x)$  relations, obtained for different piston velocities and electric current for double-sided damper T-MR-SIMR are presented in Fig. 2.11. The sine displacement excitation was applied. The results were obtained by the authors for three different gap heights:  $5 \cdot 10^{-4}$ ,  $7 \cdot 10^{-4}$  and  $10 \cdot 10^{-4}$  m. The damper behaviour was investigated experimentally at the ambient temperature of  $21^\circ\text{C}$ . The temperature of the device remained constant during the experiment.

Increasing the electric current intensifies the magnetic field flux and thus, increases the yield stress  $\tau_0(B)$ . Consequently the damping force is enhanced. The larger the electric current is, the higher value of the force is obtained. For this type of damper's design there is no gas accumulator and therefore the obtained force responses are almost X-axis symmetrical.

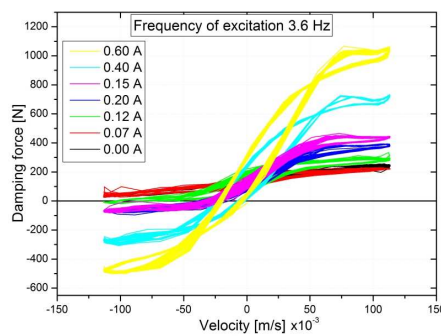
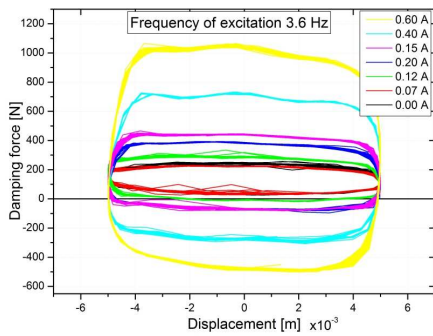
The results obtained for the commercial damper Lord RD-1005-3 with a gas spring are presented in Fig. 2.12, and extensively discussed in [9]. A higher input current results in a larger force response in the force-displacement profiles. The response is no longer symmetrical, since the gas spring element introduces additional force of 180 N. Increasing the frequency, larger damping force is obtained. Nevertheless this impact is minor, compared to the influence of the magnetic field.

a) gap height  $5 \cdot 10^{-4}$  m and frequency 1.7 Hzb) gap height  $7 \cdot 10^{-4}$  m and frequency 3.3 Hzc) gap height  $10^{-3}$  m and frequency 5.0 Hz

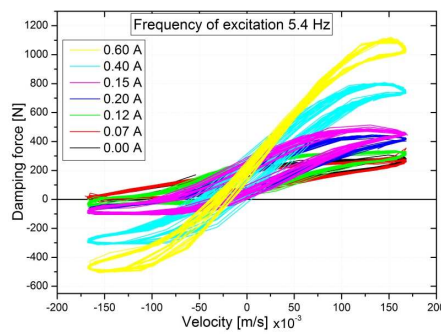
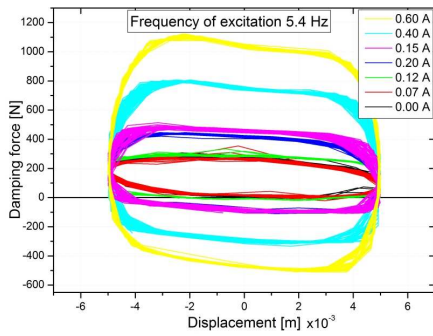
**Figure 2.11.** Experimental characteristics for  $F(x)$  relation for different gap height's of T-MR-SIMR damper prototype unit.



a) force vs. displacement for 1.5 Hz      b) force vs. velocity for 1.5 Hz



c) force vs. displacement for 3.6 Hz      d) force vs. velocity for 3.6 Hz



e) force vs. displacement for 5.4 Hz      f) force vs. velocity for 5.4 Hz

**Figure 2.12.** Experimental characteristics for  $F(x)$  relation of commercial damper Lord RD-1005-3 with a gas spring.

### Damper with Compressible Magnetorheological Fluid

Here the MR damper with a non-standard MR fluid is investigated. The commercial MR fluid was removed from T-MR-SIMR damper unit and replaced with a modified composition of the fluid. The fluid involves additives of resilient spherical particles which were stirred with a ferrous iron powder, and mixed with synthetic oil. This resulted in an additional elastic force that can be developed when the fluid is compressed due to the pressure change between the chambers of the damper. The microstructural observation indicates that the polymer-gas additive affects the package density of iron particles in the carrier fluid of the MR suspension, both with and without the magnetic field. Thus, the density of the MR fluid was reduced. Moreover, the polymer microspheres additive was found to increase twice the volume of the MR suspension. The fluid's magnetic permeability depends on the volume fraction of iron particles. Increasing the amount of magnetic particles allows to modify the characteristic of the fluid to be more responsive to magnetic stimulus.

The trace of damping force obtained at different frequencies of sine excitation is shown in Fig. 2.13. For no magnetic field applied and frequency of excitation 0.3 Hz (Fig. 2.13a), the movement of the rod was resisted at almost constant force. For the frequency of 1.8 Hz and no magnetic field applied, additional elastic force was present. When the internal pressure in both chambers is large enough to compress the microspheres, the elastic force is increased (Fig. 2.13b and 2.14b). For the non-zero coil current, the device exhibits additional force due to the incremented value of the yield shear stress and compression caused by the pressure difference.

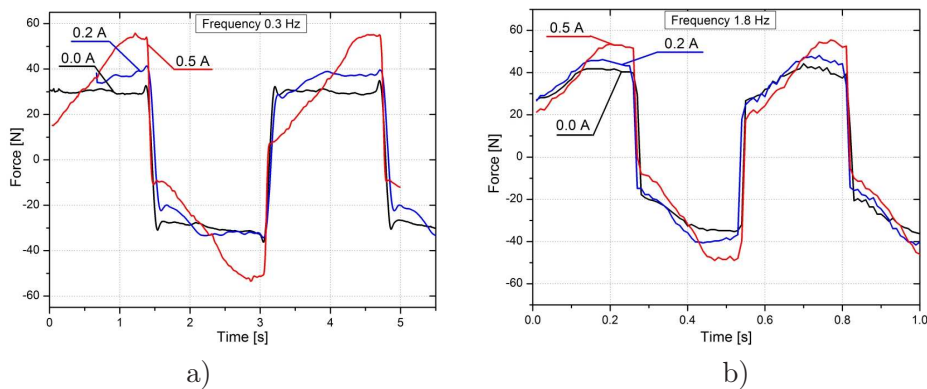


**Figure 2.13.** Damping force vs. time for unit with modified compressible fluid under sinusoidal excitation 0.3 Hz a), and sinusoidal excitation 1.8 Hz b).

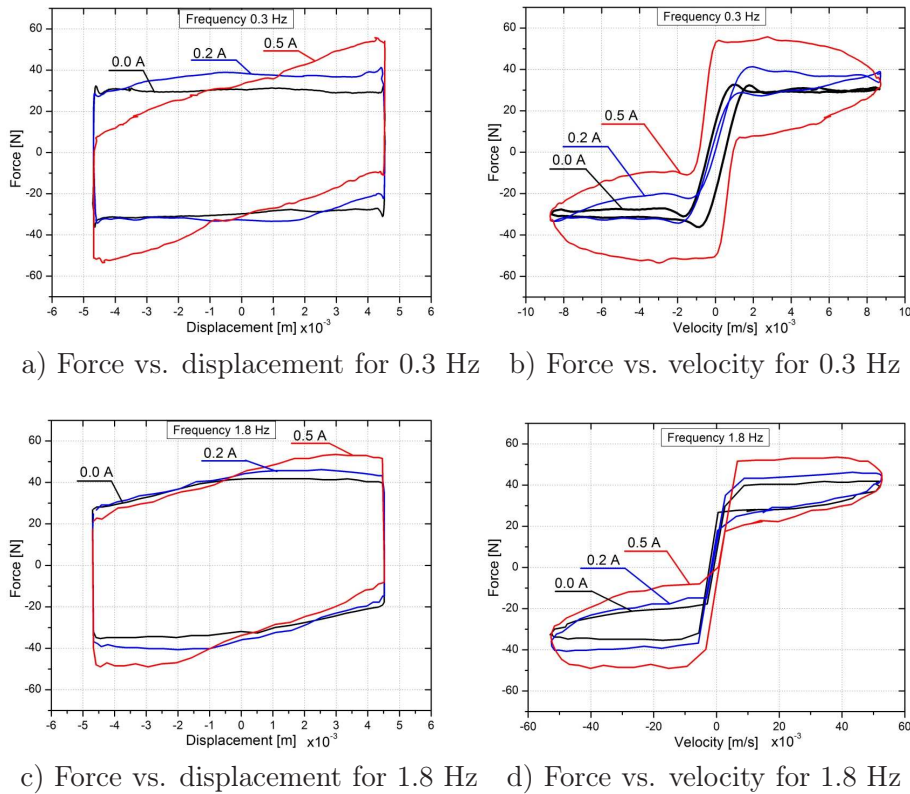


**Figure 2.14.** Experimental characteristics of force–displacement and force–velocity loops for compressible MR fluid for sinusoidal excitation.

The area enclosed by the force–displacement loops (Fig. 2.14a and c) represents the energy dissipated in a single vibrations cycle. Figure 2.15 shows that when the current increases, the initial increase of dissipation is notable. When the current enhances above certain value, no more dissipation energy is developed because the material becomes magnetically saturated. Figures 2.14b and 2.14d show the force–velocity curves for two frequencies of excitation and different coil current. The increase of the magnetic field involves the increase of the force required to yield the MR fluid is higher and develops the hysteresis loop response.

Experiments showed that the compressible fluid used in linear stroke dashpot allows to adjust the stiffness, with the remaining possibility to control the damping properties by an external magnetic field. The addition, the gas-filled spheres reduces the density of the fluid and therefore the weight of the device, and prevents the sedimentation of the ferrous particles. Presented

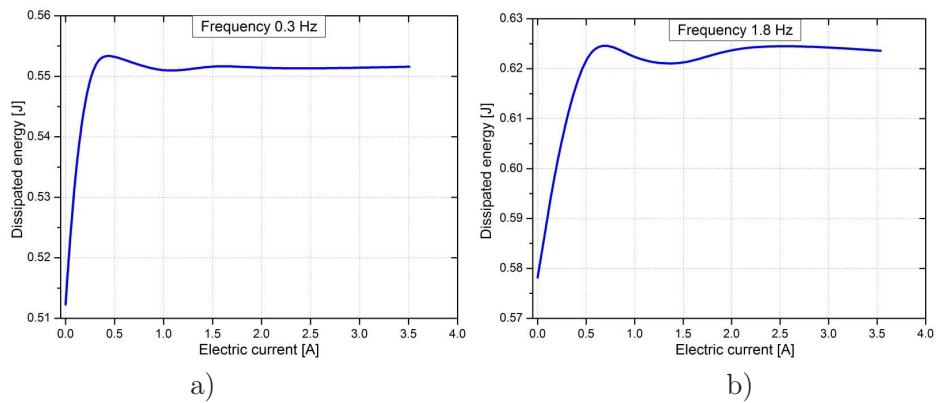


**Figure 2.15.** Dissipation energy for different electric current and frequency of excitation 0.3 Hz a) and 1.8 Hz b).

results indicate that the new type of magnetorheological fluid can meet requirements in different types of applications and can be applied in standard MR devices, giving new possibility to control the vibration of structures with a liquid spring-like features.

### 2.1.3. Rotary Damper

The rotating MR devices like brakes and clutches, operate in a direct-shear mode. The design and cross-section of the prototype rotary MR device is presented in Fig. 2.16. The shear stress in the narrow gap, formed between

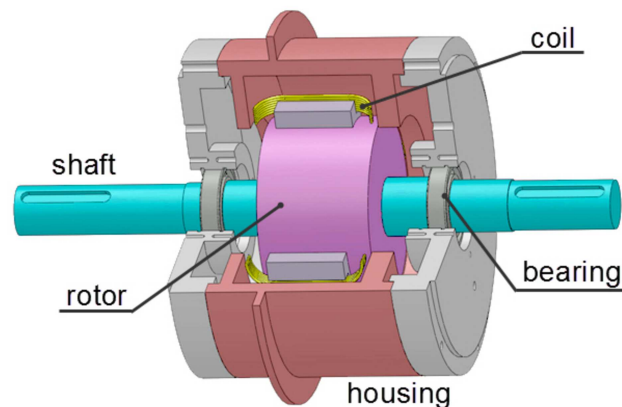


**Figure 2.16.** Construction of the rotary magnetorheological brake.

the rotor and the housing is controlled by changes of the magnetic field, the same as for linear stroke devices. The vector of the magnetic field is perpendicular to the direction of the fluids flow. The magnetic field intensity can be adjusted by the electric current in the coil winding. The coil is mounted in the way that enables rotations with the shaft. The electric current is supplied by electrical brushes. The construction of the solenoid should enable a step change in the value of the magnetic field and minimisation of the magnetic remanence effect. The photography of the real device is presented in Fig. 2.17a. This large scale brake is designed for heavy military vehicles of special purpose. It can work as a brake or in a clutch configuration in torque transmission systems [4].

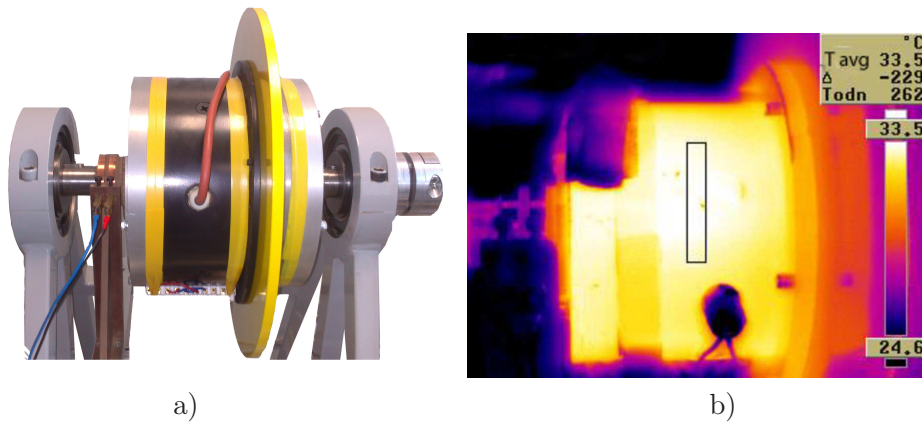


**Figure 2.17.** Photography of the large scale rotary magnetorheological brake a), and thermal camera photography showing heating of the device b).

The experiment allowed to examine carefully the response of the MR brake for different magnetic field strengths, taking into consideration parameters important for the real-life applications: rotational speed, temperature and exploitation time. Recording the temperature of the MR fluid inside the gap is hard to achieve and impractical. Instead, experiments were carried on using thermal camera to measure the temperature of the housing (Fig. 2.17b). Figure 2.18 presents the braking torque value in time, for rotational speed 3 rpm. The measurements were taken at constant temperature of the device 21°C. For the low speed, the temperature remains constant, and thus the braking torque does not change in time. The relations between the braking torque and the rotational speed, for different values of coil current and higher rotation speed are presented in Fig. 2.19. The braking torque

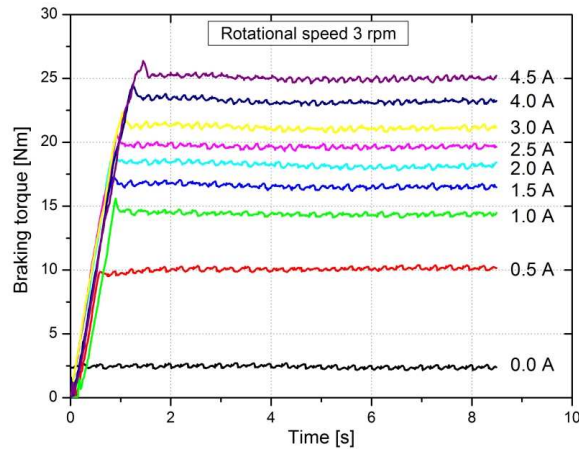


**Figure 2.18.** Evolution of the braking torque in time for rotation speed 3 rpm – temperature remains constant.

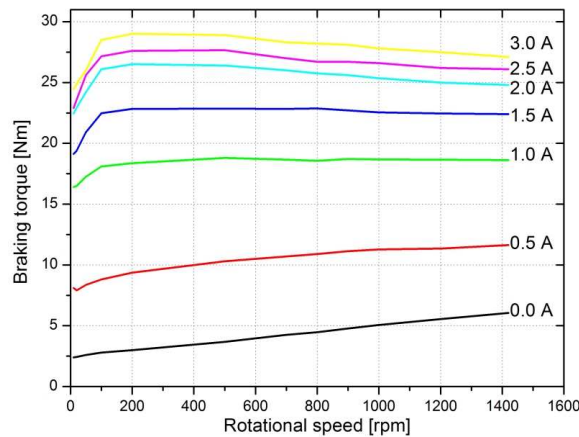


**Figure 2.19.** Braking torque as a function of rotational speed, for different values of coil current – temperature increases in time.

increases with increase of the coil current. For 0.5 A the average torque value was 10 Nm, while for 2.0 A torque increased to 25 Nm. The coil current over 2.0 A results in just a minor enhance of the braking torque. This is due to the fact that used magnetic fluid type MRF-132DG reaches saturation for magnetic field strength 300 kA/m.

At increasing rotational speed, the breaking torque should grow respectively if no heating up is present. However, the temperature of the device rises due to the disintegration of the MR fluid particle chains formed in the

presence of the magnetic field. This leads to a notable reduction of the yield stress of the non-Newtonian fluid, and thus the braking torque noticeably declines (Fig. 2.20).

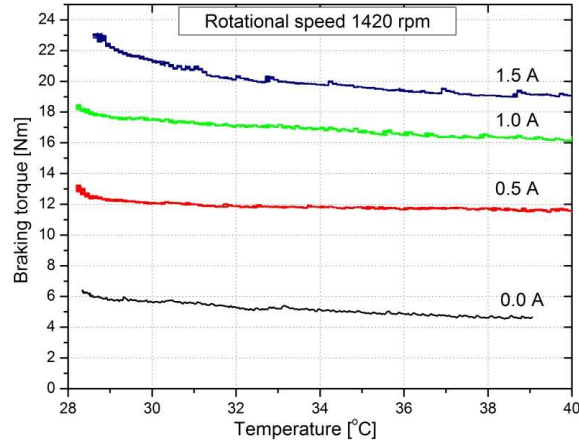


**Figure 2.20.** Decrease of the braking torque as a function of temperature of the device for constant rotational speed.

Taking into consideration time dependencies in Fig. 2.21, it can be stated that the MR brake can work efficiently for periods of 100 s for speed up to 500 rpm and high electric current before overheating. For 1420 rpm, the device can work continuously only for short periods of 60 s with maximum coil current without being overheated.

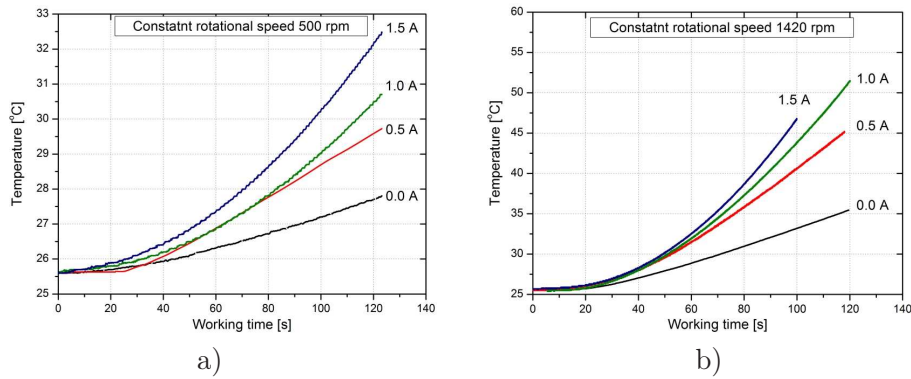


**Figure 2.21.** Temperature of the device over working time, obtained for 500 rpm a) and for 1420 rpm b).

### 2.1.4. Designing Linear Stroke Magnetorheological Dampers

Basic computations concerning the design of the magnetic circuit and the parameters of the linear stroke damper operating in the valve mode will be discussed below.

#### Geometry of the Damper

Let us denote the basic geometrical parameters of the damper as presented in Fig. 2.22. First we propose the initial diameter of the piston and the rod, on the basis on certain application requirements.

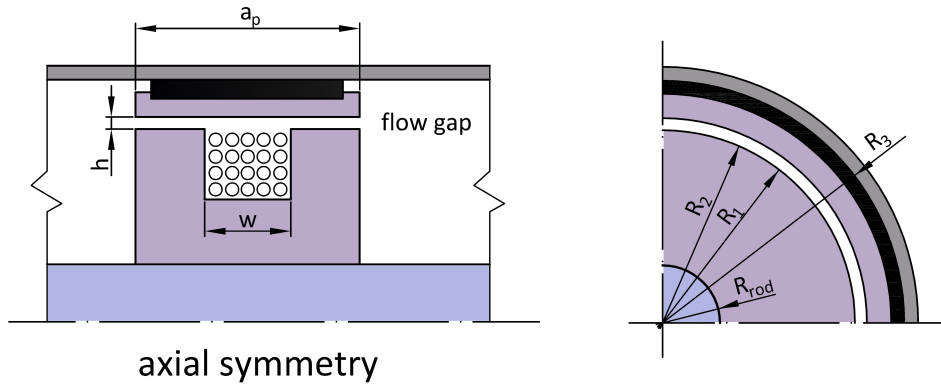


**Figure 2.22.** Basic damper parameters denotation:  $R_1$ ,  $R_2$  – outer and inner gap radius,  $R_3$  – piston radius,  $R_{rod}$  – rod radius,  $h$  – gap height,  $w$  – coil width,  $a_p$  – piston length.

The effective average circumference of the gap is

$$b = \pi(R_1 + R_2). \quad (2.2)$$

The effective gap area is

$$A_{gap} = b \cdot h, \quad (2.3)$$

where  $h = R_1 - R_2$  is the height of the gap. The total damping force may be expressed as a sum of particular forces

$$F_{damp} = F_\tau + F_\mu + F_t, \quad (2.4)$$

where  $F_\tau$  is the controlled force, related to the actual yield stress of the activated MR fluid,  $F_\mu$  is the viscous resistance force, and  $F_t$  is the friction force. In the valve mode, the flow is simplified by assuming the parallel plates

and Bingham's fluid model. For the axial symmetry boundary conditions, the pressure gradient equations reduce to the 5th degree equation [53]

$$3(\chi - 2\sigma)^2[\chi^3 - (1 + 3\sigma - \nu)\chi^2 + 4\sigma^3] + \sigma\nu^2\chi^2 = 0, \quad (2.5)$$

where  $\chi$  is the dimensionless pressure gradient, and  $\sigma$  is the dimensionless stress gradient. The dimensionless velocity can be expressed as follows

$$\nu = \frac{bh\nu}{2Q}, \quad (2.6)$$

where  $\nu$  is the velocity of the piston. The volumetric flow rate of the MR fluid can be calculated as

$$Q = \nu \cdot A_p, \quad (2.7)$$

where  $A_p$  is the area of the piston. The pressure gradient is given as

$$\chi = \frac{bh^3\Delta p}{12Q\mu a}, \quad (2.8)$$

while the stress gradient equals to

$$\sigma = \frac{bh^2\tau_0}{12Q\mu}. \quad (2.9)$$

$a = a_p - w$  is the length of the area where the MR fluid is influenced by the magnetic field. In the absence of the magnetic field the dimensionless stress  $\sigma = 0$ . Therefore the Eq. (2.5) simplifies to

$$\chi = 1 - \nu = 1 - \frac{bh\nu}{2Q}. \quad (2.10)$$

From (2.8) and (2.10) we claim that the pressure drop caused by the viscous flow can be expressed as

$$\Delta p_\mu = \frac{12A_p a_p \nu \mu \chi}{bh^3}. \quad (2.11)$$

The damping force related only to the viscosity of the fluid can be expressed as

$$F_\mu = \Delta p_\mu A_p. \quad (2.12)$$

Substituting the relation (2.11) to (2.12) we obtain

$$F_\mu = \frac{12A_p^2 a_p \nu \mu \chi}{bh^3}. \quad (2.13)$$

The total viscous force is obtained combining Eqs. (2.10) and (2.13)

$$F_\mu = \left(1 - \frac{bhv}{2Q}\right) \frac{12A_p a_p Q \mu}{bh^3}. \quad (2.14)$$

Noting that  $A_p \gg b$ , we obtain simplified form

$$F_\mu = \frac{12A_p^2 a_p v \mu}{\pi(R_1 + R_2)h^3}. \quad (2.15)$$

The approximate solution to Eq. (2.5) is

$$\chi(\sigma, v) = 1 + 2.07\sigma - v + \frac{\sigma}{1 + 0.4\sigma}. \quad (2.16)$$

The pressure drop in the gap caused by the non-zero yield stress value, can be expressed as

$$\Delta p_\tau = c \frac{\tau_0(B)a}{h}, \quad (2.17)$$

where  $c$  is the constant approximated with the accuracy of 3% by the relation [55]

$$c = 2,07 + \frac{1}{1 + 0.4\sigma}. \quad (2.18)$$

Taking into consideration the simplifying assumptions, we can determine the value of the damping force, controlled with the magnetic field

$$F_\tau = k_p \Delta p_\tau A_p, \quad (2.19)$$

where  $k_p$  is the constant correction factor, related to the distortion of the magnetic field. Usually the roundness of the magnetic field lines and fringing increase the obtained force. From Eqs. (2.15) and (2.19), one can notice that reducing the height of the gap increases the maximum damping force of the device. The final form of the sum of the forces is

$$F_{damp} = k_p c \frac{\tau_0(B)a A_p}{h} + \frac{12A_p^2 a_p v \mu}{\pi(R_1 + R_2)h^3} + F_f. \quad (2.20)$$

The value of the friction force  $F_f$  depends on the type of the used sealing, construction materials, type of their machining, piston velocity and other parameters. The friction force value can be estimated on the basis of experimental data.

Additionally, it is necessary to determine the maximum value of the energy dissipated by the damper. The value of the energy corresponds to the

work which is done by the non-Newtonian fluid, during its flow through the gap, and can be calculated as

$$W = Q(\Delta p_\tau + \Delta p_\mu). \quad (2.21)$$

Another important parameter is the control range, which is the ratio of the controllable force to the non controllable component

$$D = \frac{F_\tau}{F_\mu + F_f} = \frac{c\tau_0(B)bh^2\Delta p}{12W\mu + F_f}. \quad (2.22)$$

The maximum value of this parameter results in the highest range of the controlled damping force.

The presented order of calculations allows to obtain initial parameters which are crucial for the proper design of the linear stroke damper with the MR fluid. However, we must emphasize that the above relations are simplified in our complex problem and they give only approximated results. The assumed simplifications of the phenomena connected with the operation of the device have major influence on the computational inaccuracies. The study on the discrepancies between the computed and real-life results were examined in [9].

The increase of the gap height increases the disparity between the computational and the experimental value of the damping force. The continuous line in Fig. 2.23 shows the experimental data for the maximum force  $F_{damp}$ , for the highest coil current. It was compared with the computational results marked as the dotted line. For the gap height  $5 \cdot 10^{-4}$  m the calculated values

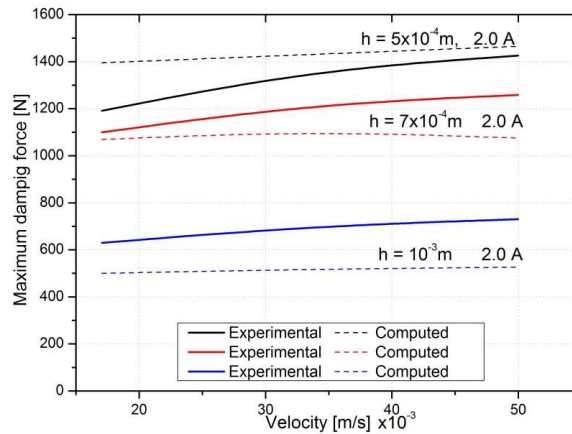


**Figure 2.23.** Comparison of the theoretical and experimental damping force value.

tend to the experimental ones, as the velocity of the piston increases. For other gap heights, the results diverge. In the case of the gap heights  $7 \cdot 10^{-4}$  and  $10^{-3}$  m, with the increase of the velocity, the total error of the force estimation also increases. The greater the annular gap is, the inaccuracy caused by the simplification of the parallel plates flow model is higher. For the higher gap, the magnetic flux lines distort. It leads to extending of the zone in which the fluid is in the active state. This may explain the undervaluation of the computed damping force value for the gap height of  $7 \cdot 10^{-4}$  m and  $10^{-3}$  m compared with the experimental results.

The precise computations of the magnetic induction are complicated and accurate experimental research are time, and effort consuming. The  $\tau_0(B)$  dependency is usually only approximated and imprecise. It negatively influences the accuracy of further computations. By analysing the average error value over the piston velocity, it can be stated that the increase of the piston velocity causes an increase of an error of the damping force estimation. This error grows when the height of the gap increases. The smallest error values related to the damping force are obtained for the narrow gap. Depending on the coil current, the average error vs. the piston velocity varies from 3% to 6%. The value of the error over coil current ranged from 3% to 11%. It can be concluded that the most accurate calculations can be obtained for the smallest gap heights, due to the possibility of the precise determination of the magnetic field, and the smallest error of the simplified model of the flow between the parallel plates.

### Magnetic Circuit Design

We must consider coupled problems of electromagnetism, fluid mechanics, and thermal phenomena, while designing the magnetorheological devices. The simplified models allow to study the impact of the magnetic circuit dimensions, properties of the used materials and performance of the device with fair accuracy.

The effective magnetic circuit design of the magnetorheological device should meet the following requirements:

- they should have low magnetic reluctance, which allows concentrating the magnetic field in the damper's gap,
- they should provide the highest possible magnetic field that restricts energy losses,
- they should reduce the amount of the material required to generate the magnetic field with given parameters in a shortest possible time.

When designing the magnetic circuit, we need to consider:

- axial symmetry of the magnetic transducer,
- nonlinear magnetisation characteristics of the MR fluid and the solenoid's core material,
- magnetic fringing, distortions and energy losses in the contact between interfaces.

It is recommended to consider the applicable magnetic core material from the one made of low carbon steel with high magnetic permeability and saturation. For the best performance the carbon content of the steel should be lower than 0.15% [71]. Usually AISI-12L14, AISI-1008, AISI-1010 or AISI-1018 type of steel is used. The following computations are considered for direct current power supply in ambient temperature. The magnetic field flux is perpendicular to the direction of the flow inside the gap, as presented in Fig. 2.24.

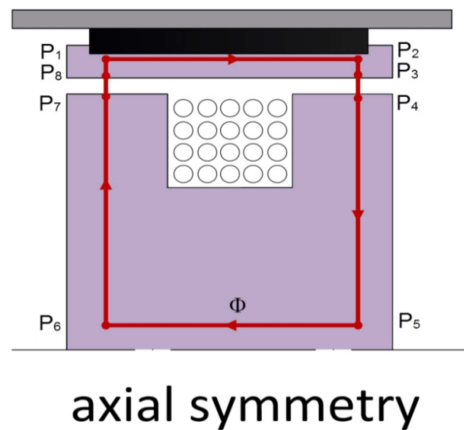


**Figure 2.24.** Simplified path of the magnetic field inside the magnetorheological damper assembly.

The value of magnetic field induction  $B_k$  for  $k$ -th element of the circuit is denoted as

$$B_k = \mu_0 \mu_k H_k, \quad (2.23)$$

where  $\mu_0 = 4\pi \cdot 10^{-7}$  H/m is the absolute permeability of vacuum,  $\mu_k$  is the relative permeability of the  $k$ -th section,  $H_k$  is the magnetic field strength in  $k$ -th element. Based on the equality of the magnetic flux in individual

sections, and assuming that all sections are made of the same material we can write the equality of the magnetic flux in the fluid and the steel core

$$\Phi_{fluid} = \Phi_{core} \quad \text{or} \quad B_{fluid}A_{fluid} = B_{core}A_{core}. \quad (2.24)$$

For the flat surface and the uniform magnetic field the dependence of the magnetic flux  $\Phi$  needs the correction, to take into consideration the magnetic field distortions

$$\Phi = B_k \tilde{A}_k, \quad (2.25)$$

where  $\tilde{A}_k$  is the effective area of the  $k$ -th section, assuming distortions and magnetic fringing, and  $B_k$  is the magnetic induction in this section. Particularly for the magnetorheological fluid we can write

$$\Phi_{fluid} = B_{fluid} \tilde{A}_{fluid}. \quad (2.26)$$

From the magnetisation characteristic of the selected solenoid's material we can define the operating induction value

$$B_{core} = \frac{B_{fluid} \tilde{A}_{fluid}}{A_{core}}. \quad (2.27)$$

For the selected ARMCO 0.2% C type of steel, from the B-H magnetisation characteristics (Fig. 2.25), the value of the magnetic field was defined as  $H_{steel} = 500$  kA/m and the magnetic induction  $B_{steel} = 0.88$  T.

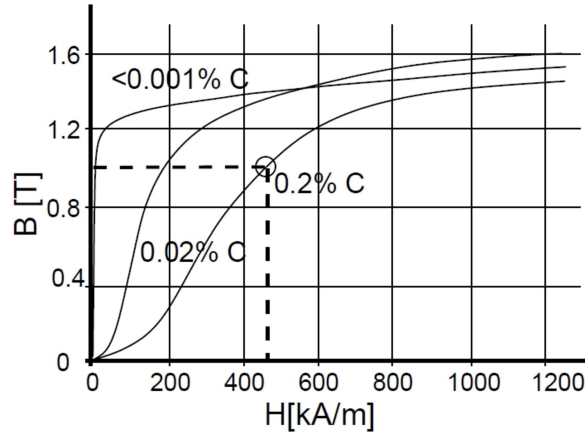


**Figure 2.25.** Magnetisation curves for certain magnetic materials: low carbon ARMCO iron, silicon iron and normal iron.

Further analysis of the remaining elements of the magnetic circuit is based on the Kirchoff's law for the magnetic circuits. The required number of the coil turns and the electric current to generate the desired magnetic flux is specified below

$$\oint H dl = NI = \sum_{k=1}^n H_k l_k, \quad (2.28)$$

where  $H$  is the magnetic flux intensity,  $N$  is the number of coil turns,  $I$  is the coil supply current, and  $l_k$  is the length of the magnetic flux in section  $k$ . The magnetic reluctance can be computed as

$$\mathfrak{R} = \frac{MMF}{\Phi} = \frac{NI}{\Phi}, \quad (2.29)$$

where MMF is the magnetomotive force. In the case of classic MR device's circuit we can extract the elementary magnetic circuits of the structure as presented in Fig. 2.26a and then reduce them to the circuit presented in Fig. 2.26b.

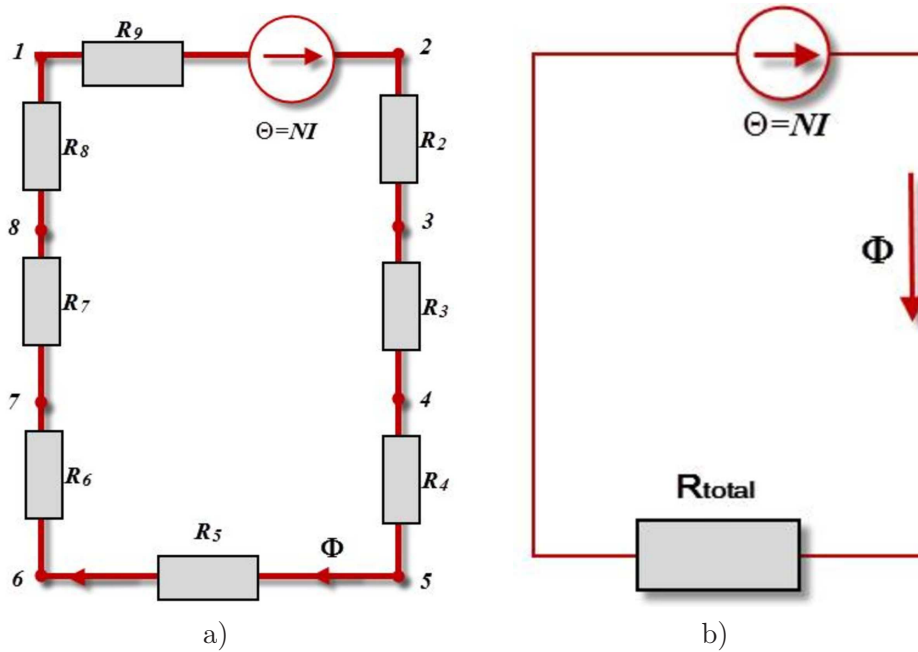


**Figure 2.26.** Elementary a) and reduced magnetic circuit of the magnetorheological device assembly b).

The reluctance can also be noted from the Ohm's law for the magnetic circuits

$$MMF = \Phi \sum_{k=1}^n \mathfrak{R}_k. \quad (2.30)$$

Finally the expression for the approximated number of the coil turns is obtained

$$N = \frac{\mathfrak{R}_{total} \Phi}{I} = \frac{\mathfrak{R}_{total} \mu_0 \mu_{fluid} H_{fluid} A_{fluid}}{I}. \quad (2.31)$$

The resistance of the coil winding can be computed as follows

$$R_W = \frac{l_w \rho_w}{A_w}, \quad (2.32)$$

where  $l_w$  is the total length of the coils winding,  $\rho_w$  is the resistivity of the coils wire, and  $A_w$  is the cross sectional area of the wire. The magnetic circuit power equals to

$$P = I^2 R_W. \quad (2.33)$$

Optimisations of the magnetic circuit parameters can be achieved using the finite element method (FEM), which takes into account nonlinear properties of the used materials. In the finite element analysis, the coil and magnetic gap models were defined for the axi-symmetric problem, with symmetric boundary conditions. In Fig. 2.27 half of the cross section through the

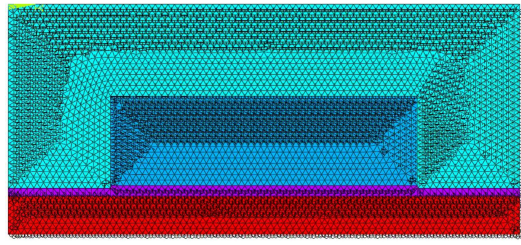


**Figure 2.27.** Finite element mesh of the magnetorheological damper's piston, coil and the gap.

damper is presented with the implemented finite element mesh. The value of the current density in the coil is defined as

$$J = \frac{NI}{A}. \quad (2.34)$$

The non-linear B-H magnetisation characteristics was introduced for each of the materials to the ANSYS program. Figure 2.28 shows a cross section of the 2D plane with the plotted amplitude of the magnetic induction  $B$  and the magnetic field intensity  $H$  inside the gap.

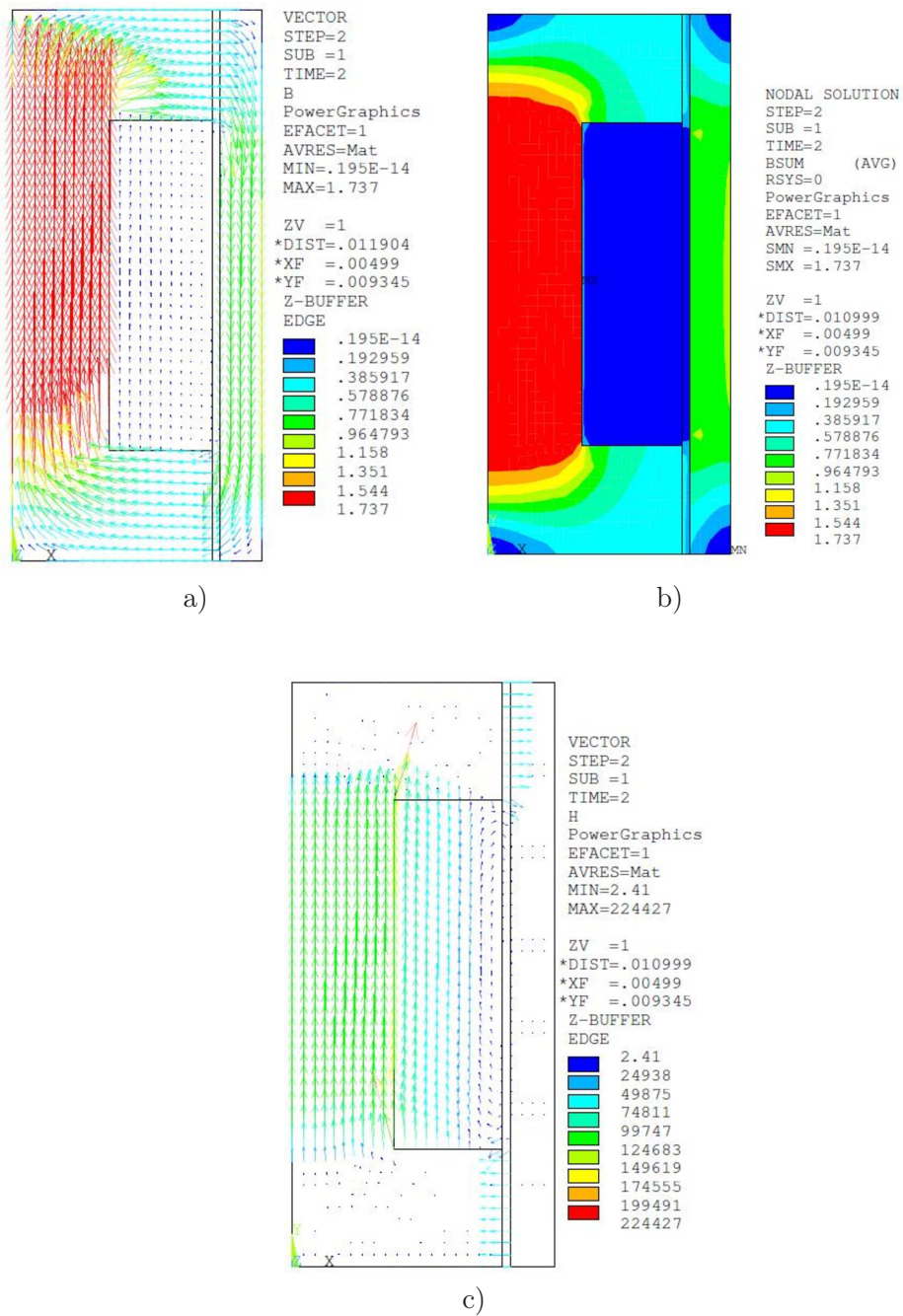


**Figure 2.28.** Vector of the magnetic flux density a), nodal solution for magnetic flux density b), and the magnetic field vector c).

### 2.1.5. Designing Rotary Magnetorheological Devices

The magnetorheological devices subjected to rotary motion operate in a direct shear mode. Usually the liquid is filling the gap which is formed by the outer diameter of the rotor and the inner diameter of the stationary housing. Another solution is achieved when the liquid is located in the slot formed by the lateral surfaces of the movable and fixed parts of the structure. There are also solutions combining these two constructions.

Let us assume one part of the structure fixed and the other one rotating at the angular velocity  $\omega$ . The linear velocity  $\nu$  of the liquid particles is the highest at the surface of the moving cylinder and decreases to zero at the fixed cylinder's surface. Denoting the geometrical parameters as in Fig. 2.29 we can determine the angular velocity of the liquid layer. It depends on the radius  $r$  as

$$\omega = \frac{\nu}{r}. \quad (2.35)$$

The strain rate is

$$\dot{\gamma} = \frac{d\gamma}{dt} = \frac{rd\omega}{dr}. \quad (2.36)$$

The torque can be computed as

$$M = 2\pi r^2 a \tau, \quad (2.37)$$

where  $a$  is the length of the rotor.

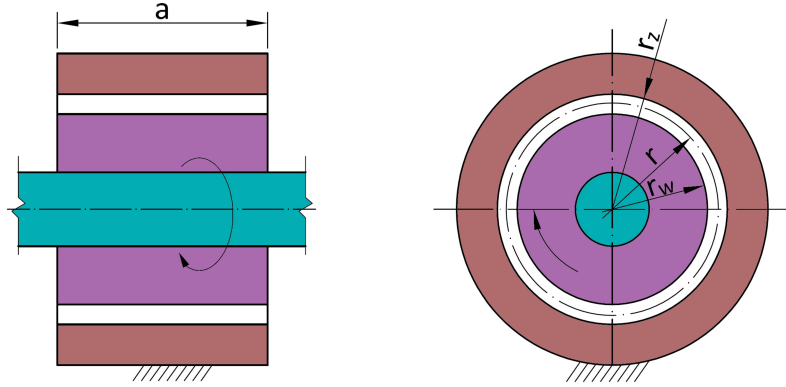


**Figure 2.29.** Scheme of the gap of the rotary magnetorheological device.

For the viscoplastic Bingham model of the MR fluid the tangential stress is given by the relations

$$\begin{aligned} \tau &= G\gamma \text{ for } \tau < \tau_0, \\ \tau &= \tau_0 + \dot{\gamma}\mu_p \text{ for } \tau > \tau_0. \end{aligned} \quad (2.38)$$

Finally we can write

$$d\omega = \frac{M}{2\pi\mu_p a r^3} dr - \frac{\tau_0}{\mu_p r} dr. \quad (2.39)$$

After integration we get the torque relation

$$M = 4\pi a \left[ \frac{r_w r_z}{r_w^2 - r_z^2} \left( \mu_p \omega + \tau_0 \ln \frac{r_w}{r_z} \right) \right]. \quad (2.40)$$

The third possibility to obtain a magnetorheological device is to place the fluid between two rotating discs, which form a slit. The computations are similar to the presented above. We assume that one of the discs is fixed, while the other one is rotating.

## 2.2. Magnetorheological Elastomers

Magnetorheological elastomers (MRE) are the new branch in the group of magnetorheological materials. They are the solid analogues of the fluids but the magnetizable particles are dispersed in a non-magnetic, solid polymer matrix. Usually they are composed of randomly mixing particles in the matrix or alternatively, using strong uniaxial magnetic field to induce dipole moments in the particles, pointing along the constant magnetic field. When the elastomer matrix is cured, the ferrous particles chains are locked and embedded in the matrix, as shown in Fig. 2.30.

The magnetorheological elastomers exhibit unique mechanical performance comparing with other materials. Shearing of the cured elastomer

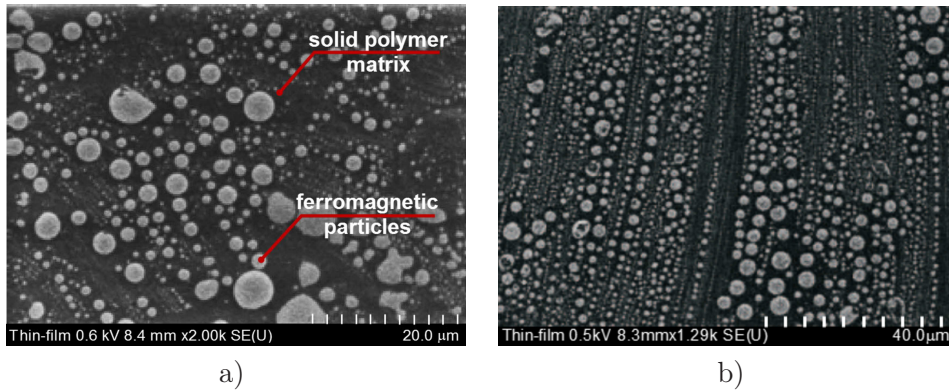


**Figure 2.30.** Alignment of ferromagnetic particles in the magnetorheological elastomer: randomly dispersed particles a), and aligned particles b) [31].

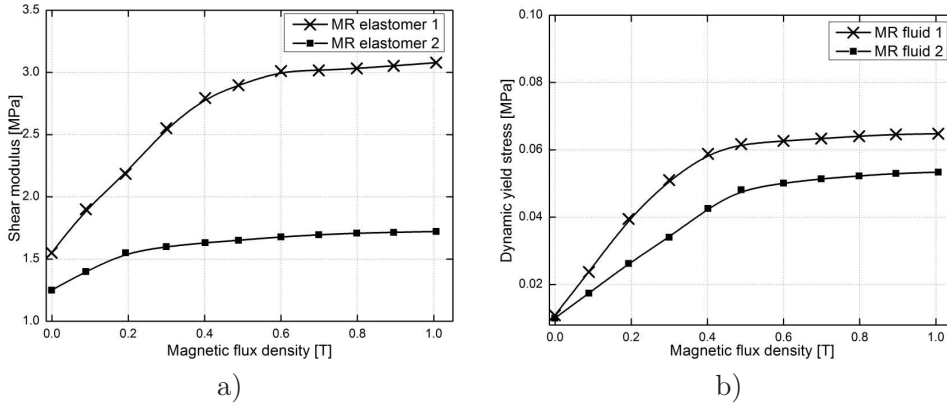


**Figure 2.31.** Comparison of typical characteristics of magnetorheological elastomer a) and fluid b).

causes particle displacement from the low net energy state. It requires additional work, which increases with the applied magnetic field. Thus it results in a field dependent shear modulus (Fig. 2.31a), while fluids have a field-dependent yield stress (Fig. 2.31b). The particles within elastomers typically operate in the pre-yield regime while the MR fluids usually operate in the post-yield continuous shear or flow regime. This makes MR fluids and elastomers complementary materials, rather than competitive to each other. From Fig. 2.31a it can be seen that the shear modulus of elastomer increases with the magnetic induction, until the material reaches the magnetic saturation. Further enhancement of the magnetic field does not affect the value of the shear modulus. The fraction of the magnetisable particles should be sufficient to provide the required on-state mechanical properties.

The main advantage of the MR elastomers over the fluids is their stability against sedimentation, coagulation and particle clustering [40]. As a consequence of the fact that the chain-like particle structures are locked in the matrix material during the process of curing, the rearrangement of the particles is eliminated when the external magnetic field is applied. Consequently the response time of MRE is significantly shorter than for the fluids.

Elastomers are easy to process, which gives possibility of embedding them between beams or plates to obtain a layered structure. Furthermore, the size and shape of the pad can be designed to meet particular requirements. The urge for container to keep the MR fluid in place is eliminated for the elastomers. Also they do not change their properties rapidly with the temperature, as it can be observed for the fluids.

Although much research on MRE is still at a primary stage, undoubtedly they are predestined for the applications focused on three main areas:

- **sound and vibration control**, especially for the vehicle applications, like the tuned vibration absorbers [20, 84] (Fig. 2.32a),
- **controllable stiffness change and deformation**, like in the stiffness tunable mounts and suspensions used to stabilize buildings (Figs. 2.32b, c) [2], variable impedance surfaces, or adaptive spring elements for the system's natural frequency shift (Fig. 2.32d) [17, 33],
- **sensors and magnetoactive actuators** like the one described in US20056877193 [50] and US20040074066 [73] which reports the complex releasable fastener system with MRE hooks; it provide changes in shape, orientation or flexural modulus of the fastener elements.

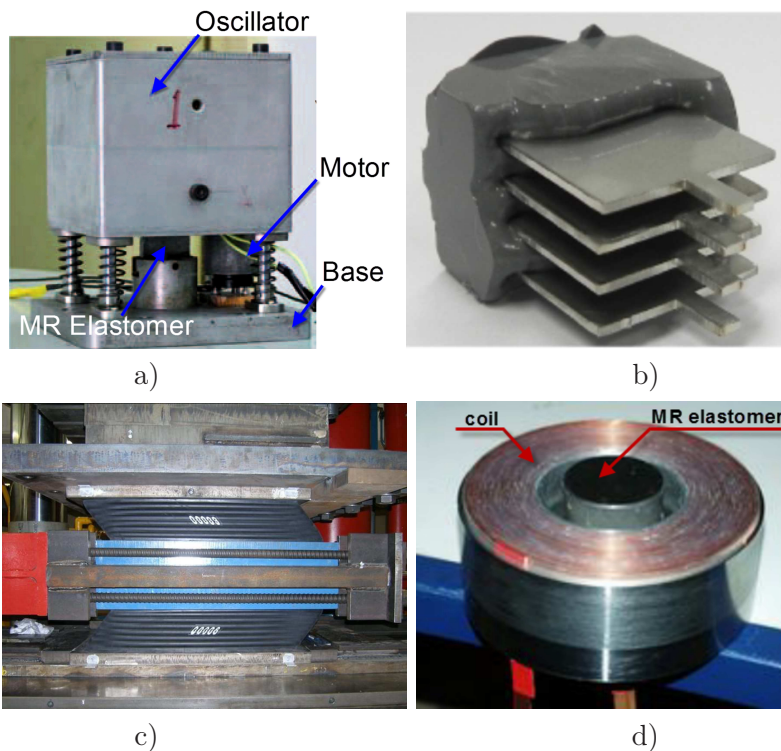


**Figure 2.32.** Exemplary, prototype applications of magnetorheological elastomers: vibration absorber a), laminated MRE isolator b), elastomeric bearings c), controllable spring elements d).

The use of smart materials in layered structures with the participation of controllable materials is a natural way to meet the requirements imposed by the innovative industries. A series of theoretical papers on smart sandwich structures deals with the parametric instability regions, natural frequencies, and the loss factors for different values of the electric or magnetic fields [48, 88]. Also an experimental work related to the assessment of the dynamic parameters of layered structures using electrorheological and magnetorheological materials with varying electric or magnetic field was carried out [28, 67, 79]. In US7086507 [24], the authors elaborated the device for vibration isolation of mechanical systems for random shock events by changing the storage and loss modulus of the MRE core embodied between magnetic activation layers. In [47] the authors study the transverse deflection of a three-layered magnetorheological elastomer embedded viscoelastic cored sandwich beam with conductive and non-conductive skins. They studied how the size and locations of the MRE patches influence the vibration properties of the structure. Ying and Ni [89] adapted the MRE for damping of the micro-vibration of a clamped-free sandwich beam under stochastic micro-motion excitation. In several studies the influence of the magnetic field on the vibration suppression capabilities of such beams is described in the form of variations in loss factors, vibration amplitudes and shifts in natural frequency values [35, 59, 80, 87].

Nevertheless, elastomers compared with fluids have only found limited applications, mainly due to the fact that the field-dependent modulus change is not wide enough to meet the demands of the particular applications. Groups of researchers have taken effort to improve the parameters, reporting on elastomers with magnetorheological effect enhanced several times [54, 64]. Further material technology development is crucial for significant improvement of the characteristics of these materials.

There are numerous industrial applications which may be the potential recipient of the smart elastomer based solutions. Vibrations generated by the vehicle drive system and the suspension could be suppressed by the self-adaptive absorbers, or smart lightweight suspension beams (Fig. 2.33a), stabiliser bar (Fig. 2.33b) or suspension bushings in order to reduce the shudder effect. The electrical current could be supplied from the automotive electrical system. It would be particularly useful to adjust the vibration of the adjacent structures in response to present conditions such as vehicle speed, load, road type and weather conditions. The seismic performance efficiency of the base isolation system, which decouples the civil structures from the ground motion can be highly improved by adapting the smart materials. The controlled elastomers with stiffness-tuning ability strive to

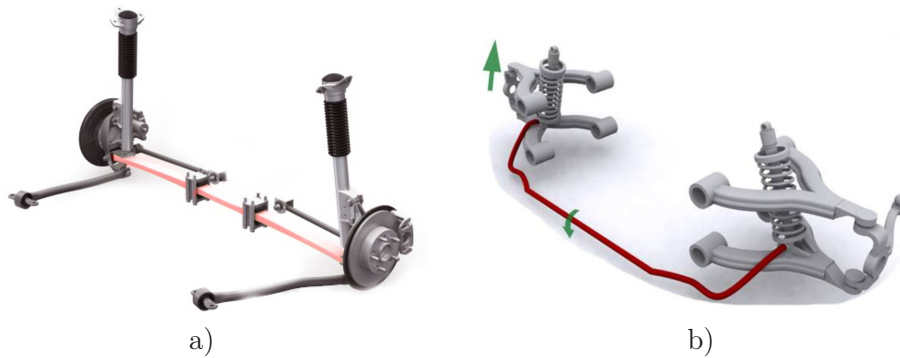


**Figure 2.33.** Potential application for magnetorheological elastomers: wheel guiding transverse springs a), stabiliser bar b). (Source: Freyrom, ZF).

alleviate limitations of existing passive-type base isolators, which works well on a site with a stiff soil condition, but are not effective on a site with a softer soil.

### 2.2.1. Beam with Magnetorheological Elastomer

The layered beam with the magnetorheological damping element was studied by the authors. The smart elastomer was placed at the tip of two parallel aluminium beams, presented in Fig. 2.34. Both of them were 720 mm long, and had a rectangular cross-section  $40 \times 0.5$  mm.

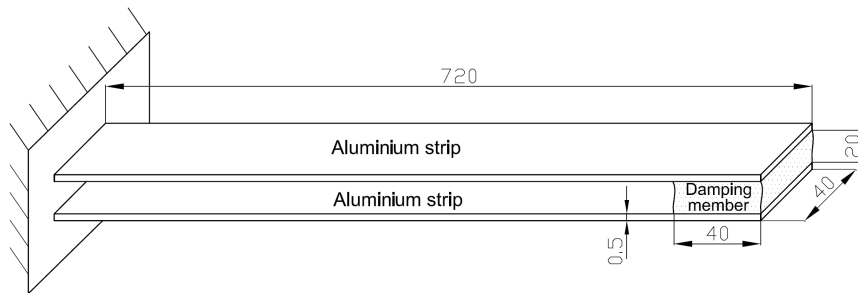


**Figure 2.34.** Dimensions (in mm) of the sandwich beam with the MRE damping member.

The beams were connected at the tip by the MR elastomer element. The shear modulus of the elastomer was 310 kPa for no magnetic field, and 330 kPa for magnetic flux density of 0.5 T, which was the maximum approachable value. Two island-pole electromagnets were used as actuators to

control the properties of the smart core in the desired manner. The magnets were placed on opposite sides of the beam. The first magnet's pole was N-type polarised while the other magnet's pole was S-type. That type of configuration (Fig. 2.35) increased the maximum value of the induced magnetic field flux density between poles up to 0.5 T and created a field flux that was normal to the sheared area of the elastomer.

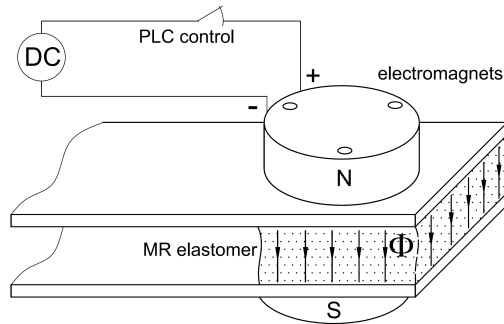
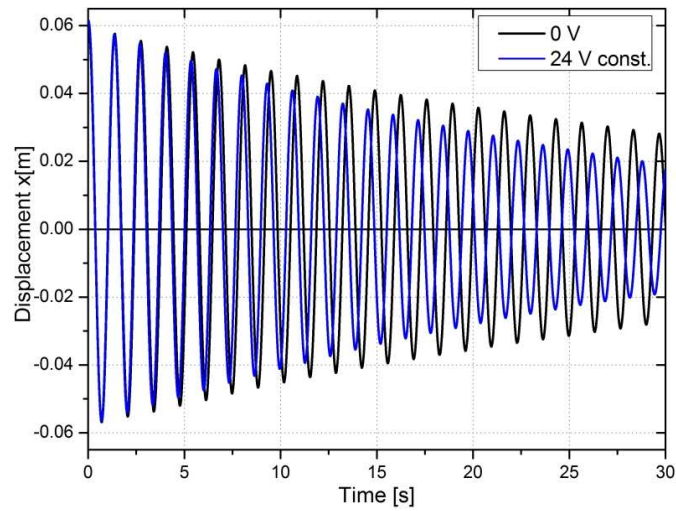


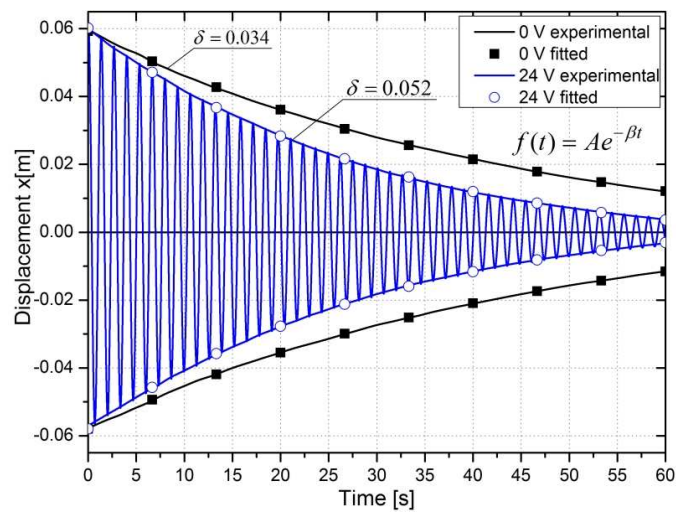
**Figure 2.35.** Polarization and placement of the electromagnets on the cantilever beam with the embedded MR elastomer.

The presented results of the displacement were considered for the tip of the beam, where the maximum amplitude occurs. Only the first mode of vibration was studied. The plots show how the magnetic field affects the X-component of the amplitude of the displacement of the beam's tip for an initial deflection 0.06 m. Two different cases were studied: MRE not activated and MRE turned on constantly in time (Fig. 2.36). The embedded MR elastomer undergoes changes in its modulus, which influences the apparent stiffness and damping of the whole composite.

By examining the free-decay time traces, one may find that when the MRE is activated, a significant reduction of the amplitude of vibrations is observed when compared to no magnetic field. The envelopes of the displacement curves were plotted in Fig. 2.36b. After 60 s, the amplitude of the displacement for 0 T (0 V DC) is 12 mm, which was 20% of the initial deflection (black line). For the MRE activated constantly (blue line), the amplitude after 60 s of vibrations decreased to 4.2 mm. It is 7% of the initial value. The activated magnetic flux density was 0.5 T for 24 V DC, which was the value inducing maximum magnetorheological effect. It resulted in the highest value of the shear modulus. The computed logarithmic decrement of damping was 0.034 for 0 V, and 0.052 for the case when the magnetorheological elastomer was activated.



a)



b)

**Figure 2.36.** Displacement in time for the MRE damping element a), and the envelopes of the displacement for the activated elastomer b).

Further analysis required to transform the time domain figures into the frequency dependencies. The Fourier transform (FT) yields the average characteristics of the amplitude and the frequency contents over the full time span of the signal. The amplitude on the FT plots is the relative strength of the

harmonic component present in the original signal. Since the strengths are relative to the original signal value, the Y-scale of the graphs is dimensionless. The results in Fig. 2.37 show the free vibrations response with the frequency of 0.75 Hz for no magnetic field. The frequency shifts toward the higher values when the MRE is activated. This is the natural consequence of the fact that the activated elastomer characterises with an intensified flexural rigidity since the stronger particle interactions are formed by the magnetic field.

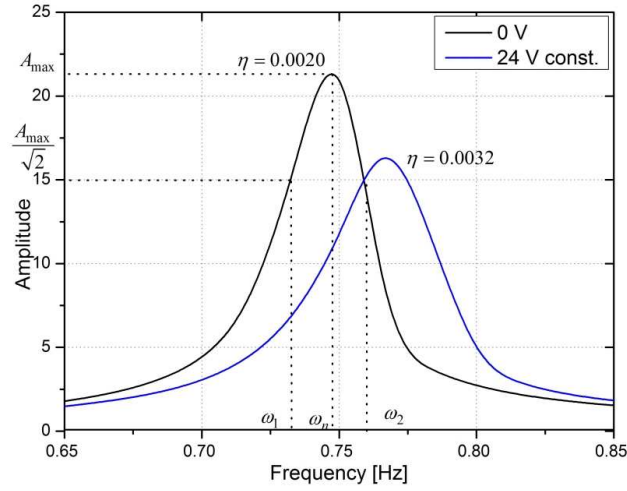


**Figure 2.37.** Frequency response of the structure for different cases of damping.

Meanwhile, the peaks representing the vibration amplitudes decline due to the increased damping. The damping coefficient was estimated using the half-power bandwidth method. It may give us an overall idea about the damping of the system, when the average damping is constant in time and related to viscous effects in the material. In this method the damping is evaluated from frequencies on either sides of the peak in frequency spectrum observed at resonance condition. The non-dimensional damping ratio is defined as the ratio of the frequencies observed at the two half power points of the natural frequency:

$$\psi = \frac{\omega_2 - \omega_1}{2\omega_n}, \quad (2.41)$$

where  $\omega_1, \omega_2$  are the half power frequencies and  $\omega_n$  is the natural frequency. The loss factor is computed as

$$\eta = \frac{\psi}{2\pi}. \quad (2.42)$$

For the case when no magnetic field was applied, the damping ratio was  $\eta = 0.0020$ . The damping ratio increased to  $\eta = 0.0032$  when the elastomer was activated.

The experimental analysis illustrated the influence of the magnetic field on the transient response, damping capacity, and frequency of the system. The results showed that the frequency of the considered beam increases and vibration amplitude beam decreases when the magnetic field is active.

### 2.3. Granular Materials

The granular damping methods have been widely studied over the years. However, none of them may be considered as the one using smart material. In this part of the book we would like to introduce an alternative type of granular structure. It utilises granular material placed in a special hermetic elastic envelope. The combination of granular material and airtight envelope gives new structure features unattainable for other materials. The detailed construction and principles of operation are discussed in the following sections. However, for full understanding of this new concept, the properties of classic, not classified as smart granular structures, need to be reviewed first.

Most of the solutions presented in the literature lack the possibility of adjusting the damping parameters of the system, when they are passively based on the dissipative nature of particle interactions in the granular material. They may be compared to a derivative of a single-mass impact dampers (Fig. 2.38a). This is a relatively simple concept, where particles of a small size are placed in a container that is attached to the structure, as illustrated in Fig. 2.38b. Particle movement causes the dissipation of a part of the energy through non-conservative interactions, which combine collisions, impact loss, friction, slips, deformations, etc. This mechanism was applied in linear stroke particle impact dampers as presented in [62, 63], or bean-bag dampers [51]. Further it was used for damping of beam vibrations, by placing the stiff box at the tip of an oscillating cantilever [3, 43]. Furthermore, the solution was found to be effective for the beams under centrifugal loads [22] (Fig. 2.39a).

Instead of placing the granules inside the artificially attached container, the bulk material can fill specially prepared cavities inside the beam (Fig. 2.39b) [83]. Park and Palumbo in [52] described the structural vibration damping capabilities of loose lightweight particles, filling cavities in sandwich beams. The vibration of the structure induces vibration of the micro particles in the cavities, which dissipate energy into the heat due to

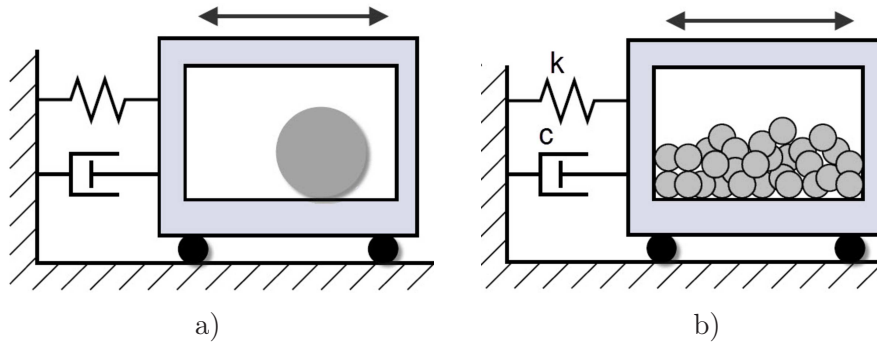


**Figure 2.38.** Schematics of different types of particle impact dampers. Impact damper a) and particle damper b).

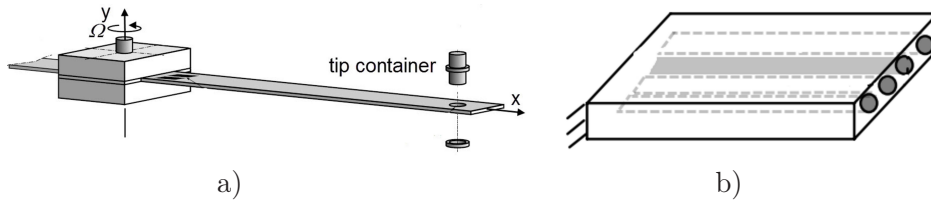


**Figure 2.39.** Granular material as a damping medium used for damping beams under centrifugal loads a) and damping of plates with specially prepared cavities b).

the internal damping. In [44] the authors investigated vibration damping of beams filled with tightly packed elastomeric beads. The authors in [74] investigated damping behaviour of the laminated honeycomb cantilevers with fine solder balls placed in the hexagonal cells. The displacement attenuation was achieved by the exchange of momentum through the repeated collisions between the balls and the face sheets. The mechanism was found to be effective in reducing the amplitude without significantly shifting the natural frequency of the cantilever. In all of the mentioned studies it was shown that the conduction of the energy into the micro-sized granular material and the following dissipation increase the vibration damping significantly.

### 2.3.1. Granular Structure Subjected to Underpressure

The damping solution utilising granular material subjected to underpressure is notably different from the solutions in the publications mentioned above, and it uses completely different principle. In our case, the granules are no longer loosely packed in the container, since their movement is restricted by the hermetic elastic envelope. Placing the granular material in the airtight

envelope with the remaining possibility of adjusting the underpressure value among the granules (Fig. 2.40), results in structure features typical for smart materials. One can find the analogy from the real the life to the vacuum packed food products like peanuts or coffee grains, which form a solid body, until the package is opened. The dominant mechanism and level of energy dissipation depends primarily on the state of the granular matter that the particular damper is operating in. While the typical granular damper seems to operate in the gas-like phase, the presented solution is based on the solid- or semi-solid phase, as the granules constantly maintain contact.

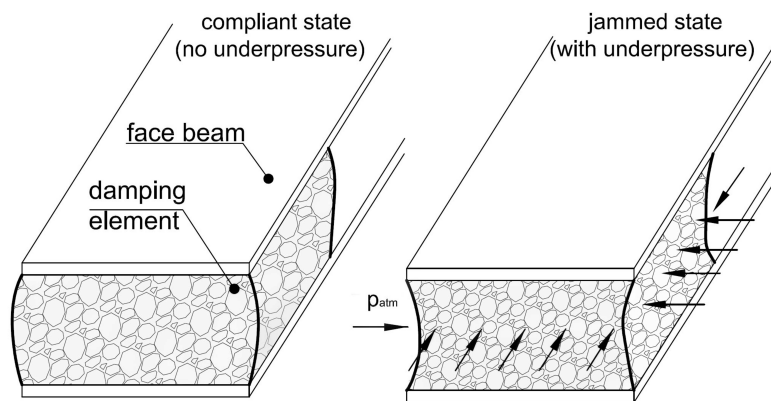


**Figure 2.40.** Scheme of the beam with the granular damping member controlled by the underpressure value (compliant state and jammed state).

The proposed pneumatic structure exploits fluid-like to solid-like reversible phase transition of the granular material, known as the jamming [12, 16]. The transition to a jammed state is forced by subjecting the structure to an underpressure, and the properties of the structure can be real-time controlled by adjusting the value of the partial vacuum. The particle interactions in the jammed state can be weakened or intensified, depending on the level of compression which is adjusted by the underpressure. Due to the shear deformation of the granular member, the beam exhibits damping behaviour.

According to the definition of smart material formulated by Ahmad [1], this special granular structure may be called *smart*, if the material *is capable of responding to the stimulus in a predetermined manner and extent, in a short time, and reverting to its original state as soon as the stimulus is removed*, which is a feature unattainable by the classic granular dampers.

The underpressure intensifies the mechanisms which enhance the rigidity of the structure and the energy of dissipation, like the friction and slips



**Figure 2.41.** Example of medical applications of granular structures subjected to underpressure: medical stiffener a) and haptic upper-arm orthotic b).

among the particles and between the particles and the enclosure, hence it enables the reduction of the free transverse vibrations. For the considered size of the particles, the phase transition is temperature-independent. Other mechanisms, such as the particle intrusion, occur when the granules change their position or orientation. The particle can also be pushed over an underlying layer as the particle hopping takes place [15]. The particle deformation can promote or inhibit the total deformation [38]. The level of deformation of particles depends on the hardness and stiffness of the granular material [32].

The applications of underpressure granular materials in special envelopes nowadays are mainly limited to medical services like the vacuum medical pillows, mattresses or splints which form a firm, uniform support for parts of the body (Fig. 2.41a) [41]. Furthermore interesting prototype constructions are developed, like the vacuum granular endoscope guide [38], laparoscopy camera shaft [30] or the upper-arm orthotic [45] (Fig. 2.41b). By controlling the inside air pressure, the orthotic can exert a stiffness or viscosity on the joints. The interesting field of research are the soft robots that move respectively to the underpressure [66] (Fig. 2.42a) or the universal robotic gripper with an elastic cell filled with granules (Fig. 2.42b), which allows picking differently shaped objects [13].

A little amount of works has been reported to date on the damping capacity of granular structures with controllable underpressure. The concept itself was introduced and briefly characterized in [6]. The main research effort was directed towards determination of the damping and elastic properties of the pneumatic granular structure used in a linear stroke damper, subjected to axial forces [8]. The rheological models of granular conglomerates under partial vacuum were presented in [90]. The constitutive model was later expanded to a six parameters rheological model capable of captur-

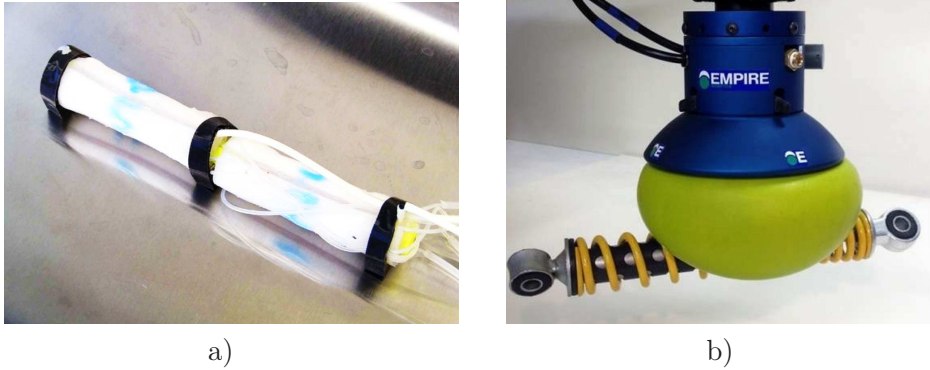


**Figure 2.42.** Examples of non-medical applications of granular structures subjected to underpressure: jamming unimorph snake robot a), and universal robotic gripper Versaball b) (Source: EmpireRobotics).

ing the response of the conglomerate subjected to an axial cyclic loading [92]. The experimental approach to the analysis of the vibration of a steel beam, fully covered with a sleeve filled with granules was given in [91] and later compared with a simplified model of the dynamic behaviour in [10].

### Principles of Operation

The jamming process itself has been widely studied in the literature on soil mechanics, and the basic principals may be explained by analysing the effective stress among the granules. The static pressure is one of the key factors that influences the state of the granular material and thus its parameters. Some basic relations help to understand how the pneumatic control can influence the behaviour of the system, by affecting static pressure. Let us consider the stresses in a plane section of the granular structure. For simplicity, a section with two granules in contact is specified (Fig. 2.43). The following force equation can be stated

$$N = A_c p_c + (A_g - A_c) p , \quad (2.43)$$

where  $A_c$  is the contact surface,  $A_g$  is the single granule's cross-section area,  $p_c$  is the stress on the contact surface and  $p$  is the pressure of the medium among the granules. The total stress value can be formulated as

$$\sigma = \frac{A_c}{A_g} p_c + \left(1 - \frac{A_c}{A_g}\right) p . \quad (2.44)$$

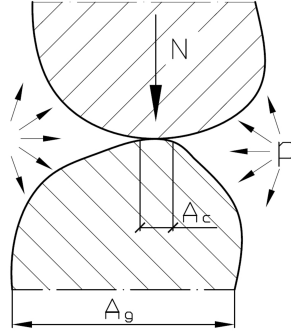


**Figure 2.43.** Contact between two granules of the structure.

According to Terzaghi's principle, all of the measurable effects caused by the change of stress, such as the compression, distortion and change of the shearing resistance, are due to the changes in the effective stress  $\sigma'$ . It describes the forces inside the skeleton

$$\sigma' = \frac{A_c}{A_g} p_c . \quad (2.45)$$

If we note that  $A_c/A_g \ll 1$ , then

$$\sigma' = \sigma - p . \quad (2.46)$$

In the considered case, a partial vacuum is applied to change the properties of the airtight structure. The value of the pressure  $p$  is negative, so the effective stress increases. The underpressure intensifies the mechanisms which enhance the rigidity of the structure and the dissipation of the system. As a result, we obtain a new type of structural material with the possibility of changing its parameters.

### 2.3.2. Beam with Smart Granular Structure

The construction of the proposed complex beam incorporates granular structure that allows changing the damping characteristics by varying the pressure value inside it. The distinctive feature of such a beam is the ability to control the dissipation energy by varying the control signal, hence it enables reduction of transverse vibrations [11]. The details covering the fabrication, dimensions and principles of operation of the discussed beam are discussed below.

The structure is composed of parallel face sheets forming a sandwich beam. They are connected by a thin (0.2 mm) elastomer layer made of

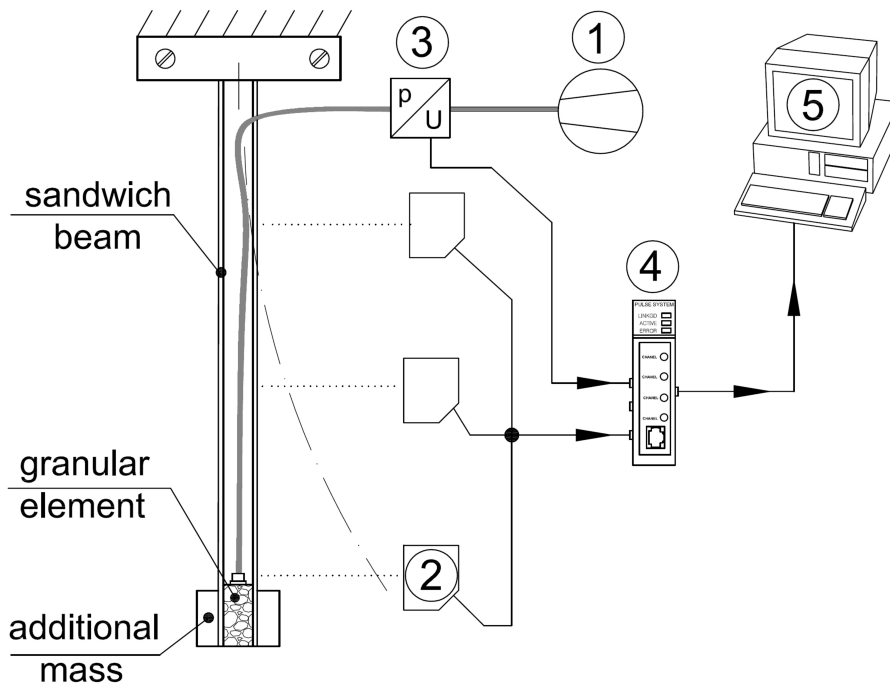


**Figure 2.44.** Schematic diagram of the experimental setup: 1 – vacuum pump, 2 – laser displacement sensors, 3 – digital underpressure sensor, 4 – data acquisition system, 5 – signal analysis software.

PVC foil, which forms a hermetic envelope. The envelope is filled with a homogeneous granular material. It can be placed on the whole length of the beams, or just locally in certain points, where we would like to introduce damping. There is also a decent possibility to construct a beam, with the metal core covered externally by an elastic sleeve filled with the granular material.

The configuration of the beam used for the studies is presented in Fig. 2.44. When the pump is switched off, the granular structure is in compliant state and the beam can easily bend when the particles are free to move inside the envelope. Evacuating the air from the envelope allows triggering the jammed state of the granules.

The mechanism of triggering the jammed state and controlling the damping ratio is reliable and relatively simple to apply, although many parameters like grain's shape, size and material, affect the efficiency of it. Four test specimens, each one filled with a distinct type of granules, which differed in size, shape or structural material were investigated. Figure 2.45



**Figure 2.45.** Types of the tested granular materials, from the left: plastic rollers, plastic spheres, steel spheres and plastic cubes.

**Table 2.1.** Properties of the types of granular material filling

Name	Material	Grain size [mm]	Specimen weight [g]
Rollers	ABS	$\phi 2 \times 3$	30
Plastic spheres	PVC with $\text{BaCO}_3$	$\phi 6$	65
Steel spheres	stainless steel	$\phi 4$	130
Cubes	PMMA (Perspex)	$2 \times 2 \times 2$	40

presents macro photographs of the granules. Certain properties of the granular materials used for the experimentation are collected and presented in Table 2.1. The final dimensions of the locally placed damping element were equal to  $50 \times 40 \times 20$  mm. The parallel face beams of the specimen were made of aluminium. Both of them are 720 mm long, and have the rectangular cross-section  $40 \times 0.5$  mm.

For each type of granular material, the displacement amplitude was recorded in order to measure the influence of the underpressure on the response of the cantilever. The underpressure value at the entrance of the hose connector was monitored during each measurement and was set to constant value chosen from the range 0–0.07 MPa which corresponds to 0–70% vacuum.

Figure 2.46 illustrates the influence of the constant underpressure in the component with the roller filling on the amplitude of the displacement for initial deflection 0.06 m and zero initial velocity. The underpressure was set individually before every measurement and remained constant during vibrations, so that all of the measurements were performed after the initial jamming. The obtained trial was a damped sine waveform, with the frequency and the amplitude depending on the set value of underpressure.

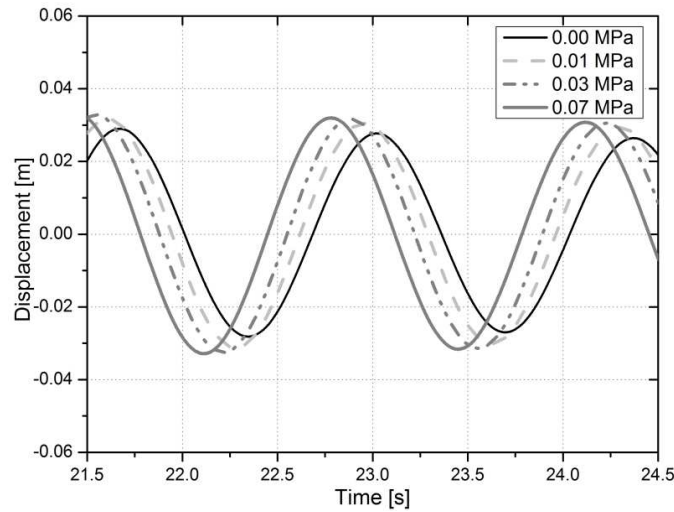
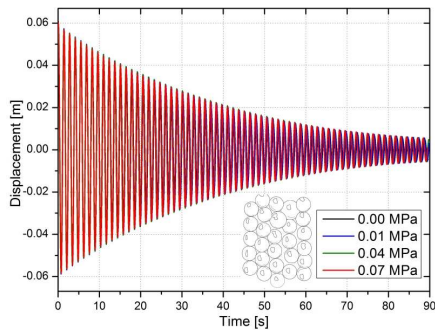


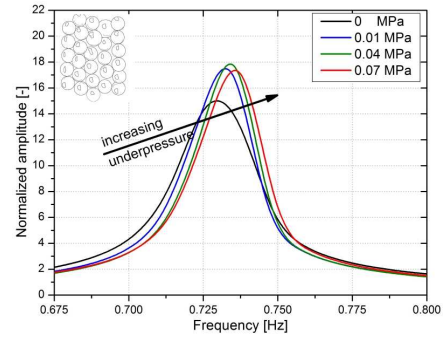
**Figure 2.46.** Displacement for constant underpressure, granular structure filled with rollers.

By examining the free-decay time traces of the displacement, one may find that the displacement amplitude slightly increases when compared to the compliant state for 0 MPa, as the jammed state interactions are intensified by the higher underpressure value. The loss of the damping efficiency is rather small and is mainly related to the restriction on the movement of the granules, which can no longer slide easily. These observations were true for all types of the examined materials as presented in the left column of Fig. 2.47. By analysing the minimum and maximum beam deflections, the envelopes of the responses were obtained. The amplitude decreases exponentially at the almost constant rate, so the envelopes were approximated by the exponentially modulated decay curves, typically used for systems with viscous damping. This gave us a very fine agreement. In Fig. 2.48a, the exemplary experimental curve (scatter) is plotted against the best fitted curve (solid line) for the roller granules subjected to 0.07 MPa.

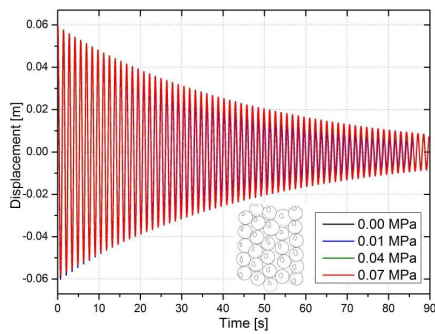
Right columns on Figs. 2.47 and 2.48b present the variation of the natural frequencies for a beam partially treated with the granular structure with rollers. The amplitude on the FFT plot is the relative strength of the harmonic component present in the original signal. The frequency slightly shifts toward the higher values when the jamming is intensified by the negative pressure. The jammed material has a higher density of force chain network, and thus an intensified flexural rigidity. This was also true for all of the



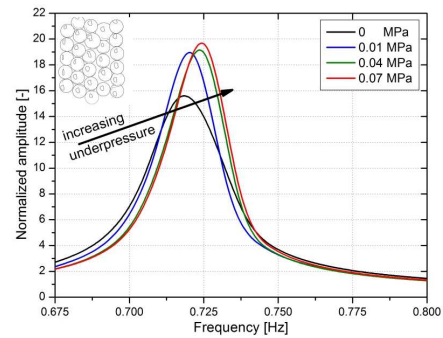
a) displacement for plastic spheres



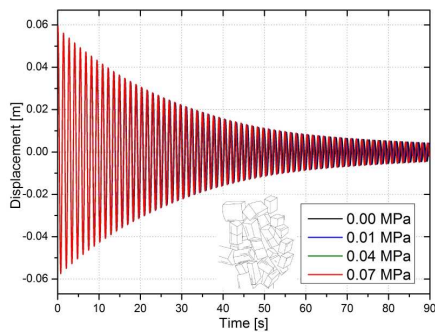
b) frequency for plastic spheres



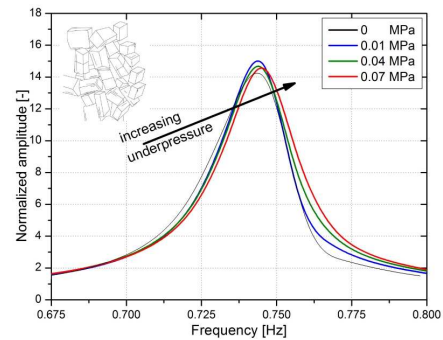
c) displacement for steel spheres



d) frequency for steel spheres



e) displacement for cubes



f) frequency for cubes

**Figure 2.47.** Displacement and frequency responses for constant value of underpressure for different types of granular materials.

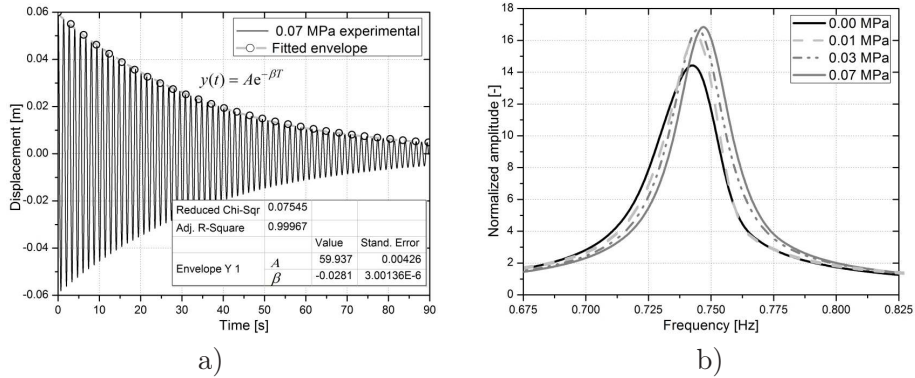


**Figure 2.48.** Experimental and exponentially fitted envelope for constant 0.07 MPa a), and frequency response for different values of constant underpressure b), granular structure filled with rollers.

examined materials, but with different intensities. The rollers exhibited the highest change.

The comparison of the logarithmic decrement of damping for different filling materials is presented in Fig. 2.49a. The highest logarithmic decrement value was observed for the cubic granules. The second best damping performance was obtained for the rollers. Both types of the spheres exhibit slightly smaller logarithmic decrements of damping, with the steel spheres having the lowest damping value. This is a consequence of the fact that the

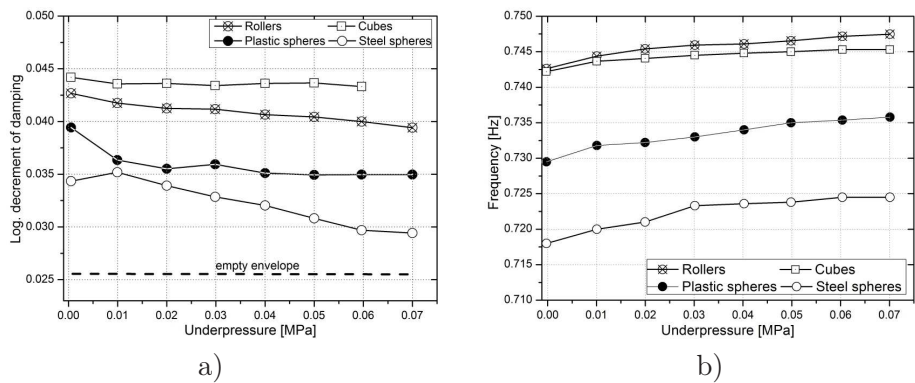


**Figure 2.49.** Logarithmic decrement of damping for constant underpressure for different types of granules a), and frequency vs. underpressure for different granular materials b).

small cubic granules initially exhibit stronger force chains and high rolling resistance, compared to other shapes. On the other hand, as the underpressure value is increased from 0 to 0.07 MPa, the absolute change of the logarithmic decrement is the most notable for the spherical granules while cubes exhibit minor change. The edgy cubic particles initially form a highly ordered structure which is hard to reorganise. Spherical granules can be quite easily reorganised, since they have no edges that restrict certain movements. The performance of the roller granules can be located somewhere between the edgy and the spherical surfaces, giving high initial damping. Also the possibility to alternate the damping value is very fine.

The intensified jamming shifts the natural frequencies to higher values when the underpressure is applied (Fig. 2.49b). The damping element filled with steel spheres was the heaviest one, so the frequency for it was the lowest. On the other hand, the cubic and roller fillings were the lightest and they exhibited the highest frequencies. For the considered case, when only a part of the beam was treated with the granular damping member, the absolute frequency change was rather small, but the tendency seemed to be clear. For the steel and plastic spheres, the increase reached 1%. For the roller and cubic shaped granules, the increase was 0.7% and 0.3%, respectively.



# Bibliography

- [1] I. Ahmad. Smart structures and materials. In *Smart Materials, Structures and Mathematical Issues: the 15th World Conference on Earthquake Engineering*, pages 13–16, Virginia Polytechnic Institute and State University, 1988.
- [2] L. A. Albanese and K. A. Cunefare. Performance of MRE based vibration absorbers. *Journal of Intelligent Material Systems and Structures*, 19:551–563, 2008.
- [3] K. T. Andrews and M. Shillor. Vibrations of a beam with a damping tip body. *Mathematical and Computer Modelling*, 35(9):1033–1042, 2002.
- [4] J. Bajkowski. *Magnetorheological fluids and dampers* (in Polish). Wydawnictwa Komunikacji i Łączności, Warszawa, 2014.
- [5] J. Bajkowski and J. M. Bajkowski. Influence of temperature and rotational speed on the properties of magnetorheological brake. In *Proc. of the 5th International Conference Design and Modeling of Mechanical Systems, Lecture Notes in Mechanical Engineering*, pages 143–149, Springer-Verlag Berlin Heidelberg, 2013.
- [6] J. Bajkowski, W. Grzesikiewicz, M. Hać, and P. Tadzik. Parameter determination of half-active damping of vibration of mechanical systems by using granulated materials. In *Materials of International Congress Dycons'99*, pages 67–74, Ottawa, Canada, 1999.
- [7] J. Bajkowski, J. Nachman, M. Shillor, and M. Sofonea. A model for a magnetorheological damper. *Mathematical and Computer Modeling*, 48(1):56–68, 2001.
- [8] J. Bajkowski and R. Zalewski. Influence of a single grain material on isotropic hardening parameters of granular structures under compression in uniaxial tensile tests. *Proc. of the Institute of Vehicles*, 63(4):119–126, 2006.
- [9] J. M. Bajkowski. Design, analysis and performance evaluation of the linear, magnetorheological damper. *Acta Mechanica et Automatica*, 6(1):5–9, 2012.
- [10] J. M. Bajkowski and R. Zalewski. Transient response analysis of a steel beam with vacuum packed particles. *Mechanics Research Communications*, 60C(1):1–6, 2014.
- [11] M. Bajkowski, B. Dyniewicz, and C.I. Bajer. Damping properties of a beam with vacuum-packed granular damper (dot: 10.1016/j.jsv.2014.12.036). *Journal of Sound and Vibration*, 2015.
- [12] G. Biroli. Jamming: A new kind of phase transition. *Nature Physics*, 3:222–223, 2007.
- [13] E. Brown, N. Rodenberg, J. Amend, and A. Mozeika. Universal robotic gripper based on the jamming of granular material. *Proc. of the National Academy of Sciences of the United States of America*, 107(44):18809–18814, 2010.
- [14] T. Butz and O. von Stryk. Modelling and simulation of electro- and magnetorheological fluid dampers. *Journal of Applied Mathematics and Mechanics*, 82(1):3–20, 2002.

- [15] M. E. Cates, J. P. Wittmer, J. P. Bouchaud, and P. Claudin. Jamming, force chains and fragile matter. *Physical Review Letters*, 81:1841–1844, 1998.
- [16] B. Chakraborty and R. P. Behringer. Jamming of granular matter. *Encyclopedia of Complexity and System Science*, 4697:4997–5021, 2009.
- [17] L. Chen, L. X. Gong, and W. H. Li. Microstructures and viscoelastic properties of anisotropic magnetorheological elastomers. *Smart Materials and Structures*, 16:2645–50, 2007.
- [18] D. D. L. Chung. Modeling of vibration damping in composite structures. *Journal of Materials Science*, 36:5733–5737, 2001.
- [19] R. M. Crane, A. L. Santiago, and C. P. Ratcliffe. Modeling of vibration damping in composite structures. *Advanced Materials for Vibro- Acoustic Applications*, 2:1–9, 1996.
- [20] H. X. Deng and X. L. Gong. Application of magnetorheological elastomer to vibration absorber. *Communications in Nonlinear Science and Numerical Simulation*, 13:1938–47, 2008.
- [21] S. Deshmukh and G. H. McKinley. Rheological behaviour of magnetorheological suspensions under shear, creep and large oscillatory shear (LAOS) flow. In *Proc. of XIVth International Congress on Rheology*, pages 1–9, Seoul, Korea, 2004.
- [22] D. N. J. Els. *The effectiveness of particle dampers under centrifugal loads*. Ph.D thesis, Stellenbosch University, 2009.
- [23] A. Fuchs, A. Rashid, Y. Liu, B. Kavlicoglu, and H. Sahin. Compressible magnetorheological fluids. *Journal of Applied Polymer Science*, 115:3348–3356, 2010.
- [24] F. Gordaninejad G. H. Hitchcock and A. Fuchs. Controllable magnetorheological elastomer vibration isolator, 2006. US Patent 7,086,507.
- [25] C. Gabriel and H. M. Laun. Combined slit and plate-plate magnetorheometry of a magnetorheological fluid and parameterization using the Casson model. *Rheologica Acta*, 48:755–768, 2009.
- [26] D. Gamota and F. Filisko. Dynamic mechanical studies of electrorheological materials: moderate frequencies. *Journal of Rheology*, 35:399–425, 1991.
- [27] D. C. Harris. History of magnetorheological finishing. *Proc. of SPIE*, 8016:1–22, 2001.
- [28] G. Hu, M. Guo, W. Li, H. Du, and G. Alici. Experimental investigation of the vibration characteristics of a magnetorheological elastomer sandwich beam under non-homogeneous small magnetic fields. *Smart Materials and Structures*, 20(12):127001, 2011.
- [29] S. D. Jacobs, D. Golini, Y. Hsu, E. Puchebner, D. Strafford, and W. I. Kordon-ski. Tribological characteristics in modified magneto-rheological fluid. *Proc. SPIE*, 2576:282–372, 1995.
- [30] A. Jiang, K. Althoefer, and P. Dasgupta. The core-snake, the variable stiffness laparoscopic camera. In *Proc. of the Hamlyn Symposium on Medical Robotics*, pages 7–9, London, UK, 2013.
- [31] M. R. Jolly, J. D. Carlson, and B. C. Munoz. A model of the behaviour of magnetorheological materials. *Smart Materials and Structures*, 4(1):607–614, 1996.
- [32] D. Kadau, D. Schwesig, J. Theuerkauf, and D. Wolf. Influence of particle elasticity in shear testers. *Granular Matter*, 8(1):35–40, 2006.
- [33] M. Kallio, T. Lindroos, S. Aalto, E. Järvinen, and T. Kärnä. Dynamic compression testing of a tunable spring element consisting of a magnetorheological elastomer. *Smart Materials and Structures*, 16:506–514, 2007.

- [34] W. I. Kordonski and S. R. Gorodkin. Magnetorheological fluid-based seal. *Journal of Intelligent Material Systems and Structures*, 7(5):569–572, 1996.
- [35] C. Lee. Finite element formulation of a sandwich beam with embedded electro-rheological fluids. *Journal of Intelligent Material Systems and Structures*, 6(5):718–728, 1995.
- [36] D. Lee, Y. Choi, and N. M. Wereley. Performance analysis of ER/MR impact damper systems using Herschel-Bulkley model. *Journal of Intelligent Material Systems and Structures*, 13(7-8):525–531, 2002.
- [37] W. Li, X. Zhang, and H. Du. Development and simulation evaluation of a magnetorheological elastomer isolator for seat vibration control. *Journal of Intelligent Material Systems and Structures*, 23(9):1041–1048, 2012.
- [38] A. J. Loeve, O. S. Van de Ven, J. G. Vogel, P. Breedveld, and J. Dankelmann. Vacuum packed particles as flexible endoscope guides with controllable rigidity. *Granular Matter*, 12(6):543–554, 2010.
- [39] M. T. Lopez, G. Vertelov, G. Bossis, P. Kuzhir, and J. D. G. Duran. New magnetorheological fluids based on magnetic fibers. *Journal of Materials Chemistry*, 17(4):3839–3844, 2007.
- [40] M. T. Lopez, A. Zugaldia, F. González-Caballero, and J. D. G. Duran. Sedimentation and redispersion phenomena in iron-based magnetorheological fluids. *Journal of Rheology*, 50(4):543–561, 2006.
- [41] M. D. Luscombe and J. L. Williams. Comparison of a long spinal board and vacuum mattress for spinal immobilization. *Emergency Medicine Journal*, 20(1):476–478, 2003.
- [42] A. Maher, F. Ramadan, and M. Ferra. Modeling of vibration damping in composite structures. *Composite Structures*, 46:163–170, 1999.
- [43] K. M. Mao, M.Y Wang, and Z. W. Xu ad T. N. Chen. Simulation and characterization of particle damping in transient vibrations. *Journal of Vibration and Acoustics*, 126:202–211, 2004.
- [44] J. G. McDaniel and P. Dupont. A wave approach to estimating frequency-dependent damping under transient loading. *Journal of Sound and Vibration*, 231(2):433–449, 2000.
- [45] T. Mitsuda, M. Wakabayashi, S. Kawamura, and S. Kuge. Wearable haptic display by the use of a particle mechanical constraint. In *Proc. of the 10th Symposium on Haptic Interfaces for Virtual Environment and Teleoperator Systems*, pages 1–6, Orlando, USA, 2002.
- [46] S. O. Reza Moheimani. A survey of recent innovations in vibration damping and control using shunted piezoelectric transducers. *IEEE Transactions on Control Systems Technology*, 11(4):482–494, 2003.
- [47] B. Nayak, S. K. Dwivedy, and K. Murthy. Vibration analysis of a three-layer magnetorheological elastomer embedded sandwich beam with conductive skins using finite element method. In *Proc. of the Institution of Mechanical Engineers. Part C*, Orlando, USA, 2012.
- [48] B. Nayak, S.K. Dwivedy, and K.S. Murthy. Dynamic analysis of magnetorheological elastomer-based sandwich beam with conductive skins under various boundary conditions. *Journal of Sound and Vibration*, 330:1837–1859, 2011.
- [49] S. Otani, H. Hiraishi, M. Midorikawa, H. Fujitani, and T. Saito. Development of smart systems for building structures. In *SPIE's 7th Annual International Symposium on Smart Structures and Materials*, pages 1–8, Newport Beach, California, 2000.

- [50] R. A. Ottaviani, J. C. Ulicny, and M. A. Golden. Magnetorheological nanocomposite elastomer for releasable attachment applications, April 12 2005. US Patent 6,877,193.
- [51] A. Papalou and S. F. Masri. Response of impact dampers with granular materials under random excitation. *Earthquake Engineering and Structural Dynamics*, 25:253–267, 1996.
- [52] J. Park and D. L. Palumbo. Damping of structural vibration using lightweight granular materials. *Experimental Mechanics*, 49:697–705, 2009.
- [53] R. Phillips. *Engineering applications of fluids with a variable yield stress*. Ph.D thesis, University of California, Berkley, 1969.
- [54] K. Popp, P. B. Kosasih, X. Z. Zhang, and W. H. Li. Fabrication and characterization of MR elastomers with high MR effects. In *15th International Congress on Sound and Vibration*, pages 258–265, Daejeon, Korea, 2008.
- [55] J. C. Poynor. *Innovative designs for magneto-rheological dampers*. M.Sc. Degree Thesis, Virginia Polytechnic, 2001.
- [56] I. Pramudya, J. Sutrisno, A. Fuchs, B. Kavlicoglu, H. Sahin, and F. Gordaninejad. Compressible magnetorheological fluids based on composite polyurethane microspheres. *Macromolecular Materials and Engineering*, 298(8):888–895, 2013.
- [57] J. Rabinow. The magnetic fluid clutch. *American Institute of Electrical Engineers Transactions*, 67:1308–1315, 1948.
- [58] J. Rabinow. Magnetic fluid clutch. *National Bureau of Standards Technical News Bulletin*, 32(4):54–60, 1948.
- [59] V. Rajamohan, R. Sedaghati, and S. Rakheja. Vibration analysis of a multi-layer beam containing magnetorheological fluid. *Smart Mater. Struct.*, 19(1):015013, 2010.
- [60] C. A. Rogers. Workshop summary. *ARO Smart Materials, Structures and Mathematical Issues*, 110(1):1–9, 1988.
- [61] N. Rosenfeld, M. Wereley, R. Radakrishnan, and S. T. Sudarshan. Behavior of magnetorheological fluids utilizing nanopowder iron. *International Journal of Modern Physics B*, 16(17):2392–2398, 2002.
- [62] M. Saeki. Impact damping with granular materials in a horizontally vibrating system. *Journal of Sound and Vibration*, 251(1):153–161, 2002.
- [63] M. Sanchez, G. Rosenthal, and L. A. Pugnaroni. Universal response of optimal granular damping devices. *Journal of Sound and Vibration*, 331:4389–4394, 2012.
- [64] A. S. Semisalova, N. S. Perov, G. V. Stepanov, E. Kramarenkoa, and A. R. Khokhlova. Strong magnetodielectric effects in magnetorheological elastomers. *Soft Matter*, 9:11318–11324, 2013.
- [65] K. H. Song, B. J. Park, and H. J. Choi. Effect of magnetic nanoparticles additive on characteristics of magnetorheological fluids. *IEEE Transactions on Magnetics*, 45(10):4045–4048, 2009.
- [66] E. Steltz, A. Mozeika, J. Rembisz, and N. Corson. Jamming as an enabling technology for soft robotics. *Electroactive Polymer Actuators and Devices*, 7642:225–229, 2010.
- [67] Q. Sun, J.-X. Zhou, and L. Zhang. An adaptive beam model and dynamic characteristics of magnetorheological materials. *Journal of Sound and Vibration*, 261:465–481, 2003.
- [68] F. Svaricek, Ch. Bohn, P. Marienfeld, H.-J. Karkosch, and T. Fueger. *Automotive Applications of Active vibration control*. Vibration Control. SCIYO, Rijeka, Croatia, 2010.
- [69] M. D. Symans and M. C. Constantinou. Passive fluid viscous damping systems for seismic energy dissipation. *Journal of Earthquake Technology*, 35(4):185–206, 1998.

- [70] T. Takagi. A concept of intelligent materials. *Journal of Intelligent Material Systems and Structures*, 1:149–156, 1990.
- [71] Thomas Lord Research Center. *Engineering note: designing with MR fluids*. Lord Corporation Materials Division, Cary, North Carolina, 2000.
- [72] S. C. Tung, D. S. Rule, V. R. Iyengar, and A. A. Alexandridis. Wear testing development and test procedures for evaluation of seal materials. *General Motors Defensive Disclosure Publication*, 457007:1127–1140, 2002.
- [73] J. C. Ulicny and M. A. Golden. Releasable fastener system and process, April 22 2004. US Patent 0074066.
- [74] B. Wang and M. Yang. Damping of honeycomb sandwich beams. *Journal of Materials Processing Technology*, 105:67–72, 2000.
- [75] X. Wang and F. Gordaninejad. A magneto-rheological fluid-elastomer vibration isolator. *Smart Structures and Materials: Damping and Isolation*, 5760(217):3839–3844, 2005.
- [76] X. Wang and F. Gordaninejad. A new magnetorheological fluid-elastomer mount: phenomenological modeling and experimental study. *Smart Materials and Structures*, 18(9):1–9, 2009.
- [77] F. Weber, J. Distl, and M. Maślanka. Semi-active TMD concept for Volgograd bridge. In *Proc. of the Society for Experimental Mechanics Series: Topics in Dynamics of Civil Structures*, pages 79–88, 2013.
- [78] B. Wei, X. Gong, W. Jiang, L. Qin, and Y. Fan. Study on the properties of magnetorheological gel based on polyurethane. *Journal of Applied Polymer Science*, 118(5):2765–2771, 2010.
- [79] K. Wei, G. Meng, W. Zhang, and S. Zhu. Experimental investigation on vibration characteristics of sandwich beams with magnetorheological elastomers cores. *Journal of Central South University of Technology*, 15:239–242, 2008.
- [80] K. Wei, W. Zhang, P. Xia, and Y. Liu. Nonlinear dynamics of an electrorheological sandwich beam with rotary oscillation. *Journal of Applied Mathematics*, 2012:1–17, 2012.
- [81] Y. K. Wen. Method for random vibration of hysteretic systems. *Journal of Engineering Mechanics*, 102(2):249–263, 1991.
- [82] W. M. Winslow. Electrorheological coupling. *Journal of Applied Physics*, 20:1137–1140, 1949.
- [83] Z. Xu and M. Y. Wang. Particle damping for passive vibration suppression: numerical modeling with experimental verification. In *Proc. of Design Engineering Technical Conferences*, pages 1–9, Illinois, USA, 2003.
- [84] Z. B. Xu, X. L. Gong, G. J. Liao, and X. M. Chen. An active-damping-compensated magnetorheological elastomer adaptive tuned vibration absorber. *Journal of Intelligent Material Systems and Structures*, 21:1039–47, 2010.
- [85] N. Yamaguchi, M. Nakao, T. Furuta, and T. Mikoshiba. Development of cylindrical passive damper using high damping rubber. In *Proc. of the Fifteenth World Conference on Earthquake Engineering*, pages 1–10, Lisbon, Portugal, 2012.
- [86] Z. Yang, H. Gu, J. Du, J. Gao, B. Zhang, X. Zhangb, and B. Xua. Self-assembled hybrid nanofibers confer a magnetorheological supramolecular hydrogel. *Tetrahedron*, 63(31):7349–7357, 2007.
- [87] J.-Y. Yeh. Vibration analysis of sandwich rectangular plates with magnetorheological elastomer damping treatment. *Smart Mater. Struct.*, 22(3):035010, 2013.

- 
- [88] Z.-F. Yeh and Y.-S. Shih. Dynamic characteristics and dynamic instability of magnetorheological material-based adaptive beams. *Journal of Composite Materials*, 40(15):1333–1359, 2006.
- [89] Z. G. Ying and Y. Q. Ni. Micro-vibration response of a stochastically excited sandwich beam with a magnetorheological elastomer core and mass. *Smart Materials and Structures*, 18(1):1–13, 2009.
- [90] R. Zalewski. Constitutive model for special granular structures. *International Journal of Non-Linear Mechanics*, 45(3):279–285, 2010.
- [91] R. Zalewski and J. M. Bajkowski. Experimental analysis of beam vibrations damping with the special ABS granular structure. *Machine Dynamics Research*, 35(3):98–106, 2011.
- [92] R. Zalewski and Ł. Skoniecki. Six parameters rheological model for special granular structures. *Machine Dynamics Research*, 35(3):107–116, 2011.

# Chapter 3

## Controlled Structures

The development of appropriate control strategies in individual adaptation of vibrating structures requires knowledge of respective mathematical models. Equations of motion discussed in this chapter are described by the partial differential equations. In this case, the classic vibration solutions are based on the Fourier series. According to Fourier transform in space, the partial differential equation is reduced to a system of ordinary differential equations with respect to time. The size of the system of equations, and hence the number of terms of the Fourier series is limited to the necessary amount to provide the required accuracy. Properly selected mode shape functions fulfil assumed boundary conditions. The final solution is the sum of the products of the following mode shape functions of the problem and the corresponding functions of time, which are the solutions of the set of the ordinary differential equations. As an example the sine Fourier transform (3.1), (3.2) in the finite interval  $[0, L]$  is presented

$$V_j(t) = \int_0^L w(x, t) \sin \frac{j\pi x}{L} dx, \quad (3.1)$$

where

$$w(x, t) = \frac{2}{L} \sum_{j=1}^n V_j(t) \sin \frac{j\pi x}{L}, \quad (3.2)$$

fulfilling e.g. boundary conditions for the simply supported Euler beam of the length  $L$ . In order to solve the system of ordinary differential equations, the integration with respect to time is applied. Except special cases the analytical solutions are unknown. Diagonal and fixed in time matrices as-

sociated with the inertia, damping and stiffness of the system describe one of them. However, in a general case we are compelled to restrict the solution with the first term of the series, or to a numerical integration approach. The knowledge of analytical solution enables immediate information about the state of the structure without the need of continuous computations of the problem, as in the case of the numerical solutions. The semi-analytical solutions, i.e. those in which the system of ordinary differential equations is integrated numerically, are mainly used for verification solutions obtained by approached methods.

The second classical method of the solution of equations of motion is the finite element method. It is typically used for complex problems, hard to be solved analytically. In such a case in our computations the space-time finite element method was applied. This continuous Galerkin method discretizes spatial variables and time variable simultaneously. Therefore, we can postulate a balance of energy over the time interval, not only at some instants. In the formulation of the method, we integrate the physical quantities analytically in the time interval rather than numerically, as in the classical finite element method. This numerical method will be used to solve the evolutionary processes of vibrations. The velocity formulation of the space-time finite element method is used. The equations of motion are discretized both in space and time. This means that in the present numerical scheme time marching the velocity is distributed in the finite space-time element according to interpolation functions and nodal velocities in two adjacent time layers used as parameters. The analytic form of the velocity function in space and time allows the integration and differentiation with respect to these variables. Functions of displacement and acceleration determined in this way, however, still depend on the nodal velocities. Thus, as the result we have inertia, damping and stiffness matrices multiplied by velocities. The integration of the velocity function with respect to time results in the displacement function and contains the term with initial displacements in time layer. Initial displacements in each time step of the time stepping scheme in the final equation of force equilibrium express nodal forces at the beginning of time interval. Acceleration and displacement functions allow the analytical determination of the energy of the system. The energy of the external forces is derived from the right hand side of the equation of motion. Classical energy minimisation and assembly of the global system leads to the following matrix solution scheme

$$(\mathbf{M}_g + \mathbf{C}_g + \mathbf{K}_g) \begin{Bmatrix} \mathbf{v}_i \\ \mathbf{v}_{i+1} \end{Bmatrix} + \mathbf{E}_g \mathbf{w}_i = \mathbf{F}_g . \quad (3.3)$$

Here,  $i$  and  $i+1$  denote the known and actually computed state, respectively. The problem is reduced to the numerical solution of the system of algebraic Eqs. (3.3). The vector  $\mathbf{v}$  contains the velocities of the nodal displacements and angles of rotation, while the vector  $\mathbf{w}$  contains the nodal displacements and the angles of rotation.  $\mathbf{M}_g$ ,  $\mathbf{C}_g$ ,  $\mathbf{K}_g$ , and  $\mathbf{E}_g$  are the global matrices of inertia, damping, stiffness, and nodal forces, respectively, and  $\mathbf{F}_g$  is the global vector of external forces. The global matrices are assembled from elemental matrices  $\mathbf{M}$ ,  $\mathbf{C}$ ,  $\mathbf{K}$ , and  $\mathbf{E}$ , merged in proper locations of the global matrices based on the topology of the mesh. Similarly, the global load vector is assembled from elemental force vectors  $\mathbf{F}$ . The velocity vector  $\mathbf{v}_{i+1}$  is the only unknown vector in the above system of equations. Finally we must compute the displacements  $\mathbf{w}_{i+1}$  with the following formula

$$\mathbf{w}_{i+1} = \mathbf{w}_i + h[\beta \mathbf{v}_i + (1 - \beta) \mathbf{v}_{i+1}] . \quad (3.4)$$

The first attempts at space-time modelling of physical problems were published in 1964 by Gurtin [45, 46] and Herrera [48]. Defining the minimized functional resulting from the theory of convolutions, the relationship between time and the spatial variables in time-space sub-areas were derived. These sub-areas can be interpreted as space-time finite elements. Later, in 1969, Oden [68] proposed a generalization of the finite element method. Fried [41] and Argyriss, Scharpf and Chan [3, 4, 5] began to treat the spatial and time variables equally in the formulation of physical problems. The space-time finite element method was applied successfully to wave problems [1, 40, 49], and also to acoustics [90] and fluid mechanics [47]. The space-time element method can be considered as the extension of the traditional finite element method in the time domain [7]. Non-stationary partition of the structure and non-rectangular space-time elements [8, 9] enabled the solution of a new group of problems: problems with adaptive mesh [11, 13, 14], contact problems [10, 12], and large deformations [23].

This chapter presents the mathematical and numerical models of the selected problems in the dynamic structure. The first issue is the problem of the moving inertial load travelling along the finite beam span with controlled supports. The semi-analytical solution and the general numerical description of the moving mass are presented. The shaft with a controlled rotary damper subjected to a harmonic load is the next issue. Analytical, semi-analytical and numerical solution of the problem are presented. The following section describes a mathematical model of a sandwich beam with controlled parameters of the core and gives the analytical and semi-analytical solutions. Finally, a structure based on granular material controlled by partial vacuum

is presented. The mathematical model assumes mechanical properties of the granular material described by the Kelvin-Voigt model.

### 3.1. The Beam Span under the Inertial Moving Load

Inertial loads moving on strings, beams and plates with sub or super critical velocities are especially important for engineers. Rail and road transport developments need a better understanding of phenomena accompanying travelling loads. Most applications are such as the interaction between railway wheels and a rail or a track, the effect of a vehicle moving on a bridge, interaction between rail power collector and traction power network, as well as magnetic rail. Moving loads are also widely used in aerospace, automotive, and robotics industry. In railway engineering practise, problems with travelling masses are of special interest. The influence of the mass attached locally to the structure can not be neglected since the mass element is firmly attached to the base (Fig. 3.1). We can only mention that the mass of a single train wheel is 500 kg and a wheelset has a mass equal to 1500 kg. The mass density of the rail is only 60 kg per meter. A similar problem occurs in power collectors.

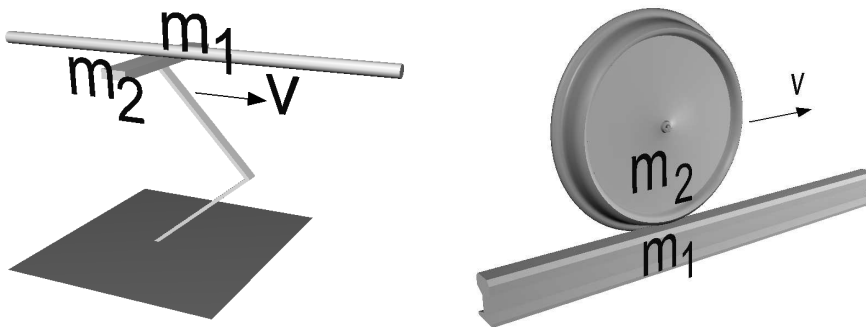


**Figure 3.1.** Examples of problems with a mass  $m_2$  travelling on a string or a beam  $m_1$ .

The speed of the rail vehicle in certain circumstances can reach the critical speed. This particular speed occurs, when the circular frequency of the exciting force is equal to the natural circular frequency of the structure. It is manifested in extreme values of structure deflections. In such a case the wave phenomena significantly differ from the responses of systems subjected to loads without inertia.

There are two types of classical problems with a travelling load: a moving massless force and a moving inertial force (Fig. 3.2). A moving massless force

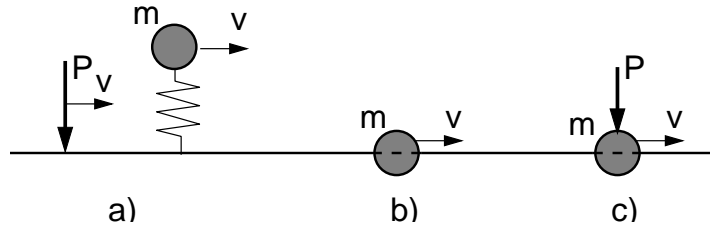


**Figure 3.2.** Massless load (a), inertial load (b), and inertial load with a massless force (c).

is a constant or harmonic non-inertial load. On the other hand, a moving inertial force depends on the current state of a vibrating structure. These forces, although of a completely different nature are often confused with each other. In most cases, exchangeability of both forces is an unacceptable simplification of the moving load physical model. Despite the wide interest in the moving loads for more than a century, still many issues remain unresolved. In the case of non-inertial loads, for example, the gravitational force or the forces described by the harmonic function, complete analytical solutions are known. Moving inertial load results in more complex models. Mathematical equations do not have respective analytical solutions. Figures 3.3 and 3.4 show the trajectories for both types of moving loads travelling along the string. The moving load velocities correspond to the fraction of the wave speed in the string. The parameters of the task are chosen so that the wave speed in the string is equal 1. Figure 3.3 illustrates the sharp edges of the trajectory. In the case of inertial load smooth trajectories were observed. In the both load cases, for the lower velocities we can observe reflections between the returning wave in the string and the point moving load. Additionally, we note an interesting property of the solution, depicted in Fig. 3.4. With increasing velocity of the moving mass the discontinuity of the trajectory near the end of the support is observed. The convergence of the solution near the end point is depicted in Fig. 3.5. The mass trajectory is plotted for increasing number of terms in the series at the 0.5 wave speed. We notice that the trajectory tends slowly to the jump at  $x = L$ . All characteristic lines are smooth. The convergence rate is low and, especially near  $x = L$ , the number of terms must be at least 50.

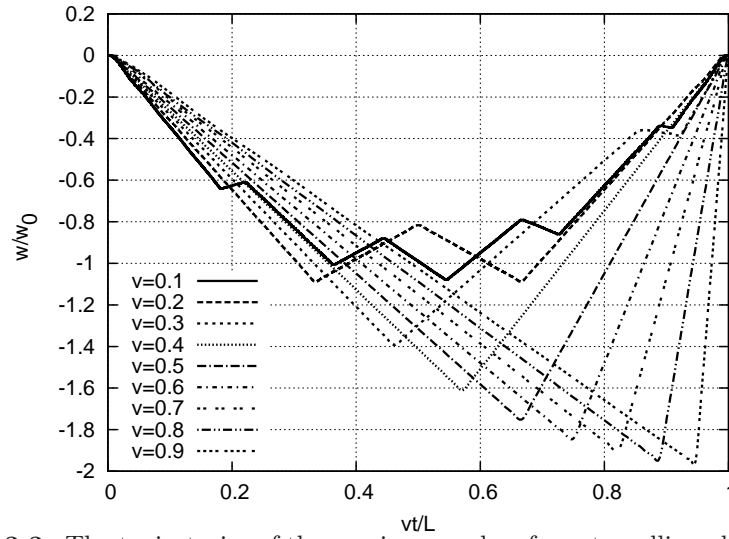


**Figure 3.3.** The trajectories of the moving massless force travelling along a string for different speed.

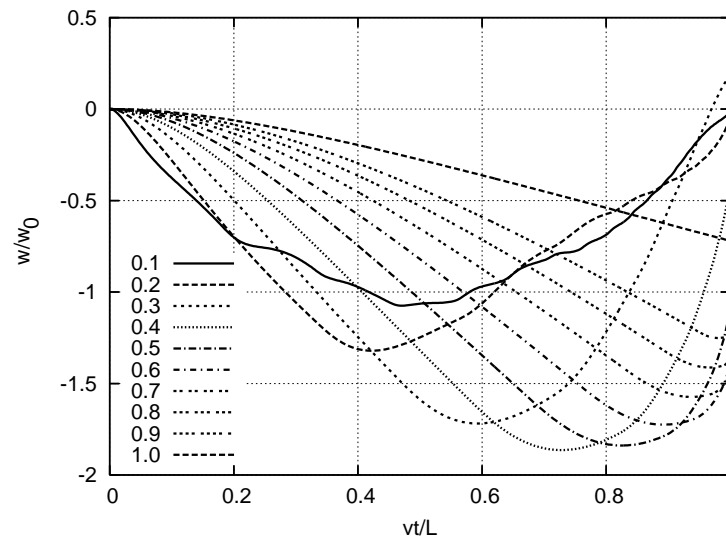


**Figure 3.4.** The trajectories of the moving inertial force travelling along a string for different speed.

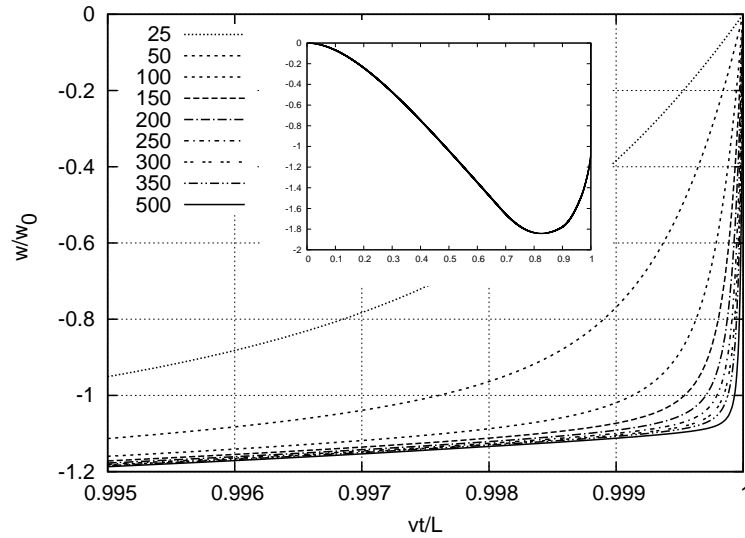


**Figure 3.5.** The convergence of the mass trajectory travelling with  $v = 0.5$  wave speed, near the end point, for various number of term (25, 50, ..., 500).

The literature on the subject is extensive. At the middle of the 19th century the pioneering works of Willis [93] and Stokes [87] were published. There are many historical reviews concerning the moving loads problem [71, 88, 94]. One can find there hundreds of references concerning load moving on beams, strings and plates. In most of the cases, the moving massless constant force was considered. This problem results in the closed solutions. The analysis of the moving massless force is relatively simple and was treated in numerous papers [42, 60, 69]. We include in this group all the papers devoted to the travelling oscillator, i.e., a mass particle joined to the base with a spring [22, 62, 73]. Although the authors call this type of the load an inertial one, we consider it as a massless force generated only by the particle's inertia. Taking into account the inertia of the moving mass results in significant mathematical complications. Saller in [82] considered the moving mass for the first time. In [52] simplifications were applied and the solution was expressed by only the first term of the trigonometric series. Time function fulfilled the second order differential equation of variable coefficients. The final solution of the differential equation of variable coefficients was proposed as an approached infinite series. In [83] the motion of the structure under the moving mass was considered. The method of variable separation was applied. The ordinary differential equation of motion under the moving mass was expressed

in generalised coordinates by using the second Lagrange equations. This consideration is relatively complex and slowly converged since the final solution is expressed in terms of the triple infinite series. The both above works can be considered as the base for the analysis of the problem of the moving mass in successive further works [24, 65] and many others. In the literature, we can find solutions based on both the differential equations [51, 58, 63] and integral equations [39, 80, 91]. These are mainly semi-analytical solutions or, as in the case of the mass particle moving along a massless string, we know the analytical solution [85]. In the paper [57], the author deals with the problem of a moving mass by the integro-differential equation. In [33], the same solution is obtained with the Fourier method applied directly to the motion differential equation. In both approaches the mathematical treatment of the distribution function results in serious questions on the continuity of the solution. The detailed discussion of this problem was given in [30]. Finally, in the paper [32] the Lagrange equation of the second kind was applied. This approach allows us to avoid troubles with treatment of the Dirac delta in the consequent mathematical solution. Especially, we do not transform the distribution function. Variable speed of the moving mass was analyzed in [2, 44, 64]. The equivalent mass influence is analyzed in [43]. The infinitely long string subjected to a uniformly accelerated point mass was also treated [79] and analytical solution of the problem concerning the motion of an infinite string on the Winkler foundation subjected to an inertial load moving at a constant speed was given [53].

In [33] were considered small vibrations of the massless and mass string subjected to a moving inertial load. The semi-analytical solution of the problem was proposed. The final solution has a form of a matrix differential equation of the second order. Numerical integration results in a solution in a full range of the velocity: sub-critical, critical, and over critical. The correct solution of the differential equation of motion of the analysed system exhibits unexpected phenomenon, a sharp gradient of the mass displacement near the end support. This new feature previously was not reported in the literature. The closed solution in the case of the massless string was analysed and its discontinuity was proved mathematically. Numerical results obtained for inertial string demonstrated the same feature. Since small vibrations are considered, the discontinuity effect was of pure mathematical interest. In the case of the Timoshenko beam the discontinuity of the mass trajectory was presented in [34].

In numerous references, authors treated the problem in a very low range of the mass speed. In such a case results are sufficiently accurate, even if the inertial term contributing to moving mass is not correctly treated by

the time integration method. Simply, the moving mass influence in such cases is minor compared with static displacements. At low speeds, significantly lower than the critical speed, the neglected inertia of a moving object does not contribute a noticeable error. At higher speeds, the deflection error can reach 50–80%. In practise, measurements of the wave speed in railway tracks treated as beams reaches values 800–1000 km/h. In the case of soaked ground, the speed can decrease to 500 km/h or less. Dynamic influence of the moving load significantly increases the structure deflection. The highest contribution of dynamic effects in structures subjected to moving loads determines the critical speed of motion. Practically, the critical mass speed equals 0.4–0.5 of the wave speed. This is the range of the speed of the modern rail vehicle.

More complex problems require the use of numerical schemes. The matrices describing the moving mass are essential for proper computer simulation of complex dynamic tasks. It is worth mentioning that the commercial packages available on the market do not support a vibration analysis of elastic bodies which would allow a direct simulation of moving loads, especially inertial ones. In consequence it is essential to develop a universal numerical tool for the wave analysis of the moving inertial loads.

A simple intuitive modification of the global inertia matrix by adding the moving mass ad hoc lumping in nodes (Fig. 3.6) is incorrect [16]. This approach ignores the complexity of the motion of the material point. The acceleration of a moving mass is expressed as a derivative which comprises the lateral acceleration, Coriolis acceleration, and the centrifugal acceleration. Numerical modelling of a moving inertial load focuses on the classical

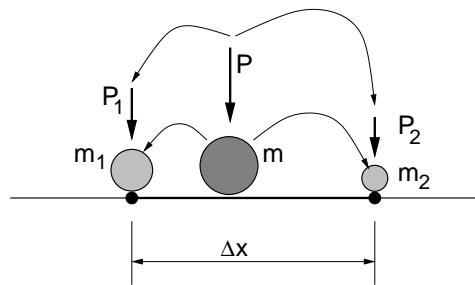


**Figure 3.6.** Ad hoc moving mass lumping in nodes.

finite element method, for example [25, 38, 78, 95]. In these papers, the derived matrices were based on polynomials of higher order and they are not comprehensive. They can not be applied to strings or Timoshenko beams, in which the nodal displacements and angles of rotation are independently

interpolated by linear functions. If the shape functions of finite elements of the beam are of higher order (such are in the Bernoulli-Euler beam), then the respective derivatives of the chain derivation in the moving coordinate system are non-zero and respective moving mass matrices are also known [18]. In the case of the Timoshenko beam, the problem is more complex, since we usually use linear shape functions for both deflection and rotation. In such a case we can use the space-time finite element approach for proper formulation of the solution algorithm [31]. The accuracy of the solution per one time step is high. The classical Newmark time integration method results in significantly lower convergence rate [35].

Classical semi-discrete approaches are effective for calculating the low frequency response. Their performance is less satisfactory in solving problems exhibiting discontinuities or sharp gradients in solutions, which are characteristic for wave problems. In these cases the space-time element method seems to be more performant. The space-time finite element method was successfully applied to simulate inertial loads travelling along a string [15]. Further improvements were achieved with special virtual functions used in variational formulation and in the solution [17]. We can assume a fine mesh near the wave front. In regions where the solution is smooth, the mesh remains coarse. Accurate solutions can be obtained without resorting to a uniform fine mesh, which is computationally expensive. A stationary spatial partition is a serious disadvantage in classical semi-discrete methods. The local mesh refinement depending on the processes evolution is disabled.

### 3.1.1. Mathematical Model

Despite the fact that the equation of motion of the Bernoulli-Euler beam is not a wave equation its mathematical simplicity and physical interpretation involved extensive researches and numerous papers dealing with the moving load. This part aims to present a way of deriving the differential equations of the Euler beam, consisting of the balance of forces and moments in the infinitesimal section of the structure. However, the main goal is to provide a method of modelling the moving load using the Dirac delta function. The inertial force acting on the relevant section of the beam is written by the formula

$$dB(x, t) = -\rho A \frac{\partial^2 w(x, t)}{\partial t^2} dx. \quad (3.5)$$

On the basis of the strength of materials, in the case of small deflections, and maintaining a sign convention we get

$$M(x, t) = -EI \frac{\partial^2 w(x, t)}{\partial x^2}. \quad (3.6)$$

According to Fig. 3.7, the balance of moments related to the centre of the element  $dx$  is given by

$$\begin{aligned} M(x, t) - M(x, t) - \frac{\partial M(x, t)}{\partial x} dx + Q(x, t) \frac{dx}{2} + \\ + Q(x, t) \frac{dx}{2} + \frac{\partial Q(x, t)}{\partial x} \frac{dx^2}{2} = 0. \end{aligned} \quad (3.7)$$

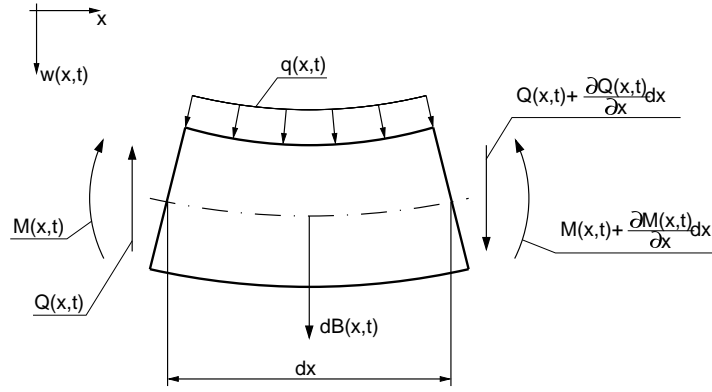


**Figure 3.7.** Balance of forces and moments in the infinitesimal section of the Euler beam.

After rearranging and neglecting small higher order  $dx^2$  we get the known formula defining the shear force

$$Q(x, t) = \frac{\partial M(x, t)}{\partial x} = -\frac{\partial}{\partial x} \left[ EI \frac{\partial^2 w(x, t)}{\partial x^2} \right]. \quad (3.8)$$

The balance of forces on the vertical axis  $w(x, t)$  (Fig. 3.7), results in

$$dB(x, t) + Q(x, t) + \frac{\partial Q(x, t)}{\partial x} dx - Q(x, t) + q(x, t) dx = 0. \quad (3.9)$$

According to (3.5) and (3.8), Eq. (3.9) takes the form

$$-\rho A \frac{\partial^2 w(x, t)}{\partial t^2} dx - \frac{\partial^2}{\partial x^2} \left[ EI \frac{\partial^2 w(x, t)}{\partial x^2} \right] dx + q(x, t) dx = 0. \quad (3.10)$$

The moving load  $q(x, t)$  acting on the section  $dx$  can be presented by the difference of the Heaviside functions (Fig. 3.8)

$$q(x, t)dx = [H(x - vt) - H(x - vt - dx)] \left[ P - m \frac{d^2 w(vt, t)}{dt^2} \right]. \quad (3.11)$$

It takes into account both the moving gravitational force and the moving

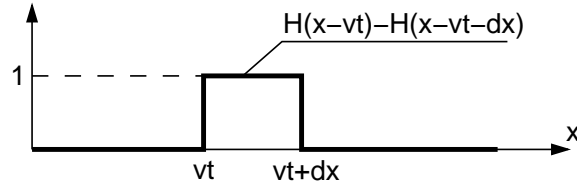


**Figure 3.8.** The difference of the Heaviside functions.

inertial load. According to (3.11) and (3.5), when the both sides are divided by  $dx$ , Eq. (3.10) takes the following form

$$\begin{aligned} EI \frac{\partial^4 w(x, t)}{\partial x^4} + \rho A \frac{\partial^2 w(x, t)}{\partial t^2} &= \\ &= \frac{H(x - vt) - H(x - vt - dx)}{dx} \left[ P - m \frac{d^2 w(vt, t)}{dt^2} \right]. \end{aligned} \quad (3.12)$$

We consider the infinitely small section of the beam ( $dx \rightarrow 0$ ) and the limit can be given by the Dirac delta

$$\lim_{dx \rightarrow 0} \frac{H(x - vt) - H(x - vt - dx)}{dx} = \delta(x - vt). \quad (3.13)$$

Finally, the Euler beam equation subjected to the moving load can be written as follows

$$EI \frac{\partial^4 w(x, t)}{\partial x^4} + \rho A \frac{\partial^2 w(x, t)}{\partial t^2} = \delta(x - vt) \left[ P - m \frac{d^2 w(vt, t)}{dt^2} \right]. \quad (3.14)$$

The acceleration of the moving mass, contains the full description of the inertial travelling load. Now, we can proceed to formulate the main dynamical problem.

Let us consider the simply supported Bernoulli-Euler beam of the length  $L$  under a concentrated mass  $m$  accompanied by a point force  $P$  travelling at

a variable velocity  $v(t)$ . Vertical displacement of the beam is denoted by  $w$ . The boundary conditions are as follows

$$w(0, t) = w''(0, t) = w(L, t) = w''(L, t) = 0. \quad (3.15)$$

The moving load is accelerated to a fix velocity, than travels through a part of the beam and finally brakes before the end support. The examined problem was shown in Fig. 3.9. Coordinates  $x_1$  and  $x_2$  describe the positions of the

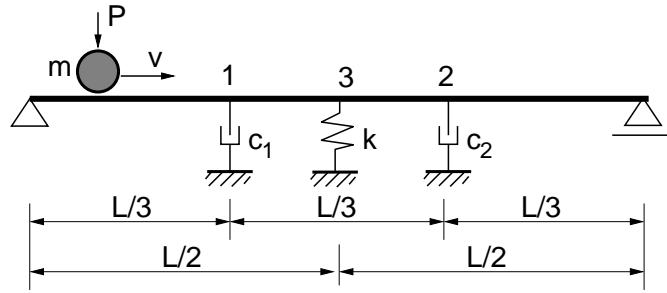


Figure 3.9. Scheme of the problem.

viscous supports. At  $x = x_3$  we place the spring that decreases the static deflection of the flexible beam. Now the differential equation of motion can be written in the following form

$$\begin{aligned} EI \frac{\partial^4 w(x, t)}{\partial x^4} + \rho A \frac{\partial^2 w(x, t)}{\partial t^2} + \sum_{i=1}^2 \delta(x - x_i) c_i \frac{\partial w(x, t)}{\partial t} + \delta(x - x_3) k w(x, t) = \\ = \delta(x - f(t)) P - \delta(x - f(t)) m \frac{d^2 w(f(t), t)}{dt^2}. \end{aligned} \quad (3.16)$$

We assume zero displacements and velocities as initial conditions

$$w(x, 0) = 0, \quad \dot{w}(x, 0) = 0. \quad (3.17)$$

At both ends the displacements are equal zero. In Eq. (3.16)  $E$ ,  $I$ ,  $\rho A$ ,  $k$ ,  $c_1$ ,  $c_2$  are the Young modulus, inertia moment of the cross section, linear mass density, stiffness and damping coefficients of supports, respectively. The viscous term enables the control of the dynamics. The acceleration of the moving mass describes the Renaudot formula [77]

$$\frac{d^2 w(f(t), t)}{dt^2} = \left[ \frac{\partial^2 w(x, t)}{\partial t^2} + 2v \frac{\partial^2 w(x, t)}{\partial x \partial t} + v^2 \frac{\partial^2 w(x, t)}{\partial x^2} + \dot{v} \frac{\partial w(x, t)}{\partial x} \right]_{x=f(t)}, \quad (3.18)$$

where

$$f(t) = x_0 + v_0 t + \frac{1}{2} \dot{v} t^2 \quad (3.19)$$

is the position of the load.  $x_0$  and  $v_0$  are the initial position and initial velocity, respectively. In fact, it is the derivative computed with the chain rule. The respective parts of the equation (3.18) describe the lateral acceleration, the Coriolis acceleration, the centrifugal acceleration, and the acceleration associated with the change of the particle velocity. The equation of motion (3.16) is the partial differential equation with variable coefficients. Additionally, due to the Dirac delta Eq. (3.16) can be considered only in the distribution sense. The analytical solution of this problem is unknown.

### 3.1.2. Semi-analytical Solution

The sine Fourier transformation (3.1) naturally fulfils boundary conditions and leads to the coupled system of the ordinary differential equations of the 2nd order with respect to time. The solution of this system requires numerical integration. For this purpose, the system of ordinary differential equations can be written in the matrix form

$$\mathbf{M} \begin{bmatrix} \ddot{V}_1(t) \\ \ddot{V}_2(t) \\ \vdots \\ \ddot{V}_n(t) \end{bmatrix} + \mathbf{C} \begin{bmatrix} \dot{V}_1(t) \\ \dot{V}_2(t) \\ \vdots \\ \dot{V}_n(t) \end{bmatrix} + \mathbf{K} \begin{bmatrix} V_1(t) \\ V_2(t) \\ \vdots \\ V_n(t) \end{bmatrix} = \mathbf{P}, \quad (3.20)$$

or in the short form

$$\mathbf{M}\ddot{\mathbf{V}} + \mathbf{C}\dot{\mathbf{V}} + \mathbf{K}\mathbf{V} = \mathbf{P}, \quad (3.21)$$

where

$$\mathbf{M} = \begin{bmatrix} 1 & 0 & \cdots & 0 \\ 0 & 1 & \cdots & 0 \\ \vdots & \vdots & \ddots & \vdots \\ 0 & 0 & \cdots & 1 \end{bmatrix} + \frac{2m}{\rho AL} \begin{bmatrix} \sin \frac{1\pi f(t)}{L} \sin \frac{1\pi f(t)}{L} & \sin \frac{1\pi f(t)}{L} \sin \frac{2\pi f(t)}{L} & \cdots & \sin \frac{1\pi f(t)}{L} \sin \frac{n\pi f(t)}{L} \\ \sin \frac{2\pi f(t)}{L} \sin \frac{1\pi f(t)}{L} & \sin \frac{2\pi f(t)}{L} \sin \frac{2\pi f(t)}{L} & \cdots & \sin \frac{2\pi f(t)}{L} \sin \frac{n\pi f(t)}{L} \\ \vdots & \vdots & \ddots & \vdots \\ \sin \frac{n\pi f(t)}{L} \sin \frac{1\pi f(t)}{L} & \sin \frac{n\pi f(t)}{L} \sin \frac{2\pi f(t)}{L} & \cdots & \sin \frac{n\pi f(t)}{L} \sin \frac{n\pi f(t)}{L} \end{bmatrix}, \quad (3.22)$$

$$\begin{aligned}
\mathbf{C} = & \frac{2c_1}{\rho AL} \begin{bmatrix} \sin \frac{1\pi x_1}{L} \sin \frac{1\pi x_1}{L} & \sin \frac{1\pi x_1}{L} \sin \frac{2\pi x_1}{L} & \cdots & \sin \frac{1\pi x_1}{L} \sin \frac{n\pi x_1}{L} \\ \sin \frac{2\pi x_1}{L} \sin \frac{1\pi x_1}{L} & \sin \frac{2\pi x_1}{L} \sin \frac{2\pi x_1}{L} & \cdots & \sin \frac{2\pi x_1}{L} \sin \frac{n\pi x_1}{L} \\ \vdots & \vdots & \ddots & \vdots \\ \sin \frac{n\pi x_1}{L} \sin \frac{1\pi x_1}{L} & \sin \frac{n\pi x_1}{L} \sin \frac{2\pi x_1}{L} & \cdots & \sin \frac{n\pi x_1}{L} \sin \frac{n\pi x_1}{L} \end{bmatrix} + \\
& + \frac{2c_2}{\rho AL} \begin{bmatrix} \sin \frac{1\pi x_2}{L} \sin \frac{1\pi x_2}{L} & \sin \frac{1\pi x_2}{L} \sin \frac{2\pi x_2}{L} & \cdots & \sin \frac{1\pi x_2}{L} \sin \frac{n\pi x_2}{L} \\ \sin \frac{2\pi x_2}{L} \sin \frac{1\pi x_2}{L} & \sin \frac{2\pi x_2}{L} \sin \frac{2\pi x_2}{L} & \cdots & \sin \frac{2\pi x_2}{L} \sin \frac{n\pi x_2}{L} \\ \vdots & \vdots & \ddots & \vdots \\ \sin \frac{n\pi x_2}{L} \sin \frac{1\pi x_2}{L} & \sin \frac{n\pi x_2}{L} \sin \frac{2\pi x_2}{L} & \cdots & \sin \frac{n\pi x_2}{L} \sin \frac{n\pi x_2}{L} \end{bmatrix} + \\
& + \frac{4m}{\rho AL} \begin{bmatrix} \frac{1\pi v}{L} \sin \frac{1\pi f(t)}{L} \cos \frac{1\pi f(t)}{L} & \frac{2\pi v}{L} \sin \frac{1\pi f(t)}{L} \cos \frac{2\pi f(t)}{L} & \cdots \\ \frac{1\pi v}{L} \sin \frac{2\pi f(t)}{L} \cos \frac{1\pi f(t)}{L} & \frac{2\pi v}{L} \sin \frac{2\pi f(t)}{L} \cos \frac{2\pi f(t)}{L} & \cdots \\ \vdots & \vdots & \ddots \\ \frac{1\pi v}{L} \sin \frac{n\pi f(t)}{L} \cos \frac{1\pi f(t)}{L} & \frac{2\pi v}{L} \sin \frac{n\pi f(t)}{L} \cos \frac{2\pi f(t)}{L} & \cdots \\ \cdots & \frac{n\pi v}{L} \sin \frac{1\pi f(t)}{L} \cos \frac{n\pi f(t)}{L} \\ \cdots & \frac{n\pi v}{L} \sin \frac{2\pi f(t)}{L} \cos \frac{n\pi f(t)}{L} \\ \vdots & \vdots \\ \cdots & \frac{n\pi v}{L} \sin \frac{n\pi f(t)}{L} \cos \frac{n\pi f(t)}{L} \end{bmatrix}, \quad (3.23)
\end{aligned}$$

$$\begin{aligned}
\mathbf{K} = & \frac{EI}{\rho A} \begin{bmatrix} \frac{1^4 \pi^4}{L^4} & 0 & \cdots & 0 \\ 0 & \frac{2^4 \pi^4}{L^4} & \cdots & 0 \\ \vdots & \vdots & \ddots & \vdots \\ 0 & 0 & \cdots & \frac{n^4 \pi^4}{L^4} \end{bmatrix} + \\
& + \frac{2k}{\rho AL} \begin{bmatrix} \sin \frac{1\pi x_3}{L} \sin \frac{1\pi x_3}{L} & \sin \frac{1\pi x_3}{L} \sin \frac{2\pi x_3}{L} & \cdots & \sin \frac{1\pi x_3}{L} \sin \frac{n\pi x_3}{L} \\ \sin \frac{2\pi x_3}{L} \sin \frac{1\pi x_3}{L} & \sin \frac{2\pi x_3}{L} \sin \frac{2\pi x_3}{L} & \cdots & \sin \frac{2\pi x_3}{L} \sin \frac{n\pi x_3}{L} \\ \vdots & \vdots & \ddots & \vdots \\ \sin \frac{n\pi x_3}{L} \sin \frac{1\pi x_3}{L} & \sin \frac{n\pi x_3}{L} \sin \frac{2\pi x_3}{L} & \cdots & \sin \frac{n\pi x_3}{L} \sin \frac{n\pi x_3}{L} \end{bmatrix} - \\
& - \frac{2m}{\rho AL} \begin{bmatrix} \frac{1^2 \pi^2 v^2}{L^2} \sin \frac{1\pi f(t)}{L} \sin \frac{1\pi f(t)}{L} & \frac{2^2 \pi^2 v^2}{L^2} \sin \frac{1\pi f(t)}{L} \sin \frac{2\pi f(t)}{L} & \cdots \\ \frac{1^2 \pi^2 v^2}{L^2} \sin \frac{2\pi f(t)}{L} \sin \frac{1\pi f(t)}{L} & \frac{2^2 \pi^2 v^2}{L^2} \sin \frac{2\pi f(t)}{L} \sin \frac{2\pi f(t)}{L} & \cdots \\ \vdots & \vdots & \ddots \\ \frac{1^2 \pi^2 v^2}{L^2} \sin \frac{n\pi f(t)}{L} \sin \frac{1\pi f(t)}{L} & \frac{2^2 \pi^2 v^2}{L^2} \sin \frac{n\pi f(t)}{L} \sin \frac{2\pi f(t)}{L} & \cdots \\ \cdots & \frac{n^2 \pi^2 v^2}{L^2} \sin \frac{1\pi f(t)}{L} \sin \frac{n\pi f(t)}{L} \\ \cdots & \frac{n^2 \pi^2 v^2}{L^2} \sin \frac{2\pi f(t)}{L} \sin \frac{n\pi f(t)}{L} \\ \vdots & \vdots \\ \cdots & \frac{n^2 \pi^2 v^2}{L^2} \sin \frac{n\pi f(t)}{L} \sin \frac{n\pi f(t)}{L} \end{bmatrix} + \\
& + \frac{2m}{\rho AL} \begin{bmatrix} \frac{1\pi \dot{v}}{L} \sin \frac{1\pi f(t)}{L} \cos \frac{1\pi f(t)}{L} & \frac{2\pi \dot{v}}{L} \sin \frac{1\pi f(t)}{L} \cos \frac{2\pi f(t)}{L} & \cdots \\ \frac{1\pi \dot{v}}{L} \sin \frac{2\pi f(t)}{L} \cos \frac{1\pi f(t)}{L} & \frac{2\pi \dot{v}}{L} \sin \frac{2\pi f(t)}{L} \cos \frac{2\pi f(t)}{L} & \cdots \\ \vdots & \vdots & \ddots \\ \frac{1\pi \dot{v}}{L} \sin \frac{n\pi f(t)}{L} \cos \frac{1\pi f(t)}{L} & \frac{2\pi \dot{v}}{L} \sin \frac{n\pi f(t)}{L} \cos \frac{2\pi f(t)}{L} & \cdots \\ \cdots & \frac{n\pi \dot{v}}{L} \sin \frac{1\pi f(t)}{L} \cos \frac{n\pi f(t)}{L} \\ \cdots & \frac{n\pi \dot{v}}{L} \sin \frac{2\pi f(t)}{L} \cos \frac{n\pi f(t)}{L} \\ \vdots & \vdots \\ \cdots & \frac{n\pi \dot{v}}{L} \sin \frac{n\pi f(t)}{L} \cos \frac{n\pi f(t)}{L} \end{bmatrix}, \quad (3.24)
\end{aligned}$$

$$\mathbf{P} = \frac{P}{\rho A} \begin{bmatrix} \sin \frac{1\pi f(t)}{L} \\ \sin \frac{2\pi f(t)}{L} \\ \vdots \\ \sin \frac{n\pi f(t)}{L} \end{bmatrix}. \quad (3.25)$$

The system of Eqs. (3.21) was numerically integrated using the classical Newmark method [20]. Finally, according to (3.2) the solution of the problem is the sum of the elements of the vector  $V_j(t)$  multiplied by the respective sine shape functions. In order to illustrate the results, the following simple dimensionless data were used: the length of the beam  $L = 1$ , mass density  $\rho = 1$ , cross-sectional area  $A = 1$ , cross-sectional inertia moment  $I = 0.01$ , Young's modulus  $E = 1$ , spring stiffness  $k = 10$ , the first damper coefficient  $c_1 = 20$ , the second damper coefficient  $c_2 = 20$ , the moving mass  $m = 1$ , the moving force  $P = -1$ . The assumed data set fulfils the theory of thin beams. Location of the springs and the dampers  $x_1$ ,  $x_2$  and  $x_3$  were assumed as shown in Fig. 3.9. Figure 3.10 presents simulation of the motion of the

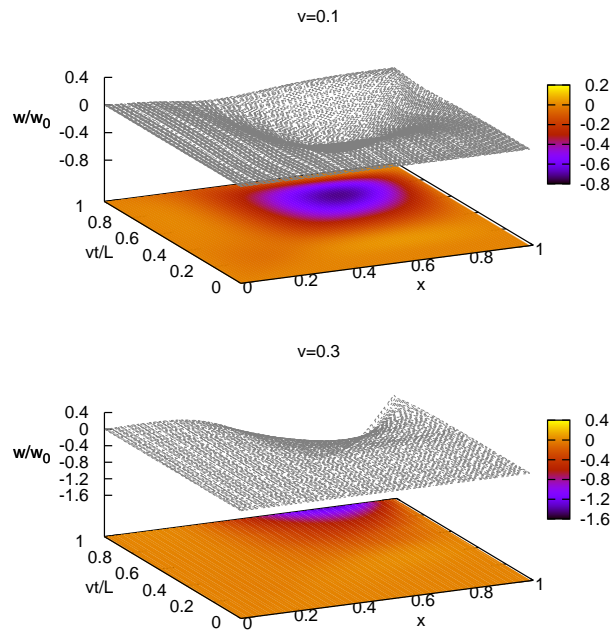


**Figure 3.10.** Simulation of the beam span motion under the moving mass at speed  $v=0.1$  and sub-critical speed  $v=0.3$ .

beam span subjected to the moving mass at  $v = 0.1$  and  $v = 0.3$  ( $v = \text{const}$ ). For this set of data the critical velocity for the simply supported Euler beam is equal to  $v_{cr} = (\pi/L)\sqrt{EI/(\rho A)} = 0.314$ .  $n = 100$  terms in the resulting series (3.2), were taken. The static deflection of the midpoint of the Euler beam  $w_0 = PL^3/(48EI)$ . According to the increasing velocity of the travelling mass, we can observe increased deflection and shifting the position of the maximum displacements of the beam in time. In addition, near the final support we notice the increase vertical acceleration of the mass.

### 3.1.3. Numerical Description of the Problem

The space-time finite element differs from the conventional finite element approach to solving initial-boundary problems. The main difference lies within the discretization of the differential equations of motion. The presented continuous Galerkin method discretizes both the spatial variables and the time variable. Therefore, we can postulate a balance of some physical quantities, such as energy in the interval of time, not just at some particular instants. In the formulation of the method, we integrate physical quantities analytically in the time interval rather than numerically, as it is in the classical finite element method. The considered problem is reduced to the numerical solution of the system of algebraic Eqs. (3.3). This approach assumes a continuous distribution of the characteristic function, i.e., the velocity in the whole space-time area in which the structure is considered. The space-time element method is a generalisation of the classical finite element method.

The discrete model of the beam with stationary placed supports and dampers is simple and can be presented in a nutshell. The influence of a moving mass particle is more complex. It can not be done with the ad-hoc mass lumping at neighbouring nodes. In the case of a non inertial load, only the right-hand side vector of the equation of motion is modified. Respective elements of the load vector have contributed terms computed proportionally to the distance from neighbouring nodes. The ad-hoc addition of the mass to respective coefficients of the inertia matrix at each time step results in solutions neither convergent nor stable. The moving mass significantly changes the numerical procedure. Presented in this section general description of the moving mass in the velocity variant of the space-time finite elements method was taken from [31].

In the case of the Euler beam, the nodal displacements are closely associated with the rotation angles. Hence, the velocity approximation in the space-time finite element is given by the following formula

$$v(x, t) = N_1 v_1 + N_2 \dot{\theta}_1 + N_3 v_2 + N_4 \dot{\theta}_2 + N_5 v_3 + N_6 \dot{\theta}_3 + N_7 v_4 + N_8 \dot{\theta}_4. \quad (3.26)$$

According to (3.26) we use a linear interpolation in time and 3rd order polynomials in space

$$\begin{aligned} N_1 &= \left(1 - 3\frac{x^2}{b^2} + 2\frac{x^3}{b^3}\right) \left(1 - \frac{t}{h}\right), & N_5 &= \left(1 - 3\frac{x^2}{b^2} + 2\frac{x^3}{b^3}\right) \frac{t}{h}, \\ N_2 &= \left(x - 2\frac{x^2}{b} + \frac{x^3}{b^2}\right) \left(1 - \frac{t}{h}\right), & N_6 &= \left(x - 2\frac{x^2}{b} + \frac{x^3}{b^2}\right) \frac{t}{h}, \\ N_3 &= \left(3\frac{x^2}{b^2} - 2\frac{x^3}{b^3}\right) \left(1 - \frac{t}{h}\right), & N_7 &= \left(3\frac{x^2}{b^2} - 2\frac{x^3}{b^3}\right) \frac{t}{h}, \\ N_4 &= \left(-\frac{x^2}{b} + \frac{x^3}{b^2}\right) \left(1 - \frac{t}{h}\right), & N_8 &= \left(-\frac{x^2}{b} + \frac{x^3}{b^2}\right) \frac{t}{h}. \end{aligned} \quad (3.27)$$

In order to determine the virtual energy we assume the virtual hat-shaped function given by

$$\begin{aligned} v^*(x) &= \left[ \left(1 - 3\frac{x^2}{b^2} + 2\frac{x^3}{b^3}\right) v_3 + \left(x - 2\frac{x^2}{b} + \frac{x^3}{b^2}\right) \dot{\theta}_3 + \right. \\ &\quad \left. + \left(3\frac{x^2}{b^2} - 2\frac{x^3}{b^3}\right) v_4 + \left(-\frac{x^2}{b} + \frac{x^3}{b^2}\right) \dot{\theta}_4 \right]. \end{aligned} \quad (3.28)$$

According to the classical energy minimisation on the basis of (3.26), (3.27) and (3.28) we obtain the inertia matrix  $\mathbf{M}$ , stiffness matrix  $\mathbf{K}$ , vector of nodal forces  $\mathbf{e}$  and the moving gravity load  $\mathbf{P}$

$$\mathbf{M} = \frac{\rho A}{h} \begin{bmatrix} -\frac{13b}{35} & -\frac{11b^2}{210} & -\frac{9b}{70} & \frac{13b^2}{420} & \frac{13b}{35} & \frac{11b^2}{210} & \frac{9b}{70} & -\frac{13b^2}{420} \\ -\frac{11b^2}{210} & -\frac{b^3}{105} & -\frac{13b^2}{420} & \frac{b^3}{140} & \frac{11b^2}{210} & \frac{b^3}{105} & \frac{13b^2}{420} & -\frac{b^3}{140} \\ -\frac{9b}{70} & -\frac{13b^2}{420} & -\frac{13b}{35} & \frac{11b^2}{210} & \frac{9b}{70} & \frac{13b^2}{420} & \frac{13b}{35} & -\frac{11b^2}{210} \\ \frac{13b^2}{420} & \frac{b^3}{140} & \frac{11b^2}{210} & -\frac{b^3}{105} & -\frac{13b^2}{420} & -\frac{b^3}{140} & -\frac{11b^2}{210} & \frac{b^3}{105} \end{bmatrix}, \quad (3.29)$$

$$\mathbf{K} = EIh \begin{bmatrix} \frac{4}{b^3} & \frac{2}{b^2} & -\frac{4}{b^3} & \frac{2}{b^2} & \frac{2}{b^3} & \frac{1}{b^2} & -\frac{2}{b^3} & \frac{1}{b^2} \\ \frac{2}{b^2} & \frac{4}{3b} & -\frac{2}{b^2} & \frac{2}{3b} & \frac{1}{b^2} & \frac{2}{3b} & -\frac{1}{b^2} & \frac{1}{3b} \\ -\frac{4}{b^3} & -\frac{2}{b^2} & \frac{4}{b^3} & -\frac{2}{b^2} & -\frac{2}{b^3} & -\frac{1}{b^2} & \frac{2}{b^3} & -\frac{1}{b^2} \\ \frac{2}{b^2} & \frac{2}{3b} & -\frac{2}{b^2} & \frac{4}{3b} & \frac{1}{b^2} & \frac{1}{3b} & -\frac{1}{b^2} & \frac{2}{3b} \end{bmatrix}, \quad (3.30)$$

$$\mathbf{e} = EI \begin{bmatrix} \frac{12}{b^3} & \frac{6}{b^2} & -\frac{12}{b^3} & \frac{6}{b^2} \\ \frac{6}{b^2} & \frac{4}{b} & -\frac{6}{b^2} & \frac{2}{b} \\ -\frac{12}{b^3} & -\frac{6}{b^2} & \frac{12}{b^3} & -\frac{6}{b^2} \\ \frac{6}{b^2} & \frac{2}{b} & -\frac{6}{b^2} & \frac{4}{b} \end{bmatrix} \mathbf{w}_0, \quad (3.31)$$

$$\mathbf{P} = \frac{mg}{4b} \begin{bmatrix} [4b^2(2\kappa^3 - 3\kappa^2 + 1) + v^2h^2(2\kappa - 1)] / b \\ [12b^2\kappa(\kappa^2 - 2\kappa + 1) + v^2h^2(3\kappa - 2)] / 3 \\ - [4b^2\kappa^2(2\kappa - 3) + v^2h^2(2\kappa - 1)] / b \\ [12b^2\kappa^2(\kappa - 1) + v^2h^2(3\kappa - 1)] / 3 \end{bmatrix}, \quad (3.32)$$

where the parameter  $\kappa$  describes the position of the moving load. The stationary supports and dampers are added to the corresponding terms of the diagonal of the global matrices  $\mathbf{C}_g$  and  $\mathbf{K}_g$ .

Although in our problem we have the stationary mesh, the mass trajectory draws non-stationary line, and in the case of the accelerated motion, a curved line in time space. The space-time finite element method seemed to be efficient, while we fail with the semi-discrete methods. The space-time interpolation of displacements and velocities of the mass position on the trajectory, between two successive time points and also in spatial points, allowed us to write and minimise the virtual energy contributed by the inertial particle in terms of nodal parameters of the spatial mesh and time coordinates. We write derivatives with respect to spacial and time variables having clear interpretation of all the resulting terms. The fundamental question was in what time, initial, final, or intermediate in time interval the required terms should be computed.

The computational scheme of the solution of the moving inertial point problem requires modification of the global matrices describing our step-by-step scheme. We must change not only the inertia matrix, but also matrices that express damping-like and stiffness-like effects, as a result of the derivation of the particle trajectory in time and the vector of the right hand side of the system of equations.

We assume a linear shape function of the velocity  $v$  in  $x$  and  $t$

$$v(x, t) = \sum_{i=1}^4 N_i(x, t) v_i. \quad (3.33)$$

In the domain  $\Omega = \{(x, t): 0 \leq x \leq b, 0 \leq t \leq h\}$  (Fig. 3.11), the matrix shape function  $\mathbf{N}$  has the following form

$$\mathbf{N} = \left[ \frac{1}{bh}(x-b)(t-h), -\frac{1}{bh}x(t-h), -\frac{1}{bh}(x-b)t, \frac{1}{bh}xt \right]. \quad (3.34)$$

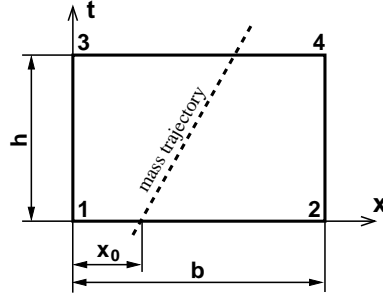


**Figure 3.11.** Mass trajectory in space-time finite element.

The displacements are computed from the velocity equation by integrating the velocity

$$w(x, t) = w(x, 0) + \int_0^t (N_1 v_1 + \dots + N_4 v_4) dt = w(x, 0) + \int_0^t \mathbf{N} \mathbf{v} dt. \quad (3.35)$$

Finally, we have

$$w(x, t) = w(x, 0) + \frac{xt^2}{2bh}(v_1 - v_2 - v_3 + v_4) + \frac{xt}{b}(-v_1 + v_2) + \frac{t^2}{2h}(-v_1 + v_3) + v_1 t. \quad (3.36)$$

The derivative  $\partial w / \partial x$  can also be computed

$$\frac{\partial w}{\partial x} = \frac{t^2}{2bh}(v_1 - v_2 - v_3 + v_4) + \frac{t}{b}(-v_1 + v_2) + \left. \frac{dw}{dx} \right|_{t=0}. \quad (3.37)$$

The last term of (3.37) denotes the initial strain  $\varepsilon_0$ . The proper choice of the virtual functions  $v^*$  is a fundamental issue in the space-time approach. Different functions result in solution schemes with different accuracy and stability. In most cases we propose a simple form with distribution  $\delta$  in  $t = \alpha h$  (Fig. 3.12)

$$v^*(x, t) = \delta(t - \alpha h) \left[ \left(1 - \frac{x}{b}\right) v_3 + \frac{x}{b} v_4 \right]. \quad (3.38)$$

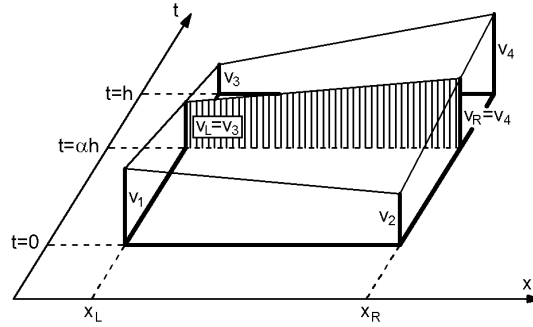


**Figure 3.12.** Virtual delta function.

Other virtual shape functions in forms of a hat shape, triangle shape, and roof shape are presented in [17].

The vertical point acceleration of the moving inertial particle is computed from the displacement of the contact point determined on the supporting structure  $w(f(t), t)$ .  $f(t)$  is the position of the mass in time. We must apply twice the chain rule of derivation in terms of time (see Eq. (3.18)). Unfortunately, we can not adapt this formula to our discrete approach since our interpolation functions must be differentiated twice. The increment of time,  $dt$ , is in consequence the increment of the spatial coordinates  $x$  as well as the time coordinates  $t$ , since space is associated with time by the mass trajectory.

The virtual energy in the space-time domain  $\Omega$ , describing a moving material point, can be written in the following form

$$\Pi_m = \int_0^h \int_0^b v^*(x, t) \cdot \delta(x - f(t)) m \frac{d^2 w(f(t), t)}{dt^2} dx dt . \quad (3.39)$$

In the domain  $\Omega$ , we assume a linear distribution of the nodal velocity in space  $x$  and time  $t$  (see (3.33) and (3.34)). In this case, it is impossible to determine all parts of (3.18). Moreover, it is impossible to reduce the order of the derivative as a result of integration by parts, due to the distribution in (3.39). The Renaudot formula (3.18) can be written in the equivalent form

$$\begin{aligned} \frac{d^2 w(f(t), t)}{dt^2} &= \frac{\partial v(x, t)}{\partial t} \Big|_{x=f(t)} + v \frac{\partial v(x, t)}{\partial x} \Big|_{x=f(t)} + v \frac{d}{dt} \left[ \frac{\partial w(x, t)}{\partial x} \Big|_{x=f(t)} \right] + \\ &+ \dot{v} \frac{\partial w(x, t)}{\partial x} \Big|_{x=f(t)} . \end{aligned} \quad (3.40)$$

According to (3.33) and (3.34) we obtain

$$\frac{\partial v(x, t)}{\partial t} = -\frac{1}{h} \left(1 - \frac{x}{b}\right) v_1 - \frac{1}{h} \frac{x}{b} v_2 + \frac{1}{h} \left(1 - \frac{x}{b}\right) v_3 + \frac{1}{h} \frac{x}{b} v_4, \quad (3.41)$$

$$\frac{\partial v(x, t)}{\partial x} = -\frac{1}{b} \left(1 - \frac{t}{h}\right) v_1 + \frac{1}{b} \left(1 - \frac{t}{h}\right) v_2 - \frac{1}{b} \frac{t}{h} v_3 + \frac{1}{b} \frac{t}{h} v_4. \quad (3.42)$$

In the case of the third term of (3.40), we assume the backward difference formula. We have then

$$\frac{d}{dt} \left[ \frac{\partial w(x, t)}{\partial x} \Big|_{x=f(t)} \right] = \frac{1}{h} \left[ \frac{\partial w(x, t)}{\partial x} \Big|_{x=f(t)} \right]^{t+h} - \frac{1}{h} \left[ \frac{\partial w(x, t)}{\partial x} \Big|_{x=f(t)} \right]^t. \quad (3.43)$$

The upper indices indicate time at which the respective terms are defined. Direct differentiation of Eq. (3.36) led to the rejection of the nodal forces arising in the mass transition between elements.

At the time of transition of the moving load between the neighbouring elements  $k$  and  $k+1$  (Fig. 3.13), the current displacements are calculated for the element  $k+1$

$$\left[ \frac{\partial w(x, t)}{\partial x} \Big|_{x=f(t)} \right]^{t+h} = \frac{1}{b} (w_4^{k+1} - w_3^{k+1}). \quad (3.44)$$

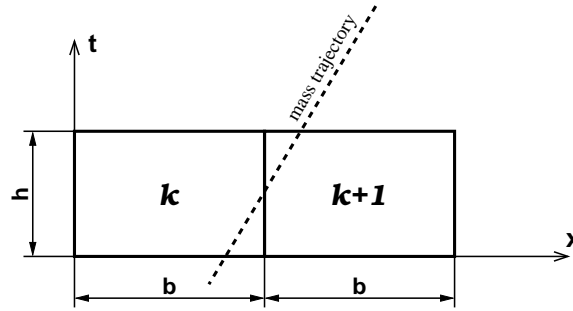


**Figure 3.13.** The transition mass between elements.

The initial displacements are computed in the element  $k$

$$\left[ \frac{\partial w(x, t)}{\partial x} \Big|_{x=f(t)} \right]^t = \frac{1}{b} (w_2^k - w_1^k). \quad (3.45)$$

The lower indices indicate the numbers of nodes (Fig. 3.11). According to (3.4), (3.44), and (3.45) the finite difference scheme (3.43) is written as follows

$$\begin{aligned} \frac{d}{dt} \left[ \frac{\partial w(x, t)}{\partial x} \Big|_{x=f(t)} \right] &= \frac{1}{bh} \left( w_2^{k+1} - w_2^k - w_1^{k+1} + w_1^k \right) + \\ &+ \frac{1}{b} \left[ -\beta v_1^{k+1} + \beta v_2^{k+1} - (1 - \beta)v_3^{k+1} + (1 - \beta)v_4^{k+1} \right]. \end{aligned} \quad (3.46)$$

The accurate solution is obtained with  $\beta = 1 - \alpha$  [7]. Therefore, we can write

$$\begin{aligned} \frac{d}{dt} \left[ \frac{\partial w(x, t)}{\partial x} \Big|_{x=f(t)} \right] &= \frac{1}{bh} \left( w_2^{k+1} - w_2^k - w_1^{k+1} + w_1^k \right) + \\ &+ \frac{1}{b} \left[ -(1 - \alpha)v_1^{k+1} + (1 - \alpha)v_2^{k+1} - \alpha v_3^{k+1} + \alpha v_4^{k+1} \right]. \end{aligned} \quad (3.47)$$

In order to calculate the virtual energy describing the motion of a moving inertial point (3.39), we assume a virtual delta function (Fig. 3.12) given by (3.38). We can control the properties of the solution procedure with the parameter  $\alpha$ . By minimising the virtual energy  $\Pi_m$  we obtain matrices describing the inertial moving load

$$\mathbf{M}_m = \frac{m}{h} \begin{bmatrix} -(1 - \kappa)^2 & -\kappa(1 - \kappa) & (1 - \kappa)^2 & \kappa(1 - \kappa) \\ -\kappa(1 - \kappa) & -\kappa^2 & \kappa(1 - \kappa) & \kappa^2 \end{bmatrix}, \quad (3.48)$$

$$\mathbf{C}_m = \frac{2m\nu}{b} \begin{bmatrix} (\kappa - 1)(1 - \alpha) & (1 - \kappa)(1 - \alpha) & (\kappa - 1)\alpha & (1 - \kappa)\alpha \\ -\kappa(1 - \alpha) & \kappa(1 - \alpha) & -\kappa\alpha & \kappa\alpha \end{bmatrix}, \quad (3.49)$$

$$\mathbf{K}_m = \frac{m\dot{\nu}h}{b} \begin{bmatrix} (1 - \kappa)\left(\frac{\alpha^2}{2} - \alpha\right) & (\kappa - 1)\left(\frac{\alpha^2}{2} - \alpha\right) & (\kappa - 1)\frac{\alpha^2}{2} & (1 - \kappa)\frac{\alpha^2}{2} \\ \kappa\left(\frac{\alpha^2}{2} - \alpha\right) & -\kappa\left(\frac{\alpha^2}{2} - \alpha\right) & -\kappa\frac{\alpha^2}{2} & \kappa\frac{\alpha^2}{2} \end{bmatrix}, \quad (3.50)$$

and

$$\begin{aligned} \mathbf{e}_m &= \frac{m\nu}{bh} \begin{bmatrix} (1 - \kappa) \left( w_2^{k+1} - w_2^k - w_1^{k+1} + w_1^k \right) \\ \kappa \left( w_2^{k+1} - w_2^k - w_1^{k+1} + w_1^k \right) \end{bmatrix} + \\ &+ \frac{m\dot{\nu}}{b} \begin{bmatrix} (1 - \kappa) \left( w_2^k - w_1^k \right) \\ \kappa \left( w_2^k - w_1^k \right) \end{bmatrix}, \end{aligned} \quad (3.51)$$

with the coefficient  $\kappa$  that describes the instantaneous position of the mass in the element

$$\kappa = \frac{f(\alpha h)}{b}, \quad 0 < \kappa \leq 1. \quad (3.52)$$

According to the current position of the moving load the matrices (3.48) and (3.49) fall into the appropriate cells of the global inertia and damping matrices describing the whole structure. Algorithm 1 presents the computational steps. The vector of nodal forces (3.51) calculated based on displacements from the current and previous step increases the right hand side vector describing the external load, i.e., the gravitational moving load. The matrices (3.48), (3.49), (3.50) and the vector (3.51) are originally developed by the authors. These general characteristic matrices of finite elements carrying an inertial particle can be applied directly to almost all types of structures.

## 3.2. The Shaft under the Harmonic Excitation

Torsional vibrations cause an expedited wear of bearings, material fatigue and an increased risk of failure. They cause noise and excessive energy consumption. The effective reduction of vibrations level below an acceptable limit is the problem of special importance. Smart design of the rotor allows to improve the exploitation conditions and to increase safety of the devices. Dynamics of rotors and shaft is widely examined in literature [26, 37, 67, 72, 76].

In practise, the detection and elimination of vibrations is difficult. The machine should be re-designed or at least the use in the critical range of parameters should be reduced to a minimum. One of a few works devoted to a rotor mechanical model [59] presents two different control schemes: the on-off scheme and the feedback linearization scheme. It is shown that a magneto-rheological damper can provide sufficient damping for ground resonance stabilization. Issues related to the discrete-continuous modelling and the selection of the damping coefficient in rotating systems were presented in [74, 86, 89]. In [36], the semi-active damping control of the torsional vibrations of a shaft was considered. Developed control strategy was verified by using the magneto-rheological brake. The advantage of the semi-active approach is evident when we consider the energy consumed by the dampers. The piezoelectric system to active torsional vibrations control was also considered [70].

---

**Algorithm 1** Space–time element method applied to a Timoshenko beam.

---

1. Define geometric and material data, velocity  $\mathbf{v}$ , length of the element  $b$ , time step  $h$ , etc.
  2. Compute element matrices of repeated structural elements and formulate global coefficient matrix.
  3. Initialise the loop parameter the number of elements carrying the mass  $iel_{rem} = 1$ .
  4. Perform computations of a single time step:
    - Number of the current step  $it = 0$ , current time of the beginning of the time interval  $t = 0$ .
    - Number of the element carrying the load  $iel = \text{INT}(t \cdot \mathbf{v}/b - eps) + 1$ ,  $eps = 0.0001$ .
    - Position of the mass on the element  $x_0 = t \cdot \mathbf{v} - (iel - 1) \cdot b$ , parameter  $\kappa = (x_0 + \mathbf{v}h)/b$ .
    - Compute mass space–time element and load vector.
    - Compute the nodal force vector of the mass element:  
 $\mathbf{e}_m = \frac{m\mathbf{v}}{bh}(w_r^{ielmem} - w_l^{ielmem} - w_r^{ielmem} + w_l^{ielmem})$  (lower index is left of right node of the element, upper index is number of element; notice that  $iel = ielem$  always except in the passage from element to element).
    - Formulate the system of algebraic equations.
    - Solve the system of equations for velocities  $\mathbf{v}$  (see (3.3))
    - Compute displacements at time  $t + h$  (see (3.4)).
    - Compute nodal forces of the beam.
    - Remember the number of the element  $iel_{rem} = iel$ .
    - Shift displacements and velocities:  $\mathbf{w}_i \leftarrow \mathbf{w}_{i+1}$ ,  $\mathbf{v}_i \leftarrow \mathbf{v}_{i+1}$ .
  5. Increment the time step.
-

### 3.2.1. Mathematical Model

The analysis of vibrations for a longer time can only be performed stochastically, i.e., assuming that the amplitudes achieve their extremal values not in accordance with a smooth function of the initial conditions and material parameters. Therefore, the deterministic way of investigation forces us to perform analytical calculation at the first stage. This will facilitate the estimation of the sensitivity of the structure to selected parameters.

The model of the shaft, however, will first be reduced to the shaft of a uniform cross section, without concentrated masses placed on it [36]. Only in such a case can we successfully carry out the mathematical analysis. First we will consider the problem with an excitation applied to the point A and with a single damper placed at the point B (Fig. 3.14).

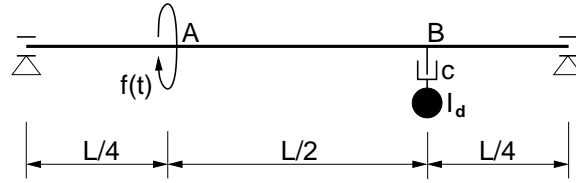


**Figure 3.14.** Scheme of the problem for theoretical analysis.

We consider the hyperbolic differential Eq. (3.53) which describes the motion of the rotating shaft. The second Eq. (3.54) describes the motion of the damper. They are coupled at the point B:

$$-GI \frac{\partial^2 \varphi}{\partial x^2} + \rho I \frac{\partial^2 \varphi}{\partial t^2} + \delta(x - x_B) c \left( \frac{\partial \varphi}{\partial t} - \frac{\partial \vartheta}{\partial t} \right) = \delta(x - x_A) f(t) , \quad (3.53)$$

$$I_d \frac{d^2 \vartheta}{dt^2} + c \left( \frac{d\vartheta}{dt} - \frac{d\varphi}{dt} \right) = 0 . \quad (3.54)$$

We assume the following boundary conditions:

$$\varphi'(0, t) = 0, \quad \varphi'(L, t) = 0 . \quad (3.55)$$

Here,  $\varphi(x, t)$  is the angular displacement in time  $t$  of the point  $x$  of the shaft,  $\vartheta$  is the angular displacement of the rotating disk of the damper with inertia  $I_d$ , and  $c$  is the damping coefficient. Two Dirac delta functions select arguments at the point where the force is applied and at the point of the damper.  $f(t)$  can be an arbitrary external load function. We assume it as a harmonic function  $F \sin(\omega t)$ .

The closed solution of the above equation is complicated. We take two ways to approximate the solution: an analytical solution with a one term expansion of the Fourier series, and a semi-analytical solution with an  $n$ -term expansion. The first solution allows us to examine features of the solution and test its sensitivity to the parameters. The second one allows on a quantitative investigation.

### 3.2.2. Analytical Solution

Now we will solve the system of differential Eqs. (3.53)–(3.55) with the angular displacements  $\varphi$  as the unknown functions. We can apply the cosine Fourier transformation

$$\Phi_j(t) = \int_0^L \varphi(x, t) \cos \frac{j\pi x}{L} dx, \quad (3.56)$$

where

$$\varphi(x, t) = \frac{1}{L} \Phi_0(t) + \frac{2}{L} \sum_{j=1}^n \Phi_j(t) \cos \frac{j\pi x}{L}, \quad (3.57)$$

which fulfils the boundary conditions. The number of terms is limited according to the required accuracy. For the reason of simplicity, we limit the solution to the first term of the series (3.57). The analytical solution allows us to, first, determine the characteristic features of the solution, such as its sensitivity to inertia and the damping of the damper, second, to compare the solution with numerical results and estimate the accuracy of the result. The equations of motion (3.53), (3.54) can be written in the form

$$\rho I \ddot{\Phi}_0(t) + \frac{c}{L} \dot{\Phi}_0(t) - c \dot{\vartheta}(t) = F \sin(\omega t), \quad (3.58)$$

$$I_d \ddot{\vartheta}(t) + c \dot{\vartheta}(t) - \frac{c}{L} \dot{\Phi}_0(t) = 0. \quad (3.59)$$

According to (3.58), the velocity of the oscillating mass is the following

$$\dot{\vartheta}(t) = \frac{\rho I}{c} \ddot{\Phi}_0(t) + \frac{1}{L} \dot{\Phi}_0(t) - \frac{F}{c} \sin(\omega t). \quad (3.60)$$

Its acceleration equals to

$$\ddot{\vartheta}(t) = \frac{\rho I}{c} \dot{\Phi}_0(t) + \frac{1}{L} \ddot{\Phi}_0(t) - \frac{F}{c} \omega \cos(\omega t). \quad (3.61)$$

Now we will focus our attention on the vibration of the rotating shaft. Substituting (3.60) and (3.61) into (3.59), we obtain the third order non-homogeneous ordinary differential equation [36]

$$\dot{\Phi}_0(t) + c \left( \frac{1}{I_d} + \frac{1}{\rho IL} \right) \ddot{\Phi}_0(t) = \frac{F\omega}{\rho I} \cos(\omega t) + \frac{Fc}{\rho II_d} \sin(\omega t) \quad (3.62)$$

with zero initial conditions

$$\Phi_0(0) = 0, \quad \dot{\Phi}_0(0) = 0, \quad \ddot{\Phi}_0(0) = 0. \quad (3.63)$$

Let us consider the Laplace–Carson transformation [29, 92]

$$\widehat{f}(p) = p \int_0^{\infty} f(t) e^{-pt} dt, \quad (3.64)$$

and original

$$f(t) = \frac{1}{2\pi i} \int_{a-i\infty}^{a+i\infty} \frac{\widehat{f}(p)}{p} e^{tp} dp. \quad (3.65)$$

According to (3.64) the differential Eq. (3.62) can be written in algebraic form

$$p^3 \widehat{\Phi}_0(p) + c \left( \frac{1}{I_d} + \frac{1}{\rho IL} \right) p^2 \widehat{\Phi}_0(p) = \frac{F\omega}{\rho I} \frac{p^2}{p^2 + \omega^2} + \frac{Fc}{\rho II_d} \frac{\omega p}{p^2 + \omega^2}. \quad (3.66)$$

Here, the following notation was introduced:

$$\beta = \frac{1}{I_d} + \frac{1}{\rho IL}. \quad (3.67)$$

After some rearrangement of the terms, we obtain

$$\widehat{\Phi}_0(p) = \frac{F\omega}{\rho I} \frac{1}{p^2 + \omega^2} \frac{1}{p + c\beta} + \frac{F\omega c}{\rho II_d} \frac{1}{p^2 + \omega^2} \frac{1}{p(p + c\beta)}. \quad (3.68)$$

In order to return to the time variable, the partial fraction decomposition was used

$$\frac{1}{(p^2 + \omega^2)(p + c\beta)} \equiv \frac{C_1 p + C_2}{p^2 + \omega^2} + \frac{C_3}{p + c\beta}, \quad (3.69)$$

$$\frac{1}{p(p^2 + \omega^2)(p + c\beta)} \equiv \frac{D_1}{p} + \frac{D_2 p + D_3}{p^2 + \omega^2} + \frac{D_4}{p + c\beta}. \quad (3.70)$$

The constants in (3.69) and (3.70) are

$$C_1 = \frac{-1}{c^2\beta^2 + \omega^2}, \quad C_2 = \frac{c\beta}{c^2\beta^2 + \omega^2}, \quad C_3 = \frac{1}{c^2\beta^2 + \omega^2}, \quad (3.71)$$

$$\begin{aligned} D_1 &= \frac{1}{c\beta\omega^2}, & D_2 &= \frac{-c\beta}{\omega^2(c^2\beta^2 + \omega^2)}, \\ D_3 &= \frac{-1}{c^2\beta^2 + \omega^2}, & D_4 &= \frac{-1}{c\beta(c^2\beta^2 + \omega^2)}. \end{aligned} \quad (3.72)$$

Now by using (3.69)–(3.72) and (3.65), the equation (3.68) can be transformed to time domain

$$\begin{aligned} \Phi_0(t) &= \frac{F}{\rho I} \frac{\omega}{c^2\beta^2 + \omega^2} \left[ \frac{c^2\beta^2 + \omega^2}{I_d\beta\omega^2} t - \frac{1}{\omega} \left( 1 + \frac{c^2\beta}{I_d\omega^2} \right) \sin(\omega t) + \right. \\ &\quad \left. + \frac{c}{\omega^2} \left( \beta - \frac{1}{I_d} \right) (1 - \cos(\omega t)) + \frac{1}{c\beta} \left( 1 - \frac{1}{I_d\beta} \right) (1 - e^{-c\beta t}) \right]. \end{aligned} \quad (3.73)$$

Finally, according to (3.57), the displacement including only the constant term can be written

$$\varphi(t) = \frac{1}{L} \Phi_0(t). \quad (3.74)$$

The solution is periodic. The displacements in time at the location of the damper related to the motion of the centre of gravity, are depicted in Fig. 3.15. The following data were assumed:  $\rho I = 1.6 \cdot 10^{-6}$  kgm,  $I_d = 0.25$  kgm<sup>2</sup>,  $L = 1$  m,  $F = 100$  Nm,  $\omega = 1$  s<sup>-1</sup>. Four values of the damping coefficient,  $c = 0.2, 0.5, 0.8,$  and  $1.0$  Nms, result in amplitudes of 1279, 893, 836, and 823 rad, respectively. We notice that the increase of the damping causes a disproportionately slower decrease of the amplitudes of torsion. With increasing damping, the mass of the damper starts to be firmly joined with the shaft and vibrates in the same phase. The energy dissipation then is significantly lower than in the case of out of phase vibrations. We will try to choose the optimal  $c$  and, what is more important, in which time interval of the single period of vibrations we should activate the dampers.

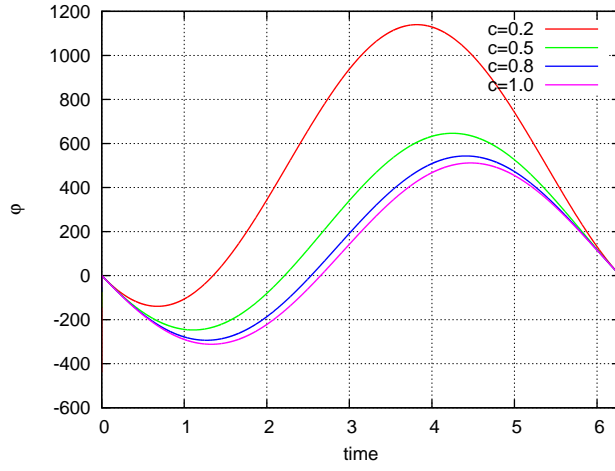


**Figure 3.15.** Displacements in time in the case of various damping constants,  $c=0.2, 0.5, 0.8,$  and  $1.0$  Nms.

### 3.2.3. Semi-analytical Solution and Numerical Model

The full expansion of (3.53) and (3.54) into infinite series is then limited to  $n$  terms and finally results in the matrix differential equation

$$\begin{aligned}
 & \begin{bmatrix} \rho I & 0 & 0 & \dots & 0 \\ 0 & \rho I & 0 & \dots & 0 \\ \vdots & \vdots & \vdots & \ddots & \vdots \\ 0 & 0 & \dots & \rho I & 0 \\ 0 & 0 & \dots & 0 & I_d \end{bmatrix} \begin{Bmatrix} \ddot{\Phi}_0 \\ \ddot{\Phi}_1 \\ \vdots \\ \ddot{\Phi}_n \\ \ddot{\vartheta} \end{Bmatrix} + \\
 & +c \begin{bmatrix} \frac{1}{L} \cos 3\pi\frac{0}{4} & \frac{2}{L} \cos 3\pi\frac{0}{4} \cos 3\pi\frac{1}{4} & \dots & \frac{2}{L} \cos 3\pi\frac{0}{4} \cos 3\pi\frac{n}{4} & -\cos 3\pi\frac{0}{4} \\ \frac{1}{L} \cos 3\pi\frac{1}{4} & \frac{2}{L} \cos 3\pi\frac{1}{4} \cos 3\pi\frac{1}{4} & \dots & \frac{2}{L} \cos 3\pi\frac{1}{4} \cos 3\pi\frac{n}{4} & -\cos 3\pi\frac{1}{4} \\ \vdots & \vdots & \ddots & \vdots & \vdots \\ \frac{1}{L} \cos 3\pi\frac{n}{4} & \frac{2}{L} \cos 3\pi\frac{n}{4} \cos 3\pi\frac{1}{4} & \dots & \frac{2}{L} \cos 3\pi\frac{n}{4} \cos 3\pi\frac{n}{4} & -\cos 3\pi\frac{n}{4} \\ -\frac{1}{L} & -\frac{2}{L} \cos 3\pi\frac{1}{4} & \dots & -\frac{2}{L} \cos 3\pi\frac{n}{4} & 1 \end{bmatrix} \begin{Bmatrix} \dot{\Phi}_0 \\ \dot{\Phi}_1 \\ \vdots \\ \dot{\Phi}_n \\ \dot{\vartheta} \end{Bmatrix} + \\
 & +GI \frac{\pi^2}{L^2} \begin{bmatrix} 0^2 & 0 & 0 & \dots & 0 \\ 0 & 1^2 & 0 & \dots & 0 \\ \vdots & \vdots & \vdots & \ddots & \vdots \\ 0 & 0 & \dots & n^2 & 0 \\ 0 & 0 & \dots & 0 & 0 \end{bmatrix} \begin{Bmatrix} \Phi_0 \\ \Phi_1 \\ \vdots \\ \Phi_n \\ \vartheta \end{Bmatrix} = F \sin(\omega t) \begin{Bmatrix} \cos \pi\frac{0}{3} \\ \cos \pi\frac{1}{3} \\ \vdots \\ \cos \pi\frac{n}{3} \\ 0 \end{Bmatrix}. \quad (3.75)
 \end{aligned}$$

Its solution requires time integration with zero initial conditions for the angular displacement and its first time derivatives. The convergence is sufficient, although it exhibits different magnitudes for the odd and even terms (Fig. 3.16).

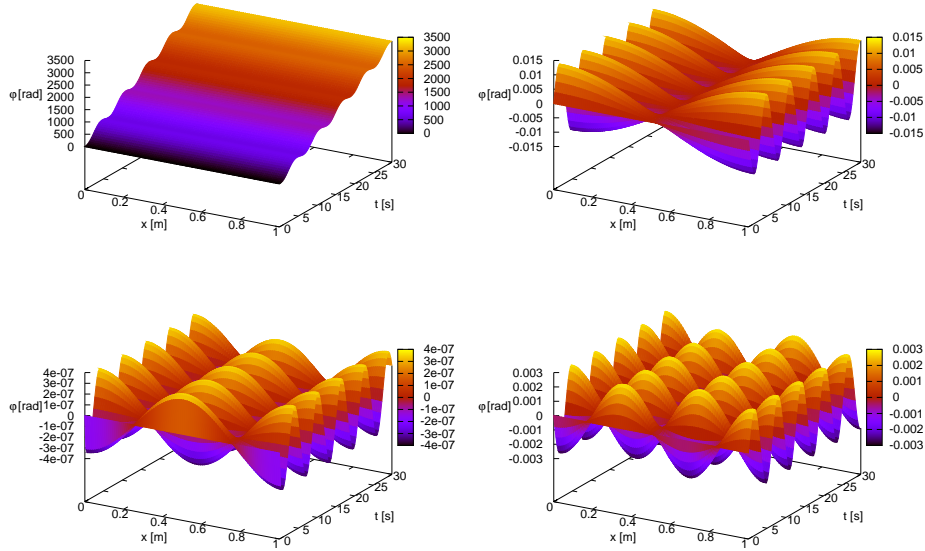


**Figure 3.16.** Successive terms of the Fourier expansion (3.75).

The semi-analytical solution is accurate. Unfortunately, we can not easily modify our structure and its boundary conditions. The finite element model is more practical. The numerical model always allows one to consider a wide range of parameters and various excitation functions. That is why in further control analysis we will use a space-time finite element approach. The velocity variant was applied. The following notations were introduced

$$\dot{\varphi} = \xi, \quad \dot{\vartheta} = \zeta. \quad (3.76)$$

According to the equation of motion (3.53) and (3.54) the linear distribution of angular velocities were assumed

$$\xi(x, t) = \sum_{i=1}^4 N_i(x, t) \xi_i, \quad (3.77)$$

$$\zeta(x, t) = \sum_{i=1}^4 N_i(x, t) \zeta_i, \quad (3.78)$$

where the shape function  $\mathbf{N}$  is given by (3.34). Adequate virtual functions were applied

$$\xi^*(x, t) = \delta(t - \alpha h) \left[ \left(1 - \frac{x}{b}\right) \xi_3 + \frac{x}{b} \xi_4 \right], \quad (3.79)$$

$$\zeta^*(x, t) = \delta(t - \alpha h) \left[ \left(1 - \frac{x}{b}\right) \zeta_3 + \frac{x}{b} \zeta_4 \right]. \quad (3.80)$$

Finally, the virtual energy of the coupled rotating system (3.53) and (3.54) can be written in the following form

$$\begin{aligned} \Pi_\xi = \int_0^h \int_0^b \xi^*(x, t) \cdot \left\{ -GI \frac{\partial^2 \varphi}{\partial x^2} + \rho I \frac{\partial \xi}{\partial t} + \right. \\ \left. + \delta(x - x_B) c (\xi - \zeta) - \delta(x - x_A) f(t) \right\} dx dt, \end{aligned} \quad (3.81)$$

$$\Pi_\zeta = \int_0^h \int_0^b \zeta^*(x, t) \cdot \left\{ I_d \frac{d\zeta}{dt} + c (\zeta - \xi) \right\} dx dt. \quad (3.82)$$

Minimisation of the virtual energy (3.81) results in matrices  $\mathbf{M}_s$ ,  $\mathbf{C}_s$ ,  $\mathbf{K}_s$ ,  $\mathbf{E}_s$  describing the shaft and the external forces  $\mathbf{F}_s$ . From (3.82) we obtain matrices  $\mathbf{M}_d$  and  $\mathbf{C}_d$  describing the attached system. Elemental matrices and vectors are assembled in global system of equations.

The left and the right part of the stiffness matrix of the shaft are tri-diagonal. The inertia matrix is a consequent one, i.e., computed taking into account finite element space-time interpolation functions (shape functions). No simple lumping was used. A small internal material damping is assumed. In practise, for simplicity, we employ a damping proportional to the velocities of angular deformations together with a numerical damping of the calculation procedure. Since such a damping is low comparing with the damping of the attached damper, we do not focus our attention on it.

### 3.3. Vibrations of the Sandwich Beam Induced by the Initial Conditions

The dynamics of layered structures was extensively investigated for many years. Pioneering work [55] refers to the transversal vibration of an infinitely long beam with the damping layer. In [27, 28] the longitudinal free

vibrations of the finite three-layer beam with viscoelastic core were examined. Transversal oscillations of the sandwich beam of the finite length with external force excitation was considered in [61]. In the significant part of the later papers the identification of loss factor [75] or stability of the system [54] is considered. In [21] a non-uniform shear stress variation across the thickness of each layer was assumed. The analytical model that takes into account the compressional vibration of the layered beam is shown in [84]. Attempts to describe sandwich beams with simple models were given in [6]. Large amplitudes of vibrations of sandwich structures, in nonlinear range are investigated in [50, 56].

Theoretical analysis can not be performed for arbitrary structures with required simplicity. For the analytical solution, we choose the simply supported beam as one of the most representative structures. The governing set of differential equations for the vibrating sandwich beam is derived in [61]. The necessary assumptions and simplifications of the analytical model are described below.

### 3.3.1. Mathematical Model

Let us consider a three-layered sandwich beam. Its cross-sectional geometry has the characteristic width  $b$  and the thicknesses of each layer is  $h_1$ ,  $h_2$ , and  $h_3$  (Fig. 3.17). Longitudinal displacements  $u$  in the  $x$  direction and transversal displacements  $w$  in the  $z$  direction of the beam are taken into account. The face-plates are assumed to be purely elastic, with Young mod-

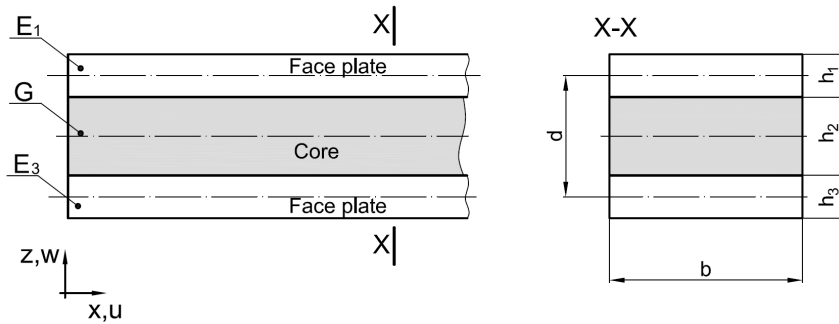


**Figure 3.17.** Dimensions and coordinate system of a three-layered beam with the viscoelastic core.

ules  $E_1$  and  $E_3$ , respectively. The core is linearly viscoelastic and defined by the shear modulus  $G$ . The obtained mathematical model is the result of some physically simplifying assumptions. The shear strains in the outer layers and the stresses in the longitudinal direction in the core are neglected. Moreover, the transversal direct strains in each layer is neglected as well, so the displacements  $w$  of the entire cross-section of the beam are constant (Fig. 3.18).

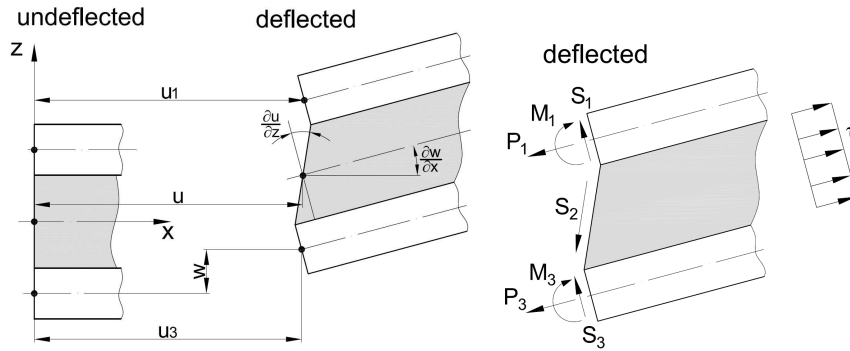


**Figure 3.18.** Displacements of a beam element (left), forces, moments and loads acting on it (right).

The shear strain in the core is given by the formula

$$\gamma = \frac{\partial w}{\partial x} + \frac{\partial u}{\partial z}. \quad (3.83)$$

The geometrical relationships in the deformed beam allows describing the term  $\partial u/\partial z$  by the displacement pattern  $u_1$ ,  $u_3$  and  $\partial w/\partial x$  of the face plates

$$\frac{\partial u}{\partial z} = \frac{1}{h_2} \left[ \left( u_1 + \frac{h_1}{2} \frac{\partial w}{\partial x} \right) - \left( u_3 - \frac{h_3}{2} \frac{\partial w}{\partial x} \right) \right]. \quad (3.84)$$

It should be mentioned that the applied dependency has certain restrictions and is accurate for  $h_2$  tending to zero. Otherwise, for large  $h_2$ , we should expect some discrepancies between the computed results and the real motion. By substituting Eq. (3.84) into Eq. (3.83), and after some rearrangements we obtain

$$\gamma = \frac{d}{h_2} \frac{\partial w}{\partial x} + \frac{u_1 - u_3}{h_2}, \quad (3.85)$$

where  $d = (h_1 + 2h_2 + h_3)/2$  is the distance between the mid-planes of the outer face plates. If we know the explicit form of  $\gamma$ , we can determine the

shear force in the core. The shear forces in both remaining layers are also computed. We assume zero longitudinal direct stress in the core

$$\tau = G \cdot \gamma. \quad (3.86)$$

The total shear force consists of three main components. The shear force of the upper beam and shear force on the lower beam (Fig. 3.18) are as follows

$$S_1 = D_1 \frac{\partial^3 w}{\partial x^3}, \quad (3.87)$$

$$S_3 = D_3 \frac{\partial^3 w}{\partial x^3} \quad (3.88)$$

and the force introduced by the core shear stress is

$$S_2 = -\tau db, \quad (3.89)$$

where  $D_1$  and  $D_3$  are the flexural rigidities of the face layers.

The total force is the sum of above three forces

$$S = S_1 + S_2 + S_3 = (D_1 + D_3) \frac{\partial^3 w}{\partial x^3} - Gdb \left[ \frac{d}{h_2} \frac{\partial w}{\partial x} + \frac{u_1 - u_3}{h_2} \right]. \quad (3.90)$$

The assumption that the transversal load is carried by the total shear force  $p = \partial S / \partial x$  on the section, after rearrangements gives the following formula

$$p = D_t \frac{\partial^4 w}{\partial x^4} - G \frac{d^2 b}{h_2} \frac{\partial^2 w}{\partial x^2} - G \frac{db}{h_2} \left( \frac{\partial u_1}{\partial x} - \frac{\partial u_3}{\partial x} \right), \quad (3.91)$$

where  $D_t = E_1 I_1 + E_3 I_3$  is the sum of the flexural rigidities of the upper and lower face plates.  $I_1$  and  $I_3$  are the cross-sectional inertia moments of face plates.

Let us denote the longitudinal force in the face plates  $P_1$  and  $P_3$ . They act in the midplane and are related to the longitudinal displacements by the relations

$$P_1 = E_1 h_1 b \frac{\partial u_1}{\partial x}, \quad (3.92)$$

and

$$P_3 = E_3 h_3 b \frac{\partial u_3}{\partial x}. \quad (3.93)$$

The total longitudinal force along the section equals to 0, so  $P_1 = -P_3$  and hence we obtain the relation

$$\frac{\partial u_1}{\partial x} = \frac{-E_3 h_3}{E_1 h_1} \frac{\partial u_3}{\partial x}. \quad (3.94)$$

Considering the physical system we can write

$$E_1 h_1 u_1 = -E_3 h_3 u_3. \quad (3.95)$$

Finally the Eq. (3.91) can be rewritten as

$$p = D_t \frac{\partial^4 w}{\partial x^4} - \frac{bGd^2 \partial^2 w}{h_2 \partial x^2} + \frac{bGd}{h_2} \left( \frac{E_1 h_1 + E_3 h_3}{E_1 h_1} \right) \frac{\partial u_3}{\partial x}. \quad (3.96)$$

The second equation coupling  $w$  and  $u_3$  is derived from the equilibrium of the longitudinal forces on an infinitesimal element of the lower face

$$\delta P_3 = -\tau \delta x. \quad (3.97)$$

This equation assumes the equilibrium of the axial forces in the outer layer and the longitudinal force resulting from the shear stress in the core. With respect to the longitudinal force on the lower face plate, Eq. (3.97) can be written in the following form

$$-\tau = E_3 h_3 b \frac{\partial^2 u_3}{\partial x^2}. \quad (3.98)$$

In order to determine the relationship between the longitudinal displacements  $u_1$  and  $u_3$ , and the relationship between their derivatives with respect to  $x$ , the condition of zero axial force on the whole section was assumed

$$\frac{\partial^2 u_3}{\partial x^2} - \frac{G(E_3 h_3 + E_1 h_1)}{E_1 h_1 h_2 E_3 h_3 b} u_3 = -\frac{Gd}{h_2 E_2 h_3 b} \frac{\partial w}{\partial x}. \quad (3.99)$$

Finally, we obtain the couple of differential equations

$$\frac{\partial^4 w}{\partial x^4} - gY \frac{\partial^2 w}{\partial x^2} + g \frac{db}{D_t} E_3 h_3 \frac{\partial u_3}{\partial x} = \frac{p}{D_t}, \quad (3.100)$$

$$\frac{\partial^2 u_3}{\partial x^2} - \frac{g}{b} u_3 = -gY \frac{D_t}{E_3 h_3 b^2 d} \frac{\partial w}{\partial x}, \quad (3.101)$$

where

$$g = \frac{G}{h_2} \left( \frac{1}{E_1 h_1} + \frac{1}{E_3 h_3} \right), \quad (3.102)$$

$$Y = \frac{d^2 b}{D_t} \frac{E_1 h_1 E_3 h_3}{E_1 h_1 + E_3 h_3}, \quad (3.103)$$

are the shear and stiffness parameters. This mathematical formulation is used for the simply supported three-layered beam with a controllable core.

### 3.3.2. Analytical Solution

Let us consider the simply supported three-layered beam of the mass density  $\mu$  and the length  $L$ , with point mass  $m$  placed in the middle of the structure. The examined sandwich beam is depicted in Fig. 3.19. The following

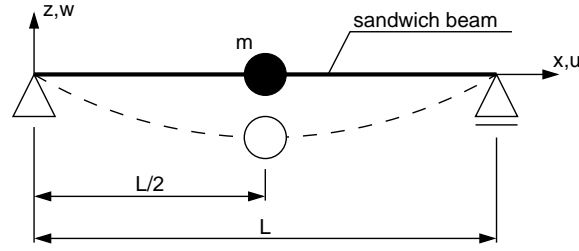


**Figure 3.19.** Simply supported sandwich beam.

boundary conditions were assumed

$$\begin{aligned} w(0, t) = w(L, t) = 0, \quad M(0, t) = M(L, t) = 0, \\ u_3'(0, t) = u_3'(L, t) = 0, \end{aligned} \quad (3.104)$$

where the total bending moment of the sandwich beam model defined in the previous section is given by the formula

$$M = M_1 + M_2 + M_3 = D_t \frac{\partial^2 w}{\partial x^2} + E_3 h_3 d b \frac{\partial u_3}{\partial x}. \quad (3.105)$$

$D_t$  is the sum of the flexural rigidity of both face plates. Vibrations of the beam are induced by the initial conditions. The structure is initially deflected according to the formula

$$w_0(x) = 4\bar{w}_0 \frac{x}{L} \left(1 - \frac{x}{L}\right). \quad (3.106)$$

Then the following initial conditions were assumed

$$w(x, 0) = w_0(x), \quad \dot{w}(x, 0) = 0, \quad u_3(x, 0) = 0. \quad (3.107)$$

The motion equations of the sandwich beam from Fig. 3.19 are described by Eqs. (3.100) and (3.101), where the transversal loading is written in the following form

$$p = -\mu \frac{\partial^2 w}{\partial t^2} - \delta \left(x - \frac{L}{2}\right) m \frac{\partial^2 w}{\partial t^2}. \quad (3.108)$$

Finally, the governing equations of considered problem take the form

$$\begin{aligned} \frac{\partial^4 w}{\partial x^4} - gY \frac{\partial^2 w}{\partial x^2} + \frac{g}{\alpha b} \frac{\partial u_3}{\partial x} + \left[ \frac{\mu}{D_t} + \delta \left( x - \frac{L}{2} \right) \frac{m}{D_t} \right] \frac{\partial^2 w}{\partial t^2} &= 0, \\ \frac{\partial^2 u_3}{\partial x^2} - \frac{g}{b} u_3 + gY \alpha \frac{\partial w}{\partial x} &= 0. \end{aligned} \quad (3.109)$$

The simplification of the above formula is enabled with the substitution

$$\alpha = \frac{D_t}{E_3 h_3 d b^2}. \quad (3.110)$$

The system of partial differential equations (3.109) can be solved by separation of variables. Transversal displacement is develop into the sine Fourier series (3.1) ( $w \rightarrow U_j$ ) while the longitudinal displacement is develop into the cosine Fourier series (3.56) ( $u_3 \rightarrow V_j$ ). The series (3.2) and (3.57) satisfy the boundary conditions (3.104). As a result of the Fourier transformation of (3.109), we obtain

$$\begin{aligned} \frac{j^4 \pi^4}{L^4} U_j(t) + gY \frac{j^2 \pi^2}{L^2} U_j(t) - \frac{g}{\alpha b} \frac{j\pi}{L} V_j(t) + \frac{\mu}{D_t} \ddot{U}_j(t) + \frac{m}{D_t} \sin \frac{j\pi}{2} \frac{\partial^2 w}{\partial t^2} \Big|_{x=\frac{L}{2}} &= 0, \\ -\frac{j^2 \pi^2}{L^2} V_j(t) - \frac{g}{b} V_j(t) + gY \alpha \frac{j\pi}{L} U_j(t) &= 0. \end{aligned} \quad (3.111)$$

According to (3.2) the acceleration of the concentrated mass  $m$  in the middle of the beam is given by the series

$$\frac{\partial^2 w}{\partial t^2} \Big|_{x=\frac{L}{2}} = \frac{2}{L} \sum_{k=1}^n \ddot{U}_k(t) \sin \frac{k\pi}{2}. \quad (3.112)$$

After rearrangement the set of Eqs. (3.111) can be written as one equation dependent on  $U_j(t)$

$$\frac{\mu}{D_t} \ddot{U}_j(t) + \frac{2m}{D_t L} \sin \frac{j\pi}{2} \sum_{k=1}^n \ddot{U}_k(t) \sin \frac{k\pi}{2} + \omega_j^4 \left( 1 + \frac{gYb}{\omega_j^2 b + g} \right) U_j(t) = 0, \quad (3.113)$$

where

$$\omega_j = \frac{j\pi}{L}. \quad (3.114)$$

The sine Fourier transformation (3.1) of initial condition of the sandwich beam (3.106) is as follows

$$U_j = \int_0^L w_0(x) \sin \frac{j\pi x}{L} dx = 8\bar{w}_0 \frac{L}{j^3 \pi^3} [1 - (-1)^j] = U_j(0_+). \quad (3.115)$$

The initial deflection of the beam is symmetrical, so the resulting series contains zeros in even terms. The system of Eqs. (3.113) can be written in a matrix form and solved numerically for unrestricted number of terms in the solution. The following data was assumed

- length of the beam  $L = 2.88$  m,
- width of the beam  $b = 0.04$  m,
- thickness of the face plates  $h_1 = h_3 = 0.5 \cdot 10^{-3}$  m
- thickness of the core  $h_2 = 5 \cdot 10^{-3}$  m
- cross-sectional inertia moment of the face plates  $I_1 = I_3 = 0.42 \cdot 10^{-12}$  m<sup>4</sup>,
- Young's modulus of the face plates  $E_1 = E_3 = 69$  GPa,
- shear modulus of the core  $G = 45$  kPa,
- mass of the sandwich beam  $\mu = 0.33$  kg/m,
- granulate mass  $m = 0.74$  kg,
- amplitude of the initial displacement  $\bar{w}_0 = 0.06$  m.

Figure 3.20 presents the solution of the problem for 1 and 10 terms of the sine Fourier expansion (3.2). We see that the first single term gives us sufficiently accurate results.

The closed analytical solution of (3.113) requires limiting to the first term of the series (3.2). The resulting ordinary differential equation has the following form

$$\left( \frac{\mu}{D_t} + \frac{2m}{D_t L} \right) \ddot{U}_1(t) + \omega_1^4 \left( 1 + \frac{gYb}{\omega_1^2 b + g} \right) U_1(t) = 0. \quad (3.116)$$

After the Laplace-Carson transformation (3.64) we obtain

$$\left( \frac{\mu}{D_t} + \frac{2m}{D_t L} \right) p^2 [\hat{U}_1(p) - U_1(0_+)] + \omega_1^4 \left( 1 + \frac{gYb}{\omega_1^2 b + g} \right) \hat{U}_1(p) = 0. \quad (3.117)$$

The solution of the algebraic form (3.117) is given by the following formula

$$\hat{U}_1(p) = \frac{p^2}{p^2 + \beta^2} U_1(0_+), \quad (3.118)$$

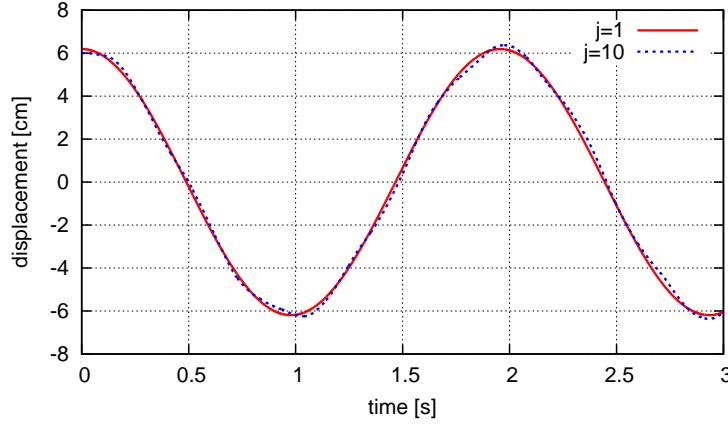


**Figure 3.20.** Free vibration of the sandwich beam with 1 na 10 terms of the Fourier expansion.

with the coefficient

$$\beta = \omega_1^2 \sqrt{\frac{D_t L}{\mu L + 2m} \left( 1 + \frac{g Y b}{\omega_1^2 b + g} \right)}. \quad (3.119)$$

Now, Eq. (3.118) can be transformed back (3.65) to the time variable

$$U_1(t) = U_1(0_+) \cos \beta t. \quad (3.120)$$

Finally, according to (3.2) the first term of transversal displacement can be written in the following form

$$w(x, t) = 32\bar{w}_0 \frac{1}{\pi^3} \cos \beta t \sin \frac{\pi x}{L}. \quad (3.121)$$

This formula is a base for our optimisation. The parameter  $\beta$  contains all the material and geometrical data. We can now simply derive both the velocity and acceleration of the layered structure.

### 3.4. The Structure Based on the Granular Material

There are many attempts to mathematical description of the mechanical behaviour of bulk materials. Broad overview of the models for loose and compacted granular materials is presented in books [66, 81]. However, relations between these models and the case when the state of granular material

is dynamically switched between two unsteady states. The concept was introduced and briefly characterised in the paper [19]. The rheological models of granular conglomerates under partial vacuum were presented in [96]. Then the rheological model was developed to six parameters. It reproduces well the axial cyclic loading [97]. Nevertheless these models can not be directly applied to sandwich beams.

This section deals with a sandwich beam comprising smart granular structure. Mathematical model of the layered beam with the controllable core is represented by a two degrees of freedom system with the Kelvin-Voigt constitutive material with a controllable stiffness of a spring and a viscous damper with variable coefficient.

### 3.4.1. Mathematical Model

Software packages like LMGC90, PFC3D or YADE are capable of modelling collections of deformable or rigid particles with various shapes and sizes, defining interaction laws (contact, friction, cohesion, fracture, wear, etc.) including multiphysic coupling. However, at this point, an in-depth look on the particle interactions in the granular structure encapsulated in an elastic envelope would be a complex and time consuming issue. Such a meticulous model would be impractical for the optimal control problem.

Let us consider two parallel cantilevers coupled by the dynamical system at free ends. The length of both beams is  $L$  and the flexural stiffness is  $EI$ . The conjugated dynamical system includes two point mass, a damper and a spring. These mechanical elements were defined by the parameters  $m$ ,  $c$  and  $k$ . All the considered parameters are real numbers, greater than zero. Generally, the vibrations of the system were described by the set of the discrete-continuous equations of motion. In order to obtain a closed analytical solution of the problem the inertia of the beams was neglected. Moreover, the stiffness of each of the continuous beams is replaced by the discrete spring. According to the scheme depicted in Fig. 3.21 the problem was reduced to a two degrees of freedom system. The simplified problem describes vibrations of the coupled ends of the beams. The transversal displacements of each of them were described by the functions  $w_1$  and  $w_2$ .

The partial differential equations describing the discrete-continuous case are given as follows

$$\begin{aligned} EI w_1'''' &= f_1(x, t), \\ EI w_2'''' &= f_2(x, t), \end{aligned} \tag{3.122}$$

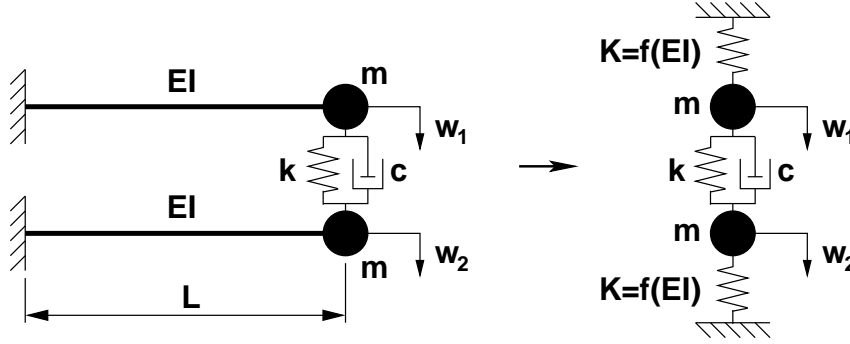


**Figure 3.21.** Phenomenological model of the two cantilever beams coupled with the granular damping structure.

where

$$\begin{aligned} f_1(x, t) &= -\delta(x - L) [m\ddot{w}_1 + c(\dot{w}_1 - \dot{w}_2) + k(w_1 - w_2)], \\ f_2(x, t) &= -\delta(x - L) [m\ddot{w}_2 + c(\dot{w}_2 - \dot{w}_1) + k(w_2 - w_1)]. \end{aligned} \quad (3.123)$$

Appropriate initial and boundary conditions are included as well.

In order to solve the discrete-continuous model with respective simplifications, the theory of distribution was applied. The properties of convolution were used to calculate the reduced stiffness of the massless cantilever beam

$$w(x, t) = G(x, s) * f(s, t) = \int_0^L G(x, s) f(s, t) ds, \quad (3.124)$$

where  $G(x, s)$  is the influence Green function, obtained by solving the basic equation according to boundary conditions for the cantilever beam

$$w_i(0, t) = w_i'(0, t) = w_i''(L, t) = w_i'''(L, t) = 0, \quad i = 1, 2. \quad (3.125)$$

The basic equation was established by replacing the right-hand side of Eq. (3.122) by the Dirac's delta  $\delta(x - s)$ . The solution of the complete equation is the convolution of the fundamental solution and the inhomogeneity (3.123). Finally, according to Eq. (3.124) we obtain

$$\begin{aligned} m\ddot{w}_1 + c(\dot{w}_1 - \dot{w}_2) + k(w_1 - w_2) + Kw_1 &= 0, \\ m\ddot{w}_2 + c(\dot{w}_2 - \dot{w}_1) + k(w_2 - w_1) + Kw_2 &= 0, \end{aligned} \quad (3.126)$$

where

$$K = \frac{3EI}{L^3}, \quad K > 0, \quad (3.127)$$

is the substitute stiffness of the beams in the simplified model. Vibrations of the system (3.126) were induced by the initial conditions as follows

$$w_i(0) = w_i, \quad \dot{w}_i(0) = \dot{w}_i, \quad i = 1, 2. \quad (3.128)$$

The simplified problem can be integrated in the analytical way.

### 3.4.2. Analytical Solution

The integral Laplace-Carson transformation (3.64) was applied in the solution of Eqs. (3.126). These equations can be solved algebraically. According to initial conditions (3.128) the set of equations can be written in the following form

$$\begin{aligned} (ms^2 + cs + k + K) \hat{w}_1(s) - (cs + k) \hat{w}_2(s) &= \\ &= ms [sw_1(0_+) + \dot{w}_1(0_+)] - cs [w_2(0_+) - w_1(0_+)], \\ (ms^2 + cs + k + K) \hat{w}_2(s) - (cs + k) \hat{w}_1(s) &= \\ &= ms [sw_2(0_+) + \dot{w}_2(0_+)] + cs [w_2(0_+) - w_1(0_+)]. \end{aligned} \quad (3.129)$$

The solutions of the above set of equations describe the response of an individual degrees of freedom. For the first degree of freedom we obtain

$$\begin{aligned} \hat{w}_1(s) &= \frac{ms^2 (ms^2 + cs + k + K) + cs (ms^2 + K)}{(ms^2 + cs + k + K)^2 - (cs + k)^2} w_1(0_+) + \\ &+ \frac{ms (ms^2 + cs + k + K)}{(ms^2 + cs + k + K)^2 - (cs + k)^2} \dot{w}_1(0_+) + \\ &+ \frac{s (kms - cK)}{(ms^2 + cs + k + K)^2 - (cs + k)^2} w_2(0_+) + \\ &+ \frac{ms (cs + k)}{(ms^2 + cs + k + K)^2 - (cs + k)^2} \dot{w}_2(0_+). \end{aligned} \quad (3.130)$$

To return to the time domain the inverse transformation (3.65) must be performed. In order to perform the inverse Laplace-Carson transform we

must apply the decomposition of the integrand into simple fractions. The roots of the polynomial of the denominator of (3.130) are as follows

$$s_{1,2} = \pm i\sqrt{\frac{K}{m}}, \quad s_{3,4} = -\frac{c}{m} \pm \frac{\sqrt{c^2 - m(K + 2k)}}{m}. \quad (3.131)$$

Identification of the parameters of a granular material is restricted by the condition

$$c^2 - m(K + 2k) < 0. \quad (3.132)$$

Finally, displacements of the first degree of freedom can be written in the following form

$$\begin{aligned} w_1(t) = & \frac{w_1(0_+) + w_2(0_+)}{2} \cos\left(t\sqrt{\frac{K}{m}}\right) + \\ & + \frac{\dot{w}_1(0_+) + \dot{w}_2(0_+)}{2} \sqrt{\frac{m}{K}} \sin\left(t\sqrt{\frac{K}{m}}\right) + \\ & + \exp\left(-\frac{c}{m}t\right) \left\{ \frac{w_1(0_+) - w_2(0_+)}{2} \left[ \cos\left(\frac{\eta}{m}t\right) + \frac{c}{\eta} \sin\left(\frac{\eta}{m}t\right) \right] + \right. \\ & \left. + \frac{\dot{w}_1(0_+) - \dot{w}_2(0_+)}{2} \frac{m}{\eta} \sin\left(\frac{\eta}{m}t\right) \right\}, \end{aligned} \quad (3.133)$$

where

$$\eta = \sqrt{m(K + 2k) - c^2}. \quad (3.134)$$

According to (3.132) the parameter  $\eta$  is a real number and greater than zero. For the second degree of freedom the displacement is given by the formula

$$\begin{aligned} w_2(t) = & \frac{w_1(0_+) + w_2(0_+)}{2} \cos\left(t\sqrt{\frac{K}{m}}\right) + \\ & + \frac{\dot{w}_1(0_+) + \dot{w}_2(0_+)}{2} \sqrt{\frac{m}{K}} \sin\left(t\sqrt{\frac{K}{m}}\right) + \\ & + \exp\left(-\frac{c}{m}t\right) \left\{ \frac{w_2(0_+) - w_1(0_+)}{2} \left[ \cos\left(\frac{\eta}{m}t\right) + \frac{c}{\eta} \sin\left(\frac{\eta}{m}t\right) \right] + \right. \\ & \left. + \frac{\dot{w}_2(0_+) - \dot{w}_1(0_+)}{2} \frac{m}{\eta} \sin\left(\frac{\eta}{m}t\right) \right\}. \end{aligned} \quad (3.135)$$

In order to illustrate the result (3.135) the simple calculation was performed. Let us assume the following data:  $K = 0.23$  N/m,  $m = 0.18$  kg,  $c = 0.031$  Ns/m and  $k = 8.7$  N/m, which fulfil the condition (3.132). The following initial conditions for both degrees of freedom were taken into account  $w_1(0_+) = 0.09$  m,  $w_2(0_+) = 0.03$  m and  $\dot{w}_1(0_+) = \dot{w}_2(0_+) = 0$ . The displacements in time of the 1st and the 2nd degree of freedom were depicted in Fig. 3.22.

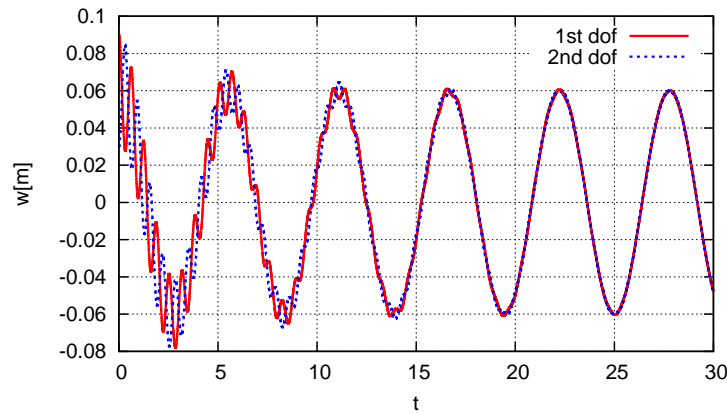


**Figure 3.22.** Displacements in time of the 1st and the 2nd degrees of freedom.

The closed solutions for particular degrees of freedom (Eqs. (3.133) and (3.135)) allow us to derive the formulas for the velocities and accelerations. We know the state of the structure at the selected time without solution of the entire problem. It allows us to elaborate the efficient semi-active control strategy of the damping parameter  $c$  and stiffness  $k$ .

# Bibliography

- [1] M. Anderson and J.-H. Kimn. A numerical approach to space-time finite elements for the wave equation. *Journal of Computational Physics*, 226(1):466–476, 2007.
- [2] I. V. Andrianov and J. Awrejcewicz. Dynamics of a string moving with time-varying speed. *Journal of Sound and Vibration*, 292:935–940, 2006.
- [3] J. H. Argyris and A. S. L. Chan. Application of the finite elements in space and time. *Ingenieur-Archiv*, 41:235–257, 1972.
- [4] J. H. Argyris and D. W. Scharpf. Finite elements in time and space. *Nuclear Engineering and Design*, 10:456–469, 1969.
- [5] J. H. Argyris and D. W. Scharpf. Finite elements in time and space. *Aeronautical Journal of the Royal Aeronautical Society*, 73:1041–1044, 1969.
- [6] D. Backstrom and A.C. Nilsson. Modelling the vibration of sandwich beams using frequency-dependent parameters. *Journal of Sound and Vibration*, 300:589–611, 2007.
- [7] C. Bajer. Space–time finite element formulation for the dynamical evolutionary process. *International Journal of Applied Mathematics and Computer Science*, 3(2):251–268, 1993.
- [8] C. I. Bajer. Triangular and tetrahedral space–time finite elements in vibration analysis. *International Journal for Numerical Methods in Engineering*, 23:2031–2048, 1986.
- [9] C. I. Bajer. Notes on the stability of non–rectangular space–time finite elements. *International Journal for Numerical Methods in Engineering*, 24:1721–1739, 1987.
- [10] C. I. Bajer. Dynamics of contact problem by the adaptive simplex–shaped space–time approximation. *Journal of Theoretical and Applied Mechanics*, 7:235–248, 1988. Special issue, supplement No. 1.
- [11] C. I. Bajer. Adaptive mesh in dynamic problem by the space–time approach. *Computers and Structures*, 33(2):319–325, 1989.
- [12] C. I. Bajer. The space-time approach to rail/wheel contact and corrugations problem. *Computer Assisted Methods in Engineering and Science*, 5(2):267–283, 1998.
- [13] C. I. Bajer, R. Bogacz, and C. G. Bonthoux. Adaptive space–time elements in the dynamic elastic–viscoplastic problem. *Computers and Structures*, 39:415–423, 1991.
- [14] C. I. Bajer and C. Bohatier. The soft way method and the velocity formulation. *Computers and Structures*, 55(6):1015–1025, 1995.
- [15] C. I. Bajer and B. Dyniewicz. Space-time approach to numerical analysis of a string with a moving mass. *International Journal for Numerical Methods in Engineering*, 76(10):1528–1543, 2008.
- [16] C. I. Bajer and B. Dyniewicz. Numerical modelling of structure vibrations under inertial moving load. *Archives of Applied Mechanics*, 79(6-7):499–508, 2009.
- [17] C. I. Bajer and B. Dyniewicz. Virtual functions of the space-time finite element method in moving mass problems. *Computers and Structures*, 87:444–455, 2009.

- [18] C. I. Bajer and B. Dyniewicz. *Numerical analysis of vibrations of structures under moving inertial load*. Springer, 2012.
- [19] J. Bajkowski, W. Grzesikiewicz, M. Hać, and P. Tadzik. Parameter determination of half-active damping of vibration of mechanical systems by using granulated materials. In *Materials of International Congress Dycons'99*, pages 67–74, Ottawa, Canada, 1999.
- [20] K.-J. Bathe. *Finite element procedures in engineering analysis*. Prentice-Hall, Englewood Cliffs, NJ, 1982.
- [21] A. Bhimaraddi. Sandwich beam theory and the analysis of constrained layer damping. *Journal of Sound and Vibration*, 179(4):591–602, 1995.
- [22] B. Biondi and G. Muscolino. New improved series expansion for solving the moving oscillator problem. *Journal of Sound and Vibration*, 281:99–117, 2005.
- [23] C. Bohatier. A large deformation formulation and solution with space-time finite elements. *Archives of Mechanics*, 44:31–41, 1992.
- [24] W. W. Bolotin. On the influence of moving load on bridges (in Russian). *Reports of Moscow University of Railway Transport MIIT*, 74:269–296, 1950.
- [25] A. O. Cifuentes. Dynamic response of a beam excited by a moving mass. *Finite Elements in Analysis and Design*, 5(3):237–246, 1989.
- [26] F.M. Dimentberg. *Flexural vibrations of rotating shafts*. Butterworths, 1961.
- [27] R.A. DiTaranto. Theory of vibratory bending for elastic and viscoelastic layered finite-length beams. *Journal of Applied Mechanics*, 32(4):881–886, 1965.
- [28] R.A. DiTaranto and W. Blasingame. Composite damping of vibrating sandwich beams. *Journal of Engineering for Industry*, 89(4):633–638, 1967.
- [29] G. Doetsch. *Introduction to the Theory and Application of the Laplace Transformation*. Springer-Verlag, 1974.
- [30] B. Dyniewicz. *Dynamic properties of the hybrid systems subjected to moving sorces of perturbances (in Polish)*. PhD thesis, IPPT PAN, Warsaw, 2008.
- [31] B. Dyniewicz. Space-time finite element approach to general description of a moving inertial load. *Finite Elements in Analysis and Design*, 62:8–17, 2012.
- [32] B. Dyniewicz and C. I. Bajer. Discontinuous trajectory of the mass particle moving on a string or a beam. *Machine Dynamics Problems*, 31(2):66–79, 2007.
- [33] B. Dyniewicz and C. I. Bajer. Paradox of the particle's trajectory moving on a string. *Archive of Applied Mechanics*, 79(3):213–223, 2009.
- [34] B. Dyniewicz and C. I. Bajer. New feature of the solution of a Timoshenko beam carrying the moving mass particle. *Archives of Mechanics*, 62(5):327–341, 2010.
- [35] B. Dyniewicz and C. I. Bajer. New consistent numerical modelling of a travelling accelerating concentrated mass. *World Journal of Mechanics*, 2(6):281–287, 2012.
- [36] B. Dyniewicz, A. Pęgowska, and C. I. Bajer. Adaptive control of a rotating system. *Mechanical Systems and Signal Processing*, 43(1-2):90–102, 2014.
- [37] F.F. Ehrich. *Handbook of rotordynamics*. McGraw-Hill, 1998.
- [38] F. V. Filho. Finite element analysis of structures under moving loads. *The Shock and Vibration Digest*, 10(8):27–35, 1978.
- [39] M.A. Foda and Z. Abduljabbar. A dynamic Green function formulation for the response of a beam structure to a moving mass. *Journal of Sound and Vibration*, 210:295–306, 1998.
- [40] D.A. French and T.E. Peterson. A continuous space-time finite element method for the wave equation. *Mathematics of Computation*, 65(214):491–506, 1996.
- [41] I. Fried. Finite element analysis of time-dependent phenomena. *AIAA Journal*, 7:1170–1173, 1989.

- 
- [42] L. Frýba. *Vibrations of solids and structures under moving loads*. Thomas Telford House, 1999.
- [43] S. N. Gavrilov. The effective mass of a point mass moving along a string on a Winkler foundation. *Journal of Applied Mathematics and Mechanics*, 70(4):641–649, 2006.
- [44] S. N. Gavrilov and D. A. Indeitsev. The evolution of a trapped mode of oscillations in a string on an elastic foundation – moving inertial inclusion system. *Journal of Applied Mathematics and Mechanics*, 66(5):852–833, 2002.
- [45] M. E. Gurtin. Variational principles for linear elastodynamics. *Archive for Rational Mechanics and Analysis*, 16:34–50, 1964.
- [46] M. E. Gurtin. Variational principles for linear initial-value problems. *Quarterly of Applied Mathematics*, 22:252–256, 1964.
- [47] P. Hansbo, J. Hermansson, and T. Svedberg. Nitsche’s method combined with space–time finite elements for ALE fluid–structure interaction problems. *Computer Methods in Applied Mechanics and Engineering*, 193(39-41):4195–4206, 2004.
- [48] I. Herrera and J. Bielak. A simplified version of Gurtin’s variational principles. *Archive for Rational Mechanics and Analysis*, 53:131–149, 1974.
- [49] G.M. Hulbert and T.J.R. Hughes. Space-time finite element methods for second-order hyperbolic equations. *Computer Methods in Applied Mechanics and Engineering*, 84(3):327–348, 1990.
- [50] M.W. Hyer, W.J. Anderson, and R.A. Scott. Non-linear vibrations of three-layer beams with viscoelastic cores I. Theory. *Journal of Sound and Vibration*, 46(1):121–136, 1976.
- [51] M. Ichikawa, Y. Miyakawa, and A. Matsuda. Vibration analysis of the continuous beam subjected to a moving mass. *Journal of Sound and Vibration*, 230:493–506, 2000.
- [52] C.E. Inglis. *A Mathematical Treatise on Vibrations in Railway Bridges*. Cambridge University Press, 1934.
- [53] Yu. D. Kaplunov. The torsional oscillations of a rod on a deformable foundation under the action of a moving inertial load (in Russian). *Izv. Akad. Nauk SSSR, MTT*, 6:174–177, 1986.
- [54] R.C. Kar and W. Hauger. Stability of a sandwich beam subjected to a non-conservative force. *Computers and Structures*, 46(5):955–958, 1993.
- [55] E.M. Kerwin. Damping of flexural waves by a constrained viscoelastic layer. *Journal of the Acoustical Society of America*, 31(7):952–962, 1959.
- [56] A.V. Krys’ko, M.V. Zhigalov, and O.A. Saltykova. Control of complex nonlinear vibrations of sandwich beams. *Russian Aeronautics (Iz. VUZ)*, 51(3):238–243, 2008.
- [57] U. Lee. Separation between the flexible structure and the moving mass sliding on it. *Journal of Sound and Vibration*, 209(5):867–877, 1998.
- [58] S. Mackertich. Response of a beam to a moving mass. *Journal of the Acoustical Society of America*, 92:1766–1769, 1992.
- [59] S. Marathe, F. Gandhi, and K.W. Wang. Helicopter blade response and aeromechanical stability with a magnetorheological fluid based lag damper. *Journal of Intelligent Material Systems and Structures*, 9(4):272–282, 1998.
- [60] P. M. Mathews. Vibrations of a beam on elastic foundation. *ZAMM – Journal of Applied Mathematics and Mechanics*, 38(3-4):105–115, 1958.
- [61] D.J. Mead and S. Markus. The forced vibration of a three-layer, damped sandwich beam with arbitrary boundary conditions. *Journal of Sound and Vibration*, 10(2):163–175, 1969.

- [62] A. V. Metrikine and S. N. Verichev. Instability of vibration of a moving oscillator on a flexibly supported Timoshenko beam. *Archive of Applied Mechanics*, 71(9):613–624, 2001.
- [63] G. Michaltsos, D. Sophianopoulos, and A. N. Kounadis. The effect of a moving mass and other parameters on the dynamic response of a simply supported beam. *Journal of Sound and Vibration*, 191:357–362, 1996.
- [64] G. T. Michaltsos. Dynamic behaviour of a single-span beam subjected to loads moving with variable speeds. *Journal of Sound and Vibration*, 258(2):359–372, 2002.
- [65] A. B. Morgaevskii. Critical velocities calculation in the case of a beam under moving load (in Russian). *Mekhanika i mashinostroenie, Izvestiya AN SSSR, OTN*, 3:176–178, 1959.
- [66] R.M. Nedderman. *Statics and kinematics of granular materials*. Cambridge University Press, Cambridge, 1973.
- [67] E.J. Nestorides. *A handbook on torsional vibration*. Cambridge University Press, 1958.
- [68] J. T. Oden. A generalized theory of finite elements, II. Applications. *International Journal for Numerical Methods in Engineering*, 1:247–259, 1969.
- [69] M. Olsson. On the fundamental moving load problem. *Journal of Sound and Vibration*, 154(2):299–307, 1991.
- [70] P.M. Przybyłowicz. Torsional vibration control by active piezoelectric system. *Journal of Theoretical and Applied Mechanics*, 33(4):809–823, 1995.
- [71] J. Panovko. Historical outline of the theory of dynamic influence of moving load (in Russian). *Engineering Academy of Air Forces*, 17:8–38, 1948.
- [72] J. Penny, M. Friswell, S. Garvey, and A. Lees. *Dynamics of rotating machines*. Cambridge University Press, 2010.
- [73] A. V. Pesterev, L. A. Bergman, C. A. Tan, T.-C. Tsao, and B. Yang. On asymptotics of the solution of the moving oscillator problem. *Journal of Sound and Vibration*, 260:519–536, 2003.
- [74] A. Pęgowska, R. Konowrocki, and T. Szolc. Experimental verification of semi-active control concepts for torsional vibrations of the electro-mechanical system using rotary magneto-rheological actuators. In *XXV Symposium on Vibrations in Physical Systems*, pages 329–334, Poznań–Będlewo, 2012.
- [75] M. Rak, M. Ichchou, and J. Holnicki-Szulc. Identification of structural loss factor from spatially distributed measurements on beams with viscoelastic layer. *Journal of Sound and Vibration*, 310:801–811, 2008.
- [76] J.S. Rao. *History of rotating machinery dynamics*. Springer, 2011.
- [77] A. Renaudot. Etude de l’influence des charges en mouvement sur la resistance, des ponts metallique a poutres droites. *Annales des Ponts et Chaussées*, 1:145–204, 1861.
- [78] J.R. Rieker, Y.-H. Lin, and M.W. Trethewey. Discretization considerations in moving load finite element beam models. *Finite Elements in Analysis and Design*, 21:129–144, 1996.
- [79] R. Rodeman, D. B. Longcope, and L. F. Shampine. Response of a string to an accelerating mass. *Journal of Applied Mechanics*, 98(4):675–680, 1976.
- [80] S. Sadiku and H. H. E. Leipholz. On the dynamics of elastic systems with moving concentrated masses. *Ingenieur-Archiv*, 57:223–242, 1987.
- [81] O. Sadvskaya and V. Sadvskii. *Mathematical modelling in mechanics of granular materials*, volume 21 of *Advanced Structured Materials*. Springer, 2012.

- [82] H. Saller. *Influence of moving load on railway track and bridges* (in German, orig.: *Einfluss bewegter Last auf Eisenbahnoberbau und Brücken*). Kreidels Verlag, Berlin und Wiesbaden, 1921.
- [83] A. Schallenkamp. Schwingungen von Trägern bei bewegten Lasten. *Ingenieur-Archiv*, 8:182–198, 1937.
- [84] C.L. Sisemore and C.M. Darvennes. Transverse vibration of elastic-viscoelastic-elastic sandwich beams: compression-experimental and analytical study. *Journal of Sound and Vibration*, 252(1):155–167, 2002.
- [85] C. E. Smith. Motion of a stretched string carrying a moving mass particle. *Journal of Applied Mechanics*, 31(1):29–37, 1964.
- [86] R. Stocki, T. Szolc, P. Tazowski, and J. Knabel. Robust design optimization of the vibrating rotor-shaft system subjected to selected dynamic constraints. *Mechanical Systems and Signal Processing*, 29:34–44, 2012.
- [87] G.G. Stokes. Discussion of a differential equation relating to the breaking of railway bridges. *Cambridge Philosophical Transactions*, 8:707–735, 1849.
- [88] W. Szcześniak. Inertial moving loads on beams (in Polish). Scientific Reports, Warsaw University of Technology, Civil Engineering 112, 1990.
- [89] T. Szolc. On the discrete-continuous modeling of rotor systems for the analysis of coupled lateral-torsional vibrations. *International Journal of Rotating Machinery*, 6(2):135–149, 2000.
- [90] L.L. Thompson and P.M. Pinsky. A space-time finite element method for the exterior structural acoustics problem: Time-dependent radiation boundary conditions in two space dimensions. *International Journal for Numerical Methods in Engineering*, 39:1635–1657, 1996.
- [91] E. C. Ting, J. Genin, and J. H. Ginsberg. A general algorithm for moving mass problems. *Journal of Sound and Vibration*, 33(1):49–58, 1974.
- [92] D.V. Widder. *The Laplace transform*. Princeton Univ. Press, 1972.
- [93] R. Willis. Preliminary essay to the Appendix B. Report of the Commissioners Appointed to Inquire into the Application of Iron to Railway Structures. *W. Clowes and Sons*, 1849.
- [94] N. Z. Yakushev. Certain problems of dynamics of the beam under moving load (in Russian). *Studies in Plates and Shells Theory, Publisher of the Kazan Univ.*, 12:199–220, 1974.
- [95] D. M. Yoshida and W. Weaver. Finite-element analysis of beams and plates with moving loads. *Journal of the International Association Bridge and Structural Engineering*, 31(1):179–195, 1971.
- [96] R. Zalewski. Constitutive model for special granular structures. *International Journal of Non-Linear Mechanics*, 45(3):279–285, 2010.
- [97] R. Zalewski and Ł. Skoniecki. Six parameters rheological model for special granular structures. *Machine Dynamics Research*, 35(3):107–116, 2011.



# Optimal Control for Vibrating Mechanical Systems

The study of optimal control problems goes back to 1950s. In that time, two important advances were made. One was Bellman's Principle of Optimality and the corresponding Dynamic Programming, formulated by Richard Bellman in 1957 [5]. Dynamic Programming is a procedure that reduces the search for the optimal control to finding the solution of a partial differential equation (the Hamilton–Jacobi–Bellman Equation) [52]. The other was the Maximum Principle formulated by Pontryagin in 1962 [40]. The Maximum Principle is a set of necessary conditions for a control function to be optimal. Based on these theories, numerous computational methods were developed during 1960s and 1970s [10] and put into practice in various engineering applications.

In this chapter, the fundamental optimal control techniques in application to vibrating mechanical systems will be studied. At first, we will give a brief state of the art on active and semi-active control methods. Next, a general finite horizon optimal control problem will be formulated. Basic solution properties and the necessary optimality condition will be given. In the sequel, we will direct our focus toward the problems related to the systems controlled by means of the smart materials. Regarding mathematical structures of such systems, these problems will be classified as the optimal control problems for bilinear systems. We will demonstrate in details the solution methods supported with several examples for semi-active oscillators. The presented methodology will be brought into vibrating structures within the next chapter.

## 4.1. State of the Art

One of the first concept of the semi-active control in mechanical systems was proposed by Karnopp, Crosby and Harwood. In the work [23] they presented the idea of active suppression of the oscillator with one degree of freedom, moving upon uneven ground. The algorithm developed by the authors – Skyhook – is today one of the most widely used in suspension control systems for vehicles. The idea was designed to improve comfort of passengers. One of the most popular issues, in which the Skyhook is applied, is the oscillator problem. The extensive results are demonstrated in the following papers [12, 20]. In some recent works, the variable dampers are incorporated also for seismic isolation. This approach is presented in the papers [45, 53]. In [19], the authors propose to control both parameters, stiffness and damping. Control decision led to maximum dissipation of energy. In general, a decrease in vibration amplitude was to be achieved.

The problem of reducing beam vibrations via active control methods is also widely considered in literature. For details see, for example, [18]. An active constrained layer is applied in the approach presented in the work [4]. A beam subjected to a harmonic load was also controlled by an active method in [37]. The analysis in the frequency domain allowed the authors to reduce the maximum amplitudes. The actively controlled string system was considered in [51]. The problem of optimal design of structures with active support is analyzed in the paper [7]. The approach presented by the authors provides a useful tool for the determination of the number, positions and generalised forces of actuators. They considered two different cases with fixed and varying load, respectively. They concluded that application of the active support essentially changes the structure response and enables significant increase of structure stiffness or decrease of maximal deflection. To the active methods in structural control we can also include the track shape control. Pawel Flont and Jan Holnicki-Szulc developed the approach that uses active smart sleepers. These smart sleepers are equipped with actuators that enable the track to shift up and down. The results are presented in details in the paper [17]. The objective was to minimise total track deflection.

Semi-active systems have also found numerous applications in structures subjected to seismic excitation. The works that should be mentioned here are: [47, 53]. The task for semi-active control system is to stabilize system when lost the equilibrium state. Solutions are obtained by minimization of the cost function determined on the infinite time interval. This refers to the Linear Quadratic Regulation method (LQR). It should be mentioned here the lack of mathematical precision in formulating and solving the minimi-

sation task in that way. The LQR method can not be directly used in the case of bilinear systems. The problem lies within the directions of damping forces acting on the structure. These directions strictly depend on the velocities of the vibration. Thus, for some time intervals there is no possibility to generate the desired controls that result from the LQR. In terms of mechanical systems the LQR method is dedicated to active control systems and can not be directly used in case of parametric control problems. However, Mohler developed the iterative method which is analogous to the LQR, but applied for bilinear systems. This method is presented in details in his work [31]. Another approach is to derive the switching rules using Lyapunov stability theory. Methods based on the so-called optimal Lyapunov functions [33] deserve a special attention here. The switched input trajectories can drive the system to the equilibrium point. The energy of the system in those cases corresponds to the exponential function with the maximum rate of convergence.

Problems of vibration control are also widely considered in the robotic systems. Technological processes aided manipulators require high accuracy, without sacrificing production rate. The large inertia of the effectors and the object of manipulation may cause significant errors in the desired trajectory. Active control methods implemented in the state feedback loops, allows to compensate these errors. The application of PD regulators were proposed, among others, by Choura and Yigit in the paper [13]. The method based on the concept of “H-infinity” and fuzzy logic was presented by Yang and Kim [35]. Kang and Mills used the piezoelectric layers as sensors and actuators [22].

Most of the active and semi-active methods that have been developed lead to feedback controls determined by state-space measures. In the case of the distributed parameter systems, such an approach is typically complex due to observer design. The alternative method is pre-computed open-loop control. This is particularly useful in problems with a well-defined excitation. In linear mechanical systems, semi-active control methods usually result in switching operations, where the parameters to be controlled (damping, stiffness) are switched between two or more values. The switching conditions are based on state or time events. Optimally switched linear systems are widely considered in literature. Interesting results may be found, for example, in the paper [14].

Intensive studies on the semi-active control of systems represented by Partial Differential Equations (PDE) have opened a lot of unsolved problems. One of them occurs if the cost function is limited to a fixed period of time. The switching scheme for control is given in implicit form and it depends

on state and adjoint state variables. Solving the corresponding Two-Point Boundary Value Problem is time consuming and in general difficult to solve in the case of multidimensional problem. Another unsolvable problem that occurs in the case of systems described by PDE is stability of a switched system. The asymptotic stability of a switched system can be proven in the simplest cases only. The extensive research on these problems was treated in terms of the Lie algebra and it was done by Liberzon et al. in the following works [27, 28].

The early idea of the semi-active control of one-dimensional continuum under a travelling load was presented in [6]. The extension of the idea was reported in the work [38]. The span was supported by a set of dampers placed on the rigid base. Open loop control of damping parameters allowed us to actively reduce the deflection of a string or a beam supporting a traveling load. The control of beam vibrations exhibited a significantly higher control efficiency than in the case of a string.

The idea of straight-line passage is based on the principle of a two-sided lever. The first part of the beam which is subjected to a moving load is supported by semi-active damper placed on the rigid base (see Fig. 4.1b). The first damper is active while the second is passive. At this stage, a part of the beam is turned around its centre of gravity, levering the right hand part with a passive damper attached. The temporal increment of displacements

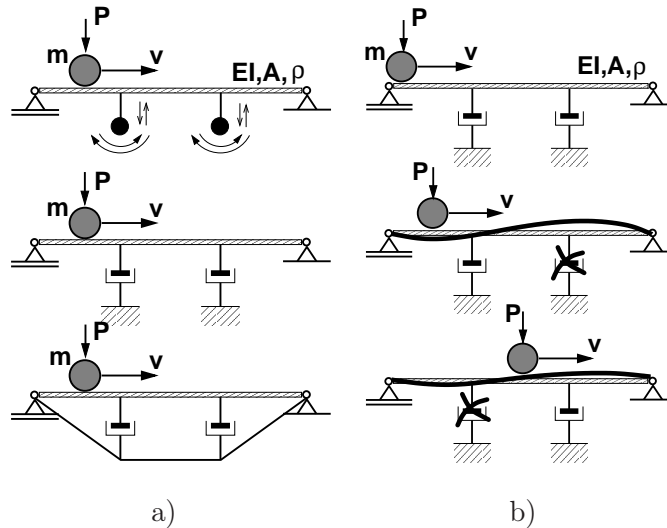


**Figure 4.1.** The idea of passive (a) and semi-active (b) control of a beam deflection under a travelling load.

on the right hand part of the beam enables us to exploit it during the second stage of passage.

Technical difficulties with the rigid support of the bottom parts of dampers require new, more practical solutions. Dampers are supported with an elastic string or bar system. However, the elastic support reduces the efficiency of the performance and also involves technological problems. In the paper [39], a new and significantly more efficient idea presented in Fig. 4.2a is considered. The main stiff simply-supported beam is covered by a supplementary beam, joined to the main beam by a set of controlled dampers. This upper beam can be assumed as a simply supported as well, since this type of boundary condition can be implemented in a natural way. Such a modification does not require the rigid base and it can be easily incorporated into existent guideways (see Fig. 4.2b). We assume the upper beam as significantly less rigid than the main lower beam. We must emphasize here that a desired dynamic effect is obtained from the relative transverse velocity of both lower and upper beams. Let us consider the second stage of the motion depicted in Fig. 4.2a. The upper beam subjected to a force is deflected. At the same time, the velocity of the lower beam allows to lever the joining damper and effectively support the upper beam. The relative velocity of both lower and upper beam enable us to design the efficient control for the straight line passage. The dynamic response of a double-beam system traversed by a constant moving load was studied in [1]. The authors explored the effects of the moving speed of the load and the damping and stiffness of the viscoelastic layer on the deflections of the beams.

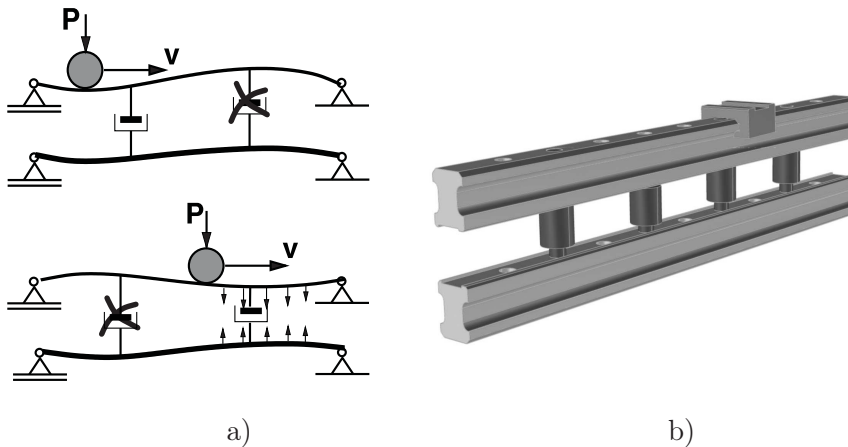


**Figure 4.2.** Semi-active linear guideway: a) principle of acting, b) real view.

## 4.2. Finite Horizon Optimal Control Problem

Most of the optimal processes in mechanical systems are performed by resolving the finite time horizon optimal control problems. These problems are repeated sequentially and the solutions are implemented through the receding horizon scheme (briefly presented in Subsec. 4.5). This technique enables to take into account change of both, model parameters and boundary conditions. Since the control inputs are bounded (the bounds are characterised by the specification of the actuators and the controlled dampers), the system is not fully controllable, and thus the optimal control problems are formulated with free-endpoint state. The methodology presented in this chapter is based on the assumption that a mechanical system is described by a set of the first order Ordinary Differential Equations (ODE). For the distributed parameter systems, the ODE representation is derived according to the methods presented within the previous chapter.

Throughout this chapter, we will use the following notation:

$x = [x_1(t), x_2(t), \dots, x_n(t)]^\top \in \mathbb{R}^n$  – state of the system with the initial state  $x(0) = x_0$  (in the numerical examples, the state will be represented by the vector  $y$ ),

$u = [u_1(t), u_2(t), \dots, u_m(t)]^\top \in \mathcal{U} \subset \mathbb{R}^m$  – set of bounded controlled inputs, where  $\mathcal{U}$  is the set of admissible controls,

$f(x, u)$  – a continuous function describing the system dynamics,

$f_0(x, u)$  – a continuous function describing the control objective,

$J$  – objective function.

Consider a dynamical system represented by

$$\dot{x}(t) = f(x(t), u(t)), \quad x(0) = x_0, \quad u \in \mathcal{U}. \quad (4.1)$$

The free-endpoint finite time horizon optimal control problem is formulated as follows

### Problem 4.1 Finite time horizon optimal control problem

$$\begin{aligned} \text{Find } u^* &= \operatorname{argmin}_{u \in \mathcal{U}} J = \int_0^{t_f} f_0(x, u) dt & (4.2) \\ \text{under } \dot{x}(t) &= f(x(t), u(t)), \quad x(0) = x_0. \end{aligned}$$

Here the set  $\mathcal{U}$  is bounded by the minimum and maximum admissible values ( $u_{\min}$  and  $u_{\max}$ ) related to the specification of the controlling device. In the case of the active control, the bounds are usually symmetrical, i.e.,  $-u_{\min} = u_{\max}$ . For the semi-active systems, both values are non-negative. The time horizon  $t_f$  can take into account the whole process or the cycle time, if the process is periodic.

For the objective function, the most common in use are based on the following norms:

$f_0(x, u) = \|x\|_Q^2 = x^\top Q x$  – with positive semi-definite matrix  $Q$ , if the goal is to minimize the vibration levels,

$f_0(x, u) = \|x - x_d\|^2$  – if the goal is to track a desired trajectory  $x_d$ .

The existence of the optimal control  $u^*$  can be verified by means of the classical Weierstrass Theorem [49]. The theorem states that any continuous function described on a compact domain takes its minimum and maximum value. For the Problem 4.1, the existence of the minimizer  $u^*$  is not fully provided by the continuity of  $J$  and the compactness of  $\mathcal{U}$ . Instead of the compactness of  $\mathcal{U}$ , it is required that compact is the set of points reachable from  $x_0$  using controls that take values in  $\mathcal{U}$  [26]. For nonlinear systems, explicit computation of reachable sets is usually not feasible. Instead, we can rely on the Filippov's theorem [16] which states that the reachable set for (4.1) is compact if the set  $\{f(x, u) : u \in \mathcal{U}\}$  is compact and convex.

### 4.2.1. First Order Necessary Optimality Condition

In this section, we will derive the first order necessary optimality condition for the Problem 4.1. The derivation will be carried out by using the calculus of variations. In the sequel, the definition of the functional derivative will be given. Based on the functional derivative, the steepest descent method to determine the optimiser  $u^*$  will be presented.

Let us consider the function  $J$  as defined in (4.2). For every control  $u$ , we have:

$$J(u + \delta u) - J(u) = \delta J(u)\delta u + r_J(u, \delta u). \quad (4.3)$$

Here,  $\delta u$  and  $\delta J$  stands for the first variation of control and objective function, respectively, and  $r_J(u, \delta u) = o(\delta u)$ , i.e.:  $r_J(u, \delta u)/\|\delta u\| \rightarrow 0$  as  $\|\delta u\| \rightarrow 0$ . The first order necessary condition for optimality of  $u = u^*$  is that the first variation of the objective function is equal to zero

$$\delta J(u) = 0. \quad (4.4)$$

To represent the condition (4.4) for the Problem 4.1, we first introduce the adjoint state  $p$ , and then rewrite the objective function as follows

$$J = \int_0^{t_f} (f_0 + p^\top (\dot{x} - f)) dt, \quad (4.5)$$

Next, we introduce the Hamiltonian of the following form

$$H(x, p, u) = p^\top f(x, u) - f_0(x, u). \quad (4.6)$$

Then, the objective function is represented by:

$$J = \int_0^{t_f} (p^\top \dot{x} - H) dt. \quad (4.7)$$

Infinitesimal change  $\delta u$  causes the variations of the functions  $\delta x$ ,  $\delta \dot{x}$ ,  $\delta p$ . This results in the following increment of the objective function

$$\delta J \delta u = \int_0^{t_f} \left\{ -\frac{\partial H}{\partial u} \delta u - \left( \frac{\partial H}{\partial x} \right)^\top \delta x + p^\top \delta \dot{x} + \left( \dot{x} - \frac{\partial H}{\partial p} \right)^\top \delta p \right\} dt. \quad (4.8)$$

Since

$$\frac{\partial H}{\partial p} = f(x, u), \quad (4.9)$$

the last term in (4.8) vanishes. Now, under the assumption

$$\delta \dot{x} = \frac{d}{dt} (\delta x), \quad (4.10)$$

the integration by parts yields

$$\delta J \delta u = \int_0^{t_f} -\frac{\partial H}{\partial u} \delta u dt - \int_0^{t_f} \left( \dot{p} + \frac{\partial H}{\partial x} \right)^\top \delta x dt + [p^\top \delta x]_0^{t_f}. \quad (4.11)$$

Respecting the fact that the state trajectory is fixed at the boundary condition, i.e.:  $\delta x(0) = 0$  and by setting

$$\dot{p} = -\frac{\partial H}{\partial x}, \quad p(t_f) = 0, \quad (4.12)$$

we finally get

$$\delta J \delta u = \int_0^{t_f} -\frac{\partial H}{\partial u} \delta u dt. \quad (4.13)$$

Summarising, the first order necessary optimality condition for the Problem 4.1 is written as follows

$$\begin{aligned} \frac{\partial H}{\partial u} &= 0, & H &= p^\top f - f_0, \\ \dot{x} &= \frac{\partial H}{\partial p}, & x(0) &= x_0, \\ \dot{p} &= -\frac{\partial H}{\partial x} & p(t_f) &= 0. \end{aligned} \quad (4.14)$$

The condition (4.14) can be effectively used only in the cases where the Problem 4.1 is stated with  $H$  being smooth enough, i.e. where  $\partial H/\partial u = 0$  leads to a control that is explicitly given as a function of state and/or adjoint state. The example of such a case is the Linear Quadratic Regulator problem, briefly studied in the next section. For more general optimal control problems, one should consider a generalized necessary optimality condition formulated by Pontryagin [40].

**Theorem 4.2.1 Pontryagin Maximum Principle, L. S. Pontryagin, 1962.**

*Assume  $u^*$  is optimal control and  $x^*$  is the corresponding trajectory. Then, there exists a function  $p^*$  such that*

$$\dot{x}^* = \frac{\partial H}{\partial p}, \quad (4.15)$$

$$\dot{p}^* = -\frac{\partial H}{\partial x}, \quad (4.16)$$

and

$$H(x^*, p^*, u^*) = \max_{u \in \mathcal{U}} H(x^*, p^*, u), \quad t \in [0, t_f]. \quad (4.17)$$

*In addition,*

$$\text{the mapping } t \rightarrow H(x^*, p^*, u^*) \text{ is constant.} \quad (4.18)$$

*Finally, we have the terminal condition*

$$p^*(t_f) = 0. \quad (4.19)$$

For proofs see, for example, [2, 15, 29].

### 4.2.2. Solution Methods

As demonstrated in (4.14), the optimality condition consists of the Two Point Boundary Value Problem. To solve this problem, the shooting [48] and the relaxation [41] methods can be applied. In the shooting method, the idea would be to find the initial condition for the adjoint state such that its terminal condition is fulfilled. The usual methods for finding roots may be employed here, such as the bisection method or the Newton's method. Relaxation method implements another approach. The time domain is represented as a set of points creating mesh. The dynamical equations are transformed into the finite difference equations. An iterative procedure is adjusting all the state and adjoint state values on the mesh to bring them into successively closer agreement with the finite-difference equations together with the boundary conditions. In many cases, shooting and relaxation methods are combined together. Both methods exhibit good performance in the case of low dimensional problems excluding solutions that are highly oscillatory or not smooth.

To solve the necessary optimality condition, we can also employ a wide range of gradient based methods. Below, we will give a solution procedure based on the method of steepest descent. Before we do it, we will now define the gradient for the Problem 4.1. From (4.13) we have

$$\delta J = \int_0^{t_f} -\frac{\partial H}{\partial u} dt. \quad (4.20)$$

The first variation  $\delta J$  is the quantity that carries the information on how the function changes, when the whole control trajectory changes by a small amount. To derive the gradient, we need to extract the information on how the functional changes, when the control value at any given time  $\tau \in [0, t_f]$  changes by a small amount. The gradient corresponding to time  $\tau$  denoted by  $\nabla_{u(\tau)} J$  can be computed as follows

$$\nabla_{u(\tau)} J = \int_0^{t_f} -\frac{\partial H}{\partial u} \delta(t - \tau) dt. \quad (4.21)$$

Here  $\delta(\cdot)$  is the Dirac delta function. From (4.21), we conclude that

$$\nabla_{u(\tau)} J = -\frac{\partial H}{\partial u} \Big|_{t=\tau}. \quad (4.22)$$

To solve the Problem 4.1, one can follow the following steps

**Procedure 4.1 Steepest descent method for the Problem 4.1**

- Step 1 Initialize:  $u^* = u_{ini}$  and assume  $\epsilon$  as small positive number.
- Step 2 Solve the state Eq. (4.1) by substituting:  $u = u^*$ .
- Step 3 Solve the adjoint state Eq. (4.12) by backward integration. Use  $u = u^*$  and the corresponding state.
- Step 4 Compute the descent directions:  $-\nabla_u J = \frac{\partial H}{\partial u} \Big|_{t=\tau}$ .
- Step 5 Update the control values:  $u^*(\tau) = u^*(\tau) - \lambda \nabla_{u(\tau)} J$ . Here the step size  $\lambda > 0$  is taken such to provide that  $u^* \in \mathcal{U}$ . Optionally perform the line search by solving the problem:  
 $\lambda^* = \arg \min_{\lambda} J(u^*(\tau) - \lambda \nabla_{u(\tau)} J)$  and update the control values by setting  $\lambda = \lambda^*$ .
- Step 6 Repeat Steps 2–5 until the terminal condition is met:  
 $\|\nabla_{u(\tau)} J\| < \epsilon$ .

The necessary optimality condition results in  $u^*$  being a local minimizer. If the structure of the objective  $J$  is not well identified, then it may be essential to run the Procedure 4.1 under different initial control guesses. That test is commonly used to justify whether the solution is global or only local minimizer. To guarantee that the necessary condition results in a global minimizer, one should consider a convex objective  $J$  over a convex set  $\mathcal{U}$ . A typical example of a convex optimal control problem is the Linear Quadratic Regulator problem. Its finite time horizon version is stated as follows

**Problem 4.2 Finite horizon Linear Quadratic Regulator problem**

$$\text{Find } u^* = \operatorname{argmin} J = \frac{1}{2} \int_0^{t_f} x^\top Q x + u^\top R u \, dt \quad (4.23)$$

under  $\dot{x} = Ax + Bu, \quad x(0) = x_0.$

Here the set of admissible control is unbounded, the symmetric matrices  $Q$  and  $R$  are assumed to be positive semi-definite and positive definite, respectively. The necessary optimality condition (4.14) results as follows:

$$\begin{aligned}
u &= R^{-1} B^\top p, \\
\dot{x} &= Ax + Bu, \quad x(0) = x_0, \\
\dot{p} &= -A^\top p + Qx, \quad p(t_f) = 0.
\end{aligned} \tag{4.24}$$

By defining  $K(t) : K(t_f) = 0$  and setting

$$p(t) = -K(t)x(t), \quad \text{for all } t \in [0, t_f], \tag{4.25}$$

the adjoint state equation takes the form

$$\dot{p} = A^\top Kx + Qx. \tag{4.26}$$

The control is rewritten as

$$u = -R^{-1} B^\top Kx. \tag{4.27}$$

From (4.25) we know that

$$\dot{p} = -\dot{K}x - K\dot{x}. \tag{4.28}$$

Combining (4.26), (4.28), the state equation and (4.27), we can compute the matrix  $K$  by backward integration of

$$A^\top K + KA - KBR^{-1}B^\top K + Q = -\dot{K}, \quad K(t_f) = 0, \tag{4.29}$$

referred as the Riccati differential equation. Identical result can be derived by using Bellman's Principle of Optimality (see, for instance, [15]).

### 4.3. Optimal Control Problem for Switched Systems

Wide group of controlled vibrating systems can be described by switched systems. As an example, we can consider a structure equipped with smart materials allowing for change of the damping or stiffness parameter between a finite set of values. Each change results in the switch of the right hand side of the system dynamics (4.1). In this section, we will discuss the finite horizon problem under the governing equation given as a discrete time switched dynamical system. We will discuss solution methodology with the emphasis on the computational difficulties, due to the switching system structure.

The finite time horizon optimal control problem for a switched system can be written as follows

**Problem 4.3 Finite horizon optimal control problem for switched system**

$$\begin{aligned} \text{Find } u^* = \operatorname{argmin}_{u \in \mathcal{U}} J &= \sum_{k=0}^{k=t_f} f_0(x(k), u(k)) \Delta t & (4.30) \\ \text{under } x(k+1) &= x(k) + \Delta t f_s(x(k), u(k), k), \quad x(0) = x_0. \end{aligned}$$

Here  $f_s$  is a switched function ( $s$  represents a switched parameter) that appears in the number of modes that results from all admissible values of the switched parameter. For simplicity, let us assume that the governing equation is given in the autonomous form, i.e., its right hand side function does not depend explicitly on time. This form can be derived by extending the state vector with the component representing time, i.e., by introducing

$$x_{\text{ext}}(k+1) = x_{\text{ext}}(k) + 1, \quad x_{\text{ext}}(0) = 0. \quad (4.31)$$

Then, the boundary conditions being represented by time series can be approximated by relevant functions of this state component. By using the extended state vector  $\bar{x} = [x, x_{\text{ext}}]^\top$  and the extended right hand side function  $\bar{f}_s = [f_s, 1]^\top$ , we can rewrite the dynamical equation in the Problem 4.3 as follows

$$\bar{x}(k+1) = \bar{x}(k) + \Delta t \bar{f}_s(\bar{x}(k), u(k)), \quad \bar{x}(k=0) = [x_0, 0]^\top. \quad (4.32)$$

There exists a variety of methods for solving the problems of optimal control of switched systems. Some of them can be applied to generally stated problems like the Problem 4.3, but the most efficient are those dedicated to certain groups of problems, where, for instance, a sequence of switched modes does not depend on the control decision and can be precisely identified. Several computational algorithms for optimization of continuous time switched systems are compared in [9]. A general study on the existence of optimal control for switched systems is presented in [8]. Depending on the length of the time horizon and the expected system behaviour, one can adopt a relevant switched system optimization techniques. For the system where the switched parameter is not a decision parameter (it depends on the state and the control), the methods based on the Maximum Principle (for example, [36] and [50]) can be employed. For more general problems of optimal control of switched systems (under non-determined switching sequence)

a suboptimal solution was proposed in [46]. In the case of piecewise-affine systems and quadratic objective functions, the method based on solving the Hamilton-Jacobi-Bellman equation was developed in [44]. In the most general cases, an optimal control problem for a switched system can be formulated as a mixed-integer programming problem [34].

#### 4.4. Distributed Optimal Control via Nash Games

In recent years, distributed controllers have attracted a special attention from the practising engineers. A good number of mechanical systems can be represented as a set of modules. The functionality and incorporated computational procedures for every module is the same. It computes its optimal decision by using local state information and necessary information arriving from other controllers. The global time consuming optimisation problem is then divided into local problems of reduced size that can be solved on-line. Modular control architectures are very convenient for system assembling and maintenance. In the case of a failure, only the malfunctioning module needs to be replaced. In addition, a decentralisation plays an important role for safety. Suppose a malfunction of the central computer computing the optimal decision for every controller. An incorrect signal is then sent to whole control system that may drive the structure to dangerous states. In distributed control architectures, this risk is reduced to local failures.

In this section, we will formulate a non-cooperative Nash game problem. The goal is to demonstrate that for a wide group of mechanical systems this formulation allows on solving an optimisation problem in a distributed manner. In particular, the Nash game approach can be effectively applied to the systems exhibiting wave-like solutions, for instance, vibrating strings. For such systems, we can define a set of interconnected subsystems (that, for instance, may be related to controlled string sections) that are involved in the Nash game problem. A consensus set of optimal decisions taken by each of the subsystems is the solution of the Nash game, and it is referred as the Nash equilibrium. A distributed controller's architecture required for solving the Nash game problem is strictly dependent on the system interconnectivity that may be represented by graph. In this section, we will be particularly interested in the systems that are interconnected through the line graphs that represent a wide class of the systems governed by partial differential equations of hyperbolic type.

Let us consider again the Problem 4.1. In the general case, where the objective function depends on the whole state vector and the system dynamics is not separable, the solution is performed through a centralised controller's architecture. By using decomposition methods, the problem can be solved in a distributed manner only under some special structures of the system and the objective function (see, for example, [42] and [43]). An alternative method for distributed optimisation is to solve a corresponding Nash game discussed below.

Let us consider a set of subsystems  $\{S_j\}$ , each with one control input  $u_j$  and its controllable state vector  $x^j$ . For each of the subsystems we associate the objective  $J_j$ . The subsystems are interconnected, and thus  $J_j$  may be also affected by some of the other control inputs. Consider the system interconnected according to the directed graph as depicted in Fig. 4.3. An arrow from  $S_i$  to  $S_j$  indicates that subsystem  $S_i$  affects subsystem  $S_j$ . In this case, we have the following objective dependencies

$$J_1(u_1), \quad J_2(u_2, \overbrace{\{u_1, u_3, u_4\}}^{u_{-2}}), \quad J_3(u_3, \overbrace{\{u_1, u_4\}}^{u_{-3}}), \quad J_4(u_4, \overbrace{\{u_1, u_3\}}^{u_{-4}}). \quad (4.33)$$

Here by  $u_{-j}$  we denote the set of control decisions except  $u_j$  that affects the objective  $J_j$ . Note that  $u_i \in u_{-j}$ , if there is a directed path from  $S_i$  to  $S_j$  in the interconnectivity graph. Under the introduced setting, the non-cooperative Nash game problem is stated as follows.

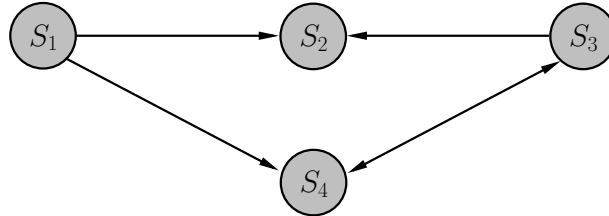


**Figure 4.3.** A generic interconnectivity graph. An arrow from  $S_i$  to  $S_j$  indicates that subsystem  $S_i$  affects subsystem  $S_j$ .

#### Problem 4.4 Non-cooperative Nash game

$$\text{Find } \{u_j^*\} \text{ such that } \forall j: u_j^* = \operatorname{argmin} J_j(u_j, u_{-j}^*). \quad (4.34)$$

The set of decisions  $\{u_j^*\}$  is called the Nash Equilibrium and this is the strategy such that no unilateral deviation in decision by any single player

is profitable for that player. For extensive studies on the Nash equilibrium solution concept a reader is referred to [3]. To guarantee that the Nash equilibrium exists, every objective function  $J_j$  needs to be continuous in all its arguments and strictly convex in  $u_j$ .

To demonstrate that the Nash equilibrium search for the system represented by Fig. 4.3 can be resolved in a distributed manner, let us now write the solution procedure:

**Procedure 4.2 Solution of the Nash game for the system depicted in Fig. 4.3**

- Step 1 Guess  $u_4^*$  and assume  $\epsilon_2, \epsilon_3, \epsilon_4$  as small positive numbers.
- Step 2 Find  $u_1^* = \operatorname{argmin} J_1(u_1)$  and send the solution to  $S_2$  and  $S_4$ .  
 $S_4$  conveys the solution to  $S_3$ .
- Step 3 Find  $u_3^* = \operatorname{argmin} J_3(u_3, \{u_1^*, u_4^*\})$  and send the solution to  $S_2$  and  $S_4$ .
- Step 4 Find  $u_2^* = \operatorname{argmin} J_2(u_2, \{u_1^*, u_3^*, u_4^*\})$ .
- Step 5 Find  $u_4^* = \operatorname{argmin} J_4(u_4, \{u_1^*, u_3^*\})$  and send the solution to  $S_3$ .  
 $S_3$  conveys the solution to  $S_2$ .
- Step 6 Repeat Steps 3–5 until  $\Delta\|J_2\| < \epsilon_2, \Delta\|J_3\| < \epsilon_3, \Delta\|J_4\| < \epsilon_4$   
 ( $\Delta\|J_j\|$  stands for incremental change of norm of the objective function  $J_j$ ).

The communication required to perform the Procedure 4.2 is that of sending and conveying the optimal decisions in the Steps 2, 3 and 5. It is easy to verify that the topology of this communication follows the system interconnectivity.

Let us now consider the systems, where the interconnectivity is represented by the line graphs as shown in Fig. 4.4. In these cases, we have the following objective dependencies

$$\begin{aligned}
 \text{case a: } & J_1(u_1), \quad J_2(u_2, \overbrace{\{u_1\}}^{u_{-2}}), \quad J_3(u_3, \overbrace{\{u_1, u_2\}}^{u_{-3}}), \quad J_4(u_4, \overbrace{\{u_1, u_2, u_3\}}^{u_{-4}}), \\
 \text{case b: } & J_1(u_1), \quad J_2(u_2, \overbrace{\{u_1, u_3, u_4\}}^{u_{-2}}), \quad J_3(u_3, \overbrace{\{u_1, u_2, u_4\}}^{u_{-3}}), \quad J_4(u_4).
 \end{aligned} \tag{4.35}$$

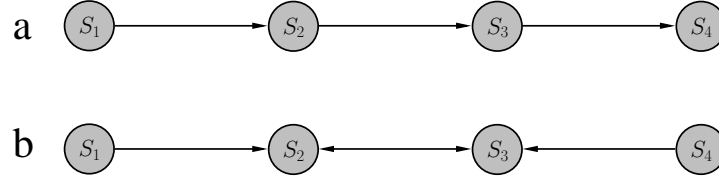


**Figure 4.4.** Line graphs representing system interconnectivity. An arrow from  $S_i$  to  $S_j$  indicates that subsystem  $S_i$  affects subsystem  $S_j$ .

To solve the corresponding Nash games, one can execute the following procedures

**Procedure 4.3a Solution of the Nash game for the system depicted in Fig. 4.4a**

- Step 1 Find  $u_1^* = \operatorname{argmin} J_1(u_1)$  and send the solution to  $S_2$ .  $S_2$  conveys the solution to  $S_3$  and  $S_3$  conveys the solution to  $S_4$ .
- Step 2 Find  $u_2^* = \operatorname{argmin} J_2(u_2, \{u_1^*\})$  and send the solution to  $S_3$ .  $S_3$  conveys the solution to  $S_4$ .
- Step 3 Find  $u_3^* = \operatorname{argmin} J_3(u_3, \{u_1^*, u_2^*\})$  and send the solution to  $S_4$ .
- Step 4 Find  $u_4^* = \operatorname{argmin} J_4(u_4, \{u_1^*, u_2^*, u_3^*\})$ .

**Procedure 4.3b Solution of the Nash game for the system depicted in Fig. 4.4b**

- Step 1 Guess  $u_3^*$  and assume  $\epsilon_2, \epsilon_3$  as small positive numbers.
- Step 2 Find  $u_1^* = \operatorname{argmin} J_1(u_1)$  and send the solution to  $S_2$ .  $S_2$  conveys the solution to  $S_3$ . Find  $u_4^* = \operatorname{argmin} J_4(u_4)$  and send the solution to  $S_3$ .  $S_3$  conveys this solution to  $S_2$ .
- Step 3 Find  $u_2^* = \operatorname{argmin} J_2(u_2, \{u_1^*, u_3^*, u_4^*\})$  and send the solution to  $S_3$ .
- Step 4 Find  $u_3^* = \operatorname{argmin} J_3(u_3, \{u_1^*, u_2^*, u_4^*\})$  and send the solution to  $S_2$ .
- Step 5 Repeat Steps 3 and 4 and until  $\Delta \|J_2\| < \epsilon_2, \Delta \|J_3\| < \epsilon_3$ .

By analysing the Procedures 4.3a and 4.3b we can observe that the systems represented by the line graphs require much less iterative processes during the Nash equilibrium search. In particular, if a decision may be transferred in only one direction (case a from Fig. 4.4), then the game can be solved without any iterative loops. For such cases, the optimisation can be performed in the real-time over large scale systems.

## 4.5. Receding Horizon Control Scheme

The efficiency of the optimal controllers is highly dependent on the knowledge of the optimised system. For the best performance, it is required to have well developed mathematical model together with precisely estimated parameters and boundary conditions. In the case of the finite horizon optimisation, this requirements must be met at least within a considered time horizon. In the systems subjected to rapidly changing external excitation (for instance, a bridge under travelling vehicles or a building subjected to an earthquake), a precise prediction of the model parameters and the boundary conditions is not feasible. Thus, the most reliable for optimisation is a method that allows on a permanent model update. This method is the receding horizon control, often referred also as the model predictive control (see, for example, [11]).

The receding horizon control method is formulated as a finite horizon optimisation to be repeated on-line. The basic principle of the method is demonstrated in Fig. 4.5. Based on the measured (or estimated) current state and the predicted evolution of the exogenous signals, the controller

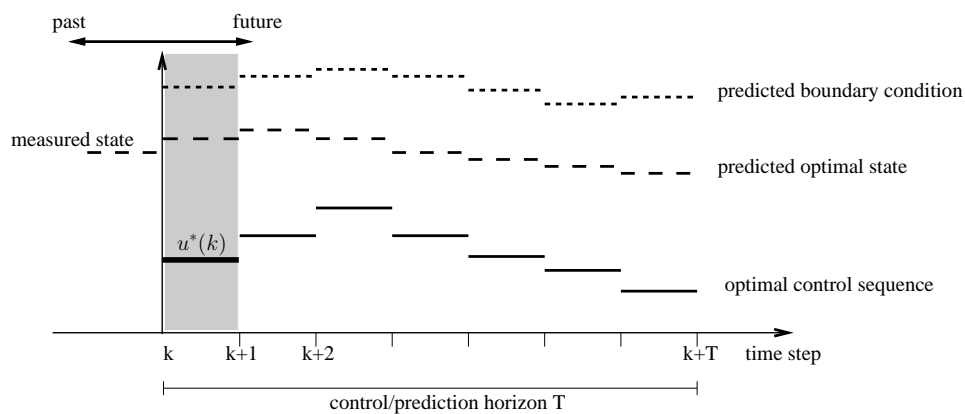


**Figure 4.5.** Principle of the receding horizon control scheme.

determines the optimal input over the control/prediction horizon. From the sequence of the optimal decisions, only the first one is applied to a system, while for the next time sample the procedure is repeated. A fundamental theory underlying the receding control scheme is the Bellman's Principle of Optimality [5] which states that: "An optimal policy has the property that whatever the initial state and initial decision are, the remaining decisions must constitute an optimal policy with regard to the state resulting from the first decision". In case of the completely deterministic systems, it can be verified that the solution of the receding horizon method is equivalent to the one obtained by using computationally heavy dynamic programming. Thus, one of the major ideas behind the receding horizon method is to determine an optimal feedback controller by performing an open-loop optimisation. The receding horizon control scheme is commonly executed with the following steps

#### **Procedure 4.4 Receding horizon control**

- Step 1 At time sample  $k$ , estimate the state  $x(k)$  and predict the evolution of the model parameters and the boundary conditions in the time period  $[k, k + T]$ .
- Step 2 Solve a finite time optimal control problem over the time period  $[k, k + T]$ .
- Step 3 Apply the optimal decision  $u^*(k)$ .
- Step 4 Increment time sample  $k = k + 1$  and continue with Step 1.

## **4.6. Optimal Control Problem for Semi-Active Systems**

There is a special group of control systems which are linear in both state space and control functions. This group is called bilinear systems and it is in the special interest of this work, due to the fact that they represent the models for semi-active controlled systems. One of the pioneers that worked on the topic of control of bilinear systems is R. R. Mohler. He began and promoted the application of optimal control methods to bilinear systems, beginning with his study of nuclear power plants in the 1960s. His work is reported in the books [30–32]. Mohler presents the problems of optimal control of bilinear systems from the perspective of engineering,

ecology and physiology. A survey on optimal control of bilinear models for pest population control was presented by Lee in [25].

In the dynamics of mechanical systems, the bilinear terms occur as the products of the state vector and variable stiffness or damping functions. Throughout the rest of this chapter, we will consider the bilinear control systems formulated as follows:

$$\dot{x}(t) = f(x, u) = Ax(t) + \sum_{i=1}^m u_i(t)B_i x(t) + \tilde{f}(x). \quad (4.36)$$

Here  $A$  and  $B_i$ ,  $i = 1, 2, \dots, m$  are constant matrices. The excitation vector  $\tilde{f}(x)$  denotes external forces acting on the system. The control functions  $u_i$  stand for variable parameters of mechanical system. For the practical reason these variables are bounded to the specified interval so the admissible values of input vector are limited to hypercube as follows

$$u(t) \in \Omega = [u_{\min}, u_{\max}]^m = \{\omega \in \mathbb{R}^m : u_{\min} \leq \omega_i \leq u_{\max}, i = 1, \dots, m\}. \quad (4.37)$$

Again, the objective function to be minimized is

$$J = \int_0^{t_f} f_0(x, u) dt. \quad (4.38)$$

In many applications, it is desired to find the control that steers the system (4.36) from an initial state  $x(0) = x_0$  to some terminal state  $x(t_f) = x_f$  such to minimise (4.38) with an admissible control (4.37). In general, this problem may have no solution due to lack of controllability, especially in the case of bilinear systems driven by bounded controls.

The widespread Linear Quadratic Regulator approach can be applied for bilinear systems. By introducing a quadratic performance index

$$J = \frac{1}{2} \int_0^{t_f} (x^\top Q x + r u^2) dt + \frac{1}{2} x^\top(t_f) P_f x(t_f), \quad (4.39)$$

it can be shown that for the system

$$\dot{x}(t) = Ax(t) + Bu(t)x(t) + bu(t) \quad (4.40)$$

there exists an optimal feedback controller, and it can be computed as a limit of the following sequence

$$u^{k+1}(t) = r^{-1} \left[ Bx^{k+1}(t) + b \right]^\top K^{k+1}(t) x^{k+1}(t). \quad (4.41)$$

Here  $K^{k+1}$  is the solution of the differential Riccati equation (for details see [21]). A key reason for using feedback is to reduce the effects of uncertainty which may appear in different forms as disturbances or imperfections in models. However, the iterative method that produces the feedback control (4.41) requires a fast computing controller. Moreover, the method is limited to particular form of the objective function (4.39). For more general problems we can compute the optimal controls by applying the first order necessary optimality condition given in the following section.

#### 4.6.1. Necessary Optimality Condition

In this section, we will discuss the impact of the Pontryagin Maximum Principle when applied to the following bilinear control problem:

##### Problem 4.5 Optimal control problem for bilinear system

$$\begin{aligned} \text{Find } u^* &= \operatorname{argmin} J = \int_0^{t_f} f_0(x) dt, \\ \text{under } \dot{x}(t) &= Ax(t) + \sum_{i=1}^m u_i(t) B_i x(t) + \tilde{f}(x), \quad x(0) = 0, \\ u(t) &\in \Omega. \end{aligned} \quad (4.42)$$

While the objective function is given as explicitly independent on control, we can easily derive the optimal controls. Hamiltonian for the Problem 4.5 is of the following form

$$H(x, p, u) = p^\top(t) \left( Ax(t) + \sum_{i=1}^m u_i(t) B_i x(t) + \tilde{f}(x) \right) - f_0(x). \quad (4.43)$$

Thus, as a result of the Pontryagin Maximum Principle optimal control functions are bang-bang type

$$u_i^*(t) = \begin{cases} u_{\max}, & p^\top(t) B_i x(t) > 0 \\ u_{\min}, & p^\top(t) B_i x(t) < 0 \end{cases}, \quad (4.44)$$

where

$$\dot{p}(t) = -\frac{\partial H}{\partial x}, \quad p(t_f) = 0. \quad (4.45)$$

**Remark:** We do not consider singular cases by assuming that the set of instants  $t$  such that  $p^\top(t) B_i x(t) = 0$  is a null set.

### 4.6.2. Prediction of Switches in Optimal Controls

In general, for multidimensional problem it is difficult to predict the structure of the solutions of (4.44). We are not able to predict whether the switches occur, i.e., if there exists an instant  $t$  such as the term  $p^\top(t) B_i x(t)$  changes its sign. In mechanical systems, where the damping coefficient is the parameter to be controlled and the objective is to dissipate the energy in the optimal sense, in some cases we can suspect that the best performance is exhibited by the system steered by a constant maximum value control. So when can we expect the optimal switching control? To answer this question let us consider the system (4.36) with  $m = 1$  for simplicity, that is

$$\dot{x} = Ax + uBx + \tilde{f}(x), \quad (4.46)$$

with the adjoint system

$$\dot{p} = -\frac{\partial H(x, p, u)}{\partial x}. \quad (4.47)$$

We propose the following theorem that states sufficient condition for the existence of the control  $u^* \neq u_{\max}$  that results in more beneficial value of the objective function given by (4.42).

**Theorem 4.6.1** *Let  $x_{u_{\max}}(t)$  and  $p_{u_{\max}}(t)$  be the solutions of the state (4.46) and the adjoint state (4.47) equations when the following constant control function is given  $u(t) = u_{\max}$ . If there exists an interval  $[t_1, t_2] \subseteq [0, t_f]$  such that for all  $t \in [t_1, t_2]$  we have  $(p_{u_{\max}}^\top(t) B x_{u_{\max}}(t)) < 0$ , then there also exists a control  $u^* \in \Omega$ ,  $u^* \neq u_{\max}$  such that  $J(u^*) < J(u_{\max})$ .*

**Proof** Let  $u^* = u_{\max} + \delta u$ . Then, we can write the differential of the cost function in the following form:

$$J(u_{\max} + \delta u) - J(u_{\max}) = \delta J(u_{\max})(\delta u) + r_J(u_{\max}, \delta u), \quad (4.48)$$

where  $\delta J(u_{\max})(\delta u)$  is first variation of the function  $J(u_{\max})$  and  $r_J(u_{\max}, \delta u) = o(\delta u)$ , i.e.,  $r_J(u_{\max}, \delta u)/\|\delta u\| \rightarrow 0$  as  $\|\delta u\| \rightarrow 0$ . For a sufficiently small  $\delta u$  the sign of the right hand side of (4.48) depends on the sign of the variation. Therefore, we need to prove that  $\delta J(u_{\max})(\delta u) < 0$ .

$$J = \int_0^{t_f} [f_0(x) + p^\top (\dot{x} - f)] dt, \quad (4.49)$$

where  $p = p(t) : [0, t_f] \rightarrow \mathbb{R}^n$  is the adjoint state. We introduce Hamiltonian of the standard form

$$H : \mathbb{R}^n \times \mathbb{R}^n \times \Omega \rightarrow \mathbb{R}, \quad H(x, p, u) = p^\top f - f_0(x), \quad (4.50)$$

$$J = \int_0^{t_f} (p^\top \dot{x} - H) dt. \quad (4.51)$$

Infinitesimal change  $\delta u$  causes variations of the functions  $\delta x(t)$ ,  $\delta \dot{x}(t)$ ,  $\delta p(t)$ . This results in the following variation of cost function:

$$\delta J(u)(\delta u) = \int_0^{t_f} \left\{ -\frac{\partial H}{\partial u} \delta u - \left( \frac{\partial H}{\partial x} \right)^\top \delta x + p^\top \delta \dot{x} + \left( \dot{x} - \frac{\partial H}{\partial p} \right)^\top \delta p \right\} dt. \quad (4.52)$$

To fulfill Eq. (4.66), the last term must be equal to zero:  $(\dot{x} - f)^\top \delta p = 0$ . Now, under the assumption  $\delta \dot{x} = \frac{d}{dt}(\delta x)$ , the integration by parts yields

$$\delta J(u)(\delta u) = \int_0^{t_f} -\frac{\partial H}{\partial u} \delta u dt - \int_0^{t_f} \left( \dot{p} + \frac{\partial H}{\partial x} \right)^\top \delta x dt + [p^\top \delta x]_0^{t_f}. \quad (4.53)$$

The second and last term vanishes by setting

$$\dot{p} = -\frac{\partial H}{\partial x}, \quad p(t_f) = 0 \quad (4.54)$$

and respecting the initial boundary condition  $\delta x(0) = 0$ . Then

$$H = p^\top (Ax + uBx + \tilde{f}(x)) - f_0, \quad (4.55)$$

$$\delta J(u)(\delta u) = - \int_0^{t_f} (p^\top Bx) \delta u dt. \quad (4.56)$$

Next, we set the variation of control as follows:

$$\delta u = \begin{cases} 0, & t \in [0, t_1) \\ \epsilon < 0, & t \in [t_1, t_2] \\ 0, & t \in (t_2, t_f]. \end{cases} \quad (4.57)$$

Then  $u^* \in \Omega$ . For such a control we conclude that

$$\begin{aligned} \forall t \in [t_1, t_2] \quad p_{u_{\max}}^\top(t) Bx_{u_{\max}}(t) < 0 &\implies \delta J(u_{\max})(\delta u) = \\ = - \int_{t_1}^{t_2} (p_{u_{\max}}^\top(t) Bx_{u_{\max}}(t)) \epsilon dt < 0. \end{aligned} \quad (4.58)$$

The Theorem 4.6.1 can be easily generalized to the system (4.36).

### 4.6.3. Numerical Example: Optimal Semi-Active Controlled Oscillator (Gradient Based Method)

In this section, we will examine the gradient descent method for one of the most common semi-active optimal control problem. The object under control is an oscillator subjected to harmonic force. As the parameter to be controlled we will take the damping coefficient. The goal is to test the efficiency of the gradient descent method (see Procedure 4.1) in the case of parametric control of the oscillating system and also to provide the comparative results for the method of parametrised switching times that will be presented in Subsec. 4.6.4.

We consider the following optimal control problem

#### Problem 4.6 Optimal control of semi-active oscillator

$$\begin{aligned} \text{Find } u^* = \operatorname{argmin} J &= \int_0^{t_f} \left\{ (y_1)^2 + (y_2)^2 \right\} dt \\ \text{under } \dot{y}_1 &= y_2, \\ \dot{y}_2 &= -ky_1 - uy_2 + P \sin(\omega y_3), \\ \dot{y}_3 &= 1. \end{aligned} \quad (4.59)$$

Here  $u(t) \in [u_{\min}, u_{\max}]$

and  $y(t) = [y_1(t), y_2(t), y_3(t)] \in \mathbb{R}^3$ ,  $y(0) = [1, -1, 0]^\top$ .

The parameters are set as follows:

$$k = 1, \quad P = 5, \quad \omega = 5, \quad u_{\min} = 10^{-5}, \quad u_{\max} = 3.$$

For the sake of application of the Pontryagin Maximum Principle, the system is given in autonomous form, where the last component of the vector state represents time. Here  $f_0$  is chosen as simple quadratic form and its value is related to the total energy of the system. So, the desired goal of the variable damping control is to provide a minimum of the integrand of the energy of the system under excitation in the specified time interval  $[0, t_f]$ . The computations will be carried out for two cases, each with different final time:  $t_f = 0.67$  and  $t_f = 1$ , respectively.

The Hamiltonian for the problem (4.59) is of the form

$$H(y, p, u) = \begin{bmatrix} p_1 \\ p_2 \\ p_3 \end{bmatrix}^\top \begin{bmatrix} y_2 \\ -ky_1 - uy_2 + P \sin(\omega y_3) \\ 1 \end{bmatrix} - (y_1)^2 - (y_2)^2. \quad (4.60)$$

Here, the adjoint system is described by the equations:

$$\begin{aligned}\dot{p}_1 &= kp_2 + 2y_1, \\ \dot{p}_2 &= -p_1 + up_2 + 2y_2, \\ \dot{p}_3 &= -\omega P p_2 \cos(\omega y_3),\end{aligned}\tag{4.61}$$

and it fulfills the terminal condition  $p(t_f) = 0$ . From the Pontryagin Maximum Principle we immediately get the optimal control

$$u^*(t) = \begin{cases} u_{\max}, & p_2 y_2 < 0 \\ u_{\min}, & p_2 y_2 > 0 \end{cases}.\tag{4.62}$$

**Corollary:** The switchings occur whenever  $p_2$  or  $y_2$  change their signs. The number of switchings and instants of switchings can not be predicted by means of the solution (4.62).

Numerical treatment of the Problem 4.6 is based on the Procedure 4.1. Here, the descent direction is

$$-\nabla_u J = \frac{\partial H}{\partial u} = -p_2 y_2.\tag{4.63}$$

The step size is assumed to be constant for every iteration  $\lambda = 1$ . The computations are terminated after performing 500 iterations. The discrete time interval  $[0, t_f]$  is split into 500 equal sub-intervals. We assume the constant control for any of these sub-intervals. The initial control is assumed to be the constant function, set to the maximum value for all sub-intervals  $u_0(t) = u_{\max}, \forall t \in [0, t_f]$ .

**Case 1:**  $t_f = 0.67$

In the first case, the time horizon, after a few attempts, is taken  $t_f = 0.67$ , so to capture at least one switching in the optimal control function. Figure 4.6 depicts the trajectory of this control. A clearly visible point of switching appears as the slope part of the trajectory (in the case of more precise computation the angle of slope approaches  $90^\circ$ ). The switching occurs in the instant when the trajectory of velocity changes the sign, i.e.,  $y_2(t_{switch}) = 0$ . It is shown in Fig. 4.7. On the other hand the trajectory of  $p_2$  (see Fig. 4.8) does not meet the abscissa (apart from the final zero condition). This results in only one switching during the time interval  $(0, t_f)$ . The values of objective function in every iteration are plotted in Fig. 4.9. Note that in the beginning of iterative procedure the initial control was set as  $u(t) = u_{\max}$ . So, we can clearly observe the improvement from constant maximum value control by replacing it with the switching one.

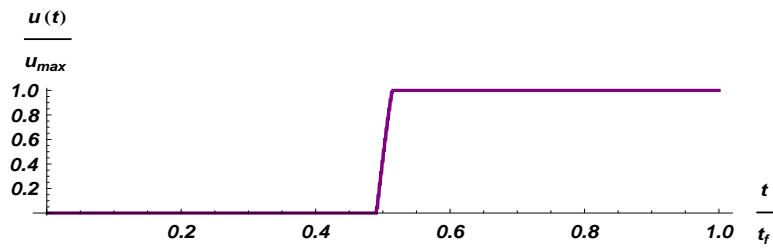


Figure 4.6. Optimized control function – the gradient method.

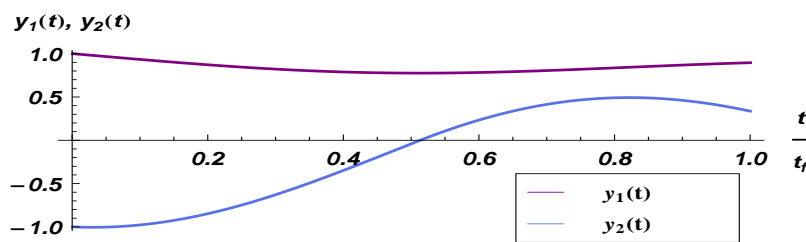


Figure 4.7. Trajectories of the optimised state.

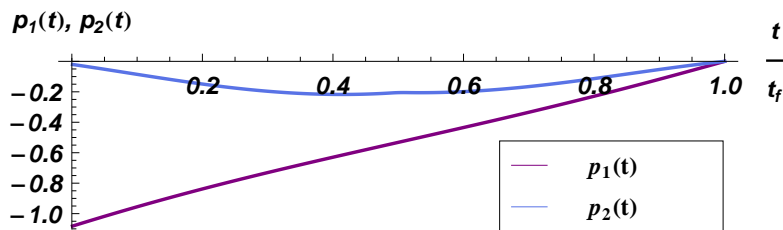


Figure 4.8. Trajectories of the corresponding adjoint state.

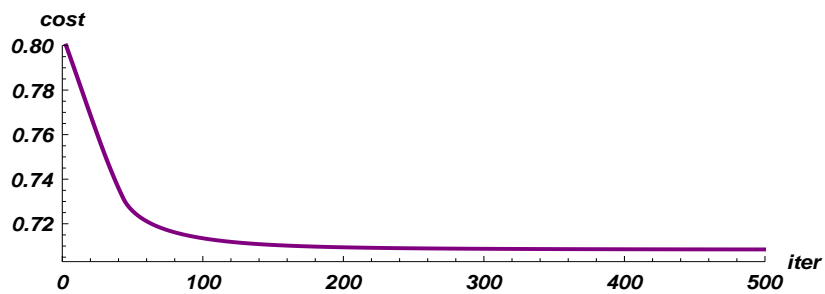
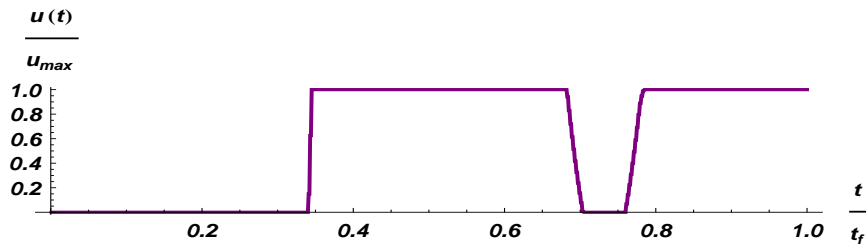


Figure 4.9. Cost function with respect to the number of iteration.

**Case 2:**  $t_f = 1$

In this case, the time interval is assumed to be  $[0, t_f] = [0, 1]$ . It captures three switches in the optimal control function as depicted in Fig. 4.10.



**Figure 4.10.** Optimised control function – the gradient method.

The first and the third switchings are caused by changing the sign of velocity  $y_2$  (Fig. 4.11), while the second one results from the crossing the abscissa by trajectory  $p_2$  (see Fig. 4.12).

In Fig. 4.13, the objective function with respect to number of iteration is presented. The rate of convergence in the presented cases is very satisfactory, even if the line search method is not applied. The computations were performed on the standard PC (Intel Pentium Core 2) and it took less then 180 seconds for any of the presented examples.

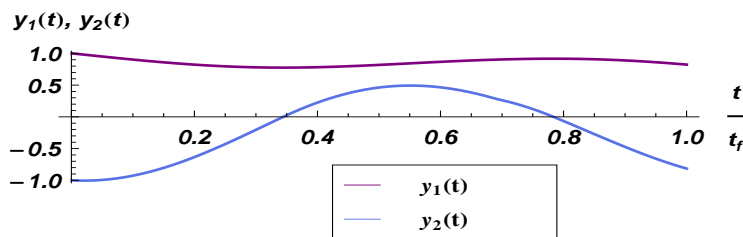


**Figure 4.11.** Trajectories of the optimised state.

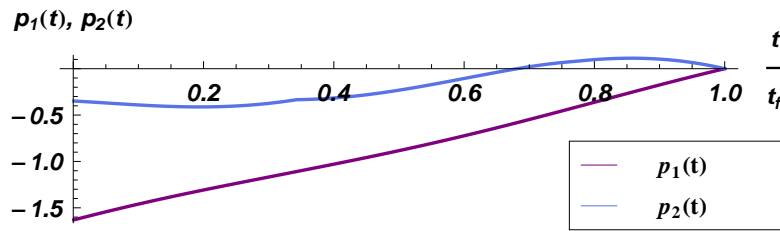


Figure 4.12. Trajectories of the corresponding adjoint state.

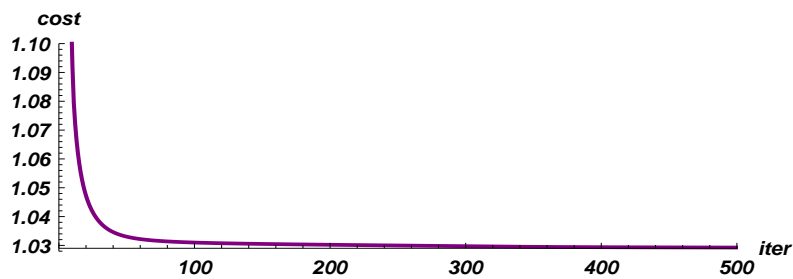


Figure 4.13. Cost function with respect to the number of iteration.

#### 4.6.4. The Method of Parameterized Switching Times

In the example presented in the previous section, we can observe that the numerical results coincide with the theoretical predictions. The postulated switching nature of optimised control is confirmed. In the case of more complex systems, we can expect difficulties in obtaining so accurate, switching shaped, numerical solutions. Increasing precision of calculations is associated with higher dimensional optimisation problem which turns in the rapid extension of time required for computations. There is a need to use more efficient numerical algorithm for computing the optimal switching control solutions. For this purpose, it is very intuitive to parametrise the switching times and reformulate the Problem 4.6. The objective function is now optimised with respect to new parameters – the switching times. In fact, the optimal control problem becomes a nonlinear programming problem, where gradient based optimisation methods can be applied.

In this section, we will develop the method of parametrised switching times which will be based on the derivative of objective function with respect to these times. In calculations, we will use the fundamental facts from the

calculus of variations as well as the property of Dirac delta function. After derivation, the complete numerical algorithm will be given.

We again investigate the bilinear control systems given in autonomous form (the last term of state vector stands for time)

$$\dot{x} = Ax + \sum_{i=1}^m u_i B_i x + \tilde{f}(x). \quad (4.64)$$

For simplicity, let us consider a system driven by only one switching control

$$u = u_{\max} \mathcal{U}(t - \tau), \quad \tau \in [0, t_f]. \quad (4.65)$$

Here,  $\mathcal{U}$  stands for the unit step function. Thus, system (4.64) can be rewritten as follows

$$\dot{x} = f(x, \tau) = Ax + u_{\max} \mathcal{U}(x_n - \tau) Bx + \tilde{f}(x). \quad (4.66)$$

Here, again  $x = x(t) : [0, t_f] \rightarrow \mathbb{R}^n$ ,  $x_n(t) = t$ ,  $f = f(x, \tau) : \mathbb{R}^n \times [0, t_f] \rightarrow \mathbb{R}^n$ . Next, we introduce the objective function to be minimised

$$J = \int_0^{t_f} f_0 dt, \quad (4.67)$$

where  $f_0 = f_0(x) : \mathbb{R}^n \rightarrow \mathbb{R}$  and  $t_f$  is fixed. The objective function subjected to system governed by (4.66) can be rewritten as follows

$$J = \int_0^{t_f} [f_0 + p^\top (\dot{x} - f)] dt. \quad (4.68)$$

where  $p = p(t) : [0, t_f] \rightarrow \mathbb{R}^n$  is the adjoint state. The Hamiltonian for the considered problem is given as follows

$$H : \mathbb{R}^n \times \mathbb{R}^n \times [0, t_f] \rightarrow \mathbb{R}, \quad H(x, p, \tau) = p^\top f - f_0. \quad (4.69)$$

By inserting the Hamiltonian into the formula for the objective function, we obtain

$$J = \int_0^{t_f} (p^\top \dot{x} - H) dt. \quad (4.70)$$

Infinitesimal change  $d\tau$  causes variations of the functions  $\delta x(t)$ ,  $\delta \dot{x}(t)$ ,  $\delta p(t)$ . This results in the following variation of the objective function

$$\delta J = \int_0^{t_f} \left\{ -\frac{\partial H}{\partial \tau} d\tau - \left( \frac{\partial H}{\partial x} \right)^\top \delta x + p^\top \delta \dot{x} + \left( \dot{x} - \frac{\partial H}{\partial p} \right)^\top \delta p \right\} dt. \quad (4.71)$$

To fulfill Equation (4.66), the last term must be equal to zero  $(\dot{x} - f) \delta p = 0$ . Now, under the assumption  $\delta \dot{x} = \frac{d}{dt}(\delta x)$ , the integration by parts yields

$$\delta J = \int_0^{t_f} -\frac{\partial H}{\partial \tau} d\tau dt - \int_0^{t_f} \left( \dot{p} + \frac{\partial H}{\partial x} \right)^\top \delta x dt + [p^\top \delta x]_0^{t_f}. \quad (4.72)$$

The second and last terms in (4.72) vanish by using the definition for adjoint state, respecting its final condition

$$\dot{p} = -\frac{\partial H}{\partial x}, \quad p(t_f) = 0 \quad (4.73)$$

and also regarding the initial boundary condition  $\delta x(0) = 0$ . For small  $d\tau$  we can now use the following approximation

$$\Delta J \approx \delta J = - \int_0^{t_f} \frac{\partial H}{\partial \tau} d\tau dt = \left( - \int_0^{t_f} \frac{\partial H}{\partial \tau} dt \right) d\tau. \quad (4.74)$$

This implies that the total derivative of the objective function with respect to switching time fulfills the following equation

$$\frac{\partial J}{\partial \tau} = - \int_0^{t_f} \frac{\partial H}{\partial \tau} dt. \quad (4.75)$$

Hamiltonian for the system (4.66) takes the following form

$$H = p^\top \left( Ax + u_{\max} \mathcal{U}(y_n - \tau) Bx + \tilde{f}(x) \right) - f_0. \quad (4.76)$$

Then, the approximated gradient of the cost function is

$$\frac{\partial J}{\partial \tau} = - \int_0^{t_f} p^\top(t) Bx(t) \frac{\partial [u_{\max} \mathcal{U}(t - \tau)]}{\partial \tau} dt. \quad (4.77)$$

Finally, we get

$$\frac{\partial J}{\partial \tau} = u_{\max} \int_0^{t_f} p^\top(t) Bx(t) \delta(t - \tau) dt = u_{\max} p^\top(\tau) Bx(\tau). \quad (4.78)$$

Now, we consider the next switching action defined by the control

$$\bar{u} = u_{\max} \mathcal{U}(t) - u_{\max} \mathcal{U}(t - \bar{\tau}), \quad \tau \in [0, t_f]. \quad (4.79)$$

By following the previous procedure, we immediately get the gradient of the objective function with respect to the switching time  $\bar{\tau}$

$$\frac{\partial J}{\partial \bar{\tau}} = -u_{\max} p^\top(\bar{\tau}) Bx(\bar{\tau}). \quad (4.80)$$

To summarize the obtained results, the switching actions and the appropriate gradients are listed below

$$\begin{aligned} \text{Switching action}(t = \tau) : [\text{off}] \longrightarrow [\text{on}], \quad \frac{\partial J}{\partial \tau} &= u_{\max} p^\top(\tau) Bx(\tau), \\ \text{Switching action}(t = \bar{\tau}) : [\text{on}] \longrightarrow [\text{off}], \quad \frac{\partial J}{\partial \bar{\tau}} &= -u_{\max} p^\top(\bar{\tau}) Bx(\bar{\tau}). \end{aligned} \quad (4.81)$$

Alternate methods for computation of switching times were presented by Mohler in [31] and Kaya et al. in [24].

Before we develop the computational algorithm, the number of controls  $m$  is presumed. Next, for such controls we assume  $n$  to be the number of switching actions  $[\text{off}] \rightarrow [\text{on}]$  or  $[\text{on}] \rightarrow [\text{off}]$ . Therefore, we can collect the switching times into two matrices:  $\tau = [\tau_{i,j}]_{m \times n}$ ,  $\bar{\tau} = [\bar{\tau}_{i,j}]_{m \times n}$ , where  $\{\tau_{i,j}\}$  and  $\{\bar{\tau}_{i,j}\}$  are increasing sequences with respect to  $j$ , where for every pair  $(i, j)$  we have  $\tau_{i,j} \in [0, t_f)$ ,  $\bar{\tau}_{i,j} \in (0, t_f]$ . Moreover, we assume that  $\tau_{i,j} < \bar{\tau}_{i,j}$  for all  $i, j$ . The state equation is then as follows

$$\dot{y} = Ay + u_{\max} \sum_{i=1}^m \sum_{j=1}^n [\mathcal{U}(t - \tau_{i,j}) - \mathcal{U}(t - \bar{\tau}_{i,j})] B_i y + \tilde{f}(y). \quad (4.82)$$

The computational algorithm based on the predefined gradient method compounds of the steps presented in the Procedure 4.5.

**Remark:** The Step 5\* can be performed with the analogy to Step 5 in the Procedure 4.1, where the control vector is now replaced by the components of matrices  $[\tau_{i,j}]$  and  $[\bar{\tau}_{i,j}]$ .

**Procedure 4.5 The method of parametrised switching times**

- Step 1 Guess initial matrices  $[\tau_{i,j}]$  and  $[\bar{\tau}_{i,j}]$ .
- Step 2 Solve the state equation (4.82) by substituting  $[\tau_{i,j}]$  and  $[\bar{\tau}_{i,j}]$ .
- Step 3 Calculate Hamiltonian (4.69), then solve the adjoint state (4.73) by backward integration.
- Step 4 Compute the derivatives (4.81) for all components of switching time matrices.
- Step 5\* Modify time switching matrices by using first-order optimisation algorithm.
- Step 6 Check whether switching times  $\tau_{i,j}$  or  $\bar{\tau}_{i,j}$  extend their limited values 0 or  $t_f$ , respectively. If so, then set these switchings to appropriate infimum or supremum of the set  $[0, t_f]$  and then go to Step 2.
- Step 7 Check if length of any of interval  $[\tau_{i,j}, \bar{\tau}_{i,j}]$  approaches zero. If so, discard those switching time, resize the matrices  $[\tau_{i,j}]$ ,  $[\bar{\tau}_{i,j}]$  and go back to Step 2.
- Step 8. Repeat Steps 2–7 until the a terminal condition (based, for example, on the norm of the gradient) is fulfilled.

The approach presented in this section is not limited to the bilinear systems only. As soon as the controls are assumed to be bang–bang or the bang–bang type results from the application of the Pontryagin Maximum Principle, the problem of finding the required controls becomes one of finding switching times.

**4.6.5. Numerical Example: Optimal Semi-Active Controlled Oscillator (Method of Switching Times)**

In this section, the method of parametrised switching times is applied to the optimal control problem formulated in Subsection 4.6.3. The goal is to examine the performance of the switching method as well as to provide the comparative results to these obtained by using previously investigated gradient method.

Assuming  $[\tau_{1,j}]$  and  $[\bar{\tau}_{1,j}]$  as the switching time matrices, the Hamiltonian for the system described in (4.59) can be written in the form

$$\begin{aligned}
 H(x, p, \tau, \bar{\tau}) = & \begin{bmatrix} p_1 \\ p_2 \\ p_3 \end{bmatrix}^\top \begin{bmatrix} y_2 \\ -ky_1 + P \sin(\omega y_3) \\ 1 \end{bmatrix} + \\
 & + \begin{bmatrix} p_1 \\ p_2 \\ p_3 \end{bmatrix}^\top \begin{bmatrix} 0 \\ -y_2 \\ 0 \end{bmatrix} u_{\max} \sum_{j=1}^n [\mathcal{U}(t - \tau_j) - \mathcal{U}(t - \bar{\tau}_j)] - (y_1)^2 - (y_2)^2.
 \end{aligned} \tag{4.83}$$

Thus, the derivatives of cost function with respect to switching times are

$$\begin{aligned}
 \text{Switching action}(t = \tau) : [\text{off}] \longrightarrow [\text{on}], \quad \frac{\partial J}{\partial \tau} = -u_{\max} p_2(\tau) y_2(\tau), \\
 \text{Switching action}(t = \bar{\tau}) : [\text{on}] \longrightarrow [\text{off}], \quad \frac{\partial J}{\partial \bar{\tau}} = u_{\max} p_2(\bar{\tau}) y_2(\bar{\tau}).
 \end{aligned} \tag{4.84}$$

Numerical computations will be performed on the discretized time interval  $[0, t_f]$ , that is split into 1000 equal subintervals. As the first order optimisation method, used in Step 5\* in the Procedure 4.5, the gradient descent is applied. The step size  $\lambda_k$  is chosen in such a way, that for every iteration the inequality holds  $\lambda_k d_k \geq [0, t_f]/1000$ . This condition provides modification of elements of  $\tau$  and  $\bar{\tau}$  in every iteration. The computation stops when all components of  $\tau$  and  $\bar{\tau}$  oscillate between two nearest values of the discretized time domain.

**Case 1:**  $t_f = 0.67$

Likewise in Subsec. 4.6.3, we first consider the problem in the time interval  $[0, t_f] = [0, 0.67]$ . The computations are performed for two cases, each with the different initial matrices: (case A)  $\tau = 0.1 t_f$ ,  $\bar{\tau} = 0.9 t_f$ , (case B)  $\tau = 0.7 t_f$ ,  $\bar{\tau} = 0.8 t_f$ . The length of matrices is assumed on the basis of results obtained by gradient method.

Figure 4.14 displays switching times convergence. The point of convergence is the same for both cases A and B.

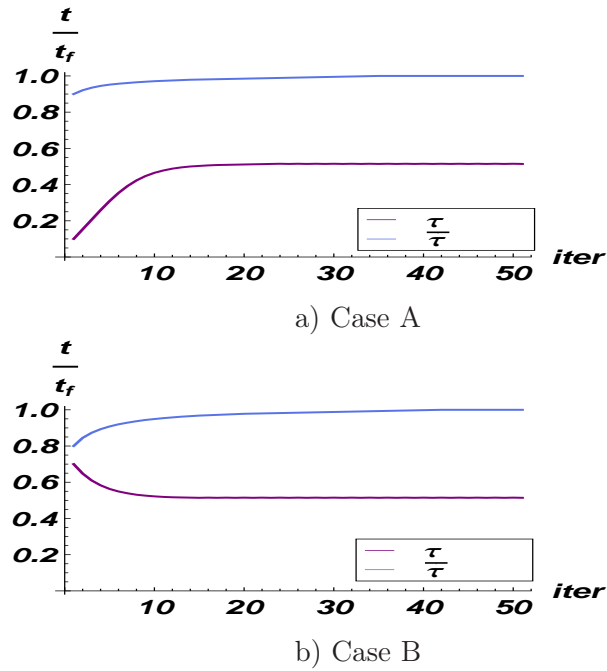


Figure 4.14. Switching time values with respect to the number of iteration.

The optimal control trajectory is show in Fig. 4.15.

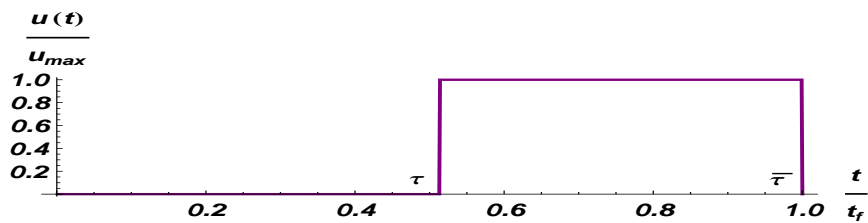


Figure 4.15. Optimised control function – the switching times method.

Comparing the solution obtained by the gradient method (Fig. 4.6), we can observe that the instant of switching denoted as  $\tau$  is equal to the coordinate of the middle point of the slope in Fig. 4.6. Thus, the coincidence of the results is very high.

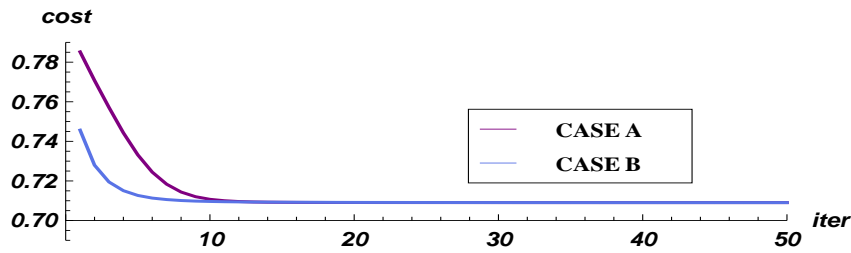


Figure 4.16. Cost function with respect to the number of iteration.

In Fig. 4.16, we present the evolution of the objective function in the iterative process. Finally, Fig. 4.17 demonstrates the optimised state and adjoint trajectories:  $y_1(t)$ ,  $y_2(t)$  and  $p_1(t)$ ,  $p_2(t)$ , respectively.

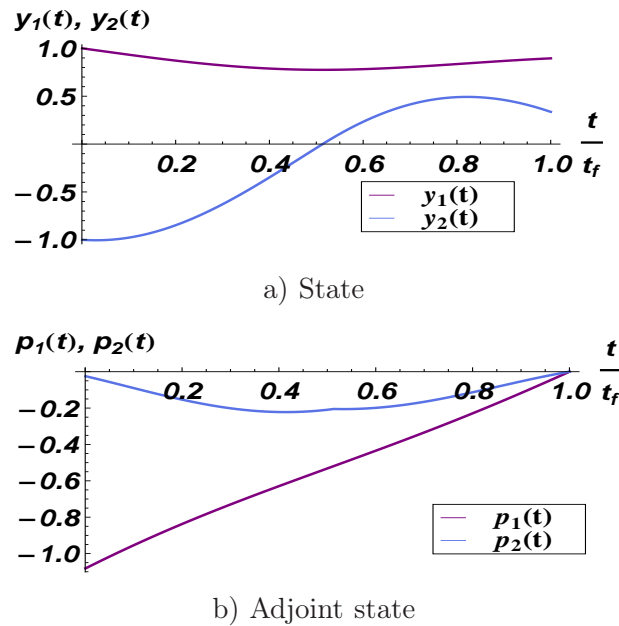
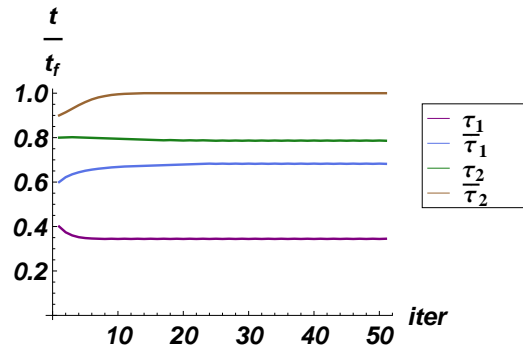


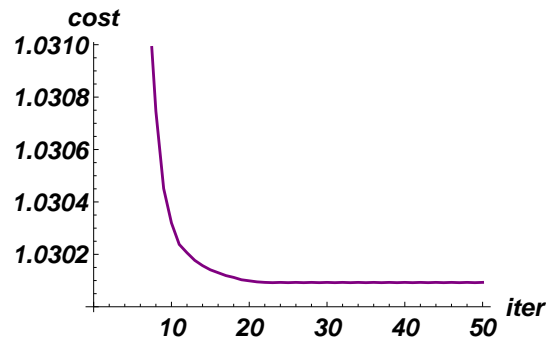
Figure 4.17. Optimized state and adjoint state trajectories.

### Case 2: $t_f = 1$

In the second case, the initial switching matrices are assumed to be  $\tau = [0.4t_f, 0.8t_f]$ ,  $\bar{\tau} = [0.6t_f, 0.9t_f]$ . The evolution of the switching times and objective function in the iterative process are shown in Fig. 4.18.



a) Switching times



b) Objective functions

**Figure 4.18.** Switching times and cost function with respect to the number of iteration.

In Fig. 4.19, the trajectory of optimized switching control is depicted. The coincidence with Fig. 4.10 is clearly visible. For comparison the state and adjoint trajectories are presented in Fig. 4.20.

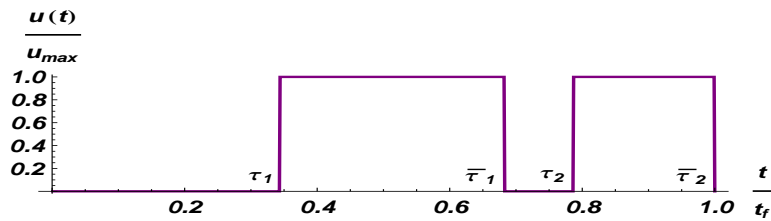


**Figure 4.19.** Optimised control function – the switching times method.

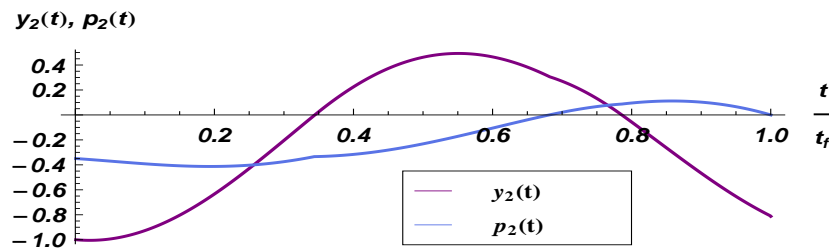


Figure 4.20. Optimized state and adjoint state trajectories.

In order to check the correctness of the Procedure 4.5, the computations were also performed with larger size of initial matrices  $\tau$ ,  $\bar{\tau}$ . In each of presented cases the algorithm forced discarding of extra switches. While the proper sizes of initial matrices are assumed, the time required for computation is reduced more than five times in comparison to the gradient method.



# Bibliography

- [1] M. Abu-Hilal. Dynamic response of a double Euler-Bernoulli beam due to a moving constant load. *Journal of Sound and Vibration*, 297:477–491, 2006.
- [2] M. Athans and P. Falb. *Optimal Control: An Introduction to the Theory and its Applications*. Dover Publications, Inc., New York, 2007.
- [3] T. Basar and G. J. Olsder. *Dynamic Noncooperative Game Theory*. SIAM Classics edition, 1999.
- [4] A. Baz. Dynamic boundary control of beams using active constrained layer damping. *Mechanical Systems and Signal Processing*, 11:811–825, 1997.
- [5] R. Bellman. *Dynamic Programming*. Princeton Univ. Pr., New Jersey, 1957.
- [6] R. Bogacz and C. Bajer. Active control of beams under moving load. *Journal of Theoretical and Applied Mechanics*, 38(3):523–530, 2000.
- [7] D. Bojczuk and Z. Mroz. Determination of optimal actuator forces and positions in smart structures using adjoint method. *Structural and Multidisciplinary Optimization*, 30:308–319, 2005.
- [8] M. S. Branicky, V. S. Borkar, and S. K. Mitter. A unified framework for hybrid control: Model and optimal control theory. *Transactions on Automatic Control*, 1998.
- [9] M. S. Branicky and S. K. Mitter. Algorithms for optimal hybrid control. *IEEE Conference on Decision and Control*, 1995.
- [10] A. E. Bryson and Jr. Yu-Chi Ho. *Applied Optimal Control*. Hemisphere, Washington, 1962.
- [11] E. F. Camacho and A. C. Bordons. *Model Predictive Control*. Springer, 2004.
- [12] Y. Chen, C. A. Tan, L. A. Bergman, and T. C. Tsao. Smart suspension systems for bridge-friendly vehicles. *SPIE Proceedings Series*, 4696:52–61, 2002.
- [13] S. Choura and A. S. Yigit. Control of a two-link rigid flexible manipulator with a moving payload mass. *Journal of Sound and Vibration*, 243:883–890, 2001.
- [14] T. Das and R. Mukherjee. Optimally switched linear systems. *Automatica*, 44:1437–1441, 2006.
- [15] L.C. Evans. *An Introduction to Mathematical Optimal Control Theory*. University of California, Berkeley, 2000.
- [16] A.F. Filippov. On certain questions in the theory of optimal control. *SIAM Journal on Control*, pages 78–84, 1962.
- [17] P. Flont and J. Holnicki-Szulc. Adaptive railway truck with improved dynamic response. *2nd World Congress of Structural and Multidisciplinary Optimization, Zakopane 97*, 4, 1997.
- [18] T. Frischgesel, K. Popp, H. Reckmann, and O. Schütte. Regelung eines elastischen Fahrwegs inter Verwendung eines variablen Beobachters. *Technische Mechanik*, 18:44–55, 1998.

- [19] Z. Fulin, T. Ping, Y. Weiming, and W. Lushun. Theoretical and experimental research on a new system of semi-active structural control with variable stiffness and damping. *Earthquake Engineering and Engineering Vibration*, 1:130–135, 2002.
- [20] D. Giraldo and Sh. J. Dyke. Control of an elastic continuum when traversed by a moving oscillator. *Journal of Structural Control and Health Monitoring*, 14:197–217, 2002.
- [21] E. P. Hofer and B. Tibken. An iterative method for the finite time bilinear quadratic control problem. *Journal of Optimization Theory and Applications*, 57(3):411–427, 1988.
- [22] B. Kang and J. K. Mills. Vibration control of a planar parallel manipulator using piezoelectric actuators. *Journal of Intelligent and Robotic Systems*, 42:51–70, 2005.
- [23] D. Karnopp, M. Crosby, and R. Harwood. Vibration control using semi-active force generators. *ASME Journal of Engineering for Industry*, 96:619–626, 1974.
- [24] C.Y. Kaya and J.L. Noakes. Computations and time-optimal controls. *Optimal Control Applications and Methods*, 17:171–185, 1996.
- [25] K. Y. Lee. *Optimal Bilinear Control Theory Applied to Pest Management in Recent Developments in Variable Structure Systems, Economics and Biology*. Springer-Verlag, Berlin, 1978.
- [26] D. Liberzon. *Calculus of Variations and Optimal Control Theory*. Princeton University Press, 2012.
- [27] D. Liberzon, J. P. Hespanha, and A. S. Morse. Stability of switched systems: a Lie-algebraic condition. *Systems and Control Letters*, 37:117–122, 1999.
- [28] D. Liberzon, J. P. Hespanha, and A. S. Morse. Lie-algebraic stability conditions for nonlinear switched systems and differential inclusions. *Systems and Control Letters*, 55:8–16, 2006.
- [29] J. Macki and A. Strauss. *Introduction to Optimal Control Theory*. Springer-Verlag, New York, 1982.
- [30] R. R. Mohler. *Controllability and Optimal Control of Bilinear Systems*. Prentice-Hall, New York, 1970.
- [31] R. R. Mohler. *Bilinear Control Processes*. Academic Press, New York, 1973.
- [32] R. R. Mohler. *Nonlinear Systems: Volume II, Applications to Bilinear Control*. Prentice-Hall, New York, 1991.
- [33] A. Ossowski. Semi-active control of free beam vibration. *Theoretical Foundations of Civil Engineering*, 11:557–566, 2003.
- [34] C.H. Papadimitriou and K. Steiglitz. *Combinatorial Optimization: Algorithms and Complexity*. Dover Publications, 1998.
- [35] H. W. Park, H. S. Yang, Y. P. Park, and S. H. Kim. Position and vibration control of a flexible robot manipulator using hybrid controller. *Robotics and Autonomous Systems*, 28:31–41, 1999.
- [36] B. Piccoli. Necessary conditions for hybrid optimization. *IEEE Conference on Decision and Control*, 1999.
- [37] M. Pietrzakowski. Active damping of beams by piezoelectric system effects of bonding layer properties. *International Journal of Solids and Structures*, 38:7885–7897, 2001.
- [38] D. Pisarski and C. Bajer. Semi-active control of 1d continuum vibrations under a travelling load. *Journal of Sound and Vibration*, 329(2):140–149, 2010.
- [39] D. Pisarski and C. Bajer. Smart suspension system for linear guideways. *Journal of Intelligent and Robotic Systems*, 62(3-4):451–466, 2011.
- [40] L. S. Pontryagin, V. G. Boltyanskii, and R. V. Gamkrelidze. *The Mathematical Theory of Optimal Processes*. Wiley, New York, 1962.

- 
- [41] W. H. Press, S. A. Teukolsky, W. T. Vetterling, and B. P. Flannery. *Numerical Recipes in C: The Art of Scientific Computing*. Cambridge University Press, Cambridge, 1992.
  - [42] A. Rantzer. Dynamic dual decomposition for distributed control. *IEEE American Control Conference*, 2009.
  - [43] A. Rantzer. Distributed control of positive systems. *arXiv*, 2012.
  - [44] A. Rantzer and M. Johansson. Piecewise linear quadratic optimal control. *Transactions on Automatic Control*, 2000.
  - [45] A. Ruangrassamee and K. Kawashima. Control of nonlinear bridge response with pounding effect by variable dampers. *Engineering Structures*, 25:593–606, 2003.
  - [46] M. S. Shaikh and P. E. Caines. On the optimal control of hybrid systems: Optimization of switching times and combinatoric schedules. *IEEE American Control Conference*, 2003.
  - [47] T. Soong. *Active Hybrid and Semi-Active Structural Control*. John Wiley and Sons, 2005.
  - [48] J. Stoer and R. Bulirsch. *Introduction to numerical analysis*. Springer-Verlag, New York, 1980.
  - [49] R. K. Sundaram. *A First Course in Optimization Theory*. Cambridge University Press, 1996.
  - [50] H. J. Sussmann. A maximum principle for hybrid optimal control problems. *IEEE Conference on Decision and Control*, 1999.
  - [51] C. A. Tan and S. Ying. Active wave control of the axially moving string. *Journal of Sound and Vibration*, 236:861–880, 2000.
  - [52] R. Vinter. *Optimal Control*. Birkhauser, Boston, 2000.
  - [53] K. Yoshida and T. Fujio. Semi-active base isolation for a building structure. *International Journal of Computer Applications in Technology*, 13:52–58, 2000.



## Engineering Problems

In the Chapter we will present four experiments that will prove the efficiency of the semi-active control of vibrating structures. Our experimental stands enable verification of theoretical derivations and numerical simulations. Usually, theoretical considerations are more optimistic and resulting efficiency exceeds experiments. Although expected phenomena are observed in both theory and practice, in the latter case, when realistic parameters were assumed: dimensions, material modules, and the speed range of some parameters, the expected effect can be lower. Also for the reason of complexity of the investigated problem, experimental results may be poor. In subsequent sections we present four test, previously analysed and simulated.

In the Subsec. 5.1 and 5.2 the simply supported beam is subjected to a moving load. Our aim is to minimise vertical displacements under the moving load and in selected stationary points.

The next test (Subsec. 5.3) was performed for rotating structure. Angular amplitudes of harmonically excited shaft have to be minimized with the use of magnetorheological dampers. The advantage of the controlled approach is significant.

The Subsec. 5.4 describes results for a cantilever sandwich beam filled at its tip with an elastomer containing ferromagnetic particles. The controlled shear modulus allows us to increase damping over the damping with permanent action. The fourth example (Subsec. 5.5) is similar to the previous one. Instead of elastomer insert a small parcel filled with granular material controlled with a vacuum is used for minimising free vibrations. The small underpressure is sufficient to obtain the improved result of damping. Three examples are devoted to bending structures. However, a wide range of problems can be treated in the same way.

## 5.1. Semi-active Control of Beam Subjected to a Moving Load

In this section, we will formulate the optimal control problem which corresponds to the problem of finding the straight line passage of a moving load upon an elastic one-dimensional body. First, we will define a corresponding objective function. Then, in order to derive the optimal controls, the Pontryagin Maximum Principle will be applied (see Subsec. 4.2.1). Finally, the adjoint system will be written.

As representative example of elastic one-dimensional body we consider the Bernoulli-Euler beam of the total length  $L$ , bending stiffness  $EI$  and density per unit length  $\mu$ . The objective is to reduce the total deflection of a load travelling over the beam at constant speed  $v$ . The objective function can be written as the  $L^2$  norm of  $w(vt, t)$ , representing the deflection of the beam at the position  $vt$  and in time  $t$

$$J = \langle w(vt, t) | w(vt, t) \rangle = \int_0^{t_f} [w(vt, t)]^2 dt. \quad (5.1)$$

Here  $t_f = L/v$  stands for the time of the passage. For the control devices we assume  $m$  rheological dampers supporting the beam at the positions  $a_i$ . Each of the dampers can operate with damping coefficient  $u_i$  within the closed interval bounded by minimum  $u_{\min}$  and maximum  $u_{\max}$  admissible values. The optimal control problem can be formulated as follows:

$$\text{Minimize } J = \int_0^{t_f} [w(vt, t)]^2 dt,$$

under

$$EI \frac{\partial^4 w(x, t)}{\partial x^4} + \mu \frac{\partial^2 w(x, t)}{\partial t^2} = - \sum_{i=1}^m \delta(x - a_i) u_i(t) \frac{\partial w(x, t)}{\partial t} + \delta(x - vt) P,$$

$$w(x = 0, t) = 0, \quad w(x = L, t) = 0,$$

$$\left( \frac{\partial^2 w(x, t)}{\partial x^2} \right) \Big|_{x=0} = 0, \quad \left( \frac{\partial^2 w(x, t)}{\partial x^2} \right) \Big|_{x=L} = 0, \quad (5.2)$$

$$w(x, t = 0) = 0, \quad \dot{w}(x, t = 0) = 0,$$

$$u(t) \in \Omega = [u_{\min}, u_{\max}]^m.$$

The equivalent optimization problem, but given in the state space representation (state given by the vector  $y$  of the size  $n$ ), can be rewritten in the form:

$$\begin{aligned} \text{Minimize } J &= \int_0^{t_f} \left[ \frac{L}{2} \sum_{k=1}^{n/2} y_{2k-1}(t) \sin \left( \frac{k\pi v y_{n+1}(t)}{L} \right) \right]^2 dt, \\ \text{subject to } \dot{y}(t) &= Ay(t) + \sum_{i=1}^m u_i B_i y(t) + f(y), \\ u(t) &\in \Omega = [u_{\min}, u_{\max}]^m. \end{aligned} \quad (5.3)$$

For such a problem we can write the Hamiltonian

$$\begin{aligned} H(y, p, u) &= p^T \left( Ay(t) + \sum_{i=1}^m u_i B_i y(t) + f(y) \right) + \\ &- \left[ \frac{L}{2} \sum_{k=1}^{n/2} y_{2k-1}(t) \sin \left( \frac{k\pi v y_{n+1}(t)}{L} \right) \right]^2. \end{aligned} \quad (5.4)$$

The problem (5.3) is analogous with the Problem 4.5 studied in the previous chapter. The application of the Pontryagin Maximum Principle yields the optimal controls of the bang-bang type

$$u_i^*(t) = \begin{cases} u_{\max}, & p^T(t) B_i y(t) > 0 \\ u_{\min}, & p^T(t) B_i y(t) < 0 \end{cases}. \quad (5.5)$$

Here the adjoint system is given in the following form

$$\begin{aligned} \dot{p} &= -\frac{\partial H}{\partial y} = -p^T \left( A + \sum_{i=1}^m u_i B_i + \frac{\partial f}{\partial y} \right) + \\ &+ \frac{\partial}{\partial y} \left\{ \left[ \frac{L}{2} \sum_{k=1}^{n/2} y_{2k-1}(t) \sin \left( \frac{k\pi v y_{n+1}(t)}{L} \right) \right]^2 \right\} \end{aligned} \quad (5.6)$$

with the terminal condition  $p(t_f) = 0$ .

Below, we will demonstrate the solution to the problem (5.3) obtained by means of both, the gradient method and the switching times method. The goal will be to establish the relevant number of switching actions to achieve good performance of resulting control system. Reduction in the number

of switches is beneficial for two reasons: the system is less sensitive for errors and the time required for computations is significantly shortened. The comparison of the objective function values obtained by different methods will be given in the end of the section.

It is worth mentioning that the gradient method used in this work leads to local optima that refer to sub-optimal solutions. The assumption that has to be made is that the objective function is locally convex with respect to control functions. By the optimization we mean the process of searching for the solution that for some objective is better than one taken as initial value in the optimization process. In fact, in this work we look for the solutions that outperform the passive cases. Thus, it is reasonable to assume the passive cases as the initial values in the optimization procedures.

We will consider a system shown in Fig. 5.1 that represents a bridge span. We assume the following elastic body: HE – A 300A steel beam (according to DIN 1025 and Euronorm 53 – 62). The parameters for the beam are as follows: the length  $L = 24$  m, the mass density  $\mu = 88.3$  kg/m, the bending stiffness  $EI = 38.3 \cdot 10^6$  Nm<sup>2</sup> ( $E = 210 \cdot 10^9$  Pa). The force  $P = 10^4$  N travels with the velocity  $v = 0.7v_{cr}$ , where  $v_{cr} = (\pi/L)\sqrt{EI/\mu}$  is the critical speed (in this case  $v_{cr} = 86.2$  m/s). In the computations, the following placements of the two active dampers are assumed:  $0.33L, 0.66L$ . For every damper the value of variable damping coefficient belongs to the set  $[u_{\min}, u_{\max}] = [10^3, 5 \cdot 10^5]$  Ns/m. 10 first harmonic modes are taken into account in the computations.

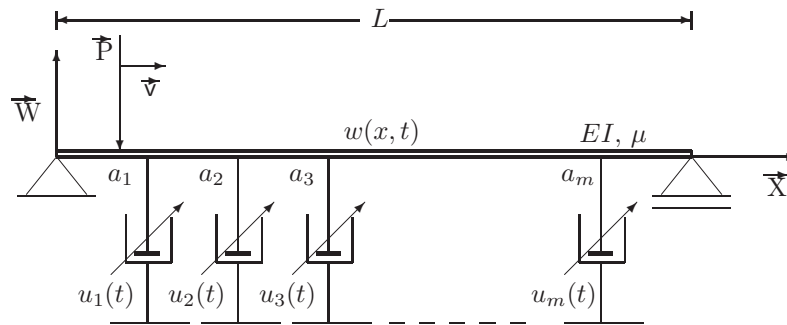


**Figure 5.1.** Bernoulli-Euler beam system supported by controlled viscous dampers.

### 5.1.1. Passive Cases

In this section, we will execute the simulations of the system 5.1 in the case of constant controls. The purpose is to show that among the passive cases the control functions which values are set to  $u_{\max}$  exhibit the best efficiency for the straight line passage of a moving load. Thus, in further investigations it is reasonable to compare the trajectories driven by these best passive controls with the variable control functions obtained by optimization. For simplicity we assume here that all controls are set to the same value. The simulation are performed for the following cases:  $u_1 = u_2 = 0.25u_{\max}$ ,  $u_1 = u_2 = 0.5u_{\max}$ ,  $u_1 = u_2 = 0.75u_{\max}$ ,  $u_1 = u_2 = u_{\max}$ . The results are presented in Fig. 5.2.

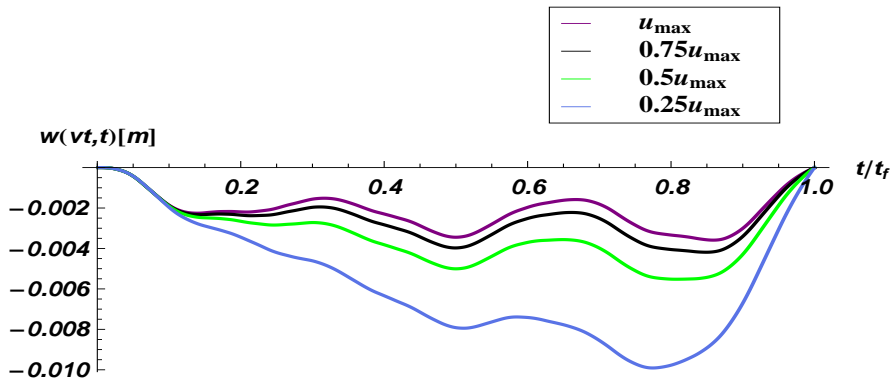
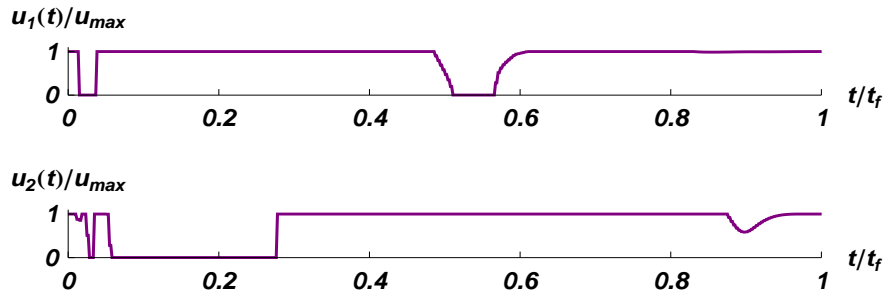


Figure 5.2. Comparison of moving load trajectories under constant controls.

### 5.1.2. Optimal Case (Gradient Based Method)

In this part, the problem (5.3) is solved by using the gradient method (see Procedure 4.1). In the computation, we assume a constant time step for every iteration. The discrete time interval  $[0, t_f]$  is split into 1000 equal sub-intervals. For each of these sub-intervals we assume constant control. The initial controls are set to the maximum values for all sub-intervals  $u_i^{initial}(t) = u_{\max}$  ( $i = 1, 2$ ),  $\forall t \in [0, t_f]$ . This refers to the passive case. The computations are terminated after performing 200 iterations.

Optimal controls are demonstrated in Fig. 5.3. The switching structures of the optimal control functions can be clearly noticed.



**Figure 5.3.** Control functions optimized by using the gradient method.

When observing the optimal controls one can distinguish four switches for control  $u_1$  and two major switching actions for control  $u_2$ . This information will be used to assume the number of switches for the application of the switching times method.

In Fig. 5.4, we demonstrate the optimized moving load trajectory (*controlled*). It is compared with the *uncontrolled* case, i.e., when the system is under constant controls  $u_i(t) = u_{\max}$  ( $i = 1, 2$ ),  $\forall t \in [0, t_f]$ . The *uncontrolled* trajectory is typical for the moving load when transversing the span supported with passive dampers. The clearly visible local maximas that occur near the instants  $t = 0.33t_f$  and  $t = 0.66t_f$  are the evidence of presence of supports. In the *controlled* case these maximas are shifted toward the line  $w = 0$  along with the whole moving load trajectory.

The values of the objective function are presented in Fig. 5.5. The *controlled* case clearly outperforms the *uncontrolled* one (*uncontrolled* state

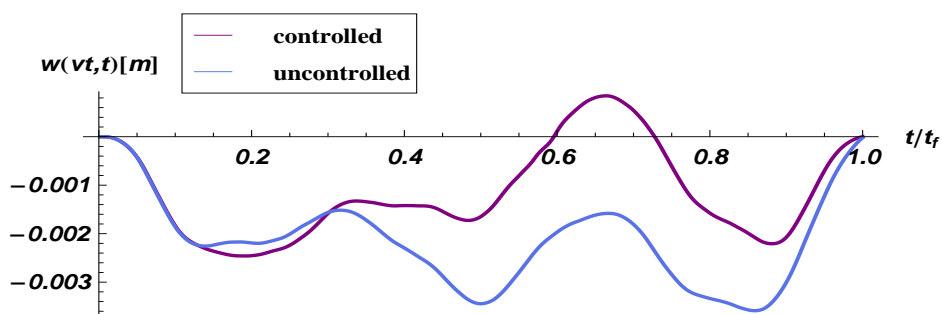


**Figure 5.4.** Moving load trajectories optimized by using the gradient method.

is set for the first iteration in the optimizing operation). The time required for computation did not exceed 500 seconds (PC, Intel Pentium Core 2).

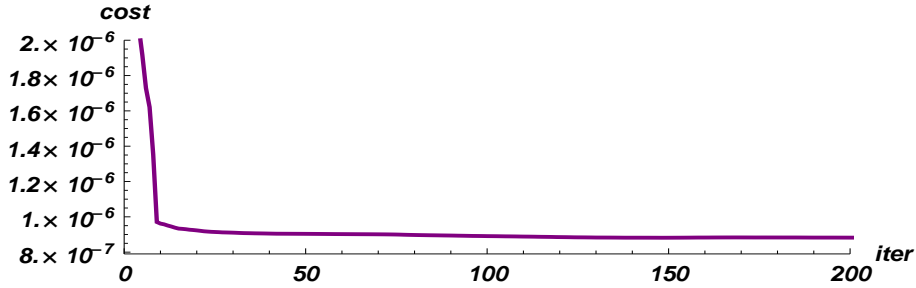


**Figure 5.5.** The objective function values versus iteration in the case of the gradient method.

### 5.1.3. Optimal Case (Switching Times Method)

The optimal control problem (5.3) will be now solved by using the switching times method. We will assume four switching actions for every control, and then will apply the Procedure 4.5. As in the case of the gradient method, the discrete time interval  $[0, t_f]$  is split into 1000 equal sub-interval and the computations are terminated after 200 iterations. The initial values for switching times matrices are assumed as follows:

$$[\tau_{i,j}] = t_f \cdot \begin{bmatrix} 0.01 & 0.5 \\ 0.1 & 0.7 \end{bmatrix}, \quad [\bar{\tau}_{i,j}] = t_f \cdot \begin{bmatrix} 0.2 & 0.8 \\ 0.5 & 0.9 \end{bmatrix}. \quad (5.7)$$

Figures 5.6, 5.7 demonstrate the switching times as the functions of iteration number. In order to highlight how  $\bar{\tau}_{2,1}$  coincide with  $\tau_{2,2}$ , below we plot in Fig. 5.8 the zoomed version of Fig. 5.7. As a result of this coincidence, the switches are discarded. Finally, it is found approximately that the optimal control are structured as follows:  $u^T = [u_{\min}, u_{\min}]$  on  $[0, 0.001)t_f$ ,  $u^T = [u_{\max}, u_{\min}]$  on  $[0.001, 0.28)t_f$ ,  $u^T = [u_{\max}, u_{\max}]$  on  $[0.28, 0.51)t_f$ ,  $u^T = [u_{\min}, u_{\max}]$  on  $[0.51, 0.63)t_f$ ,  $u^T = [u_{\max}, u_{\max}]$  on  $[0.63, 0.91)t_f$ ,  $u^T = [u_{\min}, u_{\max}]$  on  $[0.91, 0.94)t_f$ ,  $u^T = [u_{\min}, u_{\min}]$  on  $[0.94, 1)t_f$ . This is depicted in Fig. 5.9. When omitting narrow strips in the controls obtained by using the gradient methods one can find that the shapes of 5.3 and 5.9 concur.

Figure 5.10 displays a comparison of two optimized moving load trajectories. The agreement of the results is very high. In Fig. 5.11, we present

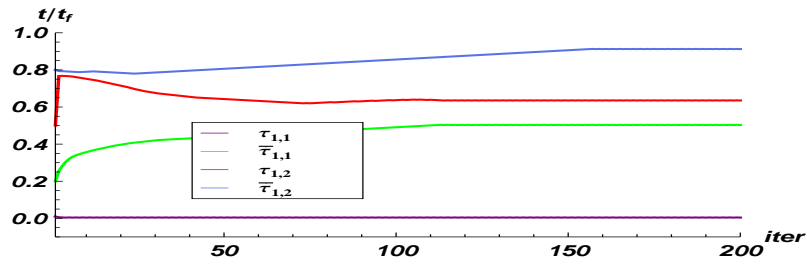


Figure 5.6. Switching times versus iteration for the control function  $u_1$ .

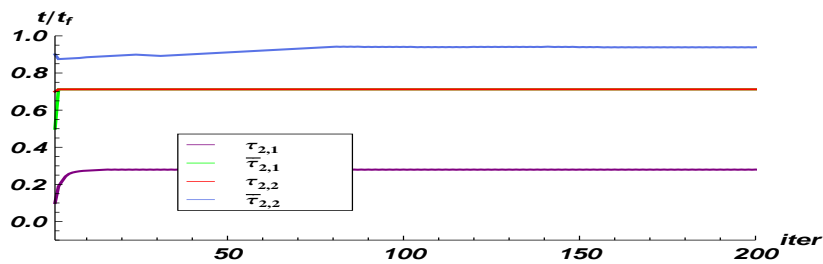


Figure 5.7. Switching times versus iteration for the control function  $u_2$ .

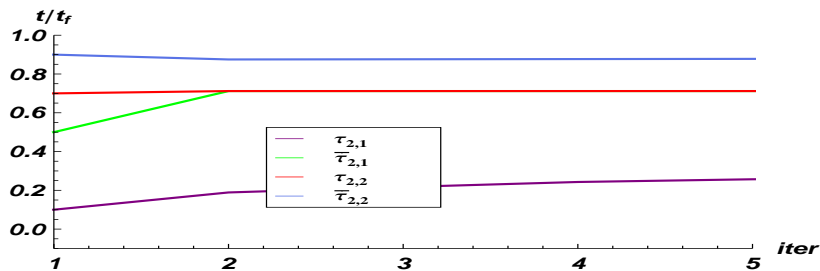


Figure 5.8. Switching times versus iteration for the control function  $u_2$  (zoomed version).

the evolution of the objective function in the iterative process. The time required for computations is approximately five to twenty times shorter than in case of the gradient method. This is an obvious result of the size of the optimization problem. In the case of the switching times method, the size was equal to 8 in contrast to the gradient method where the size was equal to 1000 for the same problem.

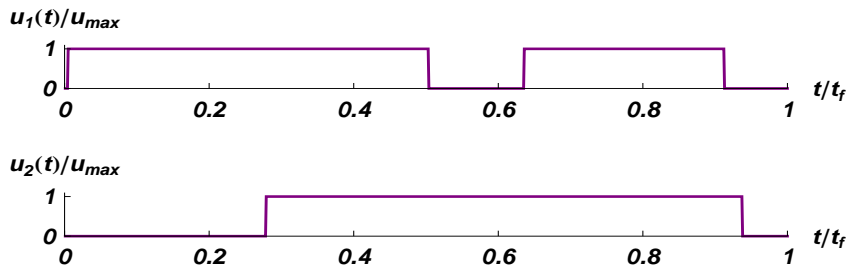


Figure 5.9. Control functions optimized by using the switching times method.

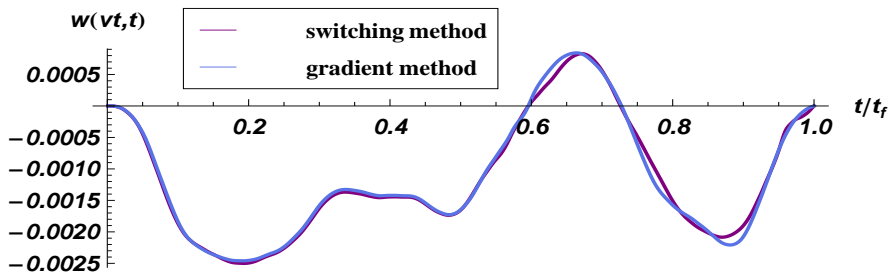


Figure 5.10. Optimized moving load trajectories. Gradient method versus switching times method.

Now we can pose the following question. What is the impact of further limitation in switching actions on the performance of the control system? To answer to this question let us consider the same optimal control problem (5.3), however this time any of the control function can switch only twice. We assume the following initial values for the switching times vectors:

$$[\tau_{i,j}] = t_f \cdot \begin{bmatrix} 0.1 \\ 0.5 \end{bmatrix}, \quad [\bar{\tau}_{i,j}] = t_f \cdot \begin{bmatrix} 0.8 \\ 0.9 \end{bmatrix}. \quad (5.8)$$

The evolution of the switching times in the iterative process is demonstrated in Figs. 5.12, 5.13.

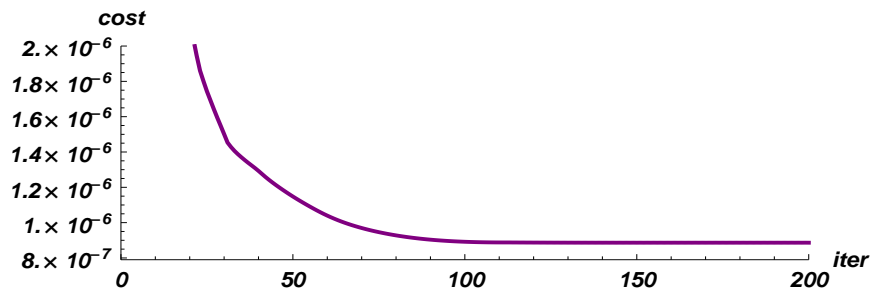


Figure 5.11. The objective function values versus iteration in the case of the switching times method.

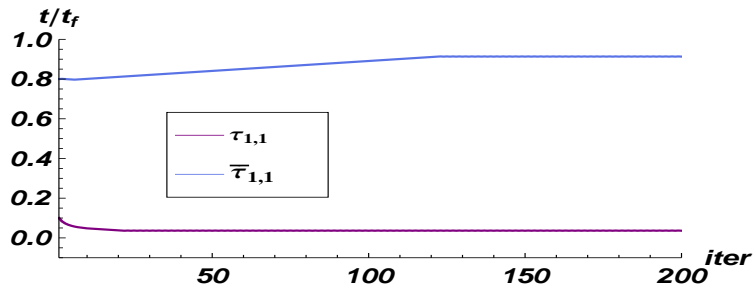


Figure 5.12. Switching times versus iteration for the control function  $u_1$ .

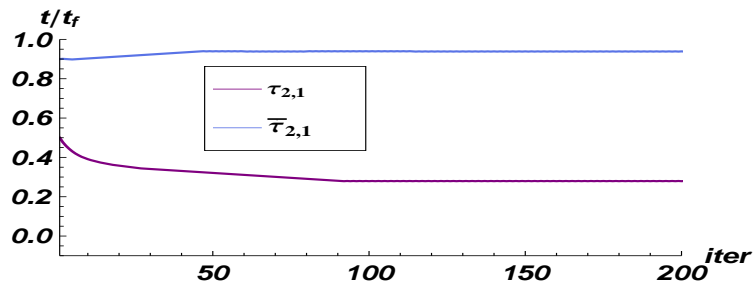


Figure 5.13. Switching times versus iteration for the control function  $u_2$ .

In this case no switching is discarded. The controls and the corresponding trajectory are presented in Figs. 5.14 and 5.15, respectively. In comparison with the previous example now the control  $u_1$  is simplified while the shape of  $u_2$  is retained with high accuracy.



Figure 5.14. Control functions optimized by using the switching times method.

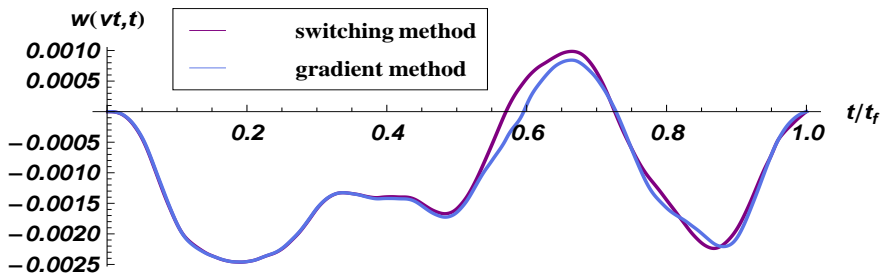


Figure 5.15. Optimized moving load trajectories. Gradient method versus switching times method (two switches per control).

This result confirms the intuitive prediction of the shapes of controls, as demonstrated in Fig. 4.1a. The left damper is activated as the first. Due to the switch off mode of the right damper, the beam is able to rotate providing a beneficial trajectory for a moving load during the second stage of the passage.

To summarize the results presented within this section, in the Table 5.1 we list the objective values obtained by each of the methods. The best efficiency is performed for the control computed by the gradient method. The system steered by the switching controls where the number of switches is

Table 5.1. Cost values comparison.

uncontrolled	controlled Gr. Method	controlled Sw. T. Method (4)	controlled Sw. T. Method (2)
$0.2167 \cdot 10^{-5}$	$0.0875 \cdot 10^{-5}$	$0.0883 \cdot 10^{-5}$	$0.0886 \cdot 10^{-5}$

equal to 2 (SW. T. METHOD (2)) exhibits comparable result with the variant of four switching actions (SW. T. METHOD(4)). Any of the presented control methods outperforms the passive (uncontrolled) cases.

## 5.2. Beam Under the Moving Mass

In this section we will focus our investigations on the control functions  $u_1(t)$  and  $u_2(t)$  of the dampers supporting the Euler beam under the inertial load (see Eq. (3.16)). The objective function  $J$  should be efficiently minimised. The control of the system can be performed in several ways to achieve the prescribed goal. From the engineering point of view, the following control functions can be considered essential:

- limited vertical displacement of selected points of the beam,
- limited vertical displacement under the travelling load,
- limited stress in the beam,
- low accelerations at selected points or under the load.

The basic parameters of the system, i.e., the bending stiffness of the beam and the range of damping coefficients, can be chosen during the design and optimisation stage as constant values. They allow us to provide the required load carrying capacity under the dynamic load. However, the damping coefficients that can vary allow of increasing the performance of the system.

Here we consider a vibrating beam in  $\Omega = \{x : 0 \leq x \leq L\}$ , with boundary conditions in  $\partial\Omega = \{0, L\}$ ,  $w(x) = 0$ ,  $w(x)'' = 0$ , subject to a gravity load, with the concentrated inertia of the moving mass. The beam is supported with a damping material  $u(x, t)$ . The state of such a system is constituted by vertical displacements  $w(x, u, t)$ , and the control input  $u(x, t)$  as the damping coefficients of the dampers. The objective of the control is to distribute the damping of each damper over time to achieve the desired vibrations, here denoted by  $w_d(x, t)$ . We assume a finite time horizon  $T$ . The optimisation problem can be written in the following form:

$$\text{Minimise } J = \frac{1}{2} \int_0^T \int_{\Omega} [w(x, u, t) - w_d(x, t)]^2 dx dt \quad (5.9)$$

subject to the constraints

$$\begin{aligned}
& EI \frac{\partial^4 w(x, t)}{\partial x^4} + \rho A \frac{\partial^2 w(x, t)}{\partial t^2} + \sum_{i=1}^2 \delta(x - x_i) u_i(t) \frac{\partial w(x, t)}{\partial t} + \\
& + \delta(x - x_3) k w(x, t) = \delta(x - f(t)) P - \delta(x - f(t)) m \frac{d^2 w(f(t), t)}{dt^2}, \\
& w(x, t)|_{t=0} = w_0(x) \quad \text{on } \Omega, \\
& \left. \frac{\partial w(x, t)}{\partial t} \right|_{t=0} = \dot{w}_0(x) \quad \text{on } \Omega, \\
& w(x, t) = 0, \quad w''(x, t) = 0 \quad \text{on } \partial\Omega \\
& u \in U.
\end{aligned} \tag{5.10}$$

$U$  is a set of admissible controls.  $U = \{u \in R^r : u_{\min} \leq u_i \leq u_{\max}, i = 1, \dots, r\}$ . In our problem we have two variables:  $r = 2$ . This minimises the displacements of a linear system of differential equations in a quadratic form. The problem is a linear quadratic hyperbolic control problem with distributed control. The treatment of this type of problem is difficult, due to the weak smoothing property of the associated solutions.

The numerical algorithms developed for optimisation problems with partial differential equations are dedicated to convex problems where the objective function is, for example, quadratic. In such cases, the problems have unique solutions. Moreover, quadratic functions enable us to derive simple formulae for the gradients by introducing the adjoint state. In our case, the objective function has local minima and a global search is required. Since gradient tools are ineffective and the number of design variables is low, we can successfully use random methods. We will intentionally employ a small number of time intervals  $n$ , since the controlled damping devices in real applications can not be switched instantaneously and a certain delay in action is typical. We will also consider larger  $n$  and compare the time trajectories of the considered design variables, i.e., the damping.

The brutal force method (systematic search) is useless due to the long computational time. One test last for example 0.1 s, and the number of test required in the case of quantification of the control variables each 0.01 in the interval  $[0, 1]$  gives 100 test. The number of variables equal 40 gives  $10^{80}$  test. We applied our own method, similar to genetic methods and partly to gradient methods. In brief, it is the Monte Carlo method, with variable number of decision variables in each several steps. Variables are drawn from

the proximity of the so far best solution. The proximity radius is changed during the process, allowing searching once near the optimum, once in wide range. We search for the solution in successively smaller cube, allowing from time to time global search. This approach tends to minimum with certain probability and in our opinion is efficient in our problem.

Let us compare the control functions for two values of damping,  $u=500$  Ns/m and 1000Ns/m. Figures 5.16 and 5.17 depict time variation of damping. We will consider three velocities:  $v=1, 2,$  and  $3$  m/s, with the accelerations and decelerations  $a = 7, 7,$  and  $4$  m/s<sup>2</sup>, respectively. Diagrams of the velocity vs. time or passed distance are depicted in Fig. 5.18. In the third scheme, the acceleration is smaller since the motor power at the higher speed is too weak to brake the motion successfully before the end. In further tests we will use the fastest motion  $v = 3$  m/s as the most characteristic case for our research. Other velocities, i.e.,  $v = 1$  and  $2$  m/s, will be used for comparison.

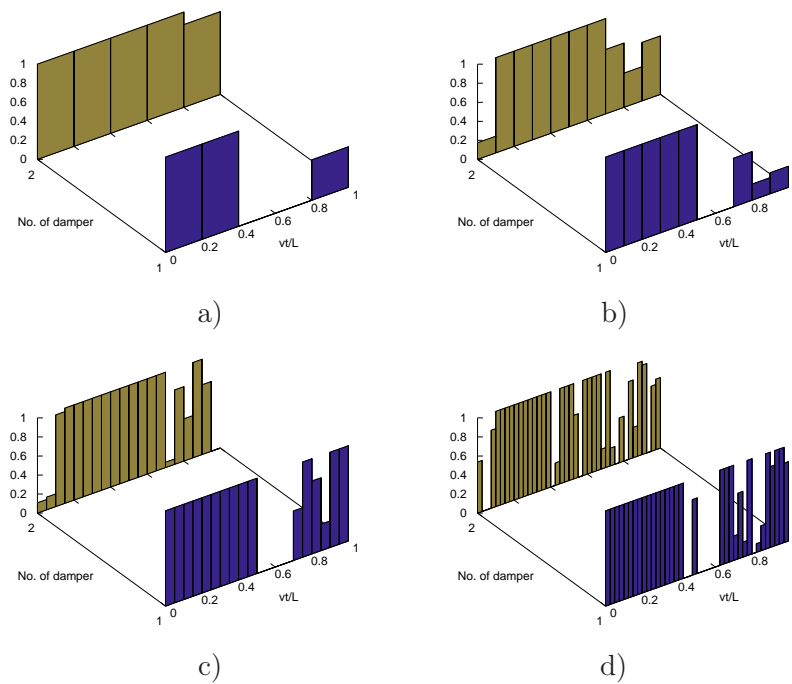


**Figure 5.16.** Control functions that minimise the displacements at the travelling point at the speed  $v = 3$  m/s and with  $u = 500$  Ns/m, for partitions into a) 5, b) 10, c) 20, and d) 40 time intervals,

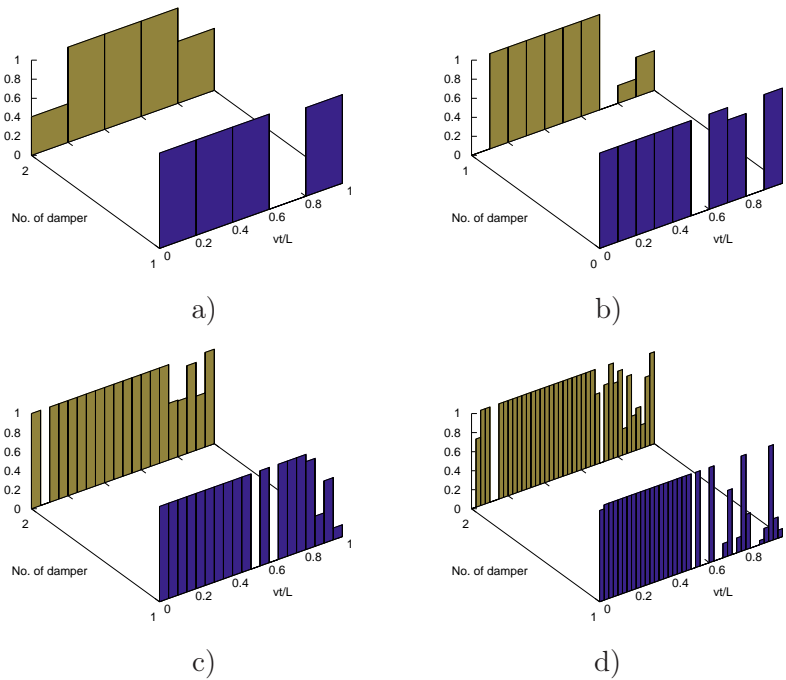


**Figure 5.17.** Control functions that minimize the displacements at the travelling point at the speed  $v = 3$  m/s and with  $u = 1000$  Ns/m, for partitions into a) 5, b) 10, c) 20, and d) 40 time intervals,

The control functions applied to both dampers that minimise the deflection under a mass travelling at the speed  $v = 3$  m/s are depicted in

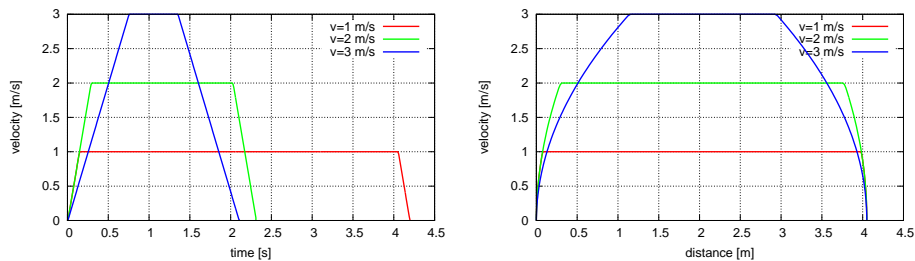


**Figure 5.18.** Three schemes of velocity applied in the experiment.

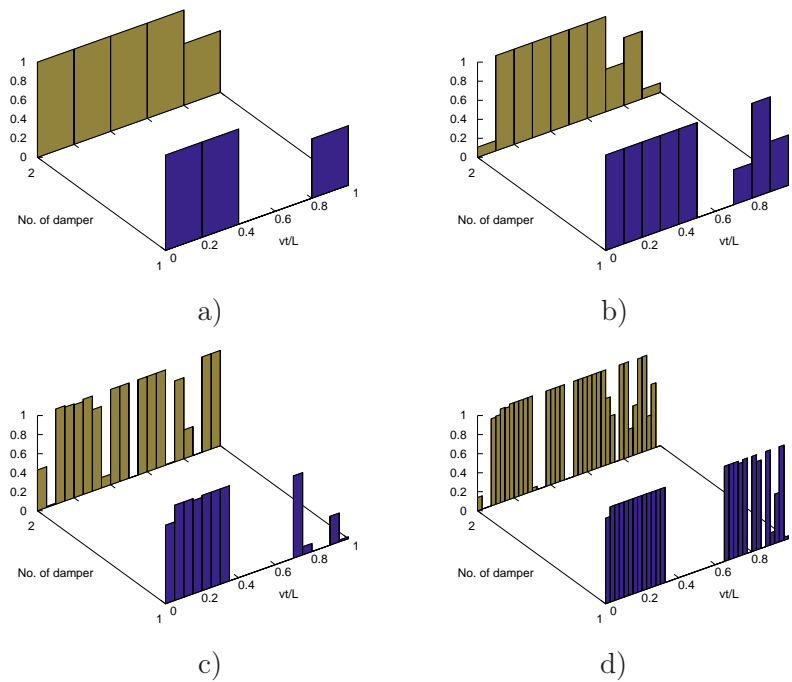


**Figure 5.19.** Control functions that minimize the displacements at the travelling point, for partitions into a) 5, b) 10, c) 20, and d) 40 time intervals.

Fig. 5.19. The increasing resolution  $n$  equals 5, 10, 20, and 40 intervals, slightly decreases the value of the objective function. The minimisation of the deflection at point No. 2 requires the control depicted in Fig. 5.20. Increasing resolution produces diagrams of control functions that can differ from each other. A slightly changed action of the damper at the early stage of the motion may require a significantly different action of the damper at subsequent stages.

The efficiency of the control computed numerically for  $v = 3$  m/s and  $a = 4$  m/s<sup>2</sup> is presented in Table 5.2. Controlled damping in each case improves the objective function.

A comparison of the displacements of the second measured point in terms of the damping coefficients is presented in Fig. 5.21. A numerical simulation of constant damping is compared with three curves that correspond to different solutions of the minimisation problem. Each of them coincides for most of the process. The curves at the final phase may differ, since the last

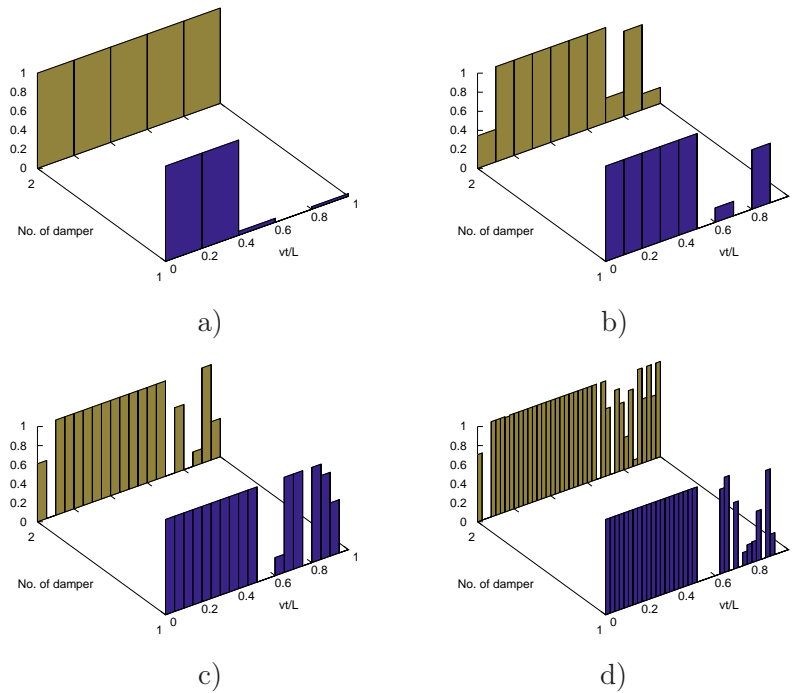


**Figure 5.20.** The control functions minimising the displacements at the second measure point, for partitions into a) 5, b) 10, c) 20, and d) 40 time intervals.

**Table 5.2.** Deflections obtained with different resolution  $n$  at  $v = 3$  m/s.

objective function	$n = 5$	$n = 10$	$n = 20$	$n = 40$	$u = \text{const.}$
min. disp. under the mass	4.4590	4.3448	4.3447	4.3444	4.4678
min. disp. of the point 2	4.7493	4.6818	4.6591	4.5636	4.8590

intervals of the control do not increase the objective function. The higher difference between the min/max damping exhibits significantly better performance of the system. We can add here that a larger number of dampers improves further the efficiency of the strategy of semi-active damping.

Let us compare the efficiency of the simulated controlled damping in the case of various velocities  $v$ . Figure 5.22 depicts the displacements of the point No. 2 under a load moving at a velocity of  $v = 1$  m/s, acceleration  $a = 7$  m/s<sup>2</sup>, and  $v = 3$  m/s,  $a = 4$  m/s<sup>2</sup>. We notice that at the lower velocity, the efficiency of displacement reduction is of the same range as in the case

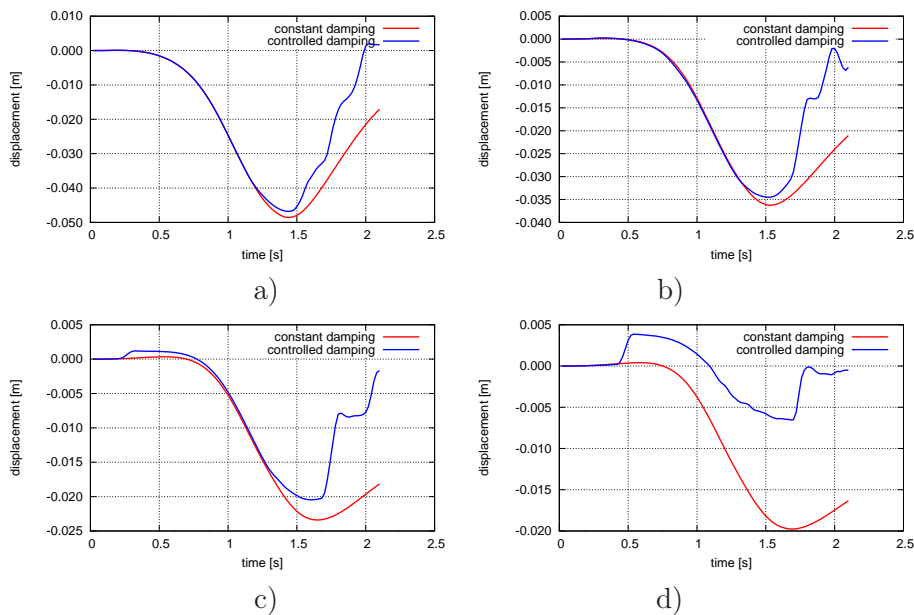


**Figure 5.21.** Displacements in time of the point 3 for different damping coefficients: a)  $u = 500$  Ns/m, b)  $u = 1000$  Ns/m, c)  $u = 2000$  Ns/m, d)  $u = 5000$  Ns/m.

of higher speed. The optimisation procedure locates our solutions in local minima that have almost the same values of the objective function.

### 5.2.1. Experimental results

The laboratory test stand consists of a single Hepco construction beam with a nominal length of 4.05 m and a cross section of  $317 \text{ mm}^2$ . The beam is a guideway for a moving inertial load. The beam is supported by two pivots that are attached to the steel plate fixed to the aluminium truss frame. By using conical shanks to connect the truss frame components, a high stiffness of the structure has been obtained. This eliminates clearances between its elements. One pivoting handle provides for rotating the beam end around the pivot axis. The second pivot has two degrees of freedom, which enables longitudinal and rotational movements of the second end of the beam. Such a support enables an increase in the vertical displacements of the beam during tests. The vertical displacements are measured by four laser displacement sensors OADM 12I6430/S35A. These sensors have a maximum

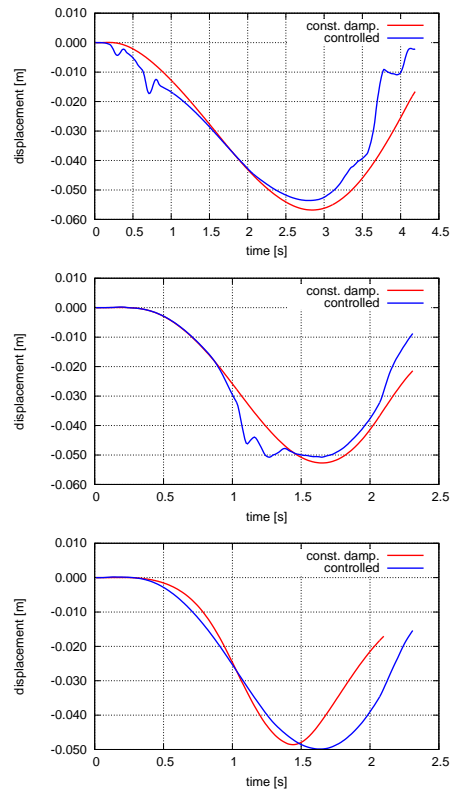


**Figure 5.22.** Comparison of displacements of point 2 in time, for  $v = 1, 2,$  and  $3$  m/s.

measurement resolution of  $0.01$  mm. Two laser sensors are mounted near the MR dampers and the third sensor measures the deflection in the middle of the beam. The last sensor is mounted on the bogie (trolley) carrying the moving mass and it measures the deflection of the beam under the moving mass.

A double-phase stepping motor FL110STH is the driving source of a mass that is movable along the beam. An electric motor of  $21$  Nm braking torque drives the rollers with radius  $r = 0.1$  m and the moving mass by means of the belt transport system shown in Fig. 5.23. The motor speed can be changed by the USN-1D8A controller and monitored by the AMT 103 rotary encoder mounted on the axis of the driving motor. Additionally, the encoder allows registration of the distance traversed by the moving mass during testing. The mass mounted on the trolley can be accelerated and decelerated with

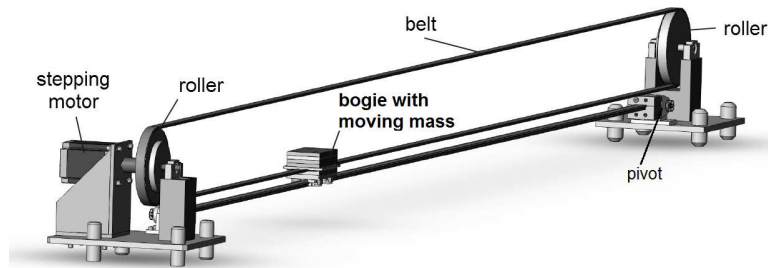


**Figure 5.23.** The belt transport system driving the moving mass [3].

rates up to  $7 \text{ m/s}^2$ . These settings enable us to get a maximum mass velocity of  $4 \text{ m/s}$ . More parameters of this test stand can be found in Table 5.3.

**Table 5.3.** Technical parameters of the test stand.

maximum torque of the driving motor	21 Nm
velocity range of the moving mass	0–4 m/s
max. acceleration and deceleration of the moving mass	$7 \text{ m/s}^2$
range value of the moving mass (min–max)	0.7–10 kg
guideway length	4.05 m
damping (min–max)	100–650 Ns/m
stiffness of one supporting spring	1000 N/m

In the middle of its length, the test stand beam is supported by a spring of stiffness  $1 \text{ N/mm}$  attached to the truss frame. These springs enable returning the beam to its initial position after passing the moving mass. The system of a single beam is supported by a set of rotary magneto-rheological (MR) dampers (brakes) mounted on the truss, too. The MR dampers are connected with the control unit by a current amplifier, which generates a control current proportional to a voltage signal which regulates the damping rate of the MR actuators. These dampers are turned on and off by a computer equipped with the control algorithm adapted in the LabView environment. It has been used to communicate with the measurement and control devices.

A suitably slender guideway is consistent with the theory of the Euler beam and provides a relatively low speed of wave propagating in the beam. The modular construction of the supporting structure allows extending the trolley route without much ado. Figure 5.24 shows the assembled test stand.



**Figure 5.24.** View of the test stand.

First we will verify the quality of the measurements and the coincidence of the numerical simulations with the experimental results. The damping coefficient of the dampers is the most difficult parameter to be determined. A magneto-rheological fluid is not exactly a viscous fluid. Its viscosity is perturbed by the metal particles that change the velocity-force relation and contribute friction. Preliminary tests of our MR dampers exhibit hysteresis that varies depending on the supply current. Figure 5.25 depicts the relation between the velocity in the range  $\pm 100$  mm/s, and the force. In the case of zero current the viscous parameter  $u$  is about 100 Ns/m. A current of  $I = 0.5$  A gives a damping of  $u = 370$  Ns/m around the point of low velocity. A current of  $I = 1$  A gives a damping of  $u = 650$  Ns/m. The damping in a wider range of velocities is lower. In further tests we will apply a current of  $I = 0.75$  A and an average damping of 500 Ns/m.

Let us compare the numerical results with the corresponding results of an experiment performed with both dampers being permanently active. Figure 5.26 depicts the displacements registered at three measuring points and the mass trajectory. They coincide sufficiently well with the numerical results. This proves that the average damping coefficient  $u = 500$  Nm/s assumed for the computations was appropriate. We must emphasise here the experimental inaccuracies concerning the supplementary inertia of the mov-

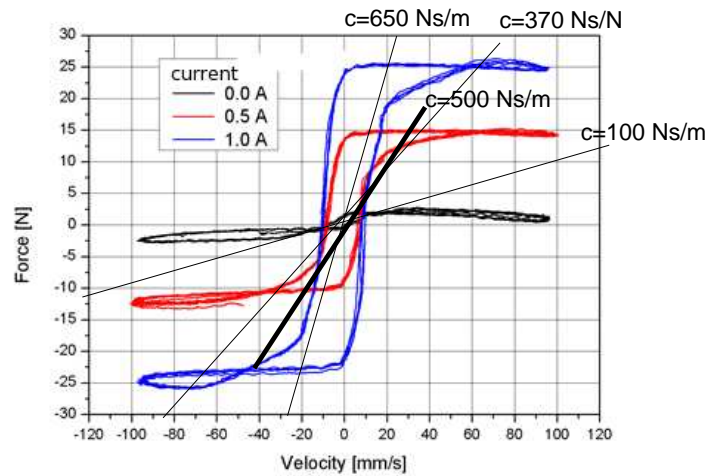


**Figure 5.25.** The velocity-force relation in the MR damper [3].

ing parts of the dampers, the static friction in the dampers, and the influence of the drive belt.

Now we will compare the simulated efficiency of the control with with the experimental data. Figure 5.27 depicts the displacements in time at three measured points and under the mass travelling at a velocity of  $v = 3$  m/s. The pair of control functions is depicted in Fig. 5.27d. The improvement of the results, at a level of 10%, is noticeable. The control functions have short breaks, sufficient for easy rearrangement of the beam near the dampers. A lower velocity,  $v = 2$  m/s, results in a lower efficiency of the control. Figure 5.28 depicts the displacements in time of three points and the displacement under the mass. The gain of the displacements in the case of the follower point is lower than in the case of the stationary points located inside the span.

## 5.2.2. Conclusions

The Section presented the strategy of semi-active damping of the vibrations of a beam under a moving inertial load. Intermediate supports as electrically controlled dampers decreased the transverse displacements. Periodically acting dampers are more efficient than permanently acting ones. The amplitudes at selected points and under the moving load are reduced by 10–40%, depending on the velocity of the load relative to the critical speed or to the wave speed. In this paper, we considered a relatively short beam,

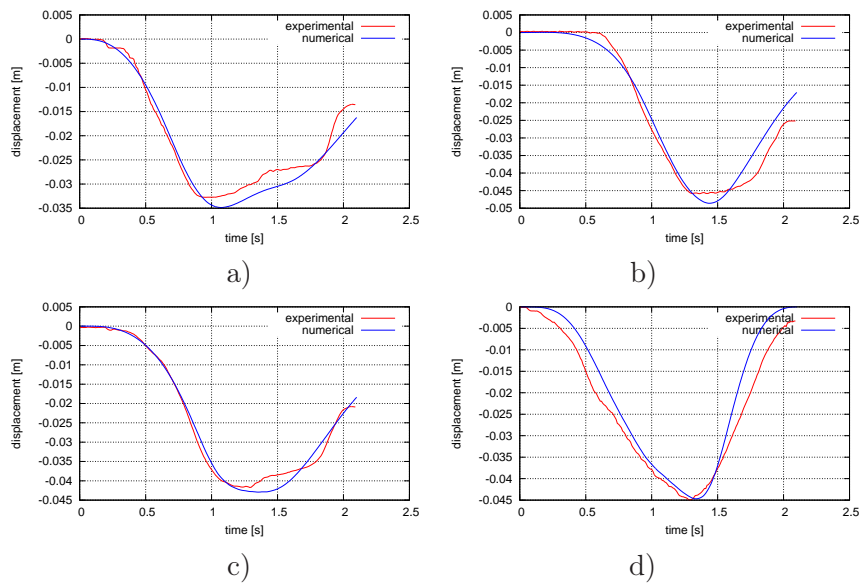


**Figure 5.26.** Coincidence of displacements in time in the 1st (a), 2nd (b), and 3rd (c) measuring point and the mass trajectory (d): numerical simulation and experiment.

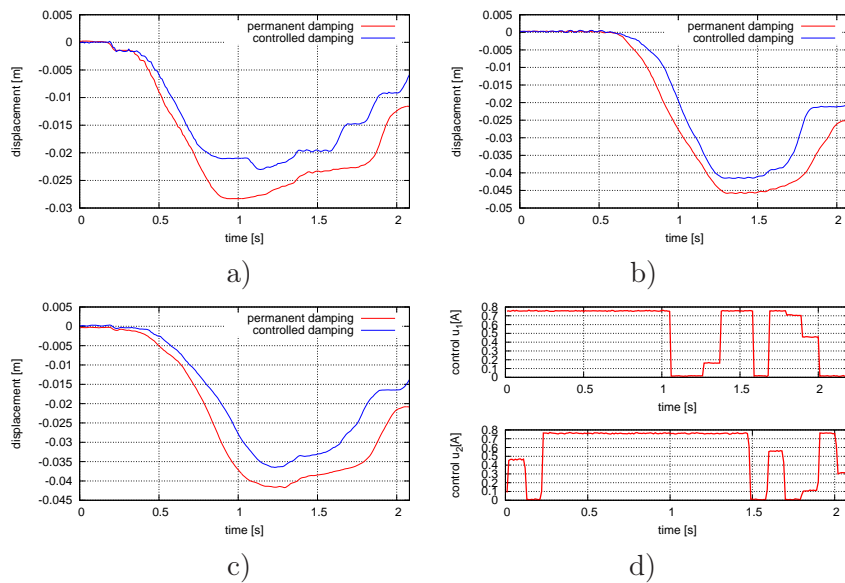


**Figure 5.27.** Displacements in time in the 1st (a), 2nd (b), 3rd (c) point, and the control functions (d), in the case of controlled damping and permanent damping at  $v = 3$  m/s,  $a = 4$  m/s<sup>2</sup>.

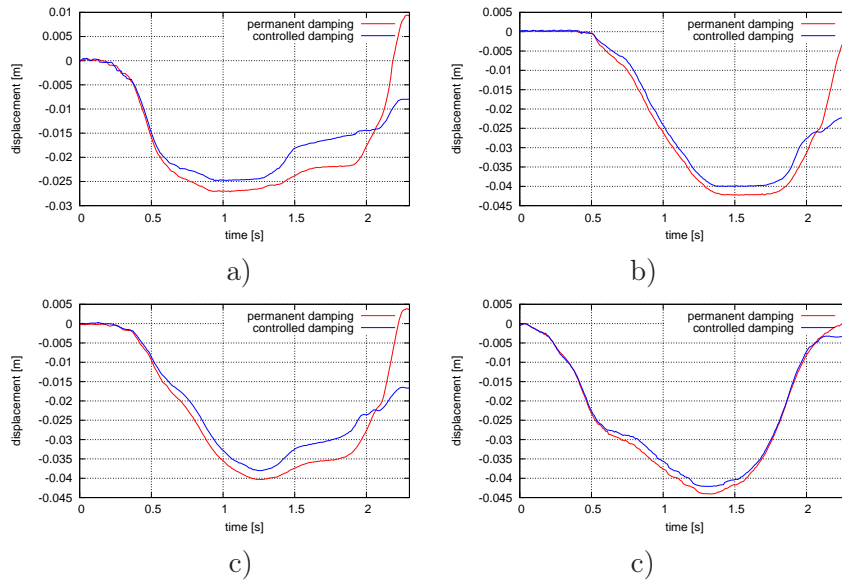


**Figure 5.28.** Displacements in time at  $v = 2 \text{ m/s}$ ,  $a = 7 \text{ m/s}^2$  in the 1st (a), 2nd (b), 3rd (c) point, and at the mass trajectory (d).

considering the fact that the load had to be first accelerated to the traveling velocity and finally decelerated before the end. The distance passed at the highest speed was short. Lower speeds allowed accelerating the inertial load faster. Then, although the segment of the constant speed is longer, at the same time lower speed exhibits the phenomenon less (Fig. 5.18). The improvement of damping in theoretical simulations of longer beams reaches 40%. In the case of the parameters in our experimental test stand, the gain is about 10%. The results would be better for a denser fluid and a higher damping coefficient. In such a case, the amplitudes permanently damped and controlled could reach the ratio 2:1.

Several disadvantages worsen our results. The complex velocity–force relation of the dampers is the first weak point. The second question is the high sensitivity of the system to certain parameters. Local minima establish the shape of the control functions that result in the objective function’s being significantly higher than the global minimum.

Further research and applications could consist in replacing the set of dampers with continuous material of variable rheological properties. Unfortunately, the fabrication of such a physical material is a challenge in itself.

### 5.3. Rotating Shaft

The real structure under consideration is here simplified. The example of the model is depicted in Fig. 5.29. The model of the shaft, however, will first be reduced to the shaft of a uniform cross section, without concentrated masses placed on it. Only in such a case can we successfully carry out the mathematical analysis. First we will consider the problem with an excitation applied to the point A and with a single damper placed at the point B (Fig. 3.14).

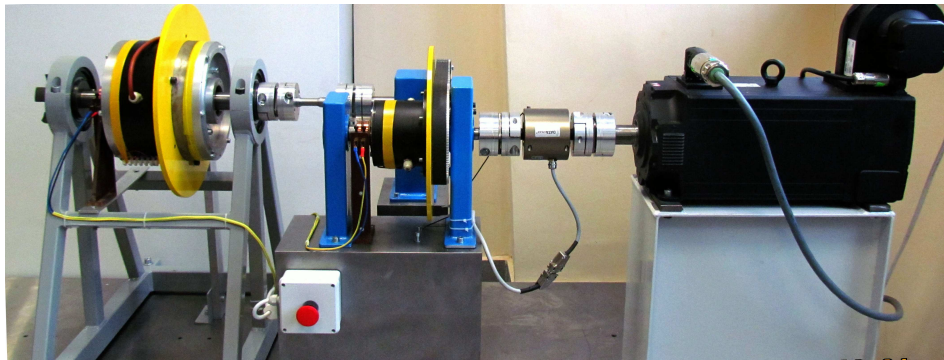


Figure 5.29. The test stand.

#### 5.3.1. Optimal Control Problem for the Vibrations

In this section, we will not give a detailed discussion of the mathematical aspects of the solution method based on control theory. We will rather focus our investigation on the engineering efficiency of the solution when are finally applied to the real structure. It, however, must minimise the objective function in an efficient range.

The control of the system can be performed in several ways. The parameters of the system, i.e., the mass and the damping of the passive absorber, can be chosen during the design stage as constant values based on the optimisation procedure. In more complicated damping systems, the damping can vary in time in a periodic way. Usually the on-off technique is used. However, the magneto-rheological dampers allow a fractional action. The higher controlled switching frequency of dampers required by high frequency vibrations practically limits the efficiency of the control method. The delay of the action of controlled dampers limits the applicability of the solution. However, in our practical test, its efficiency was demonstrated throughout the entire frequency range investigated, i.e., up to 80 Hz.

From the engineering point of view, the following control functions can be essential:

- limited stress in the shaft as the basic strength condition  $\tau(x, t) < \tau_R$ , for arbitrary points  $x$  and times  $t$ ,
- bounded natural frequencies of the structure  $\omega_L < \omega_i < \omega_U$ ,  $i = 1, 2, \dots, N$ , where  $N$  is the number of first natural frequencies being considered,
- limited amplitudes of angular displacements at selected points or throughout the entire structure.

Here, we consider a vibrating shaft in  $\Omega = \{x : 0 \leq x \leq L\}$ , subjected to a load distributed on its surface. The state of such a system is the rotational displacement field  $\varphi(x, u, t)$ , and the control input  $u(x, t)$  is the damping coefficient of the damper. The objective of the control is to distribute the damping over time to achieve the desired vibrations, here denoted by  $\varphi_d(x, t)$ . We assume a finite time horizon. The optimisation problem can be written in the following form.

$$\text{Minimize } J = \frac{1}{2} \int_0^T \int_{\Omega} [\varphi(x, u, t) - \varphi_d(x, t)]^2 dx dt \quad (5.11)$$

$$\begin{aligned} \text{subject to the constraints } \quad & \frac{\partial^2 \varphi}{\partial t^2} + u \frac{\partial \varphi}{\partial t} - \frac{\partial^2 \varphi}{\partial x^2} = f \quad \text{on } \Omega, \\ & \varphi|_{t=0} = \varphi_0 \quad \text{on } \Omega, \\ & \left. \frac{\partial \varphi}{\partial t} \right|_{t=0} = \dot{\varphi}_0 \quad \text{on } \Omega, \\ & \varphi = 0 \quad \text{on } \partial\Omega, \\ & u \in U. \end{aligned} \quad (5.12)$$

This minimises displacements of a linear system of differential equations in a quadratic form. This problem is a linear quadratic hyperbolic control problem with distributed control. The treatment of these type of problems is much more difficult, due to the weaker smoothing properties of the associated solutions.

Most of the numerical algorithms developed for the optimisation of partial differential equations are dedicated to convex problems, in particular to

problems where the objective function is quadratic. There are a few reasons for this. The most important reason is that the convex problem has a unique solution and, therefore, gradient methods can be used. Moreover, quadratic functions enable us to derive simple formulae for the gradients by introducing the adjoint state. It is also worth mentioning that in such a case, the partial differential equation for the adjoint state reflects the properties of the state equation.

For practical reasons, we adopt an objective function which minimises the amplitudes of the torque at a specified point. We will take  $n$  time intervals per period  $T$  and denote by  $c_i, i = 1, 2, \dots, n$  the damping level in each period. Then our problem is defined as follows:

$$\begin{aligned}\Omega &= \{x: 0 \leq x \leq 1\} , \\ \partial\Omega &= \{0, 1\} , \\ 0 &\leq c_i \leq 1, \quad i = 1, 2, \dots, n,\end{aligned}\tag{5.13}$$

with the governing Eq. in (5.12) having the form

$$\rho I \frac{\partial^2 \varphi}{\partial t^2} + c \frac{\partial \varphi}{\partial t} - GI \frac{\partial^2 \varphi}{\partial x^2} = f(t) \quad \text{on } \Omega .\tag{5.14}$$

Let us now try to verify whether variable damping reduces the amplitudes. The single period is divided into intervals. Variable damping is applied to each interval and its values are limited:  $0 < c \leq 1$ . Successive subdivisions result in lower amplitudes. However, we notice a high sensitivity of the solution to the control parameters. The functional is almost flat and local solutions are usually found. Gradient tools usually fail. For example, the well known package IPOpt for large-scale nonlinear optimisation performed by the interior point method exploits the first and the second derivatives. If no Hessians are provided, IPOpt approximates them using numerical methods. It is efficient at finding local solutions in large scale problems. In our case, the Monte Carlo method or genetic algorithms give significantly better results at early computational steps. Then IPOpt was used for the precise solution, taking as a starting point just the Monte Carlo solution. Successive time refinements into 10, 20, and 40 subdomains reduces the objective function to 439, 401, and 377, respectively (Fig. 5.30). The damping function takes on an almost harmonic shape with double the frequency of the displacement solution.

Let us use more terms of the Fourier expansion. In this case we must use numerical time integration methods. This semi-analytical solution allows us

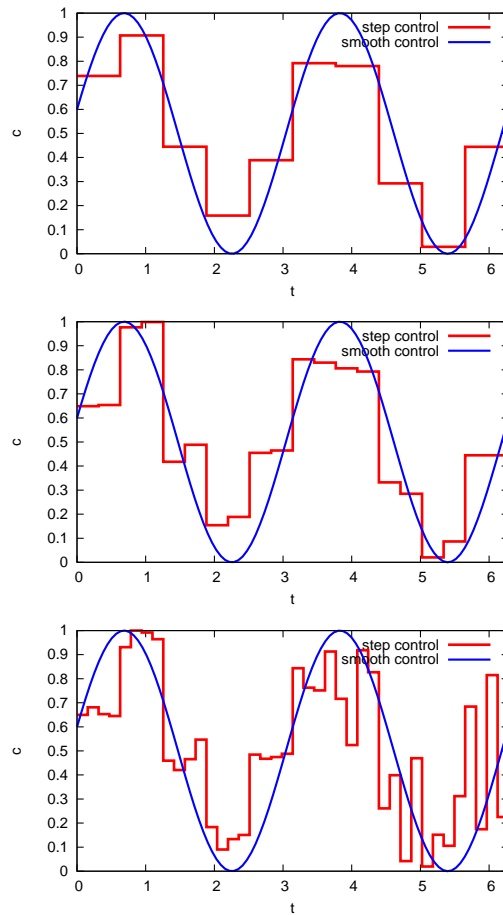


**Figure 5.30.** The control of the damper in refined subdivisions of the period of vibrations.

to estimate the error of our simplification and perform the analysis for real objects.

The finite element model was used for numerical verification of the previous analytical results. The shaft was split into 60 segments. The external load was applied to the node along  $1/4$  of its length and the damper was fixed for  $3/4$  of the length. Furthermore, the right-hand end was elastically supported with a relatively small spring  $k_{\varphi}=20$  Nm. We use the bang-bang control of the damping. The action of the damper is demonstrated in Fig. 5.31. The significantly high amplitudes of shear strain when undamped decrease in the case of an action of the damper which is permanent in time. However, the action which is variable in time reduces the deformations by

20%–50%. The applied control coincides with that obtained with the analytical model (Fig. 5.30). The Newmark method requires a  $\beta$  higher than  $1/4$ , because of the unconditional stability criterion in the case of no stiffness coefficient in the joined mass of the damper.

### 5.3.2. Experiment

The experimental verification of the theory was performed on the test stand. It differs from our previous model, since it has not a uniform cross section area and has point masses. We will try to apply our control technique to this real structure. The laboratory drive system presented in Figs. 5.29 and 5.32 imitates the functioning of an industrial rotating machine. The principle of the reduction of vibrations with the additional rotary inertia fixed to the main system with dampers and the early tests on the presented stand were described in [2]. The power is transmitted from the servo-asynchronous motor to the driven machine tool in the form of an electric brake. The drive system, which is made up of a multi-segmented shaft, is supported by bearings. It contains an electromagnetic overload coupling, two multi-disk elastic couplings with built in torque meters, two rotary dampers with magneto-rheological fluid, and a measurement control system. Moreover, this drive system is equipped with two inertial disks with adjustable mass moments of inertia and the possibility of axial positioning. This enables us to tune the drive train to the proper natural frequencies. The control voltage is applied to the magneto-rheological damper with sliders. The external magnetic field acts on the fluid inside the damper. Consequently, the characteristics of the magneto-rheological fluid are changed, in a way that controls the torsional vibrations. Since the average rotational speeds of the ring and of the shaft are similar, only small wearing effects can be expected and vibrations can be suppressed without significantly influencing the rigid body motion of the drive system. The measurement-control system consists of voltage amplifier controlled in real time by a computer using the appropriate converting systems. This enables us to monitor and register all the measurements. This is possible through the use of a control-communication unit by means of the TCP/IP protocol. The measurements were taken with frequencies above 15 kHz. This allowed accurate detection of even very rapid changes in torque. The torques are non-contact measurement. The computer carried out real time FFT analyses of the interval lengths per second and recorded the values of the two major peaks of the FFT. This allowed us to keep the value of the dominant peak, depending on the amplifiers of the control signal voltage.

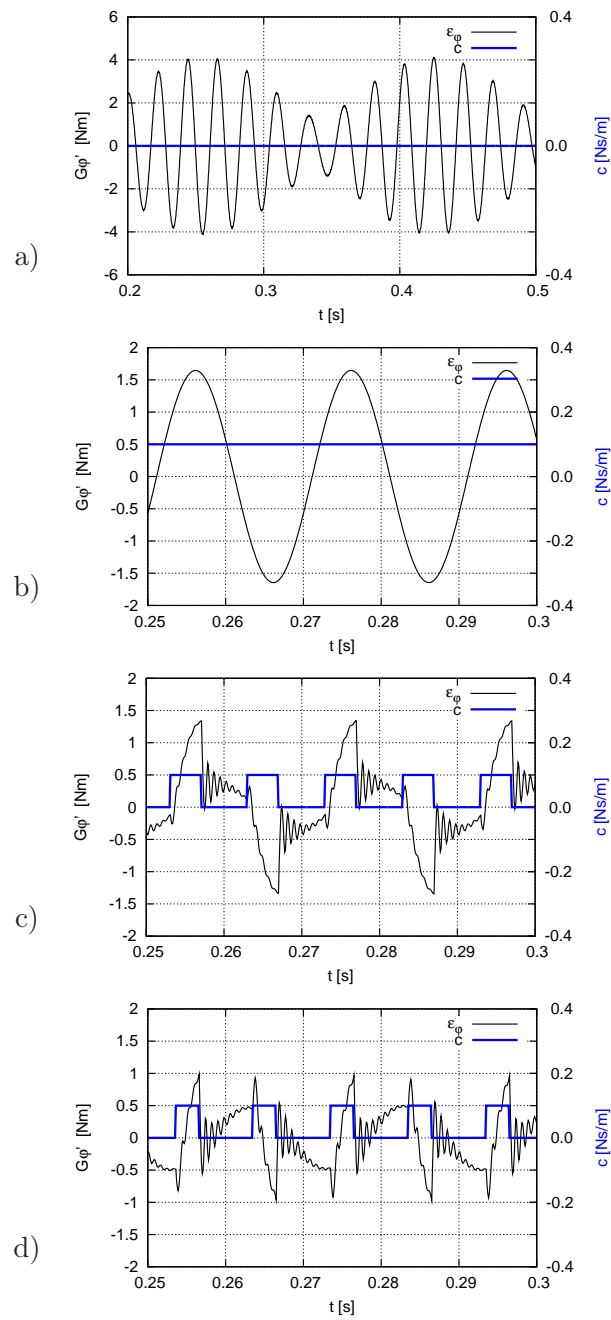


**Figure 5.31.** Torque in the case of: a) no damping, b) continual damping, c), d) selective damping.

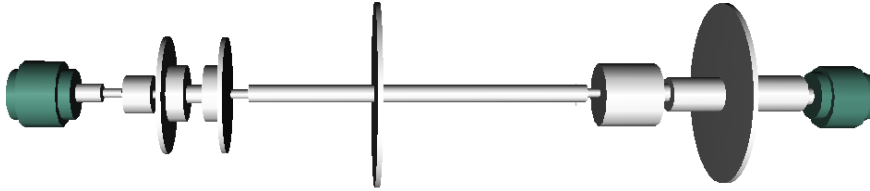


**Figure 5.32.** The scheme of the test stand.

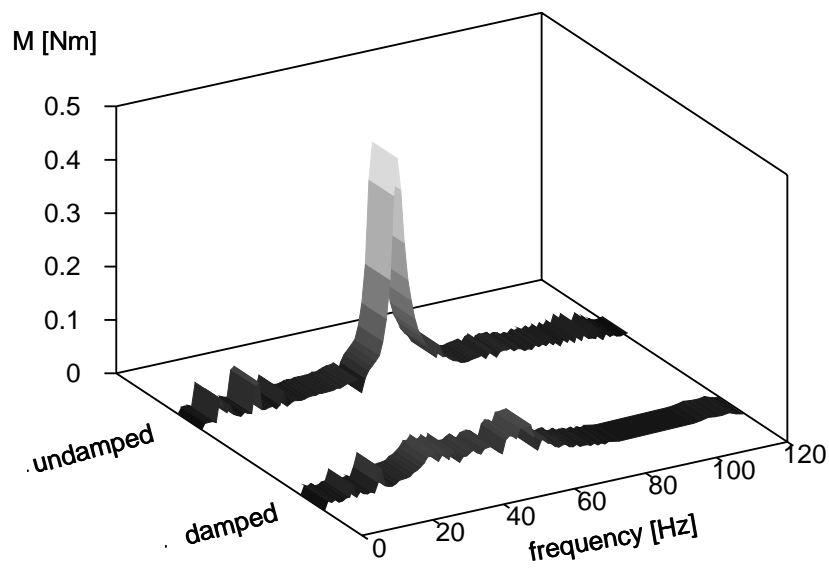


**Figure 5.33.** Maximum of the spectra for the undamped system and the continually damped system.

First let us compare the responses of the undamped experimental stand excited over a wide range of frequencies with those of the same system when continually damped at a level of  $c = 0.5$  Nms. Figure 5.33 shows, for both cases, the maxima of the spectra obtained for frequencies of excitation up to 200 Hz in steps of 1 Hz. The advantage of damping is evident. Below, we will consider two selected excitation frequencies: 45 and 50 Hz.

The left hand end of the shaft was excited by a driving motor with a sine torque. Its amplitude was set to 1 Nm. The frequency was set within the range 30–60 Hz. The right hand end was terminated with an electric brake. At this point, the boundary condition  $\varphi(L, t) = 0$  was used. This condition can be changed in other tests and, for example, a constant rotational velocity can be imposed. However, we can always shift our results as a rigid body motion.

Below we present the system response for the case of continual damping and for the case of a rectangular input signal applied to the damper. Its form is depicted in Fig. 5.34. Figure 5.35 shows the torque registered with constant and periodic damping of the damper, with excitation 50 Hz. The spectral analysis of both the response to constant damping and the response to periodic damping is presented in Fig. 5.36. We notice the advantage of the periodically activated damping. The difference between both spectra is clearly visible in Fig. 5.37. The improvement, i.e., the reduction of torque response, reaches 10%.

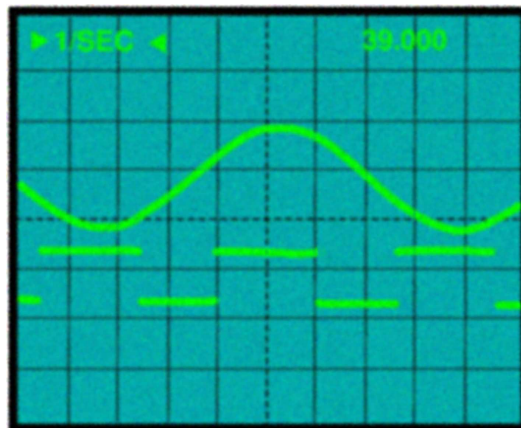


**Figure 5.34.** Example of rectangular input signal applied to the damper (beside a sine signal of excitation).

Another set of tests was carried out for rotation of the driving motor with the constant frequency  $f=45$  Hz. The torque in time in the case of both the constant and periodic damping is depicted in Fig. 5.38. The vibrations with periodic damping exhibit 15% lower amplitudes. The spectral analysis of the system response yields the same conclusion as in the previous case (Fig. 5.39). The difference between the spectra is depicted in Fig. 5.40.

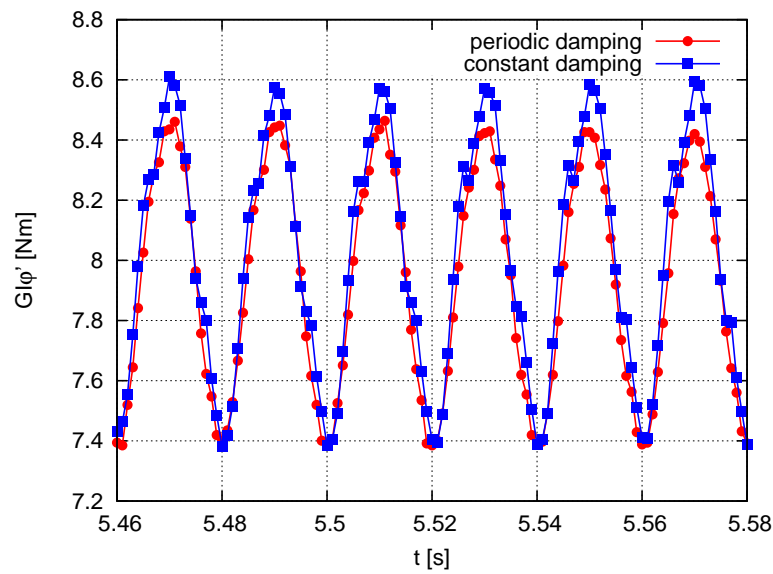


**Figure 5.35.** Torque in time experimentally registered with constant and periodic damping of the damper, excited with 50 Hz [2].

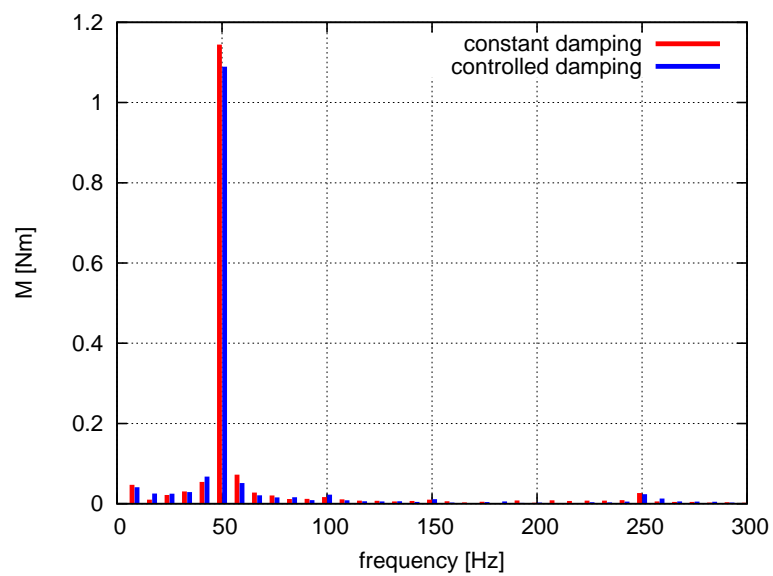


**Figure 5.36.** Comparison of torque spectrum excited with 50 Hz in the case of constant and periodic damping [2].

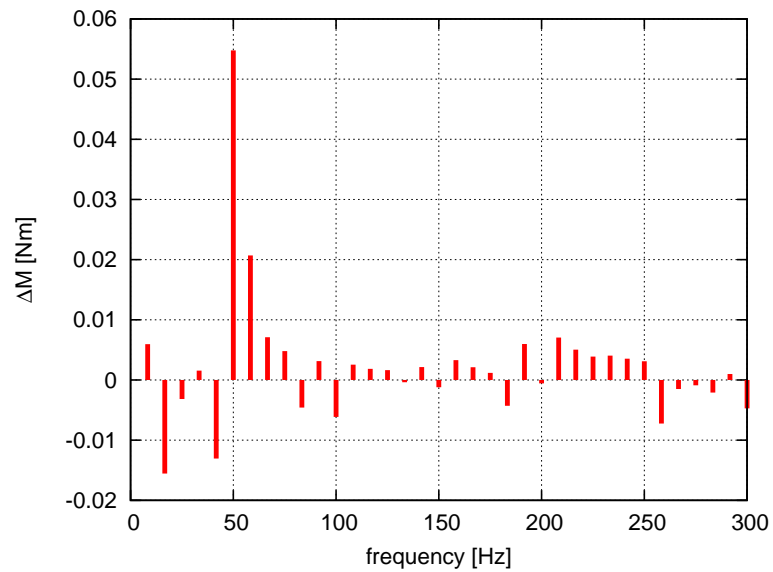


**Figure 5.37.** Difference in spectral analysis of the torque response excited with 50 Hz in the case of constant and periodic damping.

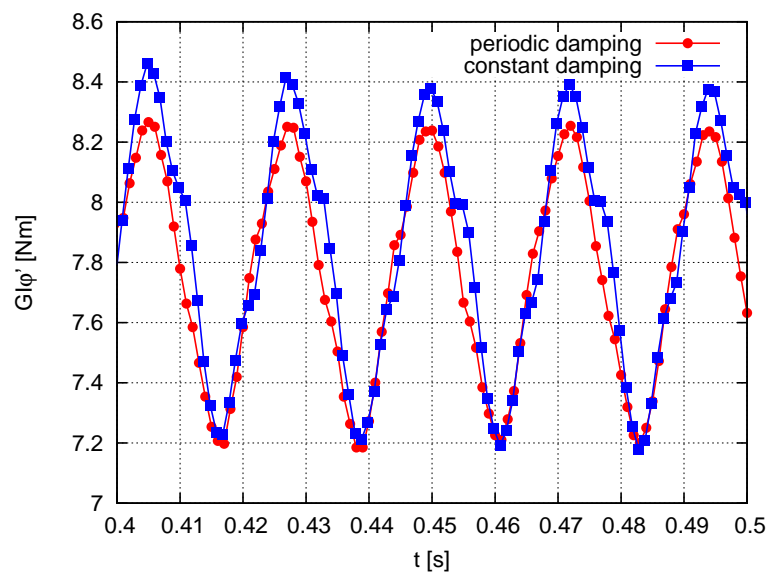


**Figure 5.38.** Torque in time experimentally registered with constant and periodic damping in the damper, excited with 45 Hz [2].

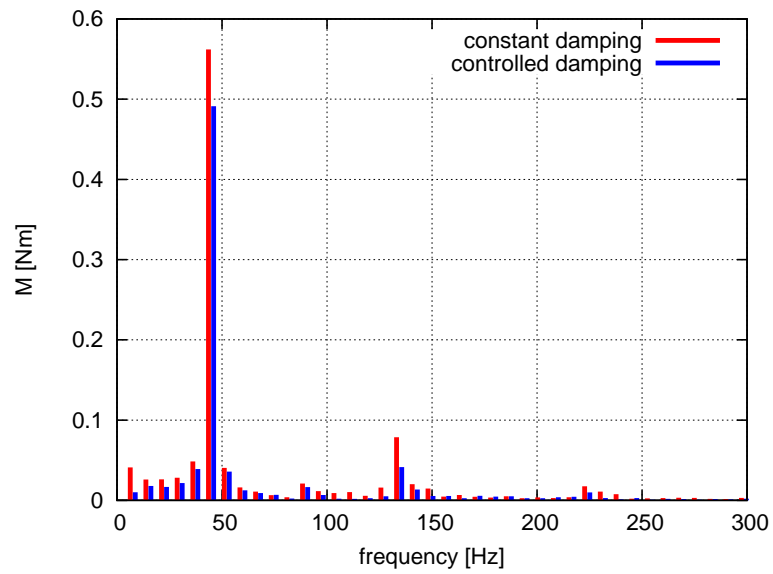


**Figure 5.39.** Comparison of torque spectra excited with 45 Hz in the case of constant and periodic damping.

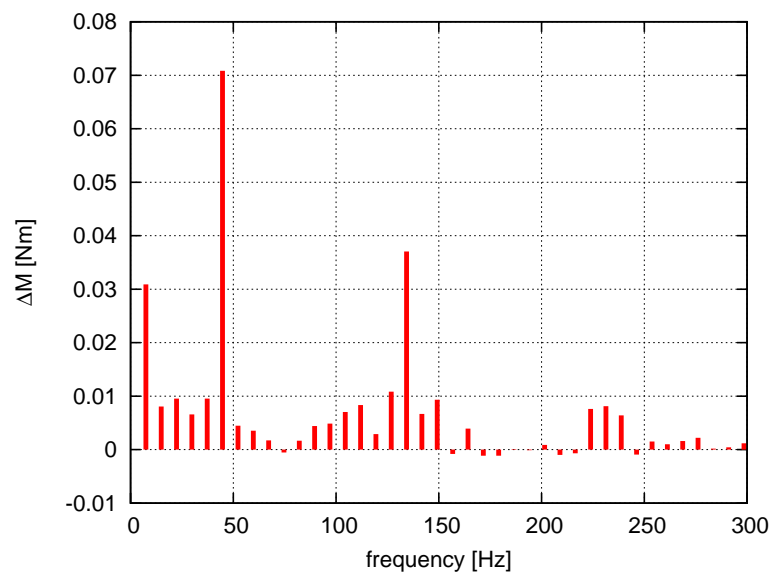


**Figure 5.40.** Difference in spectral analysis of the torque response excited with 45 Hz in the case of constant and periodic damping.

## 5.4. Sandwich Beam with Magnetic Elastomer

The control strategy, in a general case, depends on the type of the structure, the geometry and topological scheme, boundary conditions, rheological models of used material, initial conditions and the type of excitation. In our research we will prove the efficiency of the controlled damping in the case of free damped vibrations, in relation to the permanently damped structure.

Here, we will consider a vibrating beam in  $\Omega = \{x : 0 \leq x \leq L\}$ , subjected to initial displacements. The displacement field being reduced  $w(x, u, t)$  depends on the control input  $u(x, t)$  that influences the shear stiffness of the filling material. The objective of the control is to distribute the shear stiffness  $G(x, t)$  over time to achieve the highest damping of vibrations. In our problem the filling core material has a uniform shear stiffness over the length. It can only vary in time. We assume a finite time horizon. The optimisation problem can be written in the following form:

$$\text{Minimize } J = \frac{1}{2} \int_0^T \int_0^L [w(x, u, t) - w_d(x, t)]^2 dx dt \quad (5.15)$$

subject to the constraints

$$\begin{aligned} \frac{\partial^4 w}{\partial x^4} - gY \frac{\partial^2 w}{\partial x^2} + \frac{g}{\eta b} \frac{\partial u_3}{\partial x} + \left[ \frac{\mu}{D_t} + \delta \left( x - \frac{L}{2} \right) \frac{m}{D_t} \right] \frac{\partial^2 w}{\partial t^2} &= 0, \\ \frac{\partial^2 u_3}{\partial x^2} - \frac{g}{b} u_3 + gY \eta \frac{\partial w}{\partial x} &= 0, \\ w(x, 0) &= w_0(x) \quad \text{on } \Omega, \\ w &= 0 \quad \text{on } \partial\Omega, \\ u &\in U. \end{aligned} \quad (5.16)$$

The above problem displacements of a linear system of differential equations in a quadratic form. This problem is a linear quadratic hyperbolic control problem with distributed control. The treatment of these type of problems is much more difficult, due to the weaker smoothing properties of the associated solutions.

Most of the numerical algorithms developed for the optimisation of partial differential equations are dedicated to convex problems. The solution is simply obtained if the objective function is quadratic. There are a few reasons for this. The most important one is that the convex problem has

a unique solution and, therefore, less or more efficient gradient methods can be used. Moreover, quadratic functions enable us to derive simple formulae for the gradients by introducing the adjoint state.

For practical reasons, we assume an objective function which minimises the amplitudes of the displacement at a midpoint. We will take  $n$  time intervals per observation time  $T$  and denote by  $u_i$ ,  $i = 1, 2, \dots, n$  the control variable in each period  $i$ . Then our problem is defined as follows:

$$\text{Minimize } J = \frac{1}{2} \int_0^T [w(L/2, u, t) - w_d(L/2, t)]^2 dt \quad (5.17)$$

$$\Omega = \{x: 0 \leq x \leq L\} ,$$

$$\partial\Omega = \{0, L\} ,$$

$$0 \leq u_i \leq 1, \quad G_i = G_{\text{low}} \cdot (1 + 0.2 u_i) \quad i = 1, 2, \dots, n ,$$

with the governing Eq. (5.16).

In our numerical implementation of the optimisation problem we divide the limited period of observation into short intervals of identical length. In each interval the constant control function is assumed. We search for values in these intervals. The higher number of intervals is assumed, the more precise resulting control function is obtained. In the case of steady state vibrations subjected to an oscillatory force, we can successfully adjust the control to a single period of vibrations. In the case of free vibrations being controlled by a chosen material parameter, each action modifies the form of vibrations in successive cycles. Both the period of vibrations and the function of displacements in time are changed. For this reason we must consider several successive cycles and the entire process must be treated homogeneously.

Our problem is characteristic of the following features:

- the change of one control (decision) variable at a particular time influences the response of the remaining process, starting from that moment,
- less acceptable local response can result in advantageous entire response,
- neighbouring different values can assume radically different values, although mostly they have similar values,

- optimum solutions can be achieved for zero-one control variables,
- the objective function is very sensitive to control variables.

The elongated observation requires higher number of control variables. We propose the observation of four cycles divided into 40–400 intervals. Since our objective functions are not convex, the known computational methods for minimisation are ineffective (for example IPOpt package). First attempts showed the efficiency of random methods. The simple Monte Carlo method is, unfortunately, inefficient. The increased number of variables dramatically diminishes the convergence rate. Genetic algorithms, which seems to be good for some problems of minimisation, in our case also fail. We can explain the limited efficiency of the known algorithms with particular features of our task. The process is continuous in time and locally estimated control function can be demolished by few variables re-established in the proceeding moments. The change of the period of vibrations is a sufficient reason of such a scenario. That is why we optimise the problem in small groups of variables, usually defining values of the control function in successive moments. Such subsequences of variables have alternating length and move along the time of simulation, and from time to time these subsequences contain variables from the entire set, i.e. inconsecutive.

The control problem (5.15), (5.16) was computed with two levels of shear stiffness of the core:  $G_{\text{low}} = 45 \cdot 10^3$  Pa,  $G_{\text{high}} = 1.2 \times G_{\text{low}}$ . The remaining data are following: length  $L = 1.44$  m, width  $b = 0.04$  m, height  $h_1 = 0.5 \cdot 10^{-3}$  m,  $h_2 = 5 \cdot 10^{-3}$  m,  $h_3 = 0.5 \cdot 10^{-3}$  m, point mass  $m = 0.740$  kg, Young modulus of outer layers  $E_1 = E_3 = 69 \cdot 10^9$  Pa. The initial deflection of the end of the beam  $w_0 = 0.06$  m.

Small number of decision variables results in sufficiently accurate normalised control function (Fig. 5.41a). Increasing precision improves shapes of slopes in the diagram. All the values practically vary between extreme values, i.e. zero and one. Our control requires activation at times of extreme displacements and switching off at times of static equilibrium state, i.e. after 1/4 of the vibration period. The action of the activated magnetorheological elastomer is carried on during half of the total time. For comparison diagrams in Fig. 5.41 depict vibrations without control and with permanent control. It is obvious that the structure vibrating with constant-in-time low or high shear stiffness of the inner layer and excited with the same initial deflection differ only in period of vibrations.

If the form of the control function is known, we can replace the great number of variables that constitute it with much smaller number of variables that define limits of zero-one rectangular periods. In such a case we can use

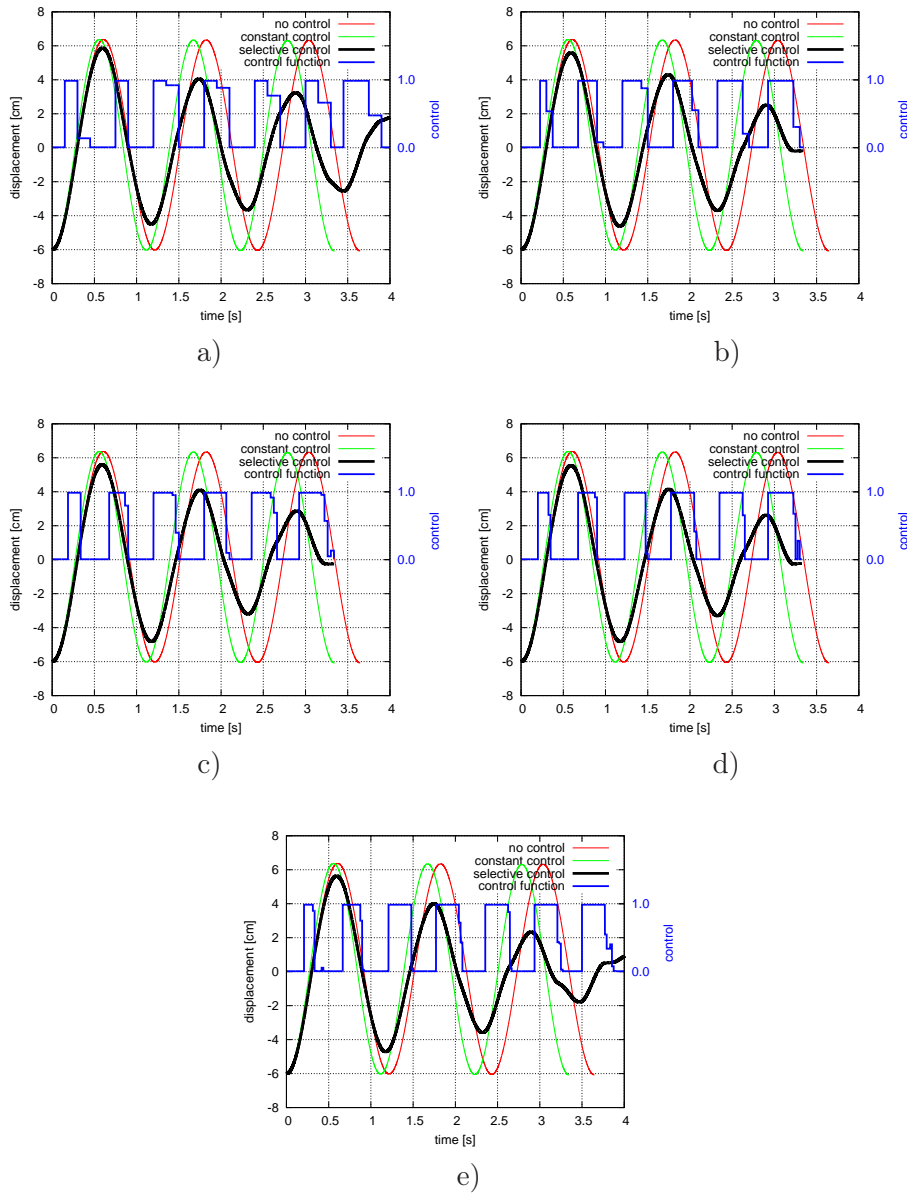


**Figure 5.41.** The control function computed with partition of the time horizon into a) 40, b) 80, c) 160, d) 240, and e) 480 time intervals.

ten or twenty variables instead of about 200. This technique was previously applied to a beam supported with a set of dampers, controlled semi-actively [5, 6].

Our control function that enables the reduction of amplitudes differs from the solution of a similar problem described in [2]. The enhanced damping of rotating shaft controlled with magnetorheological dampers occurred with sinusoidal control function.

#### 5.4.1. Experimental Verification

The experiments were carried out in order to validate, whether by placing the magnetorheological elastomer at the tip of the beam the overall damping ratio of the structure could be increased. Theoretically obtained control strategy for the smart core was verified and evaluated on the fabricated beam. The laboratory stand (Fig. 5.42) intended for the research of free vibrations of beams consists of a fixture frame, supported firmly to a steady base plate. A massive mount, acting as mechanical vice attached to the frame, allows suspending the tested beam vertically in a clamped-free configuration. In order to set initial displacement of the beam, a holding band was connected to the free tip of the beam. The band was strained to give the initial transverse displacement of 0.06 m. The data acquisition starts when the holding band is released and the beam start to oscillate around the equilibrium point. The component of the displacement of the amplitude was the basic, directly measured parameter. The displacement was measured at three points (top, middle and bottom of the beam) with dedicated laser sensors, with resolution up to 8  $\mu\text{m}$  and 10 kHz sampling frequency. The measurement system featured functions for compensation of the inaccuracy of measurements up to 15° of inclination angle. A 16-bit data acquisition card connected to the computer was used to record the measurement results. The Programmable Logic Controller (PLC) with relay outputs allows to directly program the cycles of turning the actuators on and off, depending on the control strategy. The photo of the real, deflected specimen and measurement system is presented in Fig. 5.43.

The parallel face beams are made of aluminium of Young modulus  $E = 69$  GPa. Both of them are 720 mm long, and have a rectangular cross-section 40×0.5 mm. The beams are connected at the tip by an magnetorheological elastomer element of dimensions 40×20×6 mm, which weights 20 g. The magnetorheological elastomer was custom fabricated, isotropic material of density 3560 kg/m<sup>3</sup>. The iron particles fraction was 8% of the volume. The matrix was made of rubber, cured for 20 min at 145°C. The shear modulus

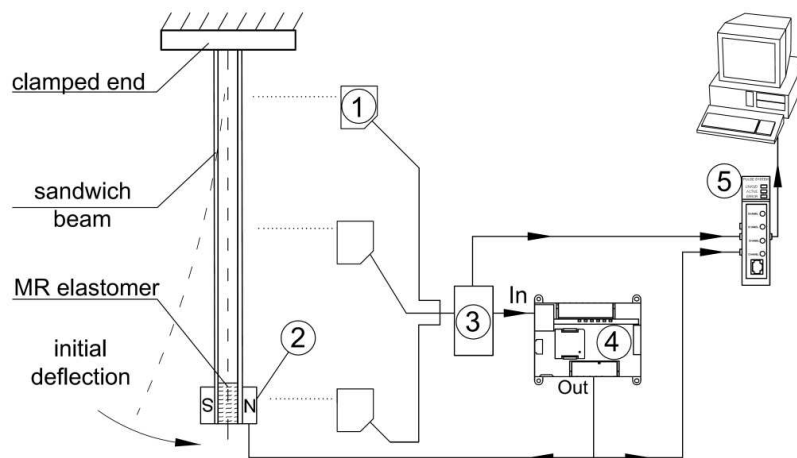


**Figure 5.42.** Schematic diagram of the experimental setup: 1 – laser displacement sensors, 2 – electromagnets, 3 – displacement signal amplifier, 4 – PLC controller, 5 – data acquisition system.

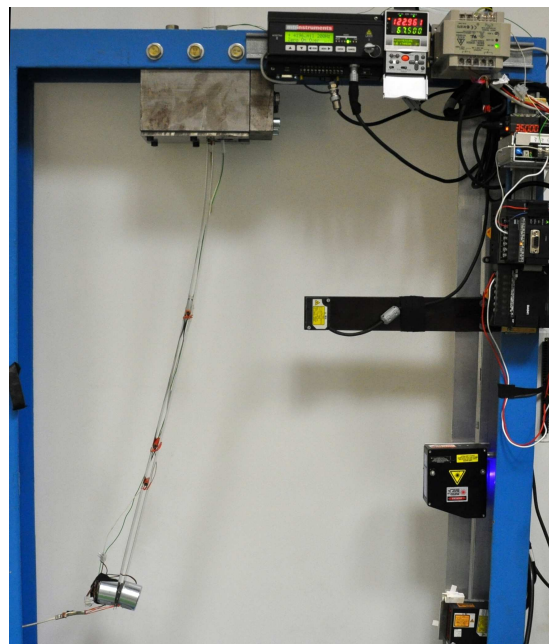


**Figure 5.43.** Photography of the deflected sandwich beam with embedded magnetorheological elastomer.

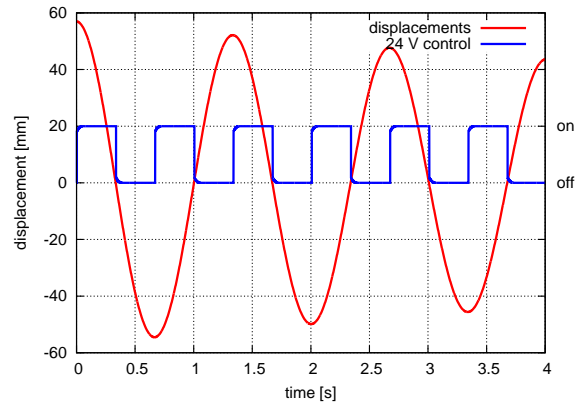


**Figure 5.44.** Control signal over time for semi-active control of the damping.

of the elastomer is  $G = 310$  kPa for no magnetic field, and  $G = 340$  kPa for magnetic field induction of 0.5 T, which is the maximum approachable value. Two island-pole electromagnets were used as actuators to control the properties of the smart core in a desired manner. They were also treated as a 0.37 kg point mass which decreases the natural frequency of the system. Each of the magnets are placed on the opposite side of the beam. The magnets are circuited in a way that the first magnet's pole is N-type polarised, and the other magnets pole is S-type. That type of configuration (Fig. 2.35) increases the maximum value of the induced magnetic field flux density between poles up to 0.5 T and creates a field flux  $\Phi$  that is normal to the sheared area of the elastomer.

The presented results of the displacements in time are considered for the tip of the beam, where the maximum amplitude occurs (signal from the bottom laser sensor), as only the 1st mode of vibration was excited. The On/Off control was performed, switching the magnetic induction between 0 and 0.5 T in the moments as presented in Fig. 5.44. The control signal was applied according to the numerically determined strategy, i.e. it achieved high level at extremal deflection and low value at zero displacement state.

Figure 5.45 illustrates first segment of 30 seconds of vibration. The presented plots show that the magnetic field affects the amplitude of the displacement of the beam's tip for initial deflection 0.06 m, in three different cases: MRE not activated, MRE turned constantly on, and MRE activated in selected moments. The case of free vibrations of a beam with the non-activated smart core is treated as the reference measurement. In this case the only damping mechanisms were related to the shear deformation of the non-activated MRE.

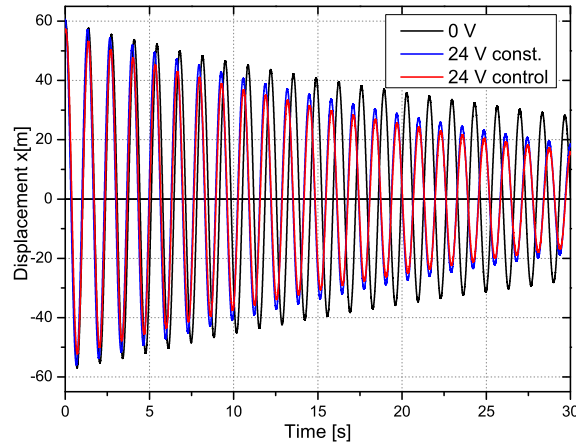


**Figure 5.45.** Displacement in time for different states of MRE damping element caused by the magnetic field.

All three curves in Fig. 2.36 exhibit damping. The elastomer, although merged locally in the sandwich beam, causes significant decrease of amplitudes both in constant and periodic magnetic action. The experiment differs in this case from our theoretical analysis. However, the efficiency of the control with a small elastic inclusion, related to the entire length of the beam is effective. Longer observations allowed us to estimate the rate of damping. After 60 s the amplitude of displacement for 0 T is 12 mm, which is a 20% of the initial deflection. If MRE was activated constantly, the amplitude after 60 s of vibrations decreased to 4.2 mm. It is 7% of the initial value. In the controlled case the amplitude dropped to 2.6 mm, i.e. to 4% of the initial value.

#### 5.4.2. Conclusions

The concept of utilising shaped magnetorheological elastomer in order to suppress a particular vibration mode of a three-layered adaptive beam has been validated. The embedded magnetorheological element undergoes changes in its modulus, which influences the apparent stiffness and damping of the whole composite. The material properties are controlled by switching the applied magnetic field. It is evident from theoretical and experimental study that the magnetic field modification affects the stiffness and the damping mechanism. As predicted by the theory, the appropriate vibration attenuation can be more or less efficient, depending on the control strategy.

Mathematical model of the structure with semi-active damping element with field dependent elastic modulus was proposed. The resulting control function has a rectangular on-off shape. Modified shear stiffness of the core layer in the theoretical analysis allows to obtain highly efficient damping. Experimental verification is less efficient since the controlled elastomer is placed only locally at the tip of the beam. The experimental analysis proved the efficiency of the control strategy on the dynamic response, damping capacity and frequency of the system.

The presented semi-active treatment can lead to further improvements of available damping systems and increase number of applications utilising properties of MRE. This gives us a chance of manufacturing a low-cost damping elements, that allow for some shape design flexibility and material tailoring variation to obtain desired dynamical performance and functionality in the structure.

## 5.5. Granular Material

The recent trend is to replace the active force actuators with devices utilising smart materials. This motivates to search for an alternative materials, eliminating disadvantages of commercially available solutions. The smart material proposed in this work is based on the idea of placing loose grains in an airtight elastic envelope, which is then merged between two elastic beams (Fig. 5.46) [1]. The proposed semi-active control strategy allowed reducing the amplitude of vibration up to 40% compared with the passive solution. The dynamic behaviour of the jammed granular materials with an underpressure variable is time were not investigated so far. The motivation for studying the damping parameters of the considered structure is the possibility of using the concept of periodically jamming and unjamming the granular structure to semi-actively suppress any vibrations. Selecting proper moments of switching the state of the granular structure aims at releasing of the strain energy accumulated during deformation. The general idea is similar to switchable-stiffness for piezo-actuators and magnetorheological materials or Prestress-Accumulation-Release strategies [4]. In our research we will prove the efficiency of a controlled damping in the case of free vibrations, in relation to the permanently damped beam.

### 5.5.1. Identification of the Parameters

Prior to solving the optimal control problem, the identification of parameters  $k$  and  $c$  of the structure had to be done. First of all, an experimental research

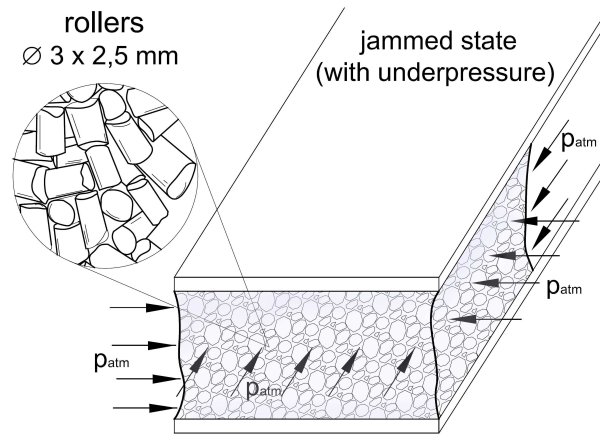


**Figure 5.46.** Construction of the cantilever with granular structure controlled by the underpressure.

of the response of the real cantilever with damping structure treated passively was considered. Four types of granular materials, different in size, shape and material were considered and examined to find the most promising one. The material was subjected to constant value of underpressure, ranging from 0 to 70% of vacuum. For every set value of underpressure, the beam was let to vibrate freely to acquire the desired characteristic. This research took major effort and was described in Chapter 2. The experiments proved that even small change of the parameters can drastically influence the efficiency of damping. The roller granules subjected to underpressure of 0.07 MPa were chosen as the most promising material for the switched damping concept.

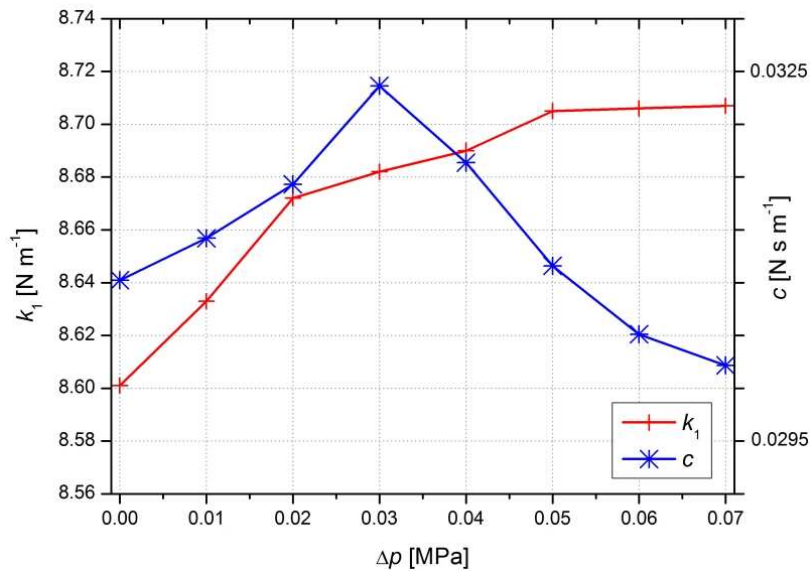
The Table 5.4 presents the computed parameters of the model of the system and estimation error  $\epsilon$ , while the Fig. 5.47 shows how they change for different values of underpressure. The estimation error  $\epsilon$  is computed as the Euclidean norm of the difference between the numerically computed displacement  $w$  and experimental displacement  $\bar{w}$ .

$$\epsilon = \|w(t) - \bar{w}(t)\|^2. \quad (5.18)$$

The minimization problem allows to identify the material parameters in the way similar to the least square method. The first 30 seconds of vibrations are compared with the chosen model of the structure. In computations the

**Table 5.4.** Parameters in the Kelvin-Voigt model for roller filling.

$\Delta p$ [MPa]	$k_1$ [ $\text{N m}^{-1}$ ]	$c$ [ $\text{N s m}^{-1}$ ]	$\epsilon$ [ $10^{-3}\text{m}$ ]
0.00	8.601	0.0308	0.083
0.01	8.633	0.0312	0.086
0.02	8.672	0.0316	0.098
0.03	8.682	0.0324	0.114
0.04	8.690	0.0318	0.104
0.05	8.705	0.0309	0.093
0.06	8.706	0.0304	0.086
0.07	8.707	0.0301	0.083

**Figure 5.47.** Trace of the parameters of the Kelvin-Voigt model.

mean error  $\epsilon$  of the displacement  $w_i$  is obtained as follows

$$\epsilon = \frac{1}{n} \sqrt{\sum_{i=1}^n (w_i - \bar{w}_i)^2}, \quad (5.19)$$

where  $n$  is the number of steps in the simulation. A set of surrogate parameters mimics the qualitative changes of the performance of the original

structure, and shows that the operating conditions can be altered by the underpressure. The stiffness  $k$  is the parameter which is of our greatest interest, as it is responsible for an effective switching control. The theoretical dependency of stiffness over underpressure presented in Fig. 5.47, can be quite well related to the experimental data. The change is monotonic and exhibits saturation, as the underpressure approaches maximum value. On the other hand, the change of damping coefficient  $c$  is not monotonic. The extremes are observed for the mid-values of underpressure, around 0.03 MPa. Compared to the experimental results of logarithmic decrement of damping, one can see that this non-monotonic behaviour is present in the original structure, but far less noticeable. Since these phenomenological models provide only two parameters to be tuned, the parameter  $c$  bonds several mechanism of damping present in the original structure, and is sensitive to the experimental data provided in the optimization problem. However, parameter  $c$  is of much less importance than the stiffness  $k$  when the parametric control is considered as the target application. Probably addition of more complex, nonlinear element to the phenomenological model would allow to extract this behaviour to a separate nonlinear parameter. This would result in decomposing the parameter  $c$  into more variables, including nonlinear friction. Nevertheless, this would far more complicate the identification problem, extend the computational time, and make future optimization difficult. As the switched stiffness is considered, the damping coefficient has far less influence on the results than the stiffness. The non-monotonic change in the experimental results may be connected with the fact, that the compressed granules may exhibit increase in the effective dissipation when the granules are still in the solid-like phase, close to the point where particles tend to roll over each other, demonstrating convective patterns, which would be achieved for the mid-values of underpressure.

### 5.5.2. Adaptive Control Strategy

First we will solve the problem of finding the control strategy for the case when the stiffness  $k$  is the only variable that we modify over time. Then, we can analyse the case when stiffness  $k$  and damping coefficient  $c$  are controlled simultaneously. One can imagine, that there are particular points of switching the variables that will result in an better damping behaviour than other. We assume the time of observation equals 1.5 of the main period of vibrations, which is divided into  $n$  number of time intervals. Then, the  $m$  successive number of amplitudes are to be minimised, preserving the oscil-

latory form of the displacements. The objective function  $I$  for the switched stiffness is formulated as

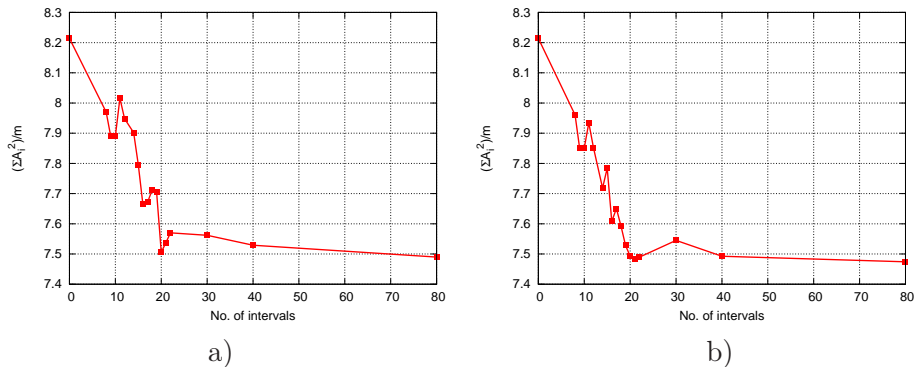
$$I = \frac{1}{m} \sum_{i=1}^m A(k)_i^2. \quad (5.20)$$

For the switched stiffness and damping coefficient, the objective function is

$$I = \frac{1}{m} \sum_{i=1}^m A(k, c)_i^2. \quad (5.21)$$

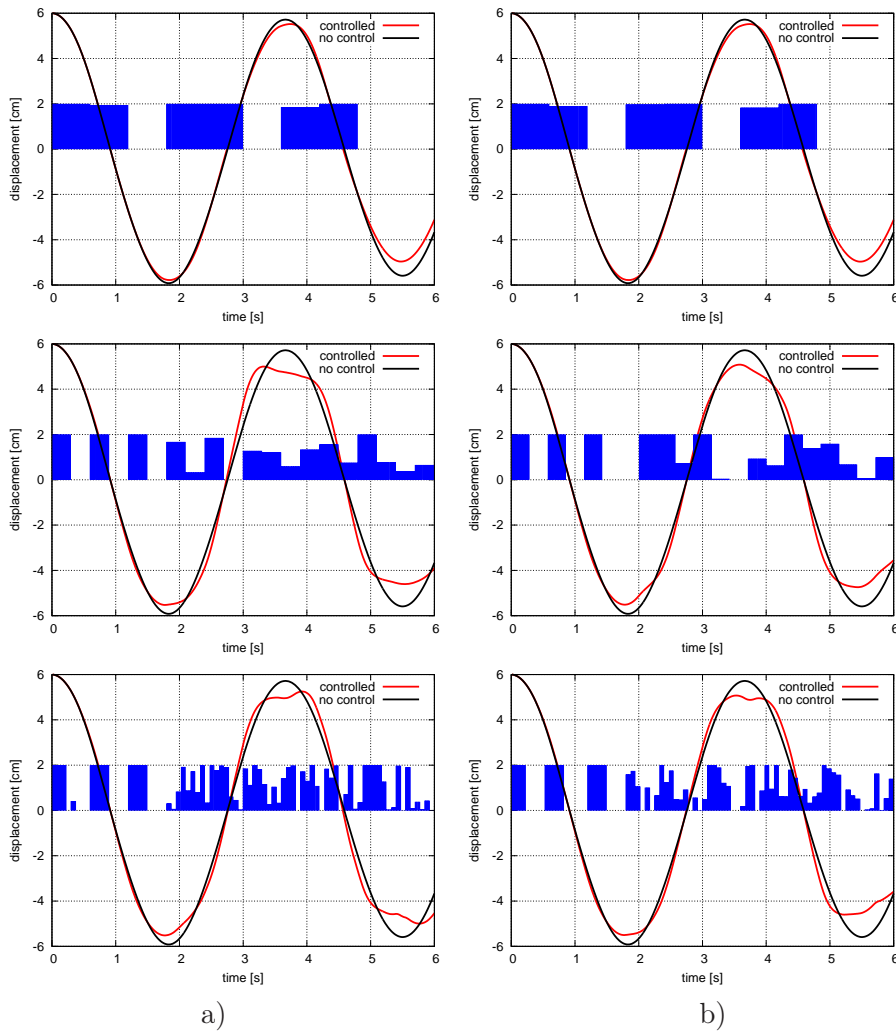
The damping is efficient when the sum of the squared values of the amplitudes significantly decreases. The number of successive amplitudes taken into account should be low to keep the problem simple. The larger number  $m$  would introduce adverse local minima and increase computational time. This would lower the regularity of the observed periodic motion of the beam, as additional cycles would be considered in the optimisation problem, making the solution complicated.

Figure 5.48 shows how does the discrete control of variable  $k$  and both  $k$  and  $c$  affects the results. It is clear, that changing the number of time intervals highly influences the results of the optimisation, so picking up the right number of  $n$  time intervals seems difficult. The first candidate is  $n = 10$  (on both plots), where the curves reach first local minimum. The next minimum indicating better results is achieved for  $n = 20$  and  $n = 21$  for Fig. 5.48a and b, respectively. Higher number of time intervals does not result in much of an additional improvement.



**Figure 5.48.** Results for switching only parameter  $k$  a) and both, stiffness  $k$  and damping coefficient  $c$  b).

Figure 5.49 presents the simulation results without any control (black line) and with control (red line), obtained for the analytical solution of



**Figure 5.49.** Displacements in time for the control of variable  $k$  performed in 10, 20, and 80 intervals (left column a) and control of  $k$  and  $c$  performed in 10, 21, and 80 intervals (right column b).

Eqs. (3.133) and (3.135). The plots in the left column show displacement over time for the case when the stiffness  $k$  is the only decision variable. Three different time resolutions of the control function are considered: 10, 20, and 80 time intervals. The plots in the right column show respective results for the case when  $k$  and  $c$  are the controlled variables. The time was split into 10, 21, and 80 intervals.

It may be noted that the change of the stiffness  $k$  is the major component that contributes significantly to the vibration abatement. The additional influence of the damping  $c$  is rather marginal. The resulting form of the control signal may be simplified by distinguishing dominant stages. In the first stage, when the vibration starts, the control signal is turned constantly on. The control variables (whether it is  $k$  or  $k$  and  $c$  simultaneously) are maximum. Then, after some time, the control signal is rapidly turned off and the control variables are equal to zero. Then, depending on the time intervals considered, the process is repeated, but the moments of switching the control On and Off changes in time. For 10 time intervals the tendency is very clear, and the particular moments of switching can be estimated from the graphs. The control requires activation at times of the extreme displacements ( $\dot{x} = 0$ ) and keeping the signal turned on, until the beam crosses the equilibrium point  $x = 0$ . Shortly after crossing the equilibrium, the control signal can be switched off until the beam reaches another maximum.

For larger number of time intervals the points of switching are not so easy to pick, but some conclusions can be drawn. For the first cycle of the response, when the sinusoidal waveform is regular, it is recommended to keep the underpressure constantly activated, and turn it Off three times, before the beam reaches another maximum deflection point. After the first cycle, further control introduces higher modes of vibration, movement is less regular and thus the control strategy becomes difficult. Optimal damping of higher modes introduces not only switching between the extremes, but also between intermediary values. That type of strategy would be hard to adapt in real structure and made it less operative. Also at some stages, moments of turning signal on and off are very short. This would be hard and impractical to achieve on a physical object, shortening the live time of electromechanical actuators controlling the underpressure. By assuming some hysteresis, the real control signal may be simplified (Fig. 5.51). The switching between two extreme values of vacuum is easy to achieve, and eliminates the necessity to continuously measure and adjust the underpressure in short periods of time. This may be classified as a Bang-Bang control strategies, where the actuator can assume only two states.

### 5.5.3. Experimental Study

The granular structure is connected through the electrovalve to the vacuum pump, supplying underpressure to the accumulator. Proper periodic switching of the electrovalve alternately connects the granular structure to the vacuum source and the atmosphere, resulting in switching between two

extreme values of the pressure. The simplified control strategy was adapted to a Programmable Logic Controller (PLC) with relay outputs, controlling the state of the electrovalve. By constant comparison of the displacement of the beam's tip with the threshold value set in the PLC, underpressure was activated and deactivated in particular moments. The process of evacuating, and supplying the air to the structure takes some time, which results in time lag effect. The delay determines the maximum frequency of the response, and thus the range of potential applications. The shape of the underpressure signal is presented in Fig. 5.51 (bottom waveform). The combination of an efficient vacuum pump, armature and fast response electrovalve allowed to switch the underpressure between 0 and maximum value up to 8 times per second, maintaining desired shape of the underpressure signal. For the described beam 3 switches per second were enough. By applying an underpressure accumulator, even less efficient pump can be used to achieve faster and more sharp shape of the switching waveform. The scheme of the test stand is presented in Fig. 5.50.

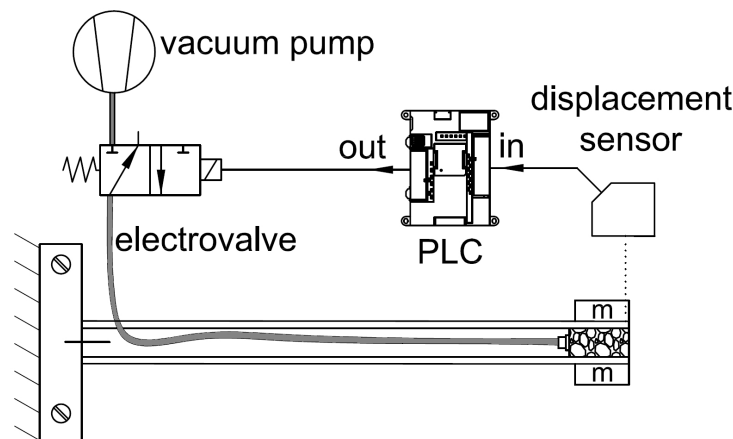


**Figure 5.50.** Schematic diagram of the experimental setup.

The parallel face beams of the specimen are made of aluminium of Young's modulus  $E = 69$  GPa. Both of them are 720 mm long, and have a rectangular cross-section  $40 \times 0.5$  mm. The beams are connected at the end by a 2 mm thin, hermetic elastomer envelope. The envelope is filled with a roller shaped granular material (Fig. 5.46). The dimensions of the damping element are  $20 \times 40 \times 50$  mm. A total of 0.37 kg mass was placed at the tip to decrease the natural frequency of the system.

The presented results of the displacement in time are considered for the tip of the beam. In Fig. 5.51 the particular moments of switching the underpressure are marked. Also the figure shows how does the underpressure inside the envelope change over time as the vacuum is switched.

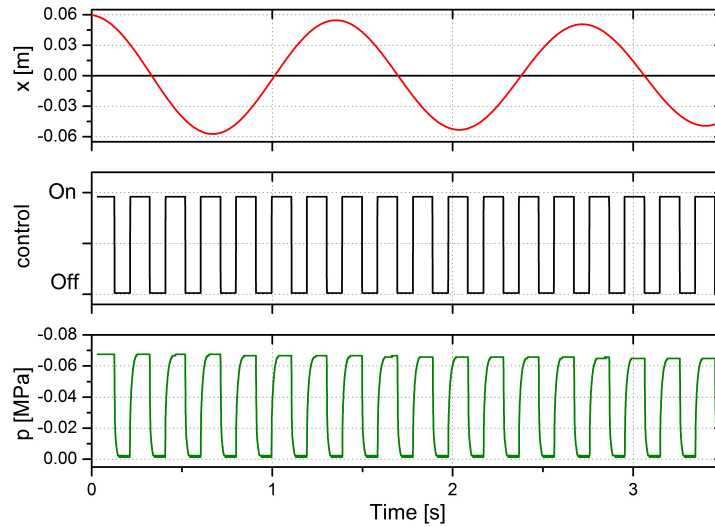


**Figure 5.51.** Displacement, control function and underpressure over time.

In Fig. 5.52 the response for controlled underpressure of the beam with the roller filling was compared with the reference results for one-time, passive selection of constant underpressure 0.07 MPa. The results confirmed that the proposed controlled jamming system outperforms the passive one, and may be efficiently utilised in mitigating the responses of the structure. For the semi-active case, after 60 s of vibration the displacement was suppressed from initial 60 mm to 3 mm (95% drop), compared to 10 mm (84% drop) for the passive damping.

The agreement between theoretical and experimental results was satisfying, nevertheless the damping capacity was less effective than the numerical results. This is the consequence of the modelling simplifications and differences between the assumed model and the real structure. Nevertheless the global trend was correct, and the computed control algorithms were proven to be effective.

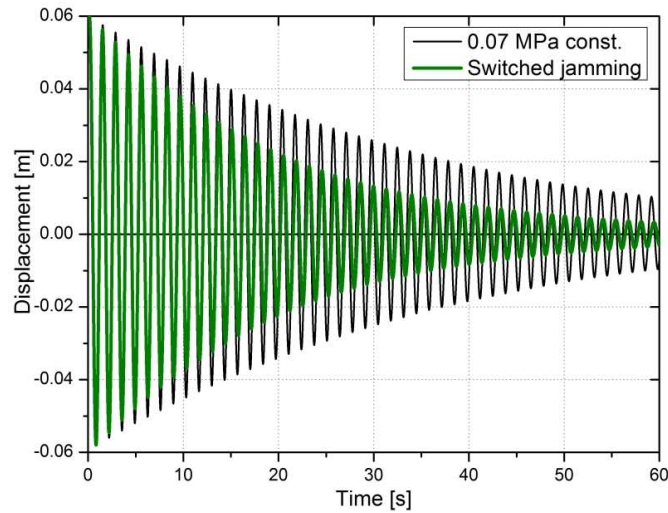


**Figure 5.52.** Displacement for passive and On/Off control.

#### 5.5.4. Conclusions

Due to its conceptual simplicity, effectiveness and low cost, the proposed solution for controlling the mechanical properties of vacuum granular structure is an interesting alternative to classic damping systems based on composites and expensive smart materials. The preliminary results showed that the switched-jamming of the granular materials placed in special envelope may be effectively used to obtain vibration attenuation. The modified Kelvin-Voigt model of the system was proposed and the equations were derived. The optimal control problem was solved, considering the concept of periodically switching the parameters of the system to efficiently attenuate the displacement's amplitude. The resulting control function has a rectangular On-Off shape, which is easy to adapt to a classic electromechanical relay system. The numerical analysis showed that the idea of periodically changing the material properties can be efficient if the switching is presumed in a proper manner. The issue of modelling the structure is still an open problem, and further model development is necessary, including the friction and slips between the grains. The investigated functional material has many application prospects, which provides an impetus for continued research in this area. The applicability is limited to low frequency excitations, since the granules need some time to reorganise. Although the idea presented in this work is in the initial phase, its potential seems to be very attractive and it deserves major attention.



# Bibliography

- [1] M. Bajkowski, B. Dyniewicz, and C.I. Bajer. Damping properties of a beam with vacuum-packed granular damper (doi: 10.1016/j.jsv.2014.12.036). *Journal of Sound and Vibration*, 2015.
- [2] B. Dyniewicz, A. Pręgoska, and C. I. Bajer. Adaptive control of a rotating system. *Mechanical Systems and Signal Processing*, 43(1-2):185–192, 2014.
- [3] B. Dyniewicz, R. Konowrocki, and C.I. Bajer. Intelligent adaptive control of the vehicle-span/track system (doi: 10.1016/j.ymssp.2014.12.007). *Mechanical Systems and Signal Processing*, 2015.
- [4] A. Mróz, A. Orłowska, and J. Holnicki-Szulc. Semi-active damping of vibrations. Prestress-Accumulation-Release strategy development. *Shock and Vibration*, 17:123–136, 2010.
- [5] D. Pisarski and C. I. Bajer. Semi-active control of 1d continuum vibrations under a travelling load. *Journal of Sound and Vibration*, 329(2):140–149, 2010.
- [6] D. Pisarski and C. I. Bajer. Smart suspension system for linear guideways. *Journal of Intelligent & Robotic Systems*, 62(3-4):451–466, 2011.



## Conclusions and Perspectives

Designing lighter, safer and more efficient damping structures which are cost effective, has been in high demand in modern vibroisolation technology. However, the vibration abatement is a complex, and frequently misunderstood subject. From the foregoing examples it can be clearly seen that defining the problem, modelling the system, designing and implementing the proper treatment is effort and time consuming process, which cannot be done by a “hit and miss” approach. Properly designed adaptive structures with smart materials allow significant improvement of the dynamic properties of systems, compared to their passive equivalents. The damping approach using smart materials provides an attractive solution because it is practical and cost-effective when compared with other alternatives. These methods utilise the motion of the system to develop control forces, so the energy requirement is lower than in case of active treatment and the system is safer in the case of malfunction.

The investigation of semi-active and adaptive methods using smart materials for shock isolation and residual vibration control, have been presented in this book. The structures with magnetorheological fluids benefit from the fact that we can control the yield stress of the fluid, and thus alter the damping parameters. For the beam with the magnetorheological elastomer the distinctive feature is the ability to control the shear modulus of the material by varying the magnetic field. For the beam with the granular structure the vibration attenuation is obtained by changing the underpressure value among the granules.

Mathematical models and numerical analysis proved that the idea of periodical changing of material properties can be very efficient if the switch-

ing is presumed in a proper manner. The smooth control functions can be successfully replaced with a periodic on/off switching function (bang–bang type). To demonstrate the validity of the control strategies obtained numerically, the experiments were carried out for the real structures like the rotating shaft, beam with the travelling inertial load, double beam system and sandwich cantilevers. Depending on the type of granular filling and the number of performed switches, it was possible to reduce the amplitude of vibrations 20%–30% faster compared to passive damping. The bang–bang control exhibited the same rate of improvement in the experimental results as in the simulations, although the theoretical form of the control function was applied in practice with a certain inaccuracy.

## 6.1. Perspectives

The elastomers and the granular structures provide some flexibility in the shape design and material tailoring variation to obtain desired dynamical performance and functionality. The change from one state of the elastomer to another takes a short time (order of milliseconds), therefore the MRE are excellent for applications where strong dynamic features are required. The granular materials encapsulated in elastic envelopes can possess almost any suitable shape which allows installing them in irregular-shaped spaces. The applicability of the special granular structures controlled pneumatically is limited to the applications with lower frequency excitations, since the granules need some time to reorganise, and it takes some time to evacuate the air from the envelope. Dampers with magnetorheological fluids can be easily adapted to structures which use classic, viscous dampers. The structures may also benefit from implementing proper control algorithms, based on the presented study of the switching concept. Each of the investigated functional smart materials has many prospective applications and provides an impetus for continued research in this area.

One of the branches of applications of the magnetorheological elastomers and fluids is the aerospace industry in which structures are mostly based on the metallic and composite layered solutions including carbon fibre-reinforced plastics, which have low internal damping. The proposed material and control strategy can be used to mitigate vibrating parts of the plane, and efficiently reduce wind flutter effects.

The automotive industry may also be a potential recipient of both of the proposed damping variants. Vibrations generated by the vehicle drive system and the suspension could be suppressed by self-adaptive absorbers, or smart

lightweight suspension beams, stabiliser rods or suspension bushings in order to reduce the shudder effect. The electrical current could be supplied from the automotive electrical system, while the underpressure could be generated by one of the pumps. It would be particularly useful to adjust the vibration of the adjacent structures in response to the present conditions such as vehicle speed, road type and whether conditions, vehicle load and similar.

The semi-active solution with an efficient control algorithm may also be used for applications where we have to deal with the fast travelling load such as train-track, vehicle-bridge, crane-weight systems or robotic linear guideways which are of a special interest for practising engineers. Existing structures could be reinforced by supplementary supports with magnetorheological elastomers and dampers controlled externally to improve the stability of the structure.

The seismic performance efficiency of the base isolation system, which decouples the civil structures from the ground motion can be highly improved by adapting the concept of smart materials controlled according to the switching strategy. The controlled elastomers with stiffness-tuning ability strive to alleviate limitations of existing passive-type base isolators, which works well on a site with a stiff soil condition, but are not effective at all on a site with a softer soil.

The granular-based system would be preferred in mitigating the low frequency vibrations of a tower pole of a wind turbine, where they can be employed as an environmentally friendly solution operating in relation to time changing wind speed and variable speed mode used in a large scale turbines. For normal operating condition the structure could be damped by the loose granular material, while the switched jamming strategy would be active for an exceeded level of vibrations.

Properly adapted, smart granular damping elements may also be used in intelligent rail ties, speed bumps, marine dock buffers, loading bumpers, fenders in the warehousing industry, pedestrians' walkways, pipeline systems, speed humps and many other types of structures. It is an attractive alternative in semi-active damping due to its conceptual simplicity, potential effectiveness and very low cost. In spite of these benefits, the proposed semi-active damping systems bear some drawbacks, primarily because they are more complex than the passive counterpart and require additional sensors, actuators and controllers. Numerous applications, which make use of controllable stiffness and the unique characteristics of smart materials, will be developed and the efforts will be paid off in the near future.

## 6.2. Recommendations

The numerical results showed that the switching times methods can be very efficient if the proper number of switchings is presumed. The effective damping ratio of the experimental system was very similar to the predicted value considering the mechanical properties of the system. However, there are some aspects found during the investigation that might be worthy of further study, as mentioned below.

The work on the travelling load created a lot of important and previously unexplored problems. It provided the qualitative results that should be extended with more complex models to make the proposed ideas fully applicable. For the travelling load, in practice we require much more complex mathematical model to approach a real physical object. The inertial forces of the object should be included to the governing equation. We could also consider many other control objectives: travel comfort, structural damage of the span, damage of the surrounding buildings. An interesting issue that rises from the work may be posed as the following: find a decentralised control method such that the desired global behaviour of the system is preserved. It might turn out that the optimal passage of a moving load can be achieved by using local interaction between some states and it is not necessary to use centralised computations.

In order to study in details the possibilities of controlling the vibrations of the beams treated with smart material, it is necessary to analyse the response of systems subjected to dynamic exploitation loads and harmonic excitations, for example reproducing the excitation caused by the vehicle riding on the bumpy road, seismic vibrations or environmental load or an impulse-excited system.

The optimal composition and geometric parameters of the damping members, and minimising their weight by selecting their optimal placement can help in maximisation of modal damping ratios and modal strain energies and can lead to significant saving in the amount of used material. The study on core architectures would be interesting. By varying configuration and dimensions of the core and the material of the face sheets of sandwich structures, it is possible to obtain various properties and desired damping performance. The study devoted to the damping performance of the pneumatically controlled granular material is cognitive and it is limited to the most fundamental issues only. In the authors' opinion, further research on the topic is to be highly recommended.

